East European Journal of Physics. 3. 478-490 (2026)
DOI: 10.26565/2312-4334-2026-3-43 ISSN 2312-4334

AB-INITIO INVESTIGATION OF THE PHYSICAL FEATURES OF Pt-Co INTERMETALLIC COMPOUNDS

H. Grimed[1,2], R. Boulechfar[1], H. Ben Sadallah[1], F. Semari[4], Y. Khenioui[5], D. Sayad[3], M. Boudjelal[4], H. Meradji[6]*, S. Ghemid[6], D. Singh[7], R. Khenata[4,8]

[1]*Laboratoire des matériaux et génie énergétique (LMGE), Université 20 Août 1955-Skikda, Algeria*
[2]*Laboratoire LRPCSI, Université du 20 Août1955, B.P 26, Skikda, 21000, Algeria*
[3]*Laboratoire d'Electronique de Skikda (LRES), Department of Electrical Engineering, University 20 Aout 1955-Skikda, 21000, Skikda, Algeria*
[4]*Laboratoire de Physique Quantique de la Matière et de Modélisation Mathématique, Université de Mascara, 29000, Mascara, Algeria*
[5]*Department of Structure and Cladding Materials, Division of Fuel Technology, Draria Nuclear Research Center, PB 43, Sebala, Draria, Algiers, Algeria*
[6]*Radiation Physics Laboratory, Department of Physics, Faculty of Sciences, Badji Mokhtar University, Annaba, Algeria*
[7]*Department of Physics, Prof. Rajendra Singh (Rajju Bhaiya) Institute of Physical Sciences for Study and Research, Veer Bahadur Singh Purvanchal University, Jaunpur-222003, U.P., India*
[8]*Algerian Academy of Sciences and Technologies, Rais Hamidou Villa- El Madania, Algiers 16000, Algeria*
**Corresponding Author Email: hocine.meradji@univ-annaba.dz*
Received April 2, 2026; revised July 11, 2026; accepted August 21, 2026

This article explores the structural, electronic, mechanical, magnetic, and thermodynamic properties of Pt-Co intermetallic compounds using the FP-LAPW (full-potential linearized augmented plane wave) method within the DFT (density functional theory) framework, as implemented in the Wien2k code. The negative formation enthalpies and cohesive energies indicate that Pt_3Co ($L1_2$), PtCo ($L1_0$), and $PtCo_3$ ($L1_2$) are stable in the ferromagnetic (FM) phase. The calculations of the lattice constants and bulk modulus align with existing theoretical and experimental values. The resulting electronic band structure establishes the metallic nature and the magnetic character of all three studied compounds. The DOS at the Fermi level, the electronic specific heat coefficient γ_{th}, polarization P%, and magnetic moment are determined. The investigation of the elastic and mechanical features illustrates that the selected materials are stable and slightly anisotropic. The Pt_3Co and $PtCo_3$ materials are inherently ductile and the PtCo is the harder compound. To enhance understanding of these materials, the quasi-harmonic Debye model is applied to scrutinize their thermal features.
Keywords: *DFT; FP-LAPW; Intermetallic; Electronic Properties; Mechanical constants*

1. INTRODUCTION

Pt-based alloys, in particular, are among the most vital intermetallic materials, finding extensive use in medical devices, thermoelectrics, and electrodes [1, 2]. Alloys of transition metals have gained importance as magnetic materials due to their potential for high-density magnetic recording [3-8]. These systems are especially noteworthy due to Pt extensive role in heterogeneous catalysis and electrochemistry [9-14]. These materials are sought after for an extensive variety of applications, together with high-density magnetic data recording [4], magneto-optics [15-19], magnetic random-access memory (MRAM) [16], oxygen reduction catalysis [16, 20-23], data storage [24], and biomedicine [25]. In the bulk Pt-Co binary alloys, three ordered phases Pt_3Co ($L1_2$), PtCo ($L1_0$), and $PtCo_3$ ($L1_2$) appear in the phase diagram [26]. These compounds have accomplished exceptional consideration in the contemporary expertise for their numerous physical characteristics. Currently, the ordered $L1_2$-Pt_3Co and $L1_2$-$PtCo_3$ compounds are widely used as in the oxygen reduction reaction (ORR) [27-36]. PtCo catalysts exhibit higher ORR activity which makes them as promising ORR catalysts [37-40].

In the scheme of DFT the Pt-based alloys and Pt-Co alloys are the subject of several studies. Gavira *et al*. [41] calculated the mechanical, magnetic, and electrical features of Pt-Co alloys and the superlattice structures Pt_3Co $L1_2$ and PtCo $L1_0$ using DFT. Karoui *et al*. [42] examined the role of magnetism in the formation energies of Co-Pt alloys using non-spin-polarized and spin-polarized ab initio computations to evaluate the stability of the $L1_0$ and $L1_2$ structures with the ABINIT code [43]. Boulechfar *et al.* inspected the stability and ductility of Pt_3Sc and Pt_3Y materials with directed covalent bonding and confirmed the structural stability [44] using the FP-LAPW technique. This later process is employed to study the magnetic and optical features of Pt_3V and Pd_3V compounds. Along with the fundamental properties such as structural, electronic and mechanical properties, the nonmagnetic and ferromagnetic states calculations indicate that the FM-$D0_{22}$ is the most stable, and pseudo gap is owing to the strong *d-d* hybridization in both ductile compounds [45]. Front *et al.* [46] measured mixing enthalpies for concentrated alloys or dissolution enthalpies in the diluted limits of Pt(Co) and Co(Pt), and lattice parameters evaluated by DFT-GGA/PW91 [47], TB-SMA potential. Alsaad *et al.* [24] explored the structural, electronic, and magnetic characteristics of M_XPt_{x-1} (M: V, Ni and Co) by means of the VASP. Chepulskii *et al*. [48] concentrated on adjusting the $L1_0$ atomic order in Co-Pt nanoparticles, providing ab initio perceptions through Monte Carlo simulations. They demonstrated

Cite as: H. Grimed, R. Boulechfar, H. Ben Sadallah, F. Semari, Y. Khenioui, D. Sayad, M. Boudjelal, H. Meradji, S. Ghemid, D. Singh, R. Khenata, East Eur. J. Phys. 3, 478 (2026), https://doi.org/10.26565/2312-4334-2026-3-43

that $L1_0$ is an adaptable structure within the fcc-constrained ground-state phase illustration of Co-Pt. Li *et al.* [49] performed the influences of pressure on the structural, electronic, mechanical, and thermodynamic features of the typical Pt_3M (M: Al, Sc, Co, Y, Hf, Zr) materials using the VASP [50]. The authors observed that the charge distribution remains largely unchanged, suggesting that no phase transition takes place within the 0–100 GPa range. Furthermore, Zosiak *et al*. [51] studied the electronic structure of Co-Pt-grounded arrangements, from bulk to nano alloys, using ab initio methods. Zhang *et al.* employed the (VASP) code to address the plastic behavior of Pt_3Hf compound [52]. Aledealat *et al.* employed Monte Carlo simulation and DFT to examine the magnetic and electronic features of binary alloys X_3Pt and XPt_3 (X: Ni, Co, or Fe), in $L1_2$ structure and the ferromagnetic states [53]. They calculated Curie temperature (*Tc*) and the magneto crystalline anisotropy for the studied alloys. By means of the CASTEP, the fundamental physical features are investigated for Pt_3X (X = Ti, Cu) [54] and Pt_3T (T: Ni, Mn) [55] intermetallic compounds. More recently, Wei [56] examined the effect of atomic doping (Au, Ir, Os, Pd, Rh, Ru) on the ground states features of Pt-based alloys using first-principles methods. The study revealed that doping increases the dislocation energy and reduces the plasticity of the solid solution.

In recent years, the $L1_0$-ordered intermetallic compounds FeX and CoX (X is a *d* transition metal) were studied using both first-principles calculations and experimental methods. Rani *et al.* explored the magnetism of $L1_0$-FeNi alloy through inducing tetragonal distortion with the interstitial doping. The results show that the structural distortion induces enormous magneto crystalline anisotropy (MCA) and the rise in MCA is larger for N-doping in Ni-layer than in Fe-layer [57]. Aledealat *et al.* [16] in the theoretical study of the magnetic features of $L1_0$-ordered FeM (M: Ni, Pt or Pd) alloys, report that the ferromagnetic configuration is the furthermost stable spin arrangement for the compounds in interest, and FePt alloy possesses a large magnetocrystalline anisotropy. Islam *et al.* [58] investigated ordered $L1_0$-CoPt nanoparticles using both experimental techniques and DFT calculations. Lethole *et al.* [5] studied mechanical, electronic, magnetic, and dynamical characteristics of M-Pt alloys (M: Mn, Ni and Co). Their achieved values reveal that MnPt and NiPt alloys stay stable at 0 K, whereas, CoPt remains marginally metastable aligning fairly well with most experimental phase stability diagrams. Recently, Zine *et al.* conducted a theoretical investigation on the structural, magnetic, electronic, and thermodynamic properties of Tetrataenite $L1_0$-FeNi alloy [59]. Subsequently, they investigated the impacts of cobalt (Co) doping on the $L1_0$-FeNi alloy [60]. The results show that the FeNi:Co(O_{Ni}) in $L1_0$-structure exhibits a big enrichment in saturation magnetization (M_s) and magnetic moments. Co-substituted FeNi alloys grasp potentials as budding entrants for the rare-earth-free permanent magnets. Notice that, according to the previous works three Pt-Co compounds possess ferromagnetic state, Pt_3Co [61, 62], PtCo [63-65] and $PtCo_3$ [63,64]. These alloys are of particular interest due to their remarkable structural and magnetic properties, as well as their wide range of applications in emerging technologies.

Although numerous studies have explored these alloys, there is still a deficiency of comprehensive research work on the detailed physical features of Pt_3Co, PtCo and $PtCo_3$ in the existing data. Consequently, the principal objective of the present investigation is to explore the impressive physical features of Pt_3Co, PtCo and $PtCo_3$ compounds, and understand the physical origins of their distinct characteristics. In this study, using the FP-LAPW technique, we explored the structural stability, the electronic, mechanical magnetic and thermodynamic features for compounds in question, in non-magnetic (NM) and ferromagnetic (FM) states.

2. COMPUTATIONAL DETAILS

The computations reported in the current investigation have been accomplished with the help of the Wien2K code [66] based on full-potential linear augmented plane-wave (FP-LAPW) technique [67] inside the framework of DFT. The generalized gradient approximation (GGA) plus Perdew–Burke–Ernzerhof (PBE) parameterization was utilized for the exchange–correlation functional [50, 68]. The cut-off parameter has been set to $R_{MT}\times K_{max} = 9$, where R_{MT} is the muffin-tin sphere radius and K_{max} is the highest value of the plane wave vector. To calculate the entire energy, 84 special k-points are exploited for the irreducible Brillouin zone in the $L1_2$ structure and 75 for the $L1_0$structure, l_{max} =10 and the charge density is Fourier-expand fit for G_{max}=13. For the muffin-tin sphere radii, we applied R_{MT} (Pt)=2.25 a.u, R_{MT} (Co)=2.00 a.u. The changes in total energy during the optimization ultimately converge to 10^{-4} Ry. The valence electron configurations: Pt: [Xe]. $4f^{14}\ 5d^9\ 6S^1\ 6p^0$ and Co: [Ar]. $4S^2\ 4p^0\ 3d^7\ 4f^0$.

3. RESULTS AND DISCUSSION

3.1. Structural features

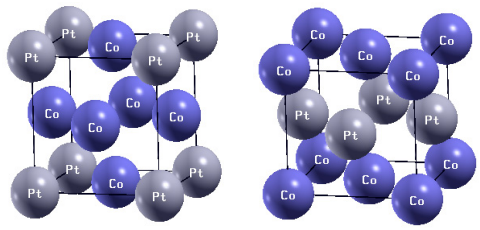

a b

Figure 1. $PtCo_3$ in $L1_2$ structure (a) and PtCo in $L1_0$ structure (b)

The Pt-Co alloy is recognized to have a robust propensity for assembling so as to its phase diagram has been investigated by three key ordered phases, the Pt_3Co ($L1_2$), PtCo ($L1_0$) and $PtCo_3$ ($L1_2$). Both compounds with stoichiometry A_3B crystallize in the cubic $L1_2$ structure (*Prototype: Cu_3Au*) with space group $Pm\bar{3}m$ (*cP4*), where the B atoms occupy the corners of the cube 1*a* (0, 0, 0), and the A atoms set on the face centres 3*c* (1/2, 1/2, 0). PtCo compound crystallizes in tetragonal $L1_0$ (*Prototype*: *AuCu*) with space group *P4/mmm* (*tP2*). This is a tetragonal distortion of the fcc structure and has two of the faces occupied by one type of atom (1*c* (1/2, 1/2, 0)) and the corner (1*a* (0, 0,0)), and the other face occupied with the second type of atom (*2e* (0, 1/2, 1/2)) (Fig. 1**)**.

To determine the structural features, the overall energy is evaluated in relation to the global volume for Pt_3Co, PtCo, and $PtCo_3$ compounds for both nonmagnetic and ferromagnetic states in the $L1_2$ and $L1_0$ structures. The overall energy values in relation to unit cell volume have been tailored via Murnaghan's equation of state [69]. The attained data by means of PBE-GGA approximation have been exposed in Fig. 2.

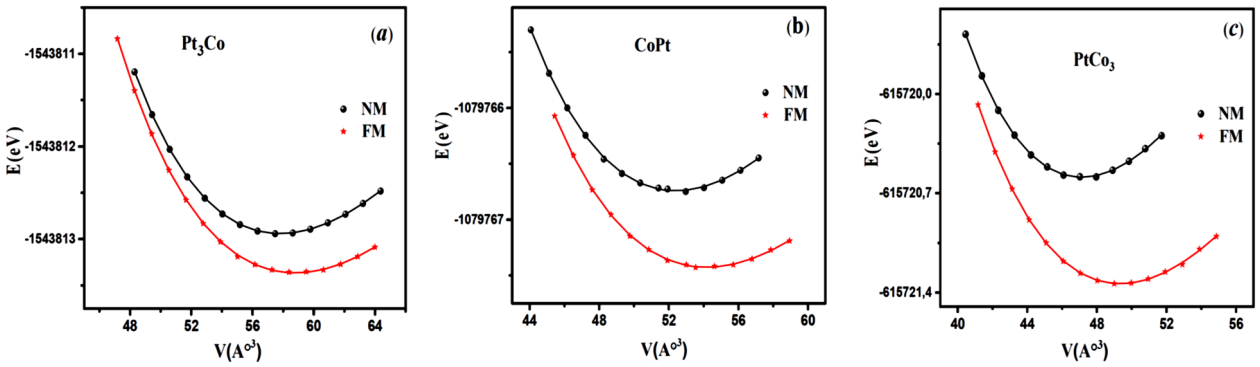

Figure 2. Entire energy vs. volume in the nonmagnetic (NM) and ferromagnetic (FM) states of (a) Pt_3Co, (b) PtCo and (c) $PtCo_3$

It can be perceived that the total energy of the ferromagnetic state is far less than that of nonmagnetic states, demonstrating that the FM state is the magnetic ground state for all materials deliberated here. The overall energy difference (ΔE) between FM and NM states at equilibrium is calculated as follows:

$$\Delta E = E_{FM} - E_{NM} \quad (1)$$

The equilibrium total energy calculation determines the crucial physical parameters such as the cohesive energy E_c and formation enthalpy ΔH_f and describes the structural stability. The values of E_c have been evaluated using the succeeding formula:

$$E_c = \left(\frac{1}{x+y}\right)\left[E_{tot}^{Pt_xCo_y} - xE_{tot}^{atom(Pt)} - yE_{tot}^{atom(Co)}\right] \quad (2)$$

where $E_{tot}^{Pt_xCo_y}$ is the aggregate energy of Pt_xCo_y alloy and $E_{tot}^{atom(Pt)}$ and $E_{tot}^{atom(Co)}$ are the energies of the isolated atoms Pt and Co, respectively.

The enthalpy of formation of these alloys was determined using:

$$\Delta H_f = \left(\frac{1}{x+y}\right)\left[E_{tot}^{Pt_xCo_y} - xE_{tot}^{Pt(solid)} - yE_{tot}^{Co(solid)}\right] \quad (3)$$

where $E_{tot}^{Pt(solid)}$ and $E_{tot}^{Co(solid)}$ are the energies per atom of Pt and Co in the solid-state, correspondingly.

In Table 1, the obtained values of ΔE, E_c and ΔH_f are equated with accessible experimental and theoretical information.

Table 1. ΔE (meV/atom), ΔH_f (eV/atom), referred to Co(fcc)/Co(hcp) and Pt (fcc) and E_c (eV/atom), for Pt_3Co, PtCo and $PtCo_3$ for both nonmagnetic (NM) and ferromagnetic (FM) cases

Compounds	ΔE	ΔH_f (NM)	ΔH_f (FM)	E_c (NM)	E_c (FM)
Pt_3Co	-106*	-0.029*/-0.034*	-0.089*/-0.084* -0.07[a] /- -/-0.1[b] -/-0.12[c] -0.067[d]/- -0.0745[e]/-	-0.802*	-0.055*
PtCo	-172*	-0.022*/-0.028* -0.02 [a] / - -0.0354[e]/ -	-0.099*/-0.088* -0.1[a] / - - /-0.110 [b] -/-0.07[c] -0.099[d]/- -0.095[f]/- -0.079[j]/- -0.089[h]/-	-2.781*	-1.96*
$PtCo_3$	-471*	-0.018*/-0.034*	-0.07*/ -0.057* -0.07[a]/- -/-0.1[b] -0.0688[d]/-	-4.69*	-3.875*

*Our calculation: [a]Ref. [42] PAW, [b]Ref. [51] PP-GGA, [c]Ref. [73] Exp, [d]Ref. [8] PP-PAW, [e]Ref. [74], PP-PAW- GGA, [f]Ref. [65] KKR-CPA, [j]Ref. [65] PP-LDA, [h]Ref. [65] PP-GGA.

The overall energy difference ΔE at the equilibrium volume, in meV/atom unit, is ordered as follows: $PtCo_3$(-471)<PtCo(-172)<Pt_3Co (-106). ΔE have a considerable value for $PtCo_3$ case, with high Co concentration, which specifies the decisive part of the spin effect in the thermodynamic stability.

The enthalpies of formation assist in predicting the stability of alloys and helps in developing their phase diagrams [70]. The formation enthalpy results are evaluated relative to the Co-fcc/Co-hcp and Pt-fcc states. From Table 1, it can be observed that the studied compounds exhibit negative enthalpies of formation for the NM and FM states, suggesting that they are chemically stable and readily synthesized. According to the present findings, 3 materials' alloying abilities are as follows: PtCo>Pt_3Co>$PtCo_3$. For FM states, lower formation enthalpies correspond to larger alloying ability [71,72], whereas, for NM states, the formation enthalpies are ordered as Pt_3Co >PtCo >$PtCo_3$. On the other hand, for each compound the ΔH_f for FM states is lower than the NM states. The negative valued cohesive energies suggest that all compounds are stable in the considered phases. The $PtCo_3$ compound possesses the higher structural stability due to the larger cohesive energy relative to the PtCo and Pt_3Co. It can be concluded that the cubic (tetragonal) $PtCo_3$ (PtCo) and Pt_3Co compounds crystalize in the FM-$L1_2$ (FM-$L1_0$) phase and these results agree well with experimental phase diagram [70]. Comparatively, our results (ΔH_f values) are in upright promise with several reported values [8,42,51,65,73,74] (Table 1). However, as far as we know, there are no accessible information in the literature for cohesive energies.

The equilibrium lattice constants (*a* and *c*), bulk modulus, *B*, and its pressure derivative B′ follow from an appropriate form of the entire energy in terms of volume to the (MEOS) Murnaghan equation of state [69]. The key results are summarized in Table 2. The comparison with the experimental results [75,77-79] and theoretical results [8,24,51,65,76] shows good overall agreement for a, c, and *B*. Both computations effectively forecast the durable impact of magnetism on chemical ordering. The results for a and c are in good agreement with the available experiments. The discrepancy between the evaluated equilibrium volumes and the corresponding experimental values is less than 2.4%.

Table 2. a (in Å), c (in Å), and c/a ratio, B in (GPa), and B′ for Pt_3Co, PtCo, and $PtCo_3$ compounds

Compounds	Method	a	c	c/a	B	B′
Pt_3Co	This work					
	GGA(NM)	3.86*	-	-	225*	5.01*
	GGA(FM)	3.88*	-	-	304*	4.74*
	Experimental	3.831[a]	-	-	-	-
	Other calculations					
		3.871[b]	-	-	-	-
		3.89[c]	-	-	-	-
	NM	3.87[d]	-	-	268.4[d]	-
	FM	3.89[d]	-	-	254.4[d]	-
		3.86[e]	-	-	-	-
		3.885[f]	-	-	-	-
PtCo	This work					
	GGA(NM)	3.798*	3.634*	0.957*	252*	4.40*
	GGA(FM)	3.808*	3.732*	0.979*	216*	4.82*
	Experimental	3.810[j]	3.695[j]	0.971[j]	-	-
	Other calculations					
	NM	3.823[d]	3.641[d]	0.952[d]	250.5[d]	-
	FM	3.821[d]	3.703[d]	0.969[d]	229.4[d]	-
		3.810[e]	3.718[e]	0.976[e]	-	-
		3.809[f]	3.708[f]	0.973[f]	-	-
		3.806[h]	3.707[h]	0.979[h]	-	-
		3.746[i]	3.622[i]	0.967[i]	-	-
		3.819[g]	3.715[g]	0.973[g]	-	-
		3.800[k]	3.693[k]	0.972[k]	-	-
$PtCo_3$	This work					
	GGA(NM)	3.61*	-	-	252.8*	4.70*
	GGA(FM)	3.668*	-	-	209.6*	4.65*
	Experimental	3.664[l]	-	-	-	-
	Other calculations					
		3.672[b]	-	-	-	-
		3.666[c]	-	-	-	-
	NM	3.612[d]	-	-	299.0[d]	-
	FM	3.661[d]	-	-	259.6[d]	-
		3.66[e]	-	-	-	-
		3.654[f]	-	-	-	-

*Our calculation: [a]Ref. [75] exp, [b]Ref. [53] PP- PAW- GGA and MC, [c]Ref. [76] PAW-GGA , [d]Ref. [51] PP-GGA, [e]Ref. [42] PAW-GGA, [f]Ref. [8] PP-PAW, [j]Ref. [77] exp, [h]Ref. [24] PP-GGA, [i]Ref. [65] PP-LDA, [g]Ref. [65] PP-GGA, [k]Ref. [78] exp, [l]Ref. [79] Exp.

3.2. Electronic structure and magnetic Properties

Proportional stability can be discussed in detail by studying the electronic properties of the compound. To comprehend the electronic structure and magnetic features of Pt-Co binary materials, the band structure along selected

high-symmetry directions in the first Brillouin zone, the total density of states (TDOS), and partial density of states (PDOS) at equilibrium lattice constants have been calculated. Although the cohesive properties suggest that the nonmagnetic states could be synthesized experimentally. The TDOS of the studied compounds have been shown in Fig. 3(a). The foremost feature is the Fermi level lying at high DOS peaks, as also reported by Karoui *et al*. for paramagnetic PtCo, thereby promoting the instability of the nonmagnetic phase toward ferromagnetism [42].

Figs. 3(b and c) show the combined band structure and TDOS (for both spins) of Pt_3Co. For simplicity, and due to their similarity, the corresponding figures for PtCo and $PtCo_3$ are not shown. The valence and conduction bands exhibit significant overlay, with numerous bands crossing the Fermi level, indicating metallic behavior in all compounds. The noticeable asymmetric band distribution of spin-up and spin-down bands reflects the strong magnetic character of the Pt–Co binary compounds.

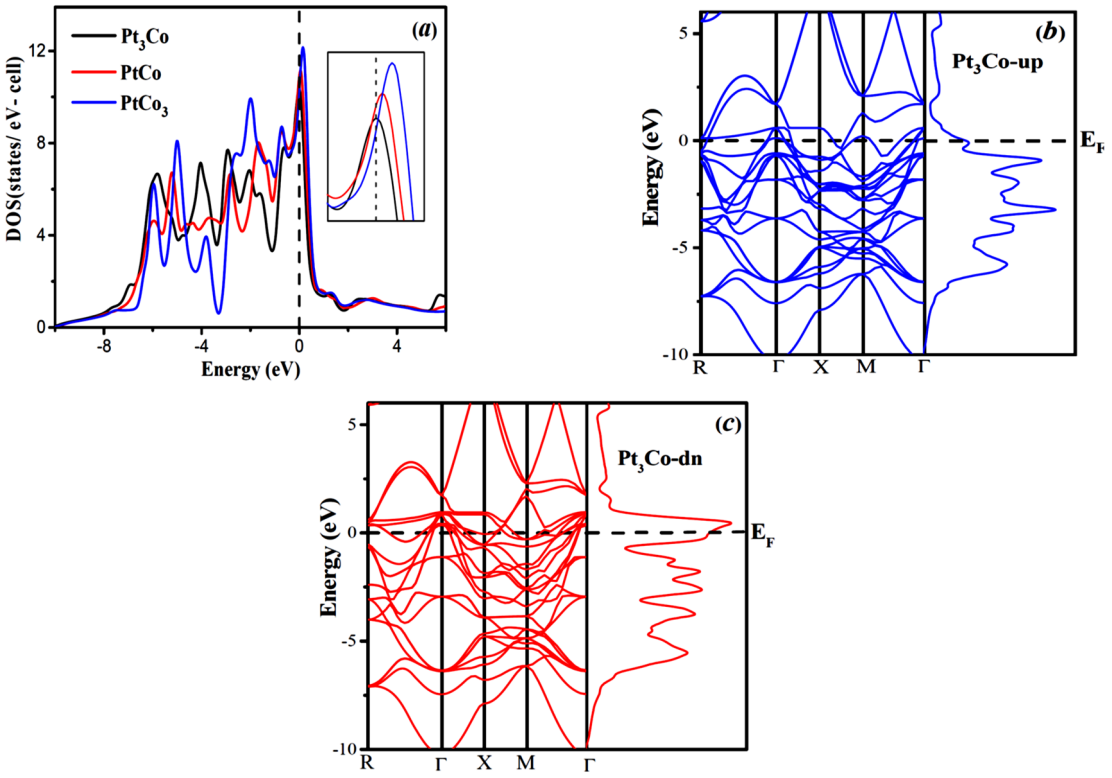

Figure 3. TDOS of Pt_3Co, PtCo and $PtCo_3$ compounds in NM states (a), band structure with the corresponding DOS of spin up (b) and spin down for Pt_3Co compound (c)

Figure 4 shows the PDOS for all compounds. It can be observed that the electronic states are strongly because of Pt-5d and Co-*3d* orbitals; and the contributions of *s* and *p* orbitals in the DOS are negligible compared to the *d* band contribution. Therefore, the Pt and Co-*d* states are the main origin of the absolute spin polarization. The bands crossing the Fermi level are chiefly composed of hybridized Pt-5*d* and Co-3*d* states. Table 3 reports the TDOS at the Fermi level N(EF), and the magnetic moment per atom. The overall magnetic moments for the investigated materials are 2.98, 4.5, and 5.66 (μB) for Pt_3Co, PtCo, and PtCo3, respectively. The results have been matched with the obtainable results [8, 24, 51, 53, 58, 82]. In addition, the degree of polarization, which is evaluated by the fractional difference between the two spin states at the Fermi level (E_F), is given below [80, 81].

$$P = \frac{n_{\uparrow}(E_F) - n_{\downarrow}(E_F)}{n_{\uparrow}(E_F) + n_{\downarrow}(E_F)} \tag{4}$$

where $n_{\uparrow}(E_F)$ *and* $n_{\downarrow}(E_F)$ are, respectively, the spin-up and spin-down DOS at the Fermi level.

The value of P discriminates the material type: P=0 corresponds to a paramagnetic state, while a finite value indicates antiferromagnetic nature. The obtained polarization values for all compounds are abridged in Table 3. It is worth mentioning that neither $n_{\uparrow}(E_F)$ nor $n_{\downarrow}(E_F)$ vanishes at E_F, resulting in a non-zero value of P, suggesting ferromagnetic systems. The electronic specific heat coefficients values are found out by means of the below equation:

$$\gamma_{th} = \pi^2 {k_B}^2 N(E_F)/3 \tag{5}$$

where k_B is the Boltzmann constant. The calculate values are 24.32, 25.08 and 23.08mJ/ mol^{-1} K^{-2} for Pt_3Co, PtCo and $PtCo_3$, respectively (Table 3).

Table 3. TDOS at N(E_F) (states/eV- cell), γ_{th} (mJ/mol. K^2), $n_\uparrow$ (E_F), $n_\downarrow$ (E_F) DOS at Fermi level for spin up and spin down, respectively, degree of polarization P %, and entire magnetic moment μ (in μB) for Pt_3Co, PtCo and $PtCo_3$.

System	N(E_F)	γ_{th}	μ	$n\uparrow(E_F)$	$n\downarrow(E_F)$	P %
Pt_3Co	10.32*	24.32*	Tot:2.98*;3.47[a];2.92[b];2.8[c];2.47[c] (Co:1.99, Pt:0.34)* (Co: 1.89, Pt: 0.24)[d]	1.54*	3.96*	-44*
PtCo	10.64*	25.08*	Tot:4.5*;4.31[e];2.38[f];2.26[j] (Co:1.91; Pt:0.41)* (Co: 1.96, Pt: 0.25)[j] (Co: 1.83, Pt: 0.37)[d] (Co:1.74; Pt:0.44)[f]	0.78*	3.67*	-64*
$PtCo_3$	9.79*	23.08*	Tot:5.66*;6.72[a];5.6[b] (Co:1.83; Pt:0.4)*	0.73*	4.19*	-70*

*Our calculation, [a]Ref. [53] PBE + U , [b]Ref.[8] PP- PAW, [c]Ref. [82] exp, [d]Ref. [83] SP-GGA, [e]Ref. [24], PP- PAW, [f]Ref. [58] PBE-GGA, [j]Ref. [51] PP.

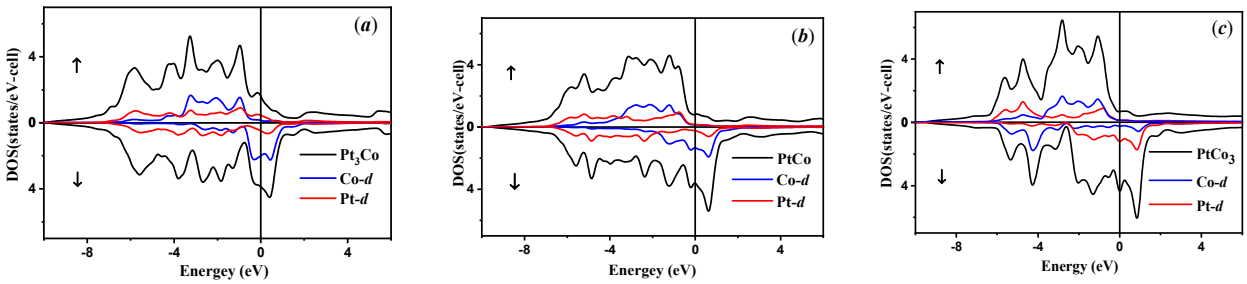

Figure 4. Spin polarized, TDOS and PDOS for Pt_3Co (a), PtCo (b), and $PtCo_3$ (c)

3.3. Single-crystal elastic properties

Recently, the study of elastic parameters has played a crucial role in materials science and engineering. The elastic constants C_{ij} reflect the mechanical response of crystals to applied external forces. In this section, we discuss the stability, ductility, anisotropy and bonding features of Pt-Co binary compounds. In the current investigation, the single-crystal elastic constants C_{ij} for the selected compounds have been evaluated using the IRelast program implemented in the WIEN2k package [66] with the PBE-GGA approximation. The attained values are tabulate in Table 4, we can observe that, for cubic structure, 3 independent elastic constants C_{11}, C_{12} and C_{44}, satisfy the Born mechanical stability criteria (C_{11}> 0, C_{44}> 0, $C_{11} + 2C_{12} > 0$, and C_{11}- C_{12} >0) and for tetragonal phase the six independent coefficient satisfy stability criteria (C_{11}> 0, C_{33}> 0, C_{44}> 0, C_{66}> 0, $(C_{11} - C_{12}) > 0$, $(C_{11} + C_{33} - 2C_{13}) > 0$ and $[2(C_{11} + C_{12}) + C_{33} + 4C_{13}] > 0$) [84].

Table 4. C_{ij} (GPa), B (GPa), G (GPa), E (GPa), B/G ratio, ν, and Hv for Pt_3Co, PtCo and $PtCo_3$

Compounds	C_{11}	C_{12}	C_{13}	C_{33}	C_{44}	C_{66}	**B**	G	E	B/G	ν	Hv
Pt_3Co	317.8*	172.5*	-	-	104.5*	-	220.9*	90.3*	241.8*	2.44*	0.31*	6.78*
	322[a]	218[a]			93.1[a]		252[a]					
							232.6[b]	93.6[b]	247.7[b]	2.48[b]	0.32[b]	
	321.2[c]	188.3[c]			117.9[c]						0.32[c]	
											0.33[d]	
PtCo ($L1_0$)	456.4*	149.4*	158.6*	305.5*	164.5*	102.5*	235.3*	132.2*	334.0*	1.77*	0.26*	14.7*
	323[a]	210[a]			87.4[a]		231[a]					
$PtCo_3(L1_2)$	302.1*	165.6*	-	-	152*	-	211.1*	110.2*	299.4*	1.90*	0.26*	11.6

*Our calculation: [a]Ref. [14] 2NN MEAM, [b]Ref. [74] PP- PAW- GGA, [c]Ref. [59] PP- PAW- GGA, [d]Ref. [100] PP- PAW- GGA.

The two elastic constants C_{11} and C_{33} describe the stiffness along the crystallographic *a (or b)* and *c* axes, respectively. For PtCo in tetragonal phase $L1_0$, we can constat that the C_{11}>C_{33}, the compound resists deformation along the *a* (or *b*)-axis more strongly than the *c*-axis (is additional compressible along the c-axis than that of along *a*- and *b*-axis), demonstrating that the bonds are stronger along <100> and <010> directions as comparation to bonds along <001> direction. C_{44} reflects the resistance to shear in the (100) plane, and C_{66} measures the resistance to shear along <110> orientation. Indicating the material is harder to shear along c-axis than in-plane.

We can see that C_{11} and C_{12} are closer in cubic compounds, indicating that the two materials have the same response to uniaxial compression and lateral deformation, whereas C_{44} ($PtCo_3$)> C_{44} (Pt_3Co) indicates $PtCo_3$ possesses superior resistance to shear deformation. On the contrary, both compounds resist longitudinal deformation more than shape deformation (C11 > C12 > C_{44}).

The comparison with the previously reported values shows a good agreement with Ref [14,49] for Pt_3Co compound and a considerable deviation for PtCo [14]. To our knowledge, no data are available in the literature for PtCo3-L12, so the results of the present investigation can serve as a guide for future investigations.

3.4. Mechanical properties and dynamic stability

The Voigt–Reuss–Hill (VRH) approximation is applied to estimate the polycrystalline mechanical parameters of materials by averaging the Voigt (upper**)** and the Reuss (lower) limits [85-87]. The polycrystalline bulk modulus (*B*) denotes resistance to volume change with uniform compression**)** and shear modulus (*G*) refers resistance to shape change, shear deformation**;** for isotropic aggregates are $B = (B_V + B_R)/2$ and $G = G_V + G_R/2$, repectively. B_V (B_R) and G_V (G_R) represent the Voigt's (Reuss's) bulk modulus and the Voigt's (Reuss's) shear modulus respectively. According to Refs. [85] and [86], Voigt and Reuss modulus are derived from the independent single-crystal constants C_{ij}.

The computed elastic modulus B and G of Pt_3Co, PtCo and $PtCo_3$ are enumerated in Table 4. Table 4 shows accord with the bulk modulus values obtained from the equation of state. This serves as proof of the consistency and accurateness of the elastic constants we've calculated for these compounds.

In accordance with our analysis, PtCo-L10 has a large bulk modulus, indicating high incompressibility. The shear modulus *G* (modulus of rigidity*)* of the studied compounds is in order: PtCo > Pt_3Co >$PtCo_3$, thus the tetragonal PtCo resists more the shear deformation (shape change without volume change) than the cubic compounds. Hence, we can predict with strong directional covalent bonds in PtCo.

The Young's modulus (*E*) and Poisson's ratio (ν) have been given below:

$$E = \frac{9BG}{3B+G} \tag{6}$$

$$\nu = \frac{3B-2G}{2(3B+G)} \tag{7}$$

The Young's modulus value of PtCo is greater than that of $PtCo_3$ and Pt_3Co, consequently, PtCo is stiffer than other compounds. The Young modulus describes the stickness of the compound [88]. Furthermore, ductility of Pt-Co binary compounds is determined based on the Pugh's criteria (*B*/*G*) [89] (critical value of Pugh's criteria is equal to 1.75: ductility >brittleness), the Pugh's criteria are larger than 1.75 for the selected materials, indicating the ductility of compounds, the PtCo behave with low ductility, *B*/*G* is 1.77, whereas Pt_3Co behave with high ductility, B/G is 2.44. Li *et al* [49, 74] have found that when *B*/*G* > 1.75, it suggests that Pt_3Co is ductile. According to Poisson's ratio values, if ν> 0.26, the material performs in a ductile manner, else it is brittle [90]. Hence, Pt_3Co is ductile and PtCo possesses a low ductility *i.e.* is brittle. According to Pettifor the Cauchy pressure, for ductile materials with metallic bonding, are positive, it's the case of the studied cubic compounds (Pt_3Co and $PtCo_3$, Table 5). The more negative the Cauchy pressure, the more directional covalent or ionic bonds, were directional bonding leads to brittleness. The positive/negative Cauchy pressure C_{12}-C_{66}/C_{13}-C_{44} suggests the mixture of bonding and weak of ductility of tetragonal PtCo material. The Vickers hardness (H_V) is applied to guesstimate the resistance of the Pt-Co binary materials to plastic deformation. the formula used to calculate H_V [91] is:

$$H_v = 2\left(\frac{G^3}{B^2}\right)^{0.585} - 3 \tag{8}$$

The evaluated hardness is itemized in Table 4. Hence, Pt_3Co has the lowermost H_V owing to its relative ductility and metallic bonds. whereas, the PtCo compound has the maximum Hv due to the stronger covalent bonding.

The longitudinal and transverse acoustic velocities v_l ($v_l = [(3B + 4G)/3\rho]^{\frac{1}{2}}$) and v_t ($v_t = G/\rho$), respectively, are determined as well as the mean sound velocity v_m ($v_m = \left[\frac{1}{3}\left(\frac{1}{{v_l}^3} + \frac{2}{v_t^3}\right)\right]^{\frac{-1}{3}}$), in order to calculate the Debye temperatur Θ_D using Refs. [92, 93]:

$$\theta_D = \frac{h}{k_B}\left[\left(\frac{3n}{4\pi}\right)\frac{N_A}{M}\right]^{\frac{1}{3}} v_m \tag{9}$$

where k_B, h, and ρ denote Boltzmann's constant, Plank's constant, and the density, correspondingly. N_A, M and n refer the Avogadro's number, the molecular weight and the number of atoms in the molecule respectively. In addition, the approximate melting temperature of the selected compounds has been evaluated using the succeeding empirical equation [94]:

$$T_m = [553\ \mathrm{K} + (5.91\ \mathrm{K/GPa})C_{11}] \pm 300\mathrm{K} \tag{10}$$

The evaluated values of the acoustic velocities (v_t, v_l and v_m**)**, Debye temperature θ_D and melting temperature T_m have been provided in Table 5 for the selected Pt_3Co, PtCo and $PtCo_3$. The values v_t, v_l *and* v_m for Pt_3Co are coincide with theoretical data [49]. The longitudinal velocities of sound in all considered alloys is considerably greater than in the transverse velocities. Out of these, $PtCo_3$ supports the highest supremely average sound velocity ($v_m = 3294.96$ m/s**)**.

Table 5. C_P=C_{12}–C_{44} for cubic, (C_{12}–C_{66})/(C_{13}–C_{44}) ratio for tetragonal structures, A^U, ν, V_l (in m/s), V_t (in m/s), V_m (in m/s), θ_D (in K) and T_m (K) for Pt_3Co, PtCo and $PtCo_3$

Compounds	C_{12}-C_{44}	C_{12}-C_{66}/C_{13}-C_{44}	A^U	V_l	V_t	V_m	$\boldsymbol{\theta_D}$	T_m∓300
Pt_3Co	68	-	0.15*	4317*	2221*	2487*	302.9*	2431*
			0.4[a]	4421[a]	2263[a]	2535[a]	308.6[a]	
			0.46[b]					
PtCo	-	47/-6	0.39*	5040*	2856*	2009*	402.0*	3176*
$PtCo_3$	14	-	0.81*	5331*	2958*	3295*	425.4*	2338*

*Our calculation: [a]Ref. [74] PP- PAW- GGA, [b]Ref. [49] PP- PAW- GGA.

A larger θ_D designates an augmented thermal conductivity [95] signifying that the $PtCo_3$ is anticipated to show a relatively greater thermal conductivity matched with the other materials. In [74], Li *et al.* described a Debye temperature (θ_D) of 308.6 K for Pt_3Co, which discloses a concordance to the achieved calculated value of 302.9 K.

From Table 5, it can be observed that all compounds melt at high temperatures. According to the experimental Pt-Co phase illustration [70] and our T_m values are over estimate. The Pt-Co system has, at low temperatures, an ordered fcc structure and a disordered one at high temperatures. The order-disorder transition temperatures were experimentally reported to be 1000, 840 and 1100 K for Pt_3Co, $PtCo_3$ and for PtCo, respectively [96]. The chemical ordering is attributed to the magnetic moment of Pt and Co atoms [97].

In addition, in the (VRH) scheme the material's anisotropy is also given via the universal anisotropic index A^U(A^U=5G_V/G_R+(B_V/B_R)–6) [98]. The evaluated results of A^U for Pt-Co intermetallic materials are gathered in Table 5. The deviation of all A^U indexes from zero (A^U = 0 for an isotropic crystal) [99] indicates the anisotropic behavior of the three compounds, with $PtCo_3$ exhibiting a relatively greater degree of elastic anisotropy.

The 3D-representation of the dependence of the elastic modules on the crystallographic direction is a modern method applied to estimate the degree of elastic anisotropy in materials. Fig. 5 depicts the 3D-representation of the Young's modulus for Pt-Co binary materials. It is clearly seen that there is a small nonconformity from spherical shape suggesting modest degree of elastic anisotropy for all compounds. In materials sciences, the spherical 3D surface shape of Young's modulus corresponds to isotropic materials.

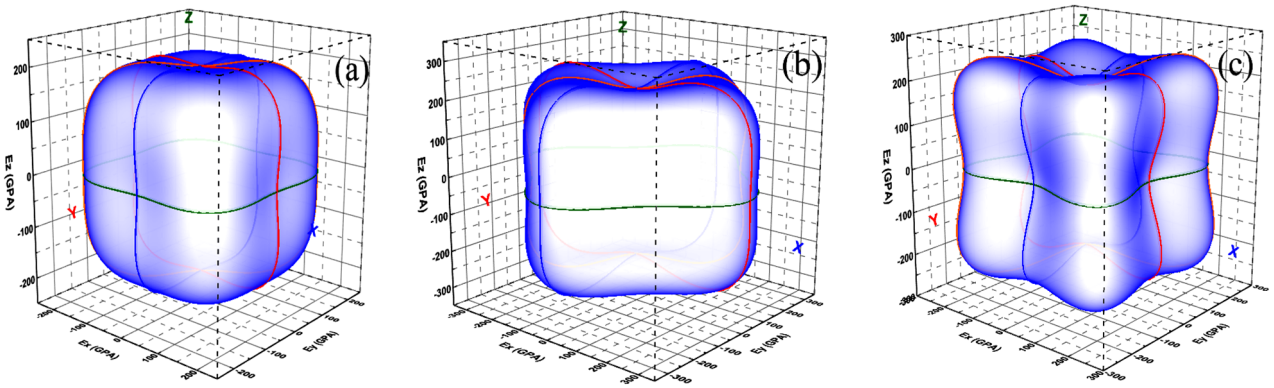

Figure 5. 3D-presentation of the surface related to Young's modulus (Y) for: Pt_3Co (a), PtCo (b),: $PtCo_3$(c) compounds

3.5. Thermal properties

In this subdivision, the thermodynamics features of ferromagnetic Pt-Co binary intermetallics materials are explored versus temperature (0-1000 K) and pressure (0-30). The main values of bulk modulus *B*, heat capacities C_V and C_P, Debye temperature θ_D, thermal expansion coefficient α, the Grüneisen parameter γ_G and entropy *S* have been tabulated in Table 6 and some of them have been shown in Fig. 6.

Table 6. Temperature and pressure dependent *B* (in GPa), C_V and C_P (in J/mol. K), α (10^5/K), θ_D (K), γ_G and *S* (in J/mol. K)

Compounds	T	P	B	C_V	C_P	*A*	θ_D	γ_G	S
Pt_3Co	0	0	229.3*	0*	0*	0*	372.1*	3.1*	0*
		30	388.5*	0*	0*	0*	475.2*	2.0*	0*
	300	0	207.1*	92.8*	96.4*	4.0*	363.4*	3.2*	117.4*
		30	380.4*	88.3*	89.2*	1.4*	472.9*	2.0*	93.5*
	900	0	121.0*	99.1*	131.5*	8.9*	319.6*	4.0*	236.6*
		30	349.6*	98.4*	102.0*	1.8*	462.7*	2.1*	200.0*
PtCo	0	0	215.6*	0*	0*	0*	405.2*	2.77*	0*
		30	366.7*	0*	0*	0*	509.5*	1.8*	0*
	300	0	195.7*	45.8*	47.4*	4.1*	396.6*	2.88*	54.7*
		30	359.7*	43.4*	43.8*	1.5*	507.0*	1.8*	43.7*

Compounds	T	P	B	C_V	C_P	A	θ_D	γ_G	S
	900	0	120.7*	49.5*	63.1*	8.6*	355.3*	3.5*	113.0*
		30	331.4*	49.1*	50.7*	1.9*	497.6*	1.8*	96.5*
$PtCo_3$	0	0	208.9*	0*	0*	0*	452.2*	2.3*	0*
		30	339.9*	0*	0*	0*	566.73*	1.8*	0*
	300	0	198.3*	89.5*	91.8*	3.5*	445.4*	2.3*	98.8*
		30	333.9*	84.1*	84.9*	1.7*	563.8*	1.8*	78.3*
	900	0	136.9*	98.5*	108.9*	5.1*	451.7*	2.2*	202.4*
		30	271.6*	97.5*	100.5*	2.0*	599.5*	1.6*	174.6*

* Our calculation.

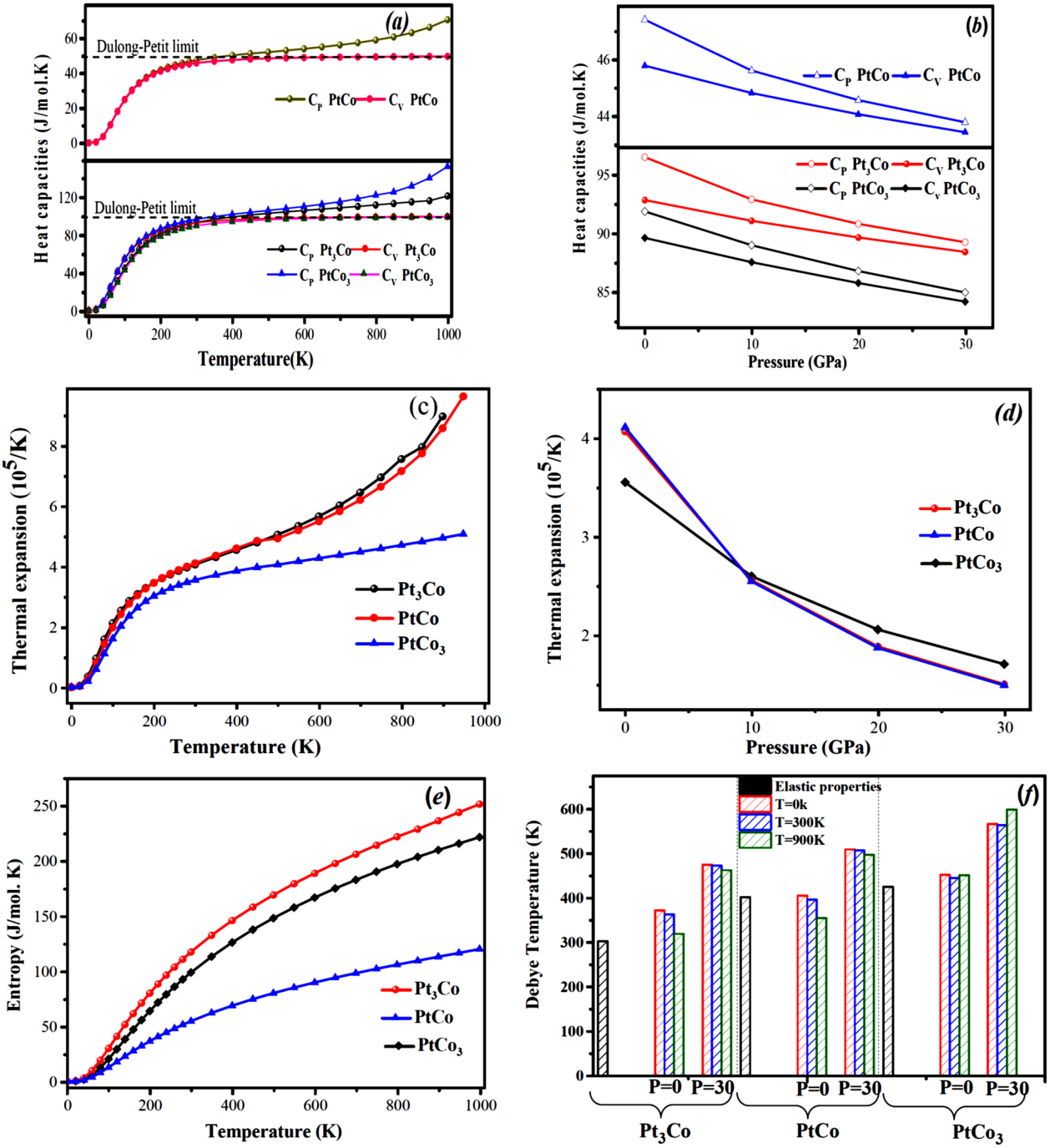

Figure 6. Temperature and pressure dependent thermodynamic parameters of Pt-Co binary materials: (a, b) C_P and C_V, (c, d) α and (e) S

Based on the quasi-harmonic Debye model and the unit cell energies E(V), obtained in the first subsection, as input data, the GIBBS code [101] is used to illustrate both temperature and pressure influences. A thorough explanation of this process is given in the literature [101]. At ambient temperature and zero pressure (P=0), the values of C_V (C_P)

are 89.5 (91.8) and 92.8 (96.4) $Jmol^{-1}$ K^{-1} for $PtCo_3$, and Pt_3Co, correspondingly, with values impending zero at low temperatures. These values are 45.8 (47.4) $Jmol^{-1}$ K^{-1}, respectively, for CoPt. From Fig. 6(a), it can be understood that both quantities upsurge with T^3 at temperatures below 400 K.Beyond this range, the anharmonic things on the heat capacity C_V become insignificant for all compounds. As a result, C_V reaches a constant value, nearby to the Dulong–Petit limit [102] (C_V=3nR = 25×n J/mol K, n: number of atoms in the unit cell), whereas C_P undergoes to rise with temperature. At a given temperature, both C_P and C_V decrease with growing pressure. The thermal expansion coefficient α has the maximum values at zero pressure and significantly drops as pressure rises at a constant temperature, showcasing the compressive nature of solids. Whereas α augment rapidly with temperature in all range of T, at elevated T the speed of increase decreases mostly for $PtCo_3$ compound (Fig. 6(c)). The thermal expansion coefficient (α) attains its highest values at zero pressure and reduces significantly as pressure increases at constant temperature, reflecting the compressive nature of solids. Although α increases rapidly with temperature across the entire range of T, the rate of increase slows at higher temperatures, most notably for the $PtCo_3$ compound (Fig. 6(d)). In addition, α for Pt_3Co and PtCo are very closer and higher than that of $PtCo_3$. To assess the order and disorder in the Pt-Co alloy based on temperature and pressure, the changes in entropy have been exposed in Fig. 6(e). It can be perceived that the entropy approaches zero at 0 K and 0 GPa, then increases with rising temperature at constant pressure. The increase in entropy indicates a growing degree of disorder within the Pt–Co alloy as the temperature rises, with this effect being particularly considerable for the Pt_3Co compound. From Table 6, we can see that both parameters B and θ_D increase (decrease) with pressure (temperature). At static states (T = 0K, P = 0 GPa), the calculated θ_D for Pt_3Co, PtCo and $PtCo_3$, are 372.1, 405.2 and 452.2 K, respectively. In Table 5, the attained θ_D values from elastic constant C_{ij} are 302.9, 402 and 425.5 K for Pt_3Co, PtCo and $PtCo_3$, respectively, and the concordance for all the studied compounds is clearly seen (Fig. 6(f)). This accord is also observed in calculated bulk modulus (Tables 4 and 6). As for the Grüneisen parameter γ_G, it rises with temperature and diminishes with pressure.

4. CONCLUSIONS

In the present investigation, DFT-based computations were conducted to examine the structural, electronic, mechanical, and thermodynamic features of the intermetallics Pt-Co. The evaluated lattice parameters show strong agreement with obtainable experimental data and preceding theoretical data. The negative formation enthalpies confirm that Pt_3Co, PtCo, and $PtCo_3$ can be synthesized and remain chemically stable in all considered structures. The investigation of the electronic band structure, DOS, and PDOS reveals that the Co–*3d* and Pt–*5d* states contribute significantly to the total DOS through strong hybridization. The noticeable asymmetry between spin up and spin down states in all compounds indicates significant magnetization. In particular, Pt_3Co, PtCo and $PtCo_3$ exhibit strong magnetic behavior because of the large spin polarization near the Fermi level. Mechanical property calculations further demonstrate the elastic stability of these compounds. Pugh's criterion, Poisson's ratio, and Cauchy pressure indicate that both Pt_3Co and $PtCo_3$ are ductile with a metallic character. In contrast, PtCo possesses a mixed bonding nature (metallic and directional covalent) and exhibits the lowest ductility (B/G=1.77), making it the hardest compound. The evaluation of the elastic anisotropy (A^U and the 3D surface of Young's modulus) suggests a relatively low degree of anisotropy for all compounds. Thermodynamic features, including the bulk modulus (B), thermal expansion coefficient (α), heat capacities (C_V, C_P), entropy (S), and Debye temperature (θ_D), were systematically examined with the quasi-harmonic Debye model, highlighting their dependence on both temperature and pressure. Overall, the PtCo alloy exhibits a significant magnetic moment, making it a promising entrant for a variability of magnetic and spintronic utilizations.

Acknowledgments

D. Singh expresses his sincere gratitude to the Department of Science & Technology, New Delhi for support under the DST-PURSE Scheme (SR/PURSE/2024/230) of V.B.S. Purvanchal University Jaunpur and to the Council of Science & Technology, U.P. (CSTUP), Lucknow for funding under research project (UP-CST/E&T/D-1235, PID-6261).

Declarations

Ethics approval and consent to participate

Consent for publication: All authors approve of the ethics.

Funding: This research did not receive any specific grant from funding agencies in the public, commercial, or not-for-profit sectors.

Competing interests: The authors have no relevant financial or non-financial interests to disclose.

Author's contributions: H. Grimed: Investigation, Resources, Writing-Original draft. **D. Sayad:** Conceptualization. **R. Boulechfar:** Formal Analysis, Supervision, Writing-Original draft. **H. Bensadalla:** Methodology. **F. Semari:** Formal Analysis, Visualization. **Y. Khenioui:** Supervision, Resources. **H. Meradji, R. Khenata:** Supervision, Writing-Reviewing and Editing. **M. Boudjelal:** Validation, Investigation. **S. Ghemid:** Software. **D. Singh:** Visualization, Writing-Original draft

Availability of data and materials: Not applicable

ORCID

R. Boulechfar, https://orcid.org/0009-0006-2015-739X; **F. Semari,** https://orcid.org/0009-0001-0778-9118; **D. Sayad,** https://orcid.org/0000-0002-8179-8127; **M. Boudjelal,** https://orcid.org/0000-0001-5772-1878; **H. Meradji,** https://orcid.org/0000-0002-3359-3725; **D. Singh,** https://orcid.org/0000-0002-3011-2375; **R. Khenata,** https://orcid.org/0000-0002-5573-1711

REFERENCES

[1] B.S. Mun, M. Watanabe, M. Rossi, V. Stamenkovic, N.M. Markovic, P.N. Ross, J. Chem. Phys. **123**, 204717 (2005). https://doi.org/10.1063/1.2126662
[2] Z.M. Liu, L.L. Ma, J. Zhang, K. Hongsirikarn, and J.G. Goodwin, Catal. Rev. **55**, 255 (2013). https://doi.org/10.1080/01614940.2013.795455
[3] N.A. Frey, and S. Sun, *Inorganic Nanoparticles: Synthesis, Application, and Perspectives*, (CRC Press, Boca Raton, 2010), pp. 33–68.
[4] J.M. Montejano-Carrizales, F. Aguilera-Granja, C. Goyhenex, V. Pierron-Bohnes, J.L. Morán-López, J. Magn. Magn. Mater. **355**, 215–224 (2014). https://doi.org/10.1016/j.jmmm.2013.10.035
[5] N.L. Lethole, P. Mukumba, and G. Makaka, J. Alloys Compd. **565**, 170298 (2023). https://doi.org/10.1016/j.jmmm.2022.170298
[6] D. Weller, A. Moser, L. Folks, M.E. Best, W. Lee, *et al*., IEEE Trans. Magn. **36**, 10 (2000). https://doi.org/10.1109/20.824418
[7] D.J. Sellmyer, M. Yu, R.A. Thomas, Y. Liu, and R.D. Kirby, Phys. Low-Dimens. Struct. **1–2**, 155–165 (1998).
[8] D. Kim, J.E. Saal, L. Zhou, S. Shang, Y. Du, Z.-K. Liu, Calphad, **35**, 323 (2011). https://doi.org/10.1016/j.calphad.2011.04.005
[9] U.A. Paulus, A. Wokaun, G.G. Scherer, T.J. Schmidt, V. Stamenkovic, V. Radmilovic, N.M. Markovic, and P.N. Ross, Electrochim. Acta, **47**, 3787 (2002). https://doi.org/10.1016/s0013-4686(02)00349-3
[10] M.T.M. Koper, Surf. Sci. **548**, 1–3 (2004). https://doi.org/10.1016/j.susc.2003.10.045
[11] W. Yu, M.D. Porosoff, and J.G. Chen, Chem. Rev. **112**, 5780 (2012). https://doi.org/10.1021/cr300096b
[12] V.R. Stamenkovic, B.S. Mun, M. Arenz, K.J.J. Mayrhofer, C.A. Lucas, G. Wang, P.N. Ross, *et al*., Nat. Mater. **6**, 241 (2007). https://doi.org/10.1038/nmat1840
[13] B.N. Grgur, G. Zhuang, N.M. Markovic, and P.N. Ross, J. Phys. Chem. B, **101**, 3910 (1997). https://doi.org/10.1021/jp9704168
[14] J.-S. Kim, D. Seol, J. Ji, H.-S. Jang, Y. Kim, and B.-J. Lee, Curr. Appl. Phys. **59**, 131-141 (2017).
[15] I. Galanakis, M. Alouani, and H. Dreyssé, J. Magn. Magn. Mater. **320**, 221(2002). https://doi.org/10.1016/s0921-4526(02)00687-7
[16] K. Aledealat, B. Aladerah, A. Obeidat, M. Gharaibeh, Heliyon, **7**, e08639 (2021). https://doi.org/10.1016/j.heliyon.2021.e08639
[17] M. Futamoto, M. Nkamura, M. Ohtake, N. Inaba, and T. Shimotsu, AIP Adv. **6**, 085302 (2016). https://doi.org/10.1063/1.4960554
[18] K.M. Krishnan, C. Nelson, C.J. Echer, R.F.C. Farrow, R.F. Marks, and A.J. Kellock, J. Appl. Phys. **83**, 6810 (1998). https://doi.org/10.1063/1.367815
[19] S.C. Tsang, C.H. Yu, H. Tang, H. He, V. Castelletto, I.W. Hamley, T. Narayanan, *et al*., Chem. Mater. **20**, 4554 (2008). https://doi.org/10.1021/cm801068j
[20] Y. Wang, X. Zhang, Y. Liu, Y. Jiang, Y. Zhang, and J. Yang, J. Mater. Sci.: Mater. Electron. **70**, 528 (2014).
[21] M. Neamtu, C. Nadejde, V.D. Hodoroaba, R.J. Schneider, L. Verestiuc, and U. Panne, Sci. Rep. **8**, 6278 (2018). https://doi.org/10.1038/s41598-018-24721-4
[22] T.S. Rodrigues, A.G.M. da Silva, and P.H.C. Camargo, J. Mater. Chem. A, **7**, 5857 (2019). https://doi.org/10.1039/c9ta00074g
[23] L.M. Rossi, N.J.S. Costa, F.P. Silva, and R. Wojcieszak, Green Chem. **16**, 2906 (2014). https://doi.org/10.1039/c4gc00164h
[24] A.M. Alssad, A.A. Ahmed, H.A. Qattous, Heliyon, **5**, e02433 (2019). https://doi.org/10.1016/j.heliyon.2019.e02433
[25] A. Obeidat, B. Aladerah, M.-K. Qaseer, J. Alloys Compd. **559**, 169501 (2022). https://doi.org/10.1016/j.jmmm.2022.169501
[26] H. Okamoto, J. Phase Equilib. Diffus. **40**, 743 (2019). https://doi.org/10.1007/s11669-019-00760-w
[27] J. Cui, Y. Zeng, Q. Zheng, Q. Peng, F. Yu, X. Wang, N. Xie, *et al*., Fuel, **142**, 292 (2025). https://doi.org/10.1016/j.ijhydene.2025.05.394
[28] R. Wu, J. Zuo, L. Zhao, Z. Zhu, Q. Li, X. Niu, and J.S. Chen, Chem. Commun. **61**, 5742 (2025). https://doi.org/10.1039/d5cc00736d
[29] Y.-L. Mai, X.-S. Xie, Z.-D. Wang, C.-F. Yan, and G.-H. Liu, Trans. Nonferrous Met. Soc. China, **50**, 114–121 (2022).
[30] H. Li, D. Wei, C. Shi, Q. Long, L. Zhou, H. Jin, J. Yu, *et al*., J. Alloys Compd. **985**, 119089 (2025). https://doi.org/10.1016/j.jelechem.2025.119089
[31] J. Shen, C. Chen, L. Song, L. Zhong, K. Shan, Y. Guo, W. Zhan, *et al*., Wang, Appl. Surf. Sci. **379**, 133066 (2025). https://doi.org/10.1016/j.fuel.2024.133066
[32] Z. Qin, L. Wu, R. He, Z. Meng, J. Pan, and J. Zeng, Appl. Surf. Sci. **475**, 143675 (2024). https://doi.org/10.1016/j.electacta.2023.143675
[33] H. Wang, J. Liu, K. Du, X. Wang, X. Li, Y. Liu, C. Min, *at al*., J. Power Sources, 616, 235127 (2024). https://doi.org/10.1016/j.jpowsour.2024.235127
[34] J. Zou, Y. Du, R. Fang, X. Duan, Y. Liu, J. Mao, L. Yu, *et al*., Fuel, **307**, 121794 (2022). https://doi.org/10.1016/j.fuel.2021.121794
[35] S. Wang, W. Xu, Y. Zhu, Q. Luo, C. Zhang, S. Tang, and Y. Du, J. Mater. Sci. **13**, 827 (2020).
[36] C. Luo, K. Wan, J. Wang, B. Li, D. Yang, P. Ming, and C. Zhang, Renew. Sustain. Energy Rev. **679**, 165 (2025). https://doi.org/10.1016/j.jcis.2024.10.063
[37] D. Fu, Z. Hu, J. Xun, X. Yu, L. Wang, S. Zeng, and F. Li, Fuel, **396**, 135250 (2025). https://doi.org/10.1016/j.fuel.2025.135250
[38] B. Ravichandran, N. Narayanan, H. Liu, W. Zhang, N. Bhuvanendran, and H. Su, J. Power Sources, **402**, 136040 (2025). https://doi.org/10.1016/j.fuel.2025.136040
[39] V. Domin, M. Prokop, T. Bystron, M. Gatalo, L. Pavko, N. Hodnik, B.F. Gomes, *et al*., Appl. Catal. B: Environ. **536**, 146707 (2025). https://doi.org/10.1016/j.electacta.2025.146707
[40] M. Kim, H.E. Bae, J. Song, T.B.N. Huynh, T.T. Pham, S.K. Cho,T. Lim, *et al*., Curr. Opin. Electrochem. **52**, 101934 (2025). https://doi.org/10.1016/j.mtener.2025.101934
[41] U. Guevara, R. López, J. Blanco, and J. Núñez, Mater. Res. Express, **6**, 096514 (2019). https://doi.org/10.1088/2053-1591/ab2c50
[42] S. Karoui, H. Amara, B. Legrand, and F. Ducastelle, J. Phys.: Condens. Matter, **25**, 056005 (2013). https://doi.org/10.1088/0953-8984/25/5/056005
[43] X. Gonze, J.-M. Beuken, R. Caracas, F. Detraux, M. Fuchs, G.-M. Rignanese, L. Sindic, *et al*., Comput. Mater. Sci. **25**, 478 (2002). https://doi.org/10.1016/s0927-0256(02)00325-7
[44] R. Boulechfar, Y. Khenioui, S. Drablia, H. Meradji, M. Abu-Jafar, S. Bin Omran, *et al*., Solid State Commun. **273**, 23 (2018). https://doi.org/10.1016/j.ssc.2018.02.005

[45] A.T. Khodja, R. Boulechfar, H. Meradji, Y. Akeb, R. Chemam, S. Ghemid, and X. Wang, Solid State Sci. **100**, 107651 (2020). https://doi.org/10.1016/j.jmgm.2020.107651
[46] A. Front, B. Legrand, G. Tréglia, C. Mottet, Surf. Sci. **679**, 128 (2019). https://doi.org/10.1016/j.susc.2018.08.024
[47] J.P. Perdew, and Y. Wang, Phys. Rev. B, **45**, 13244 (1992). https://doi.org/10.1103/physrevb.98.079904
[48] R.V. Chepulskii, and W.H. Butler, Phys. Rev. B, **86**, 155401 (2012). https://doi.org/10.1103/physrevb.86.155401
[49] Z.-B. Li, K. Xiong, C.-C. Jin, Y.-J. Sun, B.-W. Wang, S.-M. Zhang, J.-J. He, *et al*., Rare Met. **40**, 1208 (2021). https://doi.org/10.1007/s12598-020-01656-2
[50] J.P. Perdew, K. Burke, M. Ernzerhof, Phys. Rev. Lett. **77**, 3865 (1996). https://doi.org/10.1103/physrevlett.78.1396
[51] L. Zosiak, C. Goyhenex, R. Kozubski, and G. Tréglia, J. Phys.: Condens. Matter, **27**, 455503 (2015). https://doi.org/10.1088/0953-8984/27/45/455503
[52] S.-M. Zhang, K. Xiong, C.-C. Jin, Z.-B. Li, J.-J. He, and Y. Mao, Rare Met. **40**, 1020 (2021). https://doi.org/10.1007/s12598-020-01651-7
[53] K. Aledealat, B. Aladerah, and A. Obeidat, J. Alloys Compd. **363**, 115112 (2023). https://doi.org/10.1016/j.ssc.2023.115112
[54] M.A. Rahman, K. Mousumi, M.L. Ali, R. Khatun, M.Z. Rahman, S.S. Hasan, W. Hasan, *et al*., Results Phys. **44**, 106141 (2023). https://doi.org/10.1016/j.rinp.2022.106141
[55] M.N. Sadat, M.A. Rahman, D.C. Roy, M.A. Rahman, M.Z. Hasan, I. Ahmad, S. Chowdhury, *et al*., Physica B, **672**, 415402 (2024). https://doi.org/10.1016/j.physb.2023.415402
[56] Z. Wei, Y. Xie, Y. Xiao, J. Chen, J. Xue, N. Qu, and J. Zhu, J. Mater. Res. 1–11 (2025). https://doi.org/10.1557/s43578-025-01596-6
[57] P. Rani, M.K. Kashyap, R. Singla, J. Thakur, and A.H. Reshak, J. Alloys Compd. **835**, 155325 (2020). https://doi.org/10.1016/j.jallcom.2020.155325
[58] M. Islam, M.S.I. Sarker, T. Nakamura, M.K.R. Khan, F.A. Khan, M.A. Islam, and S. Sato, Mater. Chem. Phys. **269**, 124727 (2021). https://doi.org/10.1016/j.matchemphys.2021.124727
[59] Z. Zine, N. Meftah, Phys. Solid State, **66**, 416–423 (2024). https://doi.org/10.1134/s1063783424601115
[60] Z. Zine, N. Meftah, and B. Daoudi, Solid State Commun. **396**, 115769 (2025). https://doi.org/10.1016/j.ssc.2024.115769
[61] S. Imada, T. Muro, T. Shishidou, S. Suga, H. Maruyama, K. Kobayashi, and T. Kanomata, Phys. Rev. B, **59**, 8752 (1999). https://doi.org/10.1016/s0921-4526(97)00234-2
[62] J.M. Sanchez, J.L. Moran-Lopez, C. Leroux, and M.C. Cadeville, J. Phys. C: Solid State Phys. **21**, L1091–L1096 (1988). https://doi.org/10.1088/0022-3719/21/33/004
[63] J.M. MacLaren, R.R. Duplessis, R.A. Stern, and S. Willoughby, J. Appl. Phys. **41**, 4374 (2005). https://doi.org/10.1109/tmag.2005.854755
[64] A. Kootte, C. Haas, R.A. de Groot, J. Phys. : Condens. Matter, **3**, 1133 (1991). https://doi.org/10.1088/0953-8984/3/9/009
[65] A. Alam, B. Kraczek, D.D. Johnson, Phys. Rev. B, **82**, 024435 (2010). https://doi.org/10.1103/physrevb.82.024435
[66] P. Blaha, K. Schwarz, F. Tran, R. Laskowski, G.K.H. Madsen, and L.D. Marks, J. Chem. Phys. **152**, 074101 (2020). https://doi.org/10.1063/1.5143061
[67] O.K. Andersen, Phys. Rev. B, **12**, 3060 (1975). https://doi.org/10.1103/physrevb.12.3060
[68] J.P. Perdew, J.A. Chevary, S.H. Vosko, K.A. Jackson, M.R. Pederson, D.J. Singh, and C. Fiolhais, Phys. Rev. B, **46**, 6671 (1992). https://doi.org/10.1103/physrevb.46.6671
[69] F.D. Murnaghan, Proc. Natl. Acad. Sci. USA, **30**, 244 (1944). https://doi.org/10.1073/pnas.30.9.244
[70] R.G. Hennig, A.E. Carlsson, K.F. Kelton, and C.L. Henley, Phys. Rev. **71**, 100 (2005). https://doi.org/10.1103/physrevb.71.144103
[71] D. Zhou, J. Liu, S. Xu, and P. Peng, Comput. Mater. Sci. **51**, 409 (2012). https://doi.org/10.1016/j.commatsci.2011.07.012
[72] D. Zhou, J. Liu, S. Xu, and P. Peng, Comput. Mater. Sci. **86**, 24 (2014). https://doi.org/10.1016/j.commatsci.2014.01.007
[73] R. Hultgren, P.D. Desai, D.T. Hawkins, M. Gleiser, and K.K. Kelley, *Selected Values of the Thermodynamic Properties of Binary Alloys*, ASM, Metals Park, OH, 1973.
[74] Z. Li, K. Xiong, Y. Sun, C. Jin, S. Zhang, J. He, and Y. Mao, Comput. Condens. Matter, **23**, e00462 (2020). https://doi.org/10.1016/j.cocom.2020.e00462
[75] W.B. Pearson, *A Handbook of Lattice Spacings and Structures of Metals and Alloys*, (Pergamon Press, Oxford, 1964).
[76] Shuttleworth, Magnetochemistry, **6**, 61 (2020). https://doi.org/10.3390/magnetochemistry6040061
[77] C. Leroux, M.C. Cadeville, V. Pierron-Bohnes, G. Inden, and F. Hinz, J. Phys. F: Met. Phys. **18**, 2033 (1988). https://doi.org/10.1088/0305-4608/18/9/021
[78] N.I. Vlasova, G.S. Kandaurova, and N.N. Shchegoleva, J. Magn. Magn. Mater. **222**, 138 (2000). https://doi.org/10.1016/s0304-8853(00)00506-0
[79] M.J. Capitan, S. Lefebvre, Y. Calvayrac, M. Bessiere, and P. Cenedese, J. Appl. Crystallogr. **32**, 1039 (1999). https://doi.org/10.1107/s002188989900998x
[80] R.J. Soulen Jr., J.M. Byers, M.S. Osofsky, B. Nadgorny, T. Ambrose, S.F. Cheng, P.R. Broussard, *et al.*, Science, **282**, 85 (1998). https://doi.org/10.1126/science.282.5386.85
[81] F. Goumrhar, L. Bahmad, O. Mounkachi, and A. Benyoussef, Comput. Condens. Matter, **15**, 15 (2018). https://doi.org/10.1016/j.cocom.2018.03.003
[82] R.J. Lange, S.J. Lee, D.W. Lynch, P.C. Canfield, B.N. Harmon, *et al*., Phys. Rev. B, **58**, 351 (1998). https://doi.org/10.1103/PhysRevB.58.351
[83] I. Galanakis, M. Alouani, and H. Dreyssé, Phys. Rev. B, **62**, 6475 (2000). https://doi.org/10.1103/physrevb.62.6475
[84] M. Born, and K. Huang, *Dynamical Theory of Crystal Lattices*, (Clarendon Press, Oxford, 1956).
[85] W. Voigt, Ann. Phys. **38**, 573 (1889). https://doi.org/10.1002/ange.18890022003
[86] A. Reuss, Z. Angew. Math. Mech. **9**, 49 (1929). https://doi.org/10.1002/zamm.19290090104
[87] R. Hill, Proc. Phys. Soc. Lond. A 65 (1952) 349.
[88] C.H. Jenkins, and S.K. Khanna, *Mechanics of Materials*, (Elsevier, 2005).

[89] S.F. Pugh, Philos. Mag. **45**, 823 (1954). https://doi.org/10.1080/14786440808520496
[90] D.G. Pettifor, Mater. Sci. Technol. **8**, 289 (1992). https://doi.org/10.1007/978-1-4615-3382-5_17
[91] X.-Q. Chen, H. Niu, D. Li, and Y. Li, Intermetallics, **19**, 1275 (2011). https://doi.org/10.1016/j.intermet.2011.03.026
[92] O.L. Anderson, J. Phys. Chem. Solids, **24**, 909 (1963). https://doi.org/10.1016/0022-3697(63)90067-2
[93] Y. Pan, and M. Wen, Vacuum, **156**, 419 (2018). https://doi.org/10.1016/j.vacuum.2018.08.010
[94] Nianyi, W. Shangan, Z. Yong, and Z. Xiangyun, J. Alloys Compd. **234**, 130 (1996). https://doi.org/10.1016/0925-8388(95)01963-4
[95] Q. Chen, Z. Huang, Z. Zhao, and C. Hu, Comput. Mater. Sci. **67**, 196 (2013). https://doi.org/10.1016/j.commatsci.2012.08.010
[96] G. Inden, in: *Proc. Int. Conf. on Solid-Solid Phase Transformations, TMS-AIME*, (Warrendale, PA, 1983), pp. 175.
[97] J.M. Sanchez, J.L. Moran-Lopez, C. Leroux, and M.C. Cadeville, J. Phys. : Condens. Matter, **1**, 491 (1989). https://doi.org/10.1088/0953-8984/1/2/019
[98] S.I. Ranganathan, and M. Ostoja-Starzewski, Phys. Rev. Lett. **101**, 055504 (2008). https://doi.org/10.1103/physrevlett.101.055504
[99] X. Luan, Q. Zhang, H. Bao, J. Zhou, B. Zhang, G. Wu, and J. Li, Crystals, **8**, 307 (2018). https://doi.org/10.3390/cryst8080307
[100] X. Li, X. Chen, L. Han, C. Ruan, P. Lu, and P. Guan, J. Mater. Res. **31**, 2956 (2016). https://doi.org/10.1557/jmr.2016.307
[101] M.A. Blanco, E. Francisco, and V. Luaña, Comput. Phys. Commun. **158**, 57 (2004). https://doi.org/10.1016/j.comphy.2003.12.001
[102] P.L. Dulong, and A.T. Petit, Ann. Chim. Phys. **10**, 395 (1819).

AB-INITIO ДОСЛІДЖЕННЯ ФІЗИЧНИХ ОСОБЛИВОСТЕЙ ІНТЕРМЕТАЛІДІВ Pt-Co

Х. Гримед[1,2], Р. Булехфар[1], Х. Бен Садаллах[1], Ф. Семарі[4], Й. Хеніуї[5], Д. Саяд[3], М. Буджелал[4], Х. Мераджи[6], С. Гемід[6], Д. Сінгх[7], Р. Кената[4,8]

[1]Лабораторія матеріалознавства та енергетичної інженерії (LMGE), Університет від 20 серпня 1955 р., Скікда, Алжир
[2]Лабораторія LRPCSI, Університет від 20 серпня 1955 р., поштова скринька 26, Скікда, 21000, Алжир
[3]Лабораторія електроніки Скікди (LRES), Кафедра електротехніки, Університет від 20 серпня 1955 р., Скікда, 21000, Скікда, Алжир
[4]Лабораторія квантової фізики речовини та математичного моделювання, Університет Маскари, 29000, Маскара, Алжир
[5]Кафедра структурних та облицювальних матеріалів, Відділ паливних технологій, Ядерний дослідницький центр Драрія, П/с А/с 43, Себала, Драрія, Алжир, Алжир
[6]Лабораторія радіаційної фізики, кафедра фізики, факультет природничих наук, Університет Баджі Мохтара, Аннаба, Алжир
[7]Кафедра фізики, Інститут фізичних наук для вивчення та досліджень ім. професора Раджендри Сінгха (Раджу Бхайя), Університет Віра Бахадура Сінгха Пурванчала, Джаунпур-222003, Університетський патріархат, Індія
[8]Алжирська академія наук і технологій, Райс Хаміду Вілла-Ель-Маданія, Алжир 16000, Алжир

У цій статті досліджуються структурні, електронні, механічні, магнітні та термодинамічні властивості інтерметалевих сполук Pt-Co за допомогою методу FP-LAPW (повнопотенціальна лінеаризована доповнена плоска хвиля) в рамках DFT (теорії функціоналу густини), реалізованого в коді Wien2k. Негативні ентальпії утворення та енергії когезії вказують на те, що Pt_3Co ($L1_2$), PtCo ($L1_0$) та $PtCo_3$ ($L1_2$) стабільні у феромагнітній (FM) фазі. Розрахунки постійних кристалічної решітки та модуля об'ємної пружності узгоджуються з існуючими теоретичними та експериментальними значеннями. Отримана електронна зонна структура встановлює металеву природу та магнітний характер усіх трьох досліджуваних сполук. Визначено глибину нагріву на рівні Фермі, коефіцієнт електронної теплоємності γ_{th}, поляризацію P% та магнітний момент. Дослідження пружних та механічних характеристик показує, що вибрані матеріали є стабільними та злегка анізотропними. Матеріали Pt_3Co та $PtCo_3$ є за своєю суттю пластичними, а PtCo є твердішою сполукою. Для кращого розуміння цих матеріалів застосовується квазігармонічна модель Дебая для вивчення їхніх теплових властивостей.

Ключові слова: *DFT; FP-LAPW; інтерметалід; електронні властивості; механічні константи*

East European Journal of Physics. 3. 491-497 (2026)
DOI:10.26565/2312-4334-2026-3-44 ISSN 2312-4334

ELECTRON STATES IN A FIVE-LAYER SEMICONDUCTOR STRUCTURE. PART 1

R.Ya. Rasulov, V.R. Rasulov, I.A. Muminov*, M.A. Mamatova, F.U. Raxmatullayeva, S.X. Muxammadaminov
Fergana State University, Murabbiylar St., 19, Fergana, 150100, Uzbekistan
**Corresponding Author e-mail: islommuminov2207@gmail.com*
Received January 13, 2026; revised May 5, 2026; in final form July 24, 2026; accepted August 20, 2026

Transcendental equations have been obtained to determine the electron energy spectrum in a five-layer semiconductor structure with an energy dip at its center for various energy ranges. It is shown that the presence of this dip leads to an increase in the energy gaps calculated within first-order perturbation theory. It is pointed out that the origin of the energy-level shift is associated with the dependence of the electron Hamiltonian not only on the potential-energy operator but also on the kinetic-energy operator, which depends on the effective masses in each layer of the structure. As has been shown, the modification of the potential profile of a simple well due to the dip should result in a lowering of the level, whereas the difference in kinetic energies for $m_3 < m_2$ promotes an upward shift of the levels, where m_i is the effective electron mass in the i-th layer.
Keywords: *Five-layer semiconductor structure; Electron energy spectrum; Transcendental equations; Effective mass approximation; Perturbation theory; Energy level shift*

INTRODUCTION

In semiconductor micro- and nanoelectronics, multilayer structures are increasingly employed, in which individual semiconductor layers are characterized by different electrical conductivities or a qualitative modification of the energy spectrum of charge carriers occurs [1–3]. Therefore, classical and quantum-physical investigations of electronic phenomena in such structures provide an opportunity to enhance the efficiency and improve the operating parameters of devices based on them.

At the present stage of micro- and nanoelectronics development, in view of the substantially increased use of multilayer crystals, both classical and quantum-mechanical studies of the electronic phenomena occurring in them are of current interest.

In recent years, the characteristic layer thicknesses in multilayer structures formed from different semiconductors have been in the range of 1–100 nm [4–9]. Accordingly, layered structures based on nanostructures are used in electronics as a fundamentally new type of artificial materials with unusual physical properties. In turn, interest in nanostructures stimulates the development of modern atom-level technologies and research directions associated with surface-structure studies. In this regard, investigating electronic kinetic phenomena in multilayer homo- and heterostructures is of considerable interest from both experimental and theoretical viewpoints [6–11]. On the one hand, this opens the possibility of creating resonant-tunneling devices; on the other hand, it enables observation of unique properties of multilayer structures arising due to interference of de Broglie waves [12–14].

METHODS

Wave Functions of the States and the Energy Spectrum of Charge Carriers in a Multilayer Structure.

At present, the resonant-tunneling diode (RTD) forms the basis of promising nanoelectronic devices. In particular, multilayer structures with an additional rectangular potential well in the central region (Fig. 1) are used to create new generations of RTDs, for example, heterolasers with separate electronic and optical confinement [6,16]. Owing to the lowering of the potential energy, new opportunities arise for controlling the positions of quantum levels in the wide main part of the potential well.

Let us consider, in the five-layer structure with a potential well at the center shown in Fig. 1, the states of charge carriers, e.g., the wave functions, as well as the energy spectrum. In what follows, we take into account the differences in the geometrical dimensions of each layer and the variation of the effective masses of charge carriers depending on the potential-energy profile within them. In the structure whose schematic is shown in Fig. 1, the effective mass of a charge carrier in the layer is $m_n(d_n)$, where n denotes the layer thicknesses.

Throughout the paper we adopt the following unified notation. The structure consists of five layers, numbered from left to right: layer 1 (the left outer barrier, $x \leq 0$); layer 2 (the left inner well, $0 < x \leq d_2$); layer 3 (the central dip, $d_2 < x \leq d_2 + d_3$); layer 4 (the right inner well, $d_2 + d_3 < x \leq d_2 + d_3 + d_4$); and layer 5 (the right outer barrier, $x > d_2 + d_3 + d_4$). The thicknesses of the three inner layers are denoted d_2, d_3, d_4; the corresponding effective masses are m_1, m_2, m_3, m_4, m_5; and the wave numbers k_1, k_2, k_3, k_4, k_5 are defined by Eq. (5). The barrier height is $U_1 > 0$,

Cite as: R.Ya. Rasulov, V. R. Rasulov, I.A. Muminov, M.A. Mamatova, F.U. Raxmatullayeva, S.X. Muxammadaminov, East Eur. J. Phys. 3, 491 (2026), https://doi.org/10.26565/2312-4334-2026-3-44

while $U_2 > 0$ denotes the depth (magnitude) of the central dip, so that the potential takes the value $-U_2$ in layer 3. With this convention, the structure is symmetric when $d_2 = d_4$ (and consequently $k_2 = k_4, m_2 = m_4$).

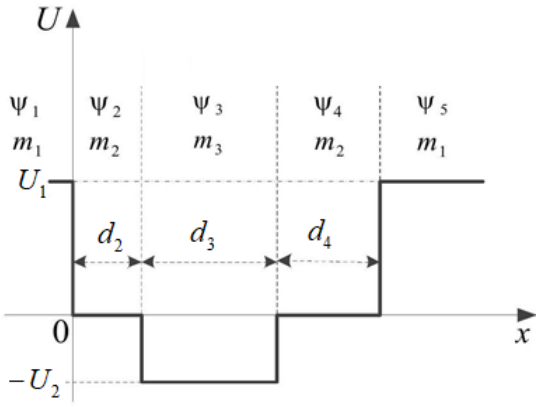

Figure 1. Potential profile of a five-layer semiconductor structure. The labels in the figure follow the unified notation introduced above: layer thicknesses d_2, d_3, d_4 (left inner well, central dip, right inner well, respectively); effective masses $m_1 - m_5$ in layers 1–5; barrier height U_1; well depth U_2.

$$\begin{cases} m_1, & x \le 0, \\ m_2, & 0 < x \le d_2, \\ m_3, & d_2 < x \le d_2 + d_3, \\ m_4, & d_2 + d_3 < x \le d_2 + d_3 + d_4 \\ m_5, & x > d_2 + d_3 + d_4, \end{cases} \tag{1}$$

$U_1 > 0$ and $U_3 > 0$ are the heights of the potential barrier in the outer layers, and $U_2 < 0$ is the depth of the potential well in the central layer, i.e.,

$$U_n = \begin{cases} U_1, x \le 0, x > d_2 + d_3 + d_4 \\ 0, 0 < x \le d_2, d_2 + d_3 < x \le d_2 + d_3 + d_4 \\ -U_2, d_2 < x \le d_2 + d_3 \end{cases} \tag{2}$$

The energy spectrum of charge carriers and their wave functions in such a structure are determined by solving the following Schrödinger equation:

$$\frac{\hbar^2}{2m_n^*} \cdot \frac{\partial^2 \psi_n(x)}{\partial x^2} + (E - U_n)\psi_n = 0, n = 1,2, \dots ,5. \tag{3}$$

Equation (3) is to be understood as the layer-wise (piecewise) form of the more general one-dimensional effective-mass Schrödinger equation with position-dependent mass $m^*(x)$, namely

$$-\left(\frac{\hbar^2}{2}\right)\left(\frac{d}{dx}\right)\left[\left(\frac{1}{m^*(x)}\right)\left(\frac{d\psi(x)}{dx}\right)\right] + U(x)\,\psi(x) = E\,\psi(x) \tag{3a}$$

in which the operator $1/m^*(x)$ is placed between the two derivatives in order to preserve the Hermiticity of the kinetic-energy operator when $m^*(x)$ is piecewise-constant [20, 21]. Within each layer $m^*(x)$ is constant and equation (3a) reduces to (3); the difference between the two formulations is therefore manifested entirely through the matching conditions at the heterointerfaces. The Bastard condition has been recently applied by the present authors to the analysis of asymmetric multilayer semiconductor structures [25] and is a standard ingredient in modern envelope-function calculations for resonant-tunneling heterostructures [22–24]. Integrating (3a) across an interface located at $x = x_i$ between layers n and $n + 1$ yields the so-called Bastard (BenDaniel–Duke) boundary conditions:

$$\psi_{\mathrm{n}}(x_{\mathrm{i}}) = \psi_{\mathrm{n}}{}^{+1}(x_{\mathrm{i}}),\ \left(\frac{1}{m_n}\right)\frac{d\psi_{\mathrm{n}}}{dx}\Big|_{x=x_i} = \left(\frac{1}{m_{n+1}}\right)\frac{d\psi_{n+1}}{dx}\Big|_{x=x_i}, \tag{3b}$$

i.e. continuity of the envelope function and continuity of the probability current $(1/m^*)\,d\psi/dx$ at every interface $x_{\mathrm{i}} \in \{0, d_2, d_2 + d_3, d_2 + d_3 + d_4\}$. The matching conditions (3b) are precisely those that lead to the homogeneous linear system (6) for the coefficients $A_{\mathrm{n}}, B_{\mathrm{n}}$, in which the symbol $\hat{k}$ appearing in the original derivation should be read as the operator $\hat{k} = -i\,(1/m^*(x))\,d/dx$ acting on the envelope. The transcendental equations (7)–(11) of the present work are obtained from the determinant of this system.

The wave functions corresponding to the layers of the structure in the Schrödinger equation can be written in the following form:

$$\begin{cases} \psi_1 = A_1 \cdot \exp(k_1 x) \\ \psi_2 = A_2 \cdot \cos(k_2 x) + B_2 \cdot \sin(k_2 x) \\ \psi_3 = A_3 \cdot \cos\big(k_3(x-d_2)\big) + B_3 \cdot \sin\big(k_3(x-d_2)\big) \\ \psi_4 = A_4 \cdot \cos\big(k_4(x-d_2-d_3)\big) + B_4 \cdot \sin\big(k_4(x-d_2-d_3)\big) \\ \psi_5 = B_5 \cdot \exp\big(-k_5(x-d_2-d_3-d_4)\big) \end{cases} \tag{4}$$

here

$$k_1 = \big(2m_1\hbar^{-2}(U_1 - E)\big)^{1/2}, k_2 = (2m_2\hbar^{-2}E)^{1/2}, k_3 = \big(2m_3\hbar^{-2}(E+U_2)\big)^{1/2} \cdot \tag{5}$$

For the general (asymmetric) structure, the wave numbers in the right inner well and in the right outer barrier are defined analogously: $k_4 = (2m_4E/\hbar^2)^{1/2}$ and $k_5 = [2m_5(U_1 - E)/\hbar^2]^{1/2}$. In the symmetric case considered below ($d_2 = d_4, m_2 = m_4, m_1 = m_5$) we have $k_2 = k_4$ and $k_1 = k_5$.

From the boundary conditions, which follow from the requirements of continuity of the wave function and the probability current density, we obtain the following results:

$$\begin{aligned} &A_1 - A_2 = 0, \cdot\, \tilde{k}_1 A_1 - \tilde{k}_2 B_2 = 0, A_2\cos(k_2 d_2) + B_2\sin(k_2 d_2) - A_3 = 0, \\ &-\tilde{k}_2 A_2 \sin(k_2 d_2) + \tilde{k}_2 B_2 \cos(k_2 d_2) - \tilde{k}_3 B_3 = 0, \cdot\, A_3\cos(k_3 d_3) + B_3\sin(k_3 d_3) - A_4 = 0, \\ &-\tilde{k}_3 A_3 \sin(k_3 d_3) + \tilde{k}_3 B_3 \cos(k_3 d_3) - \tilde{k}_4 B_4 = 0, A_4\cos(k_4 d_4) + B_4\sin(k_4 d_4) - B_5 = 0, \\ &-\tilde{k}_4 A_4 \sin(k_4 d_4) + \tilde{k}_4 B_4 \cos(k_4 d_4) + \tilde{k}_5 B_5 = 0. \end{aligned} \tag{6}$$

As a result, the energy spectra of the charge carriers are determined from the system of equations (6) by setting to zero the determinant of the matrix composed of the coefficients multiplying the unknown quantities A_n and B_n, and are expressed as follows:

$$\begin{aligned} &\big[\tilde{k}_4\sin(k_2 d_2) - \tilde{k}_3\cos(k_2 d_2)\big]\big[-\tilde{k}_2\big(\tilde{k}_1 - \tilde{k}_3\big)\cos(k_2 d_2) + \big(\tilde{k}_1\tilde{k}_3 + \tilde{k}_2^2\big)\sin(k_2 d_2)\big] \times \\ &\times \big[\tilde{k}_4\cos(k_4 d_4) + \tilde{k}_5\sin(k_4 d_4)\big] = 0 \end{aligned} \tag{7}$$

It should be noted that the solutions of equation (6) make it possible to determine the energy spectrum under the condition $U_1 > E > 0$. Similarly, to simplify the solution of the problem, if one assumes $d_2 = d_4$ and $k_2 = k_4$, then relation (6) can be written in the following form:

$$\begin{aligned} &\big[\tilde{k}_2^2\big(\tilde{k}_3^2 - \tilde{k}_1^2\big) + \big(\tilde{k}_1^2\tilde{k}_3^2 - \tilde{k}_2^4\big)tg(k_2 d_2)\big]\mathrm{tg}(k_3 d_3) + 2\tilde{k}_1\tilde{k}_2^2 k_3 \cdot [th^2(k_2 d_2) - 1] + \\ &+\tilde{k}_2\big[\tilde{k}_3\big(\tilde{k}_2^2 - \tilde{k}_1^2\big) + \tilde{k}_1\big(\tilde{k}_3^2 + \tilde{k}_2^2\big)\mathrm{tg}(k_3 d_3)\big]\big(\mathrm{tg}(k_2 d_2) + \mathrm{tg}(k_2 d_4)\big) = 0. \end{aligned} \tag{8}$$

If the last expression is treated as consisting of three terms, $f_1 = f_{11} + f_{12} + f_{13}$, then their dependences on the energy, taken in units of U_2, are shown in Fig. 2, and each of them passes through zero.

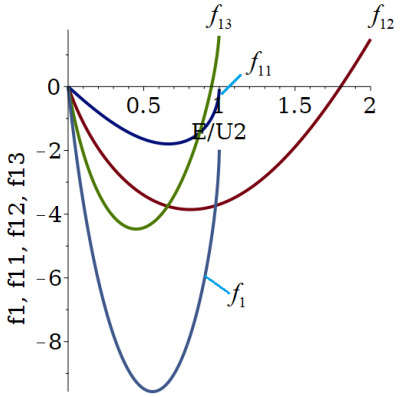

Figure 2. Dependences of the quantities f_{11}, f_{12}, and f_{13}, representing the 1st, 2nd, and 3rd terms of relation (8), as well as the quantity f_1, equal to their sum, on the energy taken in units of U_2.

However, the energies of the charge carriers inside the structure are determined from the condition $f_1 = 0$. It can be seen from this figure that, in a symmetric structure satisfying the condition $d_2 = d_4, k_2 = k_4$, no electron-confined energy

levels are formed. Here and in the subsequent numerical calculations (unless stated otherwise) [19], the following values were chosen: $d_2 = d_4 = 0.9$ nm, $d_3 = 1.84$ nm, $U_2 = 0.24$ eV, $m_2 = 0.046m_0$, $m_3 = 0.023m_0$.

From expression (7), the quantization conditions for the energies of bound states satisfying $0 \geq E > U_2$ can be written as follows:

$$\left[\tilde{k}_2^2\left(\tilde{k}_1^2 - \tilde{k}_3^2\right) + \left(\tilde{k}_2^4 - \tilde{k}_1^2\tilde{k}_3^2\right)\mathrm{th}(k_2d_2)\right]\mathrm{tg}(k_3d_3) + 2\tilde{k}_1\tilde{k}_2^2\tilde{k}_3 \cdot [1 + th^2(k_2d_2)] +$$

$$+\tilde{k}_2\left[\tilde{k}_3\left(\tilde{k}_2^2 + \tilde{k}_1^2\right) + \tilde{k}_1\left(\tilde{k}_2^2 - \tilde{k}_3^2\right)\mathrm{tg}(k_3d_3)\right]2\mathrm{th}(k_2d_2) = 0, \quad (9)$$

Remark on equations (8) and (9). The repeated factors of the type $(\mathrm{t}g(k_2d_2))^2$ and $(\mathrm{th}(k_2d_2))^2$ appearing in (8) and (9) are not typographical errors: they are obtained from the corresponding general expressions $tg(k_2d_2) \cdot tg(k_4d_4)$ and $th(k_2d_2) \cdot th(k_4d_4)$, valid for an asymmetric structure, after substituting the symmetry conditions $d_2 = d_4$ and $k_2 = k_4$ stated above. They may equivalently be written as $tg^2(k_2d_2)$ and $th^2(k_2d_2)$. The fully general (asymmetric) form, in which the corresponding factors appear as $tg(k_2d_2) \cdot tg(k_4d_4)$ and $th(k_2d_2) \cdot th(k_4d_4)$, is given in Part 2 of the present series, equation (6); the present equations (8) and (9) reduce to that expression in the symmetric limit $d_2 = d_4, k_2 = k_4$.

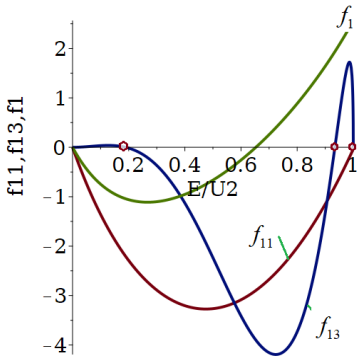

Figure 3. The quantities f_{11}, f_{12}, and f_{13} represent the 1st, 2nd, and 3rd terms of relation (9), respectively; f_1 is equal to their sum.

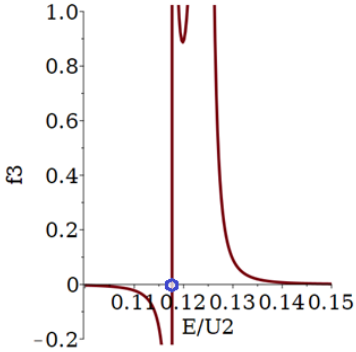

Figure 4. Dependence of the quantity f_3 on the relative energy E/U_2 (see expression (10)).

If expression (9) is regarded as consisting of three components, $f_1 = f_{11} + f_{12} + f_{13}$, then it follows from Fig. 3 that their dependences on the energy, taken in units of U_2, are such that, in a symmetric structure satisfying the condition $d_2 = d_4$, $k_2 = k_4$, three electron energy levels are formed (they are marked by red dots). If the height of the potential barrier U_1 is significantly greater in magnitude than the depth of the potential well, then the energies of the charge carriers:
a) under the condition $E > 0$

$$f3 = \left[\tilde{k}_2^2 - \tilde{k}_3^2\mathrm{tg}(k_2d_2)\mathrm{tg}(k_2d_4)\right]\mathrm{tg}(k_3d_3) + \tilde{k}_2\tilde{k}_3[\mathrm{tg}(k_2d_2) + \mathrm{tg}(k_2d_4)] = 0, \quad (10)$$

b) under the condition $0 \geq E > |U_2|$

$$f4 = \left[\tilde{k}_2^2 + \tilde{k}_3^2\mathrm{th}(k_2d_2)\mathrm{th}(k_2d_4)\right]\mathrm{tg}(k_3d_3) + \tilde{k}_2\tilde{k}_3[\mathrm{th}(k_2d_2) + \mathrm{th}(k_2d_4)] = 0 \quad (11)$$

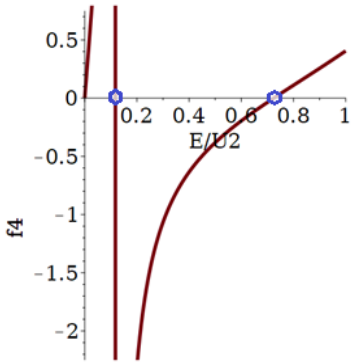

Figure 5. Dependence of the quantity $f_4$on the relative energy E/U_2 (see expression (11)).

These relations make it possible to determine them. In this case, Figs. 4 and 5 show that, in the first case, one energy level is formed, whereas in the second case, two energy levels are formed. In addition, for a structure with an infinitely high potential barrier, the coefficients in the charge-carrier wave functions (satisfying the orthonormality condition) can be determined as follows:

$$A_1 = A_2 = B_5 = 0, B_2 = A, A_3 = A \cdot \sin(k_2 d_2),$$

$$A_4 = A\left[\tilde{k}_{23}\cos(k_2 d_2)\sin(k_3 d_3) + \sin(k_2 d_2)\cos(k_3 d_3)\right], B_3 = A\tilde{k}_{23}\cos(k_2 d_2),$$

$$B_4 = -A\mathrm{ctg}(k_2 d_4)\left[\tilde{k}_{23}\cos(k_2 d_2)\sin(k_3 d_3) + \sin(k_2 d_2)\cos(k_3 d_3)\right], \quad (12)$$

here $\bar{k}_{n'n} = \frac{\bar{k}_{n'}}{\bar{k}_n} = \frac{m_n k_{n'}}{k_n m_{n'}}$. As a result, it has been established that the probability of finding charge carriers in a selected layer depends on the geometrical dimensions of the potential wells, their mutual arrangement, and also on the effective masses of the charge carriers in the layers.

Thus, during tunneling through the structure, the possibility of electron confinement in the region of the potential wells may arise [1,7], which, undoubtedly, reduces the amplitude values of the resonant current. The relative shift of the ground and first excited states can be qualitatively explained on the basis of perturbation theory [7].

In the first approximation, the calculated energy values are determined as follows [LL, Quantum Mechanics]:

$$E_n^{(2)} \approx E_n^{(0)} + \delta E_n^{(1)}, \delta E_n^{(1)} = \left\langle \psi_{n_0}^{(0)} \middle| \hat{V} \middle| \psi_{n_0}^{(0)} \right\rangle, \quad (13)$$

here, $E_n^{(0)}$ and $\psi_{n0}^{(0)}$ are the unperturbed energy and the wave function of the n-th order state, and $\hat{V}$ is the perturbation operator. Now, for the case where the potential wells of width b and depth $-U_2$ are infinitely deep, and the potential well of width d_2 is located at the center of the structure, we obtain the following result:

$$\delta E_1^{(1)} = -U_2\left[\frac{1}{d_{32}+1} + \frac{1}{\pi}\sin\left(\frac{\pi}{d_{32}+1}\right)\right], \quad \delta E_2^{(1)} = -U_2\left[\frac{1}{d_{32}+1} - \frac{1}{2\pi}\sin\left(\frac{2\pi}{d_{32}+1}\right)\right].$$

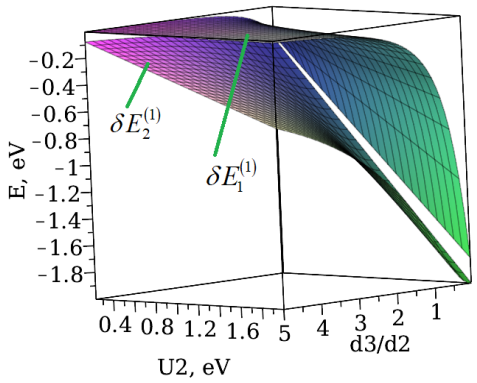

Figure 6. Two types of dependences of the energy quantities $\delta E_1^{(1)}$ and $\delta E_2^{(1)}$ on the depth of the middle potential well (U_2), as well as on the ratio of the thicknesses of the third and second layers (d_3/d_2).

It can be seen from Fig. 6 that the dependences of the energy quantities $\delta E_1^{(1)}$and $\delta E_2^{(1)}$, calculated from expression (13), on the depth of the middle potential well (U_2) and on the ratio of the thicknesses of the third and second layers (d_3/d_2) are as follows: (a) with increasing U_2, the quantity $\delta E_1^{(1)}$ remains almost unchanged quantitatively, whereas $\delta E_2^{(1)}$ decreases; (b) with increasing $d_{32} = d_3/d_2$, both quantities increase.

Expressions (14) show that a displacement of the energy-level positions in the quantum potential well leads to a lowering of the ground and excited-state levels. Obviously, to explain the positive shift of the excited state, it is necessary to take into account the difference in effective masses. In this case, according to the infinite-depth potential-well model:

$$\delta E_n^{(1)} = \frac{2}{d_2+d_3}\int_{d_3/2}^{(d_3+2d_2)/2} \sin\left(\frac{\pi n x}{d_2+d_3}\right)\left(\frac{\vec{p}^2}{2m_3} - \frac{\vec{p}^2}{2m_2} - U_2\right)\sin\left(\frac{\pi n x}{d_2+d_3}\right)dx = \\ = \left[\frac{\pi n^2\hbar^2}{2(d_2+d_3)^2}\left(\frac{1}{m_3} - \frac{1}{m_2}\right) - U_2\right]\cdot\left[\frac{d_2}{d_2+d_3} - \frac{(-1)^n}{n\pi}\sin\left(\frac{2\pi n d_2}{d_2+d_3}\right)\right]. \quad (14)$$

To clarify the problem, Fig. 7 shows the dependence of $\delta E_n^{(1)}$on the index of the energy level, where its possible values on the plot are determined by the intersection points of the curve with vertical lines drawn from the selected value of n. It can be seen from this figure that the energy levels with indices $n = 2$ and $n = 8$ can be confining levels, since they have negative values.

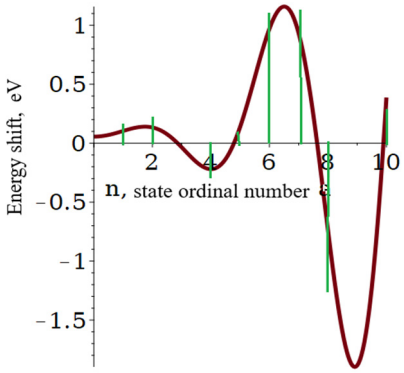

Figure 7. Dependence of the quantity $\delta E_n^{(1)}$ on the energy-level index n for a second-layer thickness $d_2 = 10$ nm.

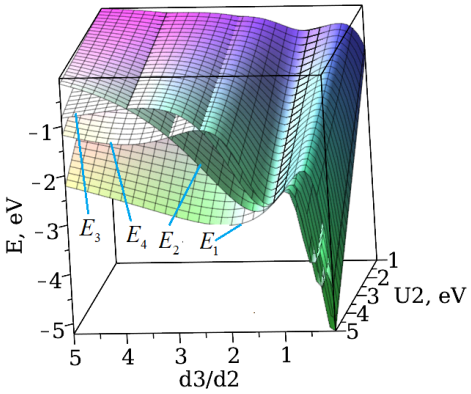

Figure 8. Plots of the state energies with indices $n = 1,2,3,4$ at a second-layer thickness $d_2 = 10$ nm as functions of the depth of the potential well in the middle region (U_2) and of the ratio of the thicknesses of the third and second layers (d_3/d_2).

Figure 8 shows the dependence of the first four energy levels on the depth of the central potential well and the thickness ratio d_3/d_2 at $d_2 = 10$ nm. The nonlinear variation of the energy surfaces demonstrates that both the depth and the relative width of the central dip significantly affect the positions and separation of the confined states.

CONCLUSIONS

The reason for the shift of the excited level is that the particle Hamiltonian in a well with a dip differs not only in potential energy but also in kinetic energy due to the difference in effective masses in different parts of the well. As shown earlier, a modification of the potential profile of a simple well caused by a dip of depth $-U_2$ should lead to a lowering of the level, whereas the difference in kinetic energies for $m_3 < m_2$ promotes an upward shift of the levels. For the first excited state ($n = 2$), the effect of the effective-mass difference is more pronounced; therefore, in a structure consisting of a potential well with an additional dip, the excited level lies higher than the excited level in a simple well (without a dip).

The calculations show that, within the first-order approximation of perturbation theory, the behavior of the energy shifts can be qualitatively explained only for small values of $d_3/(d_2 + d_3 + d_4)$; as the width of the dip increases, higher-order approximations must be taken into account.

ORCID

Rustam Y. Rasulov, https://orcid.org/0000-0002-5512-0654; **Voxob R. Rasulov,** https://orcid.org/0000-0001-5255-5612
Islom A. Muminov, https://orcid.org/0000-0002-2622-6097; **Maxliyo A. Mamatova,** https://orcid.org/0000-0001-6980-9877

REFERENCES

[1] Z.D. Kvon, "Semiconductor quantum wells and nanostructures," Nanomaterials, **13**(13), 1924 (2023). https://doi.org/10.3390/nano13131924
[2] Y. Liu, Y. Lin, Y. Hu, W. Wang, Y. Chen, Z. Liu, D. Wan, & W. Liao, "1D/2D heterostructures: synthesis and application in photodetectors and sensors," Nanomaterials, **14**(21), 1724 (2024). https://doi.org/10.3390/nano14211724
[3] V.V. Filippov, "Electron Transport Phenomena in Anisotropic and Low-Dimensional Semiconductor Structures," (Doctoral dissertation for the degree of Doctor of Physical and Mathematical Sciences). Lipetsk, 2013.
[4] H. Xu, M.K. Akbari, & S. Zhuiykov, "2D semiconductor nanomaterials and heterostructures: controlled synthesis and functional applications," Nanoscale Research Letters, **16**(1), 94 (2021). https://doi.org/10.1186/s11671-021-03551-w
[5] E. Sutter, R.R. Unocic, J.-C. Idrobo, & P. Sutter, "Multilayer lateral heterostructures of van der Waals crystals with sharp, carrier-transparent interfaces," Advanced Science, **8**(24), 2103830 (2021). https://doi.org/10.1002/advs.202103830
[6] E.L. Ivchenko, & G.E. Pikus, *Superlattices and Other Heterostructures: Symmetry and Optical Phenomena,* (Springer, Berlin, 1995).
[7] E. L. Ivchenko, *Optical Spectroscopy of Semiconductor Nanostructures*, (Alpha Science, Harrow, UK, 2005).
[8] R. G. Toscano-Negrette, J. C. León-González, J. A. Vinasco, A. L. Morales, M. Sahin, M. E. Mora-Ramos, J. Sierra-Ortega, et al., "Optical properties in a ZnS/CdS/ZnS core/shell/shell spherical quantum dot: electric and magnetic field and donor impurity effects," Nanomaterials, **13**(3), 550 (2023). https://doi.org/10.3390/nano13030550
[9] A. A. Toropov, *Electronic and Optical Properties of Irregular Superlattices Based on A_3B_5 and A_2B_6 Semiconductor Compounds* (Doctoral dissertation for the degree of Doctor of Physical and Mathematical Sciences). Saint Petersburg, 2005.
[10] J. A. Gil-Corrales, A. L. Morales, & C. A. Duque, "Self-consistent study of GaAs/AlGaAs quantum wells with modulated doping," Nanomaterials, **13**(5), 913 (2023). https://doi.org/10.3390/nano13050913
[11] L. Esaki, & R. Tsu, "Superlattice and negative differential conductivity in semiconductors," IBM Journal of Research and Development, **14**(1), 61–65 (1970). https://doi.org/10.1147/rd.141.0061
[12] R. Y. Rasulov, V. R. Rasulov, N. Z. Mamadalieva, & R. R. Sultanov, "Subbarrier and overbarrier electron transfer through multilayer semiconductor structures," Russian Physics Journal, **63**(4), 537–546 (2020). https://doi.org/10.1007/s11182-020-02067-7

[13] R. Ya. Rasulov, V. R. Rasulov, B. B. Akhmedov, I. A. Muminov, & K. K. Urinova, "Dimensional quantization in InSb and GaAs in three-zone model," Journal of Physics: Conference Series, **2697**(1), 012005 (2024). https://doi.org/10.1088/1742-6596/2697/1/012005
[14] V. R. Rasulov, R. Y. Rasulov, M. Kh. Nasirov, I. A. Muminov, & M. M. Mamatova, "Theory of size quantization in monolayers of transition metal dichalcogenides," Physica Scripta, **99**(10), 105987 (2024).
[15] E. I. Golant, & A. B. Pashkovskii, "Two-level electron wave functions in double-barrier quantum-size structures in an electric field of finite amplitude," Semiconductors (FTP), **34**(3), 334–339 (2000).
[16] E. I. Golant, & A. B. Pashkovskii, "Resonant transitions between split levels of three-barrier nanostructures and prospects for their application in submillimeter-range devices," Semiconductors (FTP), **36**(3), 330 (2002).
[17] A. B. Pashkovskii, "Parity and abrupt broadening of resonant levels in three-barrier structures," JETP Letters, **82**(3-4), 228 (2005).
[18] V. F. Elesin, "High-frequency response of double-barrier nanostructures," JETP, **121**(4), 925–931 (2002).
[19] T. P. E. Broekaert, W. Lee, & C. G. Fonstad, "Pseudomorphic $In_{0.53}$ $Ga_{0.47}As$/AlAs/InAs resonant tunneling diodes with peak-to-valley current ratios of 30 at room temperature," Applied Physics Letters, **53**(16), 1545–1549 (1988).
[20] D.J. BenDaniel, & C.B. Duke, "Space-charge effects on electron tunneling," Physical Review, **152**(2), 683–692 (1966). https://doi.org/10.1103/PhysRev.152.683
[21] G. Bastard, *Wave Mechanics Applied to Semiconductor Heterostructures*. Les Editions de Physique, Les Ulis (France); (Halsted Press, New York, 1988).
[22] V. Barsan, & M.-C. Ciornei, "Semiconductor quantum wells with BenDaniel–Duke boundary conditions: approximate analytical results," European Journal of Physics, **38**(1), 015407 (2017). https://doi.org/10.1088/1361-6404/38/1/015407
[23] M. Singh, H. Lipsanen, T. Bhardwaj, & V. Singh, "Landau quantization of a circular quantum dot using the BenDaniel–Duke boundary condition," Superlattices and Microstructures, **147**, 106690 (2020). https://doi.org/10.1016/j.spmi.2020.106690
[24] A. Atić, X. Wang, N. Vuković, N. Stanojević, A. Demić, D. Indjin, & J. Radovanović, "Resonant tunnelling and intersubband optical properties of ZnO/ZnMgO semiconductor heterostructures: impact of doping and layer structure variation," Materials, **17**(4), 927 (2024). https://doi.org/10.3390/ma17040927
[25] R.Y. Rasulov, V.R. Rasulov, K. K. Urinova, I. A. Muminov, & B. B. Akhmedov, "Analysis of kinetic properties and tunnel-coupled states in asymmetrical multilayer semiconductor structures," East European Journal of Physics, (2), 270–273 (2024). https://doi.org/10.26565/2312-4334-2024-2-27
[26] Rasulov, R. Ya., Rasulov, V. R., Muminov, I. A., Mamatova, M. A., Raxmatullayeva, F. U., & Yusupova, M. Sh. Electron states in a five-layer semiconductor structure. Part 2. East European Journal of Physics, (3), 498-504 (2026). https://doi.org/10.26565/2312-4334-2026-3-45

ЕЛЕКТРОННІ СТАНИ У П'ЯТИШАРОВІЙ НАПІВПРОВІДНИКОВІЙ СТРУКТУРІ. ЧАСТИНА 1

Р.Я. Расулов, В.Р. Расулов, І.А. Мумінов, М.А. Маматова, Ф.У. Рахматуллаєва, С.Х. Мухаммадамінов
Ферганський державний університет, вул. Мураббійлар, 19, м. Фергана, 150100, Узбекистан

Отримано трансцендентні рівняння для визначення енергетичного спектра електронів у п'ятишаровій напівпровідниковій структурі з енергетичним заглибленням у центрі для різних діапазонів енергій. Показано, що наявність цього заглиблення призводить до збільшення енергетичних щілин, обчислених у межах теорії збурень першого порядку. Зазначено, що походження зсуву енергетичних рівнів пов'язане із залежністю електронного гамільтоніана не лише від оператора потенціальної енергії, але й від оператора кінетичної енергії, який визначається ефективними масами в кожному шарі структури. Як показано, модифікація потенціального профілю простого квантового колодязя внаслідок наявності заглиблення повинна призводити до зниження енергетичного рівня, тоді як різниця кінетичних енергій за умови $m_3 < m_2$ сприяє зсуву рівнів угору, де m_i— ефективна маса електрона в *i*-му шарі.

Ключові слова: *п'ятишарова напівпровідникова структура, енергетичний спектр електронів, трансцендентні рівняння, наближення ефективної маси, теорія збурень, зсув енергетичних рівнів*

East European Journal of Physics. 3. 498-504 (2026)
DOI:10.26565/2312-4334-2026-3-45 ISSN 2312-4334

ELECTRON STATES IN FIVE-LAYER SEMICONDUCTOR STRUCTURES. PART 2

R.Ya. Rasulov, V.R. Rasulov, I.A. Muminov*, M.A. Mamatova, F.U. Raxmatullayeva, S.X. Muxammadaminov
Fergana State University, Murabbiylar St., 19, Fergana, 150100, Uzbekistan
**Corresponding Author e-mail: islommuminov2207@gmail.com*
Received January 13, 2026; revised May 5, 2026; in final form June 24, 2026; accepted August 25, 2026

Transcendental equations for determining the electron energy spectrum in a five-layer semiconductor structure with a potential barrier located at its center have been derived and analyzed for different energy ranges. It is shown that the origin of the energy-level shift is associated with the dependence of the electron Hamiltonian not only on the potential energy but also on the kinetic energy, which is governed by the effective masses of electrons in each layer of the structure. Changes in the electron energy spectrum of a five-layer semiconductor structure whose layers have different values of physical quantities characterizing the band and geometrical parameters of the sample as a function of temperature have been analyzed.
Keywords: *Five-layer semiconductor structure; Coupled quantum wells; Potential barrier; Electron energy spectrum; Transcendental quantization equations; Effective mass mismatch; Bastard boundary conditions; Temperature dependence; Kane model; resonant tunneling structures*

INTRODUCTION

The current stage of development of solid-state physics is characterized by the fact that the primary objects of research are increasingly not bulk semiconductor crystals, but thin films, multilayer thin-film structures, conducting wires, and crystallites [1–4]. The small dimensions of these structures in a certain direction, comparable to the de Broglie wavelength, lead—according to the laws of quantum mechanics—to a modification of the energy spectrum of charge carriers. The spectrum becomes discrete for motion along the axis in which the motion is confined. The presence of such "size" quantization, under certain conditions, can significantly affect the physical properties of the quantum-confined structures under consideration, giving rise to a set of unique properties that differ from those of single-crystal semiconductors [2–9].

The experience accumulated to date and the advances in epitaxial growth techniques make it possible to fabricate more complex heterocompositions containing semiconductor layers with a complex potential profile. From this perspective, the investigation of the particle energy spectrum in coupled quantum wells is of considerable interest, since in such systems it is possible to purposefully control the energy spectrum and electron scattering rates by changing not only the shape of the quantum well but also the coupling between the wells. Structures with coupled quantum wells have become the basis of many electronic and optoelectronic devices [1–4]. On the basis of these multilayer semiconductor structures, infrared (IR) lasers, IR radiation detectors, nonlinear optical elements, and high-speed transistors have been developed [1–4].

Due to the development of nanoelectronics, such problems have been revisited, and solutions have been obtained for a number of potential profiles of complex form [3, 5–16]. However, quantum-mechanical problems associated with electron motion in a multilayer semiconductor structure of arbitrary profile require treatment within the framework of perturbation theory. Therefore, below we calculate the electron energy spectrum in multilayer structures and its dependence on the sample temperature.

METHODS

Electron energy spectrum in multilayer semiconductor structures. To clarify how the shape, height, and spatial position of a potential barrier that divides a quantum well affect the resulting energy spectrum, we consider a five-region model of a layered semiconductor heterostructure, schematically shown in Fig. 1. Such a representation makes it possible to capture the essential features of quantum confinement and interlayer coupling in systems where the potential profile changes stepwise across the interfaces.

In this model, m_i denotes the effective mass of charge carriers in the i-th layer material, reflecting the layer-dependent kinetic-energy contribution to the electron Hamiltonian. The parameters U_1 and U_2 specify the positions of the conduction-band edges in the corresponding layers and therefore define the depth of the quantum well and the barrier height within the structure. The geometrical characteristics of the central part of the heterostructure are determined by the nanolayer thicknesses d_2, d_3, and d_4 which form the coupled-well region and control both the degree of confinement and the tunneling interaction between spatially separated parts of the well. This set of band and geometrical parameters

Cite as: R.Ya. Rasulov, V.R. Rasulov, I.A. Muminov, M. A. Mamatova, F.U. Raxmatullayeva, S.X. Muxammadaminov, East Eur. J. Phys. 3, 498 (2026), https://doi.org/10.26565/2312-4334-2026-3-45

provides a convenient basis for analyzing the formation and evolution of discrete electron states in multilayer quantum-well systems. As is known, the behavior of electrons in each region of the structure is described by the Schrödinger equation:

$$\frac{\hbar^2}{2m_i^*}\cdot\frac{\partial^2\psi_i(x)}{\partial x^2}+(E-U_i)\psi_i=0, \tag{1}$$

where $i=1,2,\ldots,5$ are the layer indices of the structure.

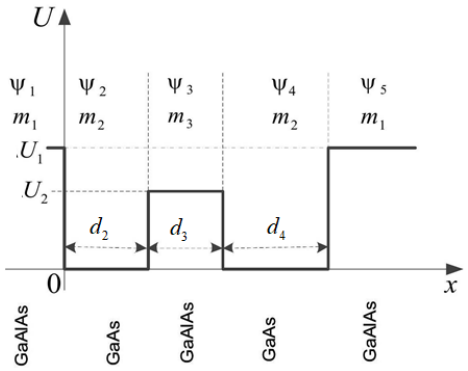

Figure 1. Conduction-band edge profile in a layered semiconductor structure.

Equation (1) is to be understood as the layer-wise (piecewise) form of the more general one-dimensional effective-mass Schrödinger equation with position-dependent mass $m^*(x)$, namely

$$-\left(\frac{\hbar^2}{2}\right)\left(\frac{d}{dx}\right)\left[\left(\frac{1}{m^*(x)}\right)\left(\frac{d\psi(x)}{dx}\right)\right]+U(x)\,\psi(x)=E\,\psi(x). \tag{1a}$$

In equation (1a) the operator $1/m^*(x)$ is placed between the two derivatives in order to preserve the Hermiticity of the kinetic-energy operator when $m^*(x)$ is piecewise-constant [19, 20]. Within each layer $m^*(x)$ is constant and (1a) reduces to (1); the matching conditions at the heterointerfaces follow automatically from the integration of (1a) across each interface and are precisely the *Bastard (BenDaniel–Duke) boundary conditions*: continuity of the envelope function $\psi_{\mathrm{n}}(x_{\mathrm{i}})=\psi_{\mathrm{n+1}}(x_{\mathrm{i}})$ and continuity of the probability current $(1/m_{\mathrm{n}})d\psi_{\mathrm{n}}/dx=(1/m_{\mathrm{n+1}})d\psi_{\mathrm{n+1}}/dx$ evaluated at every interface $x_{\mathrm{i}}\in\{0,d_2,d_2+d_3,d_2+d_3+d_4\}$. The system (4) given below is the explicit form of these matching conditions. The Bastard condition has been recently used by the present authors in the analysis of asymmetric multilayer semiconductor structures [24] and is a standard ingredient in modern envelope-function calculations for resonant-tunnelling heterostructures [21–23].

The values of the potential energies and effective masses in expression (1) are specified as follows:

$$U_i=\begin{cases}U_1, x\le 0, x>d_2+d_3+d_4,\\ 0, 0<x\le d_2, d_2+d_3<x\le d_2+d_3+d_4,\\ U_2, d_2<x\le d_2+d_3,\end{cases} \tag{2}$$

$$m_i^*=\begin{cases}m_1, x\le 0, x>d_2+d_3+d_4,\\ m_2, 0<x\le d_2, d_2+d_3<x\le d_2+d_3+d_4,\\ m_3, d_2<x\le d_2+d_3.\end{cases} \tag{3}$$

A remark on notation. Equation (3) lists only three distinct effective masses (m_1, m_2, m_3) because the structure shown in Fig. 1 is left–right symmetric ($m_5=m_1,\ m_4=m_2$). For the *general (asymmetric) case*, treated in equations (4)–(6) below, the corresponding extension reads

$$m_i^*=m_1\,(x\le 0);\ m_2\,(0<x\le d_2);\ m_3\,(d_2<x\le d_2+d_3);$$

$$m_4\,(d_2+d_3<x\le d_2+d_3+d_4);\ m_5\,(x>d_2+d_3+d_4). \tag{3a}$$

The wave numbers in the four inner and outer regions are then defined accordingly: $k_1=[2m_1(U_1-E)/\hbar^2]^{1/2}$, $k_2=(2m_2E/\hbar^2)^{1/2}$, $k_3=[2m_3(U_2-E)/\hbar^2]^{1/2}$, $k_4=(2m_4E/\hbar^2)^{1/2}$, $k_5=[2m_5(U_1-E)/\hbar^2]^{1/2}$. The symmetric structure of Fig. 1 corresponds to the special case $m_4=m_2, m_5=m_1$ (and consequently $k_4=k_2, k_5=k_1$); the formulas (4), (5), and (6) below are written in this general form, so that they remain valid for asymmetric structures with all five effective masses different.

The solution of the Schrödinger equation (for $E < U_1, U_2$) for each of the five regions is written as:

$$\begin{cases} \psi_1 = A_1 \cdot \exp(k_1 x) \\ \psi_2 = A_2 \cdot \cos(k_2 x) + B_2 \cdot \sin(k_2 x) \\ \psi_3 = A_3 \cdot \mathrm{ch}\big(k_3(x-d_3)\big) + B_3 \cdot \mathrm{sh}\big(k_3(x-d_3)\big) \\ \psi_4 = A_4 \cdot \cos\big(k_2(x-d_2-d_3)\big) + B_4 \cdot \sin\big(k_2(x-d_1+d_2)\big) \\ \psi_5 = B_5 \cdot \exp\big(-k_1(x-d_1-d_2-d_3)\big) \end{cases},$$

here, $k_1 = \sqrt{2m_1^*\hbar^{-2}|U_1 - E|},\ k_2 = \sqrt{2m_2^*\hbar^{-2}E},\ k_3 = \sqrt{2m_3^*\hbar^{-2}|U_2 - E|}$.

The Bastard boundary conditions, which follow from the requirements of continuity of the wave function and the probability current density, form the following system of equations:

$$\begin{cases} A_1 - A_2 = 0 \\ \tilde{k}_1 A_1 - \tilde{k}_2 B_2 = 0 \\ A_2\cos(k_2 d_2) + B_2\sin(k_2 d_2) - A_3 = 0 \\ -\tilde{k}_2 A_2\sin(k_2 d_2) + \tilde{k}_2 B_2\cos(k_2 d_2) - \tilde{k}_3 B_3 = 0 \\ A_3\mathrm{ch}(k_3 d_3) + B_3\mathrm{sh}(k_3 d_3) - A_4 = 0 \\ \tilde{k}_3 A_3\mathrm{sh}(k_3 d_3) + \tilde{k}_3 B_3\mathrm{ch}(k_3 d_3) - \tilde{k}_4 B_4 = 0 \\ A_4\cos(k_4 d_4) + B_4\sin(k_4 d_4) - B_5 = 0 \\ -\tilde{k}_4 A_4\sin(k_4 d_4) + \tilde{k}_4 B_4\cos(k_4 d_4) + \tilde{k}_5 B_5 = 0 \end{cases} \tag{4}$$

The resulting system (4) has nontrivial solutions with respect to the unknown energy values only when the determinant formed from the coefficients of the unknowns is equal to zero. As a result, we obtain an expression for determining the electron energy, which is convenient to present in the form:

$$\big[-\tilde{k}_2\big(\tilde{k}_1 - \tilde{k}_3\big)\cos(k_2 d_2) + \big(\tilde{k}_1\tilde{k}_3 + \tilde{k}_2^2\big)\sin(k_2 d_2)\big]\big[\tilde{k}_4\cos(k_4 d_4) + \tilde{k}_5\sin(k_4 d_4)\big]\big[\tilde{k}_4\mathrm{sh}(k_3 d_3) - \tilde{k}_3\mathrm{ch}(k_3 d_3)\big] = 0. \tag{5}$$

where $\tilde{k}_i = \frac{k_i}{m_i}$. Similarly, by solving the corresponding boundary-value problem, we obtain an expression that can be used to determine the energy spectrum for bound states when $U_1 \geq E > U_2$.

$$\big[\tilde{k}_2^2\big(\tilde{k}_3^2 - \tilde{k}_1^2\big) + \big(\tilde{k}_1^2\tilde{k}_3^2 - \tilde{k}_2^4\big)\mathrm{tg}(k_2 d_4)\big]\mathrm{tg}(k_3 d_3) + 2\tilde{k}_1\tilde{k}_2^2\tilde{k}_3 \cdot [\mathrm{tg}(k_2 d_2)\mathrm{tg}(k_2 d_4) - 1] +$$

$$+\tilde{k}_2\big[\tilde{k}_3\big(\tilde{k}_2^2 - \tilde{k}_1^2\big) + \tilde{k}_1\big(\tilde{k}_3^2 + \tilde{k}_2^2\big)\mathrm{tg}(k_3 d_3)\big][\mathrm{tg}(k_2 d_2) + \mathrm{tg}(k_2 d_4)] = 0.$$

(6)

For a well with a high potential barrier U_1($U_1 \gg U_2$), one can use the model of an infinitely deep well. In this case, the energy spectrum is determined by a transcendental equation which, for $E < U_2$, takes the form:

$$\big[\tilde{k}_2^2 + \tilde{k}_3^2\mathrm{tg}(k_2 d_2)\mathrm{tg}(k_2 d_4)\big]\mathrm{th}(k_3 d_3) + \tilde{k}_2\tilde{k}_3[\mathrm{tg}(k_2 d_2) + \mathrm{tg}(k_2 d_4)] = 0,$$

and for $E > U_2$:

$$\big[\tilde{k}_2^2 - \tilde{k}_3^2\mathrm{tg}(k_2 d_2)\mathrm{tg}(k_2 d_4)\big]\mathrm{tg}(k_3 d_3) + \tilde{k}_2\tilde{k}_3[\mathrm{tg}(k_2 d_2) + \mathrm{tg}(k_2 d_4)] = 0.$$

In the case $E < U_2$ for an infinitely deep well, the expressions for the coefficients defining the wave function, up to the normalization factor B, take the form:

$$A_1 = A_2 = B_5 = 0, B_2 = B, A_3 = B \cdot \sin(k_2 d_2), B_3 = B\frac{\tilde{k}_2}{\tilde{k}_3}\cos(k_2 d_2),$$

$$A_4 = B\left[\frac{\tilde{k}_2}{\tilde{k}_3}\cos(k_2 d_2)\mathrm{sh}(k_3 d_3) - \sin(k_2 d_2)\mathrm{ch}(k_3 d_3)\right],$$

$$B_4 = -B\left[\frac{\tilde{k}_2}{\tilde{k}_3}\cos(k_2 d_2)\mathrm{sh}(k_3 d_3) - \sin(k_2 d_2)\mathrm{ch}(k_3 d_3)\right]\mathrm{ctg}(k_2 d_4). \tag{7}$$

The obtained energy-quantization conditions make it possible to analyze the influence of the position and width of the barrier separating the quantum well on the energy spectrum of charge carriers in nanoelectronic devices based on

heterojunctions and superlattice structures with a variable doping profile. The expressions that determine the wave function in the quantum well also enable one to evaluate electron localization as a function of the potential landscape and the doping profile.

For a relatively small barrier height compared with the depth of the main part of the well ($U_2 \ll U_1$), the relative shift of the ground and first excited state energies can be qualitatively explained on the basis of perturbation theory [5,10], as was done in [6] for a well with an energy dip. In the first approximation, for a barrier of width d_3 and height U_2 located at the center of an infinitely deep quantum well of width $d_2 + d_3$, we obtain:

$$\delta E_1^{(1)} = U_2\left[\frac{d_2}{d_2+d_3} + \frac{1}{\pi}\sin\left(\pi\frac{d_2}{d_2+d_3}\right)\right], \delta E_2^{(1)} = U_2\left[\frac{d_2}{d_2+d_3} - \frac{1}{2\pi}\sin\left(\frac{2\pi d_2}{d_2+d_3}\right)\right]. \quad (8)$$

As follows from (8) and Fig. 2, as d_3/d_2 and U_2 increase, the energy levels in the quantum well shift upward, both for the ground state and for the excited state. Obviously, a more detailed explanation of the shifts of the ground and excited states requires taking into account the difference in effective masses; accordingly, within the infinite-wall quantum-well model we obtain:

$$\delta E_n^{(1)} = \left(\frac{\pi n^2\hbar^2}{2(d_2+d_3)^2}\left(\frac{1}{m_3} - \frac{1}{m_2}\right) + U_2\right)\left(\frac{d_2}{d_2+d_3} - \frac{(-1)^n}{n\pi}\sin\left(\frac{2\pi n d_2}{d_2+d_3}\right)\right). \quad (9)$$

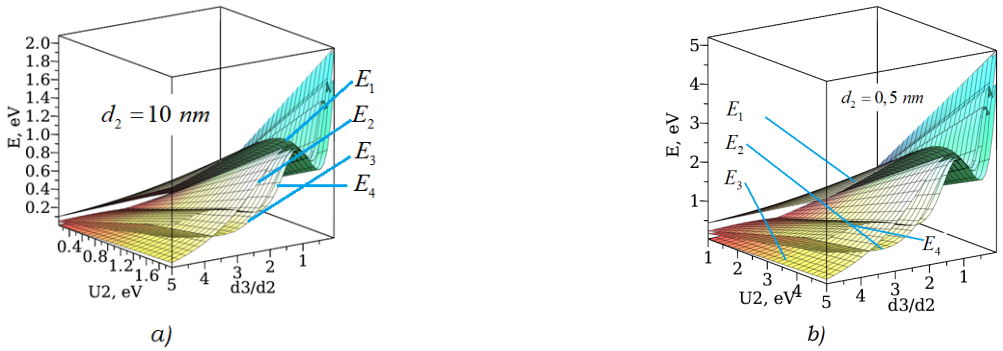

Figure 2. Dependences of the energies $E_n = \delta E_n^{(1)}(n = 1,2,3,4)$ on the depth of the potential dip (U_2) and on the thickness ratio of the 3rd and 2nd layers (d_3/d_2) for two values: $d_2 = 10$ nm and $d_2 = 0.5$ nm.

From the plots illustrating the dependence of $\delta E_n^{(1)}$ for four values $E_n(n = 1,2,3,4)$ on the thicknesses of the 2nd and 3rd layers, as well as on the ratio of their effective masses, it can be seen that the energy $\delta E_n^{(1)}$ and the energies $E_n(n = 1,2,3,4)$ depend significantly on the ratios d_2/d_3 and m_2/m_3. That is, whether the energies E_1, E_2, E_3, E_4 are larger or smaller than one another is determined by the layer thicknesses of the structure and by the relative values of the electron effective masses in the layers. This circumstance can be explained by the complexity of the dependence of the eigenenergy in the considered problem on the layer thicknesses of the structure and on the effective masses of the charge carriers.

This is related to the fact that the electron Hamiltonian [2,3] in a potential well with a barrier differs not only by the potential-energy operator but also by the kinetic-energy operator (due to the difference in effective masses in different layers of the structure).

Calculations show that modifying the potential landscape of a simple potential well by introducing a barrier of height U_2 should lead to an increase in the energy levels; simultaneously, the difference in kinetic energies for $m_3 < m_2$ also contributes to an upward shift of the levels, whereas for $m_3 > m_2$, on the contrary, it leads to a decrease in the energies. Note that within the first-order approximation of perturbation theory, it is possible to qualitatively explain the physical origin of the energy-level shifts only for small values of $d_3/(d_2 + d_3 + d_4)$; as the barrier width increases, higher-order approximations must be taken into account.

In the following calculations, the temperature dependence of the band gap by Vurgaftman

$$E_g(T) = E_g(T = 0) - \gamma_T T^2/(T + T_V), \quad (10)$$

and by Passler

$$E_g(T) = E_g(T = 0) - \frac{1}{2}\alpha\Theta_p\left[\left(1 + \left(2T/\Theta_p\right)^p\right)^{1/p} - 1\right]. \quad (11)$$

We consider the relations presented by Passler in this case, according to the multi-zone Kane model, the effective mass of an electron in the conduction band (m_c) is also temperature-dependent and is expressed as follows:

$$m_0/m_c = \{1 + 2F + E_P(E_g + 2\Delta_{SO}/3)/[3E_g(E_g + \Delta_{SO})]\}, \quad (12)$$

Here, $E_{g0} = E_g(T = 0)$. For the semiconductors used in the numerical calculations, the numerical values of the parameters α, Θ_p, and p were taken from Vurgaftman and Passler. In particular,

for $AlAs$: $E_g(T = 0\,K) = 3.099\,eV$, $E_p = 21.1\,eV$, $\alpha = 0.362\,meV/K$, $\Theta_p = 218\,K$, $\Delta_{so} = 0.28\,eV$, $F = -0.48, \gamma_T = 0.885\,meV/K$, $\beta = 530\,K$, $p = 2.32$;

for $InAs$: $\Theta_p = 143\,K$, $E_g(T = 0\,K) = 0.417\,eV$, $\gamma_T = 0.276\,meV/K$, $\beta = 93\,K$, $\alpha = 0.281\,meV/K$, $p = 2.10$, $E_p = 21.5\,eV$, $\Delta_{so} = 0.39\,eV$, $F = -2.90$.

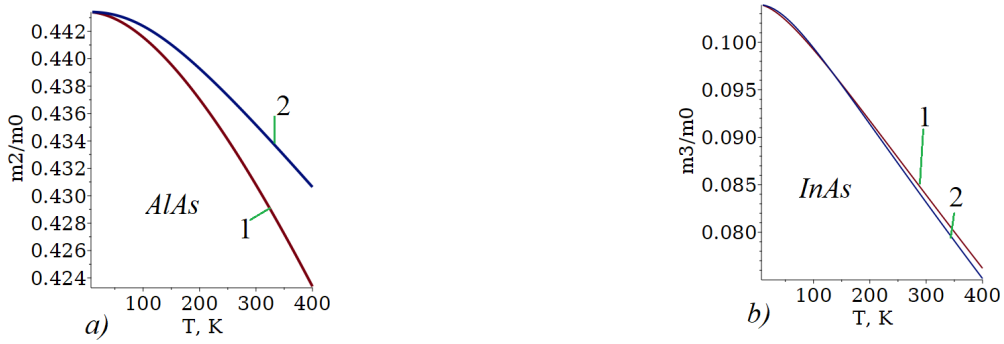

Figure 3. Temperature dependence of the electron effective mass in two semiconductors, calculated using the Vurgaftman formula (curve 2) and the Passler formula (curve 1).

From the temperature dependence of the electron effective mass in the two semiconductors (Fig. 3), it can be seen that the effective mass is almost independent of the choice between the Vurgaftman and Passler formulas, which is reflected in the subsequent results. From Figs. 4–5, it is evident that as the temperature increases, the numerical value of $E_n = \delta E_n^{(1)}$ $(n = 1,2,3,4)$ increases, but does not depend on the specific form of the temperature dependence.

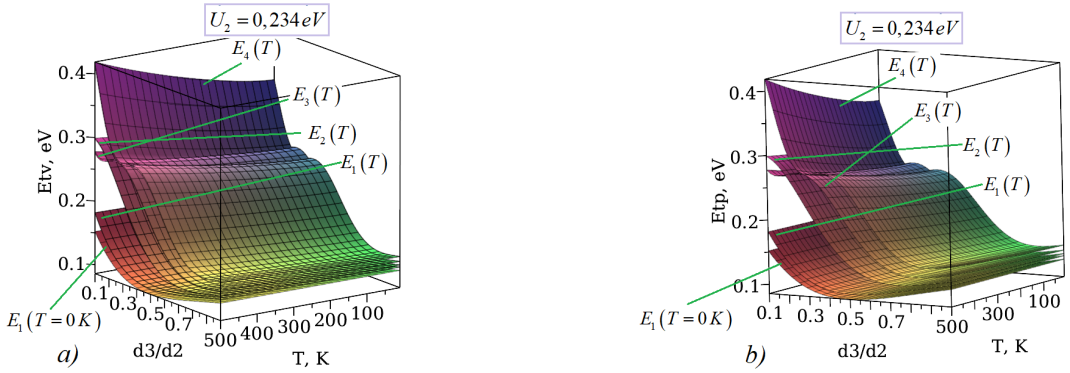

Figure 4. Dependences of the energies $E_n = \delta E_n^{(1)}$ $(n = 1,2,3,4)$ on temperature and on the thickness ratio of the 3rd and 2nd layers (d_3/d_2). Curves in (a) were calculated using the Vurgaftman formula, and in (b) using the Passler formula for $U_2 = 0.234$ eV, $d_2 = 10$ nm, $m_2 = 0.15\,m_0$, $m_3 = 0.026\,m_0$, where m_0 is the free-electron mass.

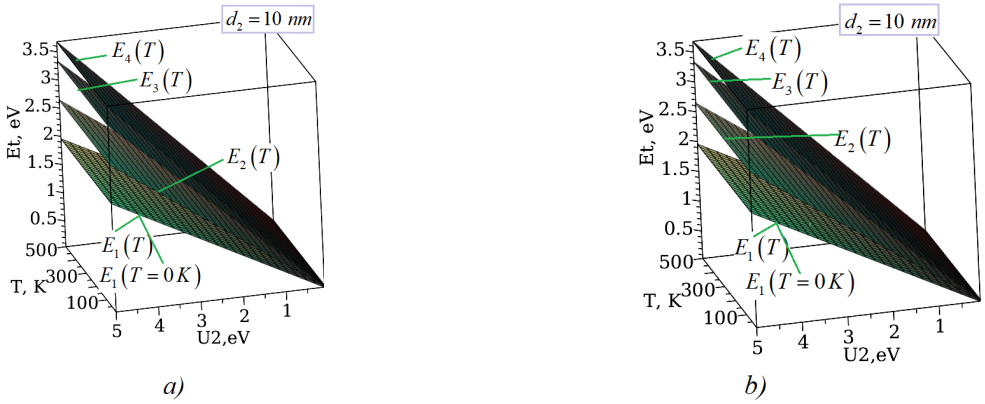

Figure 5. Dependences of the energies $E_n = \delta E_n^{(1)}$ $(n = 1,2,3,4)$ on temperature and on U_2. Curves in (a) were calculated using the Vurgaftman formula, and in (b) using the Passler formula, where $d_3 = d_2 = 10$ nm, $m_2 = 0.15\,m_0$, and $m_3 = 0.026\,m_0$.

Thus, the evolution of the electron energy spectrum in a five-layer semiconductor structure has been analyzed for the case where the individual layers differ in the key physical quantities that determine both the band alignment and the geometrical configuration of the sample. The obtained quantization conditions explicitly demonstrate that the positions of the discrete energy levels are governed not only by the potential profile (barrier height, width, and location), but also by the layer-dependent effective masses that enter the kinetic-energy operator and, therefore, shift the spectrum through mass mismatch at the interfaces.

CONCLUSIONS

The derived analytical expressions together with the numerical results indicate that the infinitely deep quantum-well approximation can serve only as a qualitative model for complex-profile wells when the confinement is sufficiently strong, i.e., for wells of relatively large depth. For shallower wells or for structures with pronounced internal barriers and material-parameter discontinuities, accurate determination of the level positions requires the full transcendental quantization relations obtained from the boundary-value problem. These relations, which account for the realistic potential landscape and the effective-mass discontinuities, provide a practical basis for predicting and tailoring the electron spectrum and carrier localization, and can therefore be applied to the design and optimization of resonant-tunneling heterostructures and related high-speed, low-inertia nanoelectronic devices.

ORCID

Rustam Y. Rasulov, https://orcid.org/0000-0002-5512-0654; **Voxob R. Rasulov,** https://orcid.org/0000-0001-5255-5612
Islom A. Muminov, https://orcid.org/0000-0002-2622-6097; **Maxliyo A. Mamatova,** https://orcid.org/0000-0001-6980-9877

REFERENCES

[1] Z.D. Kvon, "Semiconductor quantum wells and nanostructures," Nanomaterials, **13**(13), 1924 (2023). https://doi.org/10.3390/nano13131924
[2] E.L. Ivchenko, and G. E. Pikus, *Superlattices and Other Heterostructures. Symmetry and Optical Phenomena*. (Springer, Berlin, 1995).
[3] E. L. Ivchenko, *Optical Spectroscopy of Semiconductor Nanostructures*, (Alpha Science, Harrow (UK), 2005).
[4] H. Xu, M.K. Akbari, and S. Zhuiykov, "2D semiconductor nanomaterials and heterostructures: controlled synthesis and functional applications," Nanoscale Research Letters, **16**(1), 94 (2021). https://doi.org/10.1186/s11671-021-03551-w
[5] R.Ya. Rasulov, V.R. Rasulov, B.B. Akhmedov, I.A. Muminov, and K.K. Urinova, "Dimensional quantization in InSb and GaAs in three-zone model," Journal of Physics: Conference Series, **2697**(1), 012005 (2024). https://doi.org/10.1088/1742-6596/2697/1/012005
[6] V.R. Rasulov, R.Y. Rasulov, M.Kh. Nasirov, I.A. Muminov, and M.M. Mamatova, "Theory of size quantization in monolayers of transition metal dichalcogenides," Physica Scripta, **99**(10), 105987 (2024).
[7] E.I. Golant, and A.B. Pashkovskii, "Two-level electron wave functions in double-barrier quantum-confined structures in an electric field of finite amplitude," Semiconductors (Fizika i Tekhnika Poluprovodnikov), **34**(3), 334–339 (2000).
[8] E.I. Golant, and A.B. Pashkovskii, "Resonant transitions between split levels of triple-barrier nanostructures and prospects for their application in submillimeter-range devices," Semiconductors (Fizika i Tekhnika Poluprovodnikov), **36**(3), 330 (2002).
[9] A.B. Pashkovskii, "Parity and abrupt broadening of resonant levels in triple-barrier structures." JETP Letters, **82**(3–4) 228 (2005).
[10] V.F. Elesin, "High-frequency response of double-barrier nanostructures," Journal of Experimental and Theoretical Physics (JETP), **121**(4), 925–931 (2002).
[11] V.F. Elesin, "Resonant tunneling of electrons interacting with phonons," Journal of Experimental and Theoretical Physics (JETP), **123**(5), 1096–1111 (2005).
[12] V.F. Elesin, "Resonant tunneling and nonlinear response in a high-frequency field," Journal of Experimental and Theoretical Physics (JETP), **124**(2), 379–386 (2003).
[13] V.F. Elesin, and I.Yu. Kateev, "High-frequency properties of double-well nanostructures," Semiconductors (Fizika i Tekhnika Poluprovodnikov), **42**(5), 586–591 (2008).
[14] R.Y. Rasulov, V.R. Rasulov, K.K. Urinova, M.A. Mamatova, and B.B. Akhmedov, "Single and multiphoton optical transitions in atomically thin layers of transition metal dichalcogenides," East European Journal of Physics, (1), 393–397 (2024). https://doi.org/10.26565/2312-4334-2024-1-40
[15] V.R. Rasulov, R.Ya. Rasulov, M.A. Mamatova, and F. Qosimov, "Semiclassical theory of electronic states in multilayer semiconductors. Part 1," Journal of Physics: Conference Series, **2388**, 012156 (2022). https://doi.org/10.1088/1742-6596/2388/1/012156
[16] V. R. Rasulov, R.Ya. Rasulov, M.A. Mamatova, and F. Qosimov, "Semiclassical theory of electronic states in multilayer semiconductors. Part 2," Journal of Physics: Conference Series, **2388**, 012158 (2022). https://doi.org/10.1088/1742-6596/2388/1/012158
[17] T.P.E. Broekaert, W. Lee, and C.G. Fonstad, "Pseudomorphic $In_{0.53}$ $Ga_{0.47}As$/AlAs/InAs resonant tunneling diodes with peak-to-valley current ratios of 30 at room temperature," Applied Physics Letters, **53**(16), 1545–1549 (1988).
[18] S.-H. Ng, and C. Surya, "Studies of flicker noise in $In_{0.53}$ $Ga_{0.47}As$/AlAs/InAs resonant tunneling diodes," Solid-State Electronics, **35**(9), 1213–1216 (1992). https://doi.org/10.1016/0038-1101(92)90151-2
[19] D.J. BenDaniel, and C.B. Duke, "Space-charge effects on electron tunneling," Physical Review, **152**(2), 683–692 (1966). https://doi.org/10.1103/PhysRev.152.683
[20] G. Bastard, *Wave Mechanics Applied to Semiconductor Heterostructures*. Les Editions de Physique, Les Ulis (France); (Halsted Press, New York, 1988).

[21] V. Barsan, and M.C. Ciornei, "Semiconductor quantum wells with BenDaniel–Duke boundary conditions: approximate analytical results," European Journal of Physics, **38**(1), 015407 (2017). https://doi.org/10.1088/1361-6404/38/1/015407
[22] M. Singh, H. Lipsanen, T. Bhardwaj, and V. Singh, "Landau quantization of a circular quantum dot using the BenDaniel–Duke boundary condition," Superlattices and Microstructures, **147**, 106690 (2020). https://doi.org/10.1016/j.spmi.2020.106690
[23] A. Atić, X. Wang, N. Vuković, N. Stanojević, A. Demić, D. Indjin, and J. Radovanović, "Resonant tunnelling and intersubband optical properties of ZnO/ZnMgO semiconductor heterostructures: impact of doping and layer structure variation," Materials, **17**(4), 927 (2024). https://doi.org/10.3390/ma17040927
[24] R.Y. Rasulov, V.R. Rasulov, K.K. Urinova, I.A. Muminov, and B.B. Akhmedov, "Analysis of kinetic properties and tunnel-coupled states in asymmetrical multilayer semiconductor structures," East European Journal of Physics, (2), 270–273 (2024). https://doi.org/10.26565/2312-4334-2024-2-27
[25] R.Ya. Rasulov, V.R. Rasulov, I.A. Muminov, M.A. Mamatova, F.U. Raxmatullayeva, and M.Sh. Yusupova, "Electron states in a five-layer semiconductor structure. Part 1," East European Journal of Physics, (3), 491-497 (2026). https://doi.org/10.26565/2312-4334-2026-3-44

ЕЛЕКТРОННІ СТАНИ У П'ЯТИШАРОВИХ НАПІВПРОВІДНИКОВИХ СТРУКТУРАХ. ЧАСТИНА 2

Р.Я. Расулов, В.Р. Расулов, І.А. Мумінов, М.А. Маматова, Ф.У. Рахматуллаєва, С.Х. Мухаммадамінов
Ферганський державний університет, вул. Мураббійлар, 19, Фергана, 150100, Узбекистан

У роботі виведено та проаналізовано трансцендентні рівняння для визначення енергетичного спектра електронів у п'ятишаровій напівпровідниковій структурі з потенціальним бар'єром, розташованим у її центрі, для різних енергетичних діапазонів. Показано, що причина зміщення енергетичних рівнів пов'язана із залежністю гамільтоніана електрона не лише від потенціальної енергії, але й від кінетичної енергії, яка визначається ефективними масами електронів у кожному шарі структури. Проаналізовано зміни енергетичного спектра електронів у п'ятишаровій напівпровідниковій структурі, шари якої мають різні значення фізичних величин, що характеризують зонні та геометричні параметри зразка, залежно від температури.

Ключові слова: *п'ятишарова напівпровідникова структура; зв'язані квантові ями; потенціальний бар'єр; енергетичний спектр електронів; трансцендентні рівняння квантування; невідповідність ефективних мас; граничні умови Бастарда; температурна залежність; модель Кейна; резонансно-тунельні структури*

East European Journal of Physics. 3. 505-515 (2026)
DOI:10.26565/2312-4334-2026-3-46 ISSN 2312-4334

FUNDAMENTAL ROLE OF INCOMPLETE DOPANT IONIZATION IN GOVERNING ELECTROSTATICS AND CAPACITANCE RESPONSE OF n-β-Ga_2O_3/p-Si HETEROJUNCTIONS

D.A. Qalandarova[1]*, D.A. Saparbayeva[1], A.A. Medatov[2], G.T. Zaripov[3], M. Ziyayeva[4], S. Temirov[5], K.R. Sattarkulov[6], Sh. Saidova[7]
[1]National Research University "TIIAME", Tashkent 100000, Uzbekistan
[2]Department of Software Engineering, Andijan State University
[3]Bukhara State University, Bukhara 200117, Uzbekistan
[4]Jizzakh Polytechnic Institute, Jizzakh, Uzbekistan
[5]Bukhara State Medical Institute named after Abu Ali ibn Sino., Bukhara, Uzbekistan
[6]Gulistan State University, Gulistan, Uzbekistan
[7]Bukhara State University, Bukhara 200117, Uzbekistan
**Corresponding Author e-mail: dildora.qalandarova.90@gmail.com*
Received April 19, 2026; revised June 28, 2026; in final form August 13, 2026; accepted August 20, 2026

Incomplete dopant ionization plays a decisive role in determining the electrostatic behavior and capacitance characteristics of n-type β-Ga_2O_3/p-type Si heterojunctions, particularly under cryogenic operating conditions. In this work, a comprehensive physics-based analytical framework incorporating temperature-dependent dopant activation, band alignment, carrier freeze-out, and mobility degradation is developed to investigate junction electrostatics over the 77–300 K range. The analysis reveals that incomplete ionization significantly modifies carrier distribution, depletion dynamics, and electric-field formation at low temperatures. For moderately doped structures ($N_A = N_D = 4\times10^{17}$ cm^{-3}), freeze-out effects at 100 K reduce forward-bias capacitance by approximately 17%, increase depletion width by nearly 0.10 μm, and suppress the peak electric field by about 0.5 MV/cm. In contrast, heavily doped junctions ($N_A = N_D = 1\times10^{18}$ cm^{-3}) exhibit comparatively weak temperature sensitivity, with electrostatic variations below 5% due to enhanced dopant activation stability. Temperature-dependent Cp–n(V) characteristics demonstrate gradual convergence toward full-ionization behavior above 250–300 K, confirming the transition from partial to near-complete dopant activation. Furthermore, the junction capacitance follows a hyperbolic voltage dependence ($C \propto 1/\sqrt{\Delta V}$), with strong capacitance compression observed under extreme forward bias. The presented results establish a quantitative understanding of freeze-out-controlled electrostatics in Si/β-Ga_2O_3 heterostructures and provide a predictive foundation for the optimization of cryogenic, high-frequency, and high-voltage ultra-wide-bandgap semiconductor devices.
Keywords: *n-type β-Ga_2O_3; p-Si heterojunction; Incomplete dopant ionization; Junction electrostatics; Capacitance–voltage profiling; Carrier freeze-out; Temperature-dependent transport; Cryogenic electronics*

INTRODUCTION

Ultra-wide-bandgap (UWBG) semiconductors have emerged as key materials for next-generation electronic and optoelectronic technologies because of their large bandgap energy (Eg), high critical breakdown electric field (Ebr), high thermal conductivity (K), and strong thermal stability [1–4]. These properties enable reliable device operation under extreme voltages, high frequencies, elevated temperatures, and harsh radiation environments while suppressing leakage current and maintaining stable electrostatic performance [3,4]. Important device-related parameters such as depletion width (W_{p-n}), junction capacitance (C_{p-n}), peak electric field (E_{max}), carrier mobility (μ), and RC switching response strongly depend on these material characteristics. Among UWBG semiconductors, β-gallium oxide (β-Ga_2O_3) has attracted considerable attention owing to its ultra-wide bandgap of approximately 4.4–5.3 eV [5], which significantly suppresses intrinsic carrier generation (ni) and supports low off-state leakage current under high electric-field conditions. Combined with its high theoretical breakdown field [6–8], β-Ga_2O_3 is considered a promising platform for next-generation power electronics and ultraviolet optoelectronics.

Beyond its intrinsic electronic advantages, β-Ga_2O_3 also offers several practical benefits for scalable device fabrication. Its thermodynamic stability and high melting temperature (T_m) enable operation over a broad temperature range, while the availability of large-area bulk substrates supports wafer-scale integration [9,10]. In addition, β-Ga_2O_3 is compatible with high-quality epitaxial growth methods, allowing precise control of donor concentration (N_D), defect density (N_t), and interface quality [11]. The material also exhibits strong solar-blind ultraviolet optical absorption characterized by the absorption coefficient (α), making it highly suitable for deep-UV photodetection applications. These combined properties have motivated extensive research on β-Ga_2O_3-based high-voltage rectifiers [9–11], solar-blind ultraviolet photodetectors [12–15], Schottky barrier diodes [16,17], and high-power field-effect transistors [18–20], where high breakdown voltage, low capacitance, thermal robustness, and electrostatic stability are essential.

Despite these advantages, β-Ga_2O_3 homojunction devices exhibit important limitations associated with incomplete dopant ionization. The relatively deep donor activation energy (ED) in β-Ga_2O_3 causes partial carrier freeze-out at low

Cite as: D.A. Qalandarova, D.A. Saparbayeva, A.A. Medatov, G.T. Zaripov, M. Ziyayeva, S. Temirov, K.R. Sattarkulov, Sh. Saidova, East Eur. J. Phys. 3, 505 (2026), https://doi.org/10.26565/2312-4334-2026-3-46

temperatures, reducing the free-electron concentration (n) and significantly modifying junction electrostatics [21–24]. As a consequence, the effective ionized donor concentration (ND^+), depletion width (W_{p-n}), junction capacitance (C_{p-n}), built-in potential (V_{bi}), and peak electric field (E_{max}) become strongly temperature dependent. These effects are particularly pronounced under cryogenic conditions, where incomplete ionization alters carrier transport and electric-field distribution within the junction region [25–28].

To overcome these limitations, heterojunction engineering using n-type β-Ga_2O_3 combined with well-established p-type semiconductors such as silicon (Si) has emerged as an effective approach [29–32]. Silicon possesses a relatively narrow bandgap (Eg ≈ 1.12 eV), high crystalline quality, stable acceptor activation, and nearly complete dopant ionization even at low temperatures [33–36]. The acceptor concentration (N_A^-) in p-Si therefore remains comparatively stable, providing predictable electrostatic behavior and making Si an effective reference material for studying the temperature-dependent characteristics of β-Ga_2O_3-based heterostructures. Furthermore, the relatively high hole mobility (μh) and mature fabrication technology of Si support stable carrier transport and reliable heterointerface formation.

In n-β-Ga_2O_3/p-Si heterojunctions, incomplete donor ionization in β-Ga_2O_3 substantially influences electrostatic and dynamic device properties, including depletion width (W_{p-n}), junction capacitance (C_{p-n}), electric-field distribution, current density (J), and RC switching behavior [37–42]. At low temperatures, carrier freeze-out reduces the ionized dopant fraction, widens the depletion region, lowers junction capacitance, and decreases the peak electric field. These variations directly affect breakdown voltage, transient response, carrier transport efficiency, and frequency-dependent device operation [43–46]. Consequently, accurate inclusion of incomplete ionization effects is essential for predictive modeling and optimization of high-speed transistors [47–49], voltage-blocking power devices [50–52], solar-blind UV photodetectors [53–55], and cryogenic electronic systems [56–58]. In addition, understanding the relationship between temperature-dependent dopant activation and electrostatic field redistribution is critical for capacitance scaling, reliability enhancement, and thermal-performance optimization under extreme operating conditions.

In this work, we present a systematic investigation of n-β-Ga_2O_3/p-Si heterojunctions through temperature-dependent capacitance–voltage (C–V) and current–voltage (I–V) analysis integrated with physics-based electrostatic simulations. The study quantitatively evaluates the influence of incomplete dopant ionization on depletion width (W_{p-n}), junction capacitance (C_{p-n}), peak electric field (E_{max}), built-in potential (Vbi), and dynamic RC response over a broad temperature range, including cryogenic conditions. The obtained results clarify the role of carrier freeze-out in heterojunction electrostatics and establish a predictive framework for the design and optimization of UWBG-based power electronic and optoelectronic devices operating under extreme environments.

MATERIAL AND METHODS

In this study, we adopt a multiscale modeling strategy that bridges material-level and device-level simulations to examine p-Si / n-β-Ga_2O_3 heterojunctions over a temperature range from cryogenic (77 K) to room temperature (300 K). The approach explicitly accounts for temperature- and doping-dependent incomplete ionization, dopant activation energy variations, bandgap narrowing, and mobility degradation. By incorporating these factors, the framework enables precise prediction of carrier transport, junction electrostatics, and I–V characteristics, surpassing the limitations of conventional full-ionization assumptions [45–50].

2.1 Material Properties

Table 1 and Figure 1 summarize the principal material parameters of Si and β-Ga_2O_3 relevant to high-voltage, solar-blind, and extreme-environment device applications. The parameters include the bandgap energy (Eg), thermal conductivity (K), melting point (T_m), electron and hole mobility (μ_e and μ_h), and optical absorption coefficient (α). Here, Eg represents the energy separation between the valence and conduction bands, K denotes the material's ability to dissipate heat, T_m corresponds to the melting temperature, μ_e and μ_h describe electron and hole transport capability, respectively, and α characterizes the optical absorption strength in the ultraviolet region.

At 300 K, silicon (Eg ≈ 1.12 eV) exhibits a relatively narrow bandgap and nearly complete dopant ionization, resulting in a stable and well-defined hole concentration in the p-type region [51]. In contrast, β-Ga_2O_3 possesses an ultra-wide bandgap of approximately 4.8 eV, which strongly suppresses intrinsic carrier generation and enables low-leakage operation under high electric fields and elevated temperatures. These material characteristics highlight the comparative advantages of β-Ga_2O_3 for high-power, solar-blind UV, and extreme-environment electronic and optoelectronic applications. The complementary electrical and optical characteristics of Si and β-Ga_2O_3 are key to heterojunction performance. Silicon provides high crystalline quality, excellent carrier mobility, and controllable p-type doping, enabling robust transport and electrostatic control. β-Ga_2O_3 serves as the UV-active layer with deep-UV transparency, moderate absorption, and high breakdown strength, allowing efficient photocarrier collection under high voltages [10,16–18].

The n-β-Ga_2O_3/p-Si heterojunction exhibits a stable depletion profile, asymmetric electric-field distribution, and low leakage currents, making it ideal for solar-blind photodetectors, high-voltage devices, and cryogenic-to-ambient electronics. As shown in the radar plot (Figure 1), Si offers high electron/hole mobility (~150 $W\,m^{-1}\,K^{-1}$ thermal conductivity) and efficient heat dissipation, whereas β-Ga_2O_3's ultra-wide bandgap (~4.8 eV) and high breakdown field favor UV sensitivity and high-voltage operation, though limited hole mobility and lower thermal conductivity

(~27 W m^{-1} K^{-1}) constrain high-current performance. These contrasts highlight the necessity of incorporating temperature- and doping-dependent incomplete ionization in device modeling, as carrier freeze-out in β-Ga_2O_3 significantly impacts depletion width, junction capacitance, and electric-field distribution across 77–300 K.

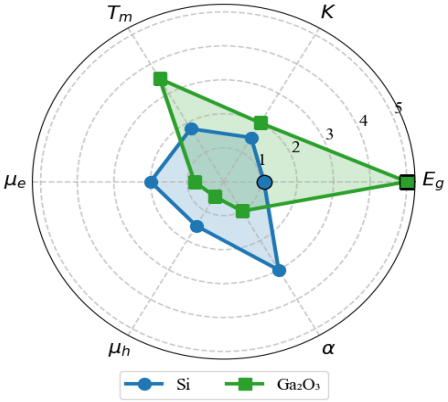

Figure 1. Normalized comparison of key material properties for Si and Ga_2O_3

Table 1. Material parameters for incomplete ionization modeling at 300 K [51].

Material	Eg (eV)	N_C (cm^{-3})	N_V (cm^{-3})	E	m_e/m_0	m_h/m_0	Ea (meV)
Si	1.12	2.8×10^{19}	1.042×10^{19}	11.7	0.26	0.4	45–50
Ga_2O_3	4.8	1.0×10^{18}	1.5×10^{19}	10.0	0.28	0.8	500–600

2.2 Physical Models

Incomplete ionization is explicitly modeled for Si and β-Ga_2O_3 to capture carrier dynamics from cryogenic to room temperature. Dopant ionization fractions are calculated using activation-energy-based models from literature [25,28,37,38]. Shallow Si donors remain nearly fully ionized over the entire range, while deep donors/acceptors in β-Ga_2O_3 exhibit pronounced freeze-out below ~200 K, reducing free-carrier density, expanding depletion widths, and modifying junction electrostatics.

Low-field carrier mobilities are described using the Arora model, accounting for impurity scattering at high doping and lattice scattering at elevated temperatures, accurately capturing mobility degradation from cryogenic to ambient conditions. Essential material parameters—including bandgap (Eg), conduction/valence band densities of states (N_C, N_V), relative permittivity (ε), electron/hole effective masses (me, mh), and donor/acceptor activation energies (Ea)—control incomplete ionization. These effects strongly dictate carrier distribution, electric-field profiles, and I–V behavior in Si/β-Ga_2O_3 heterojunctions. Incorporating temperature- and doping-dependent ionization is therefore crucial for predictive modeling and the design of high-performance, thermally resilient devices across 77–300 K.

2.3 Analytical and Numerical Modeling

The p-Si/n-β-Ga_2O_3 heterojunctions were examined using a physics-based framework to capture the combined effects of band alignment [34,45], incomplete dopant ionization [34,46], temperature-dependent carrier mobility [34,47], and self-heating [34,48] over 77–400 K, for dopant concentrations ranging from 10^{15} to 10^{19} cm^{-3} [34,49]. Conventional models, including the Varshni equation [45], do not accurately capture the temperature-dependent bandgap behavior of ultra-wide-bandgap semiconductors such as β-Ga_2O_3. Therefore, the Pässler model [38] was adopted, as it incorporates nonlinear electron–phonon interactions and provides a more reliable description of bandgap evolution from cryogenic to elevated temperatures (Eq. 1).

$$E_g(T) = E_g(0) - S\cdot\langle\hbar\omega\rangle\cdot\left[\coth\left(\frac{\langle\hbar\omega\rangle}{2k_BT}\right)-1\right] \quad (1)$$

Temperature-dependent bandgaps were modeled using the Pässler formalism [38, Eq. 1], which accounts for nonlinear electron–phonon interactions and accurately describes bandgap shrinkage from cryogenic to elevated temperatures. Here, Eg(T) and Eg(0) denote the bandgap energies at temperature T and 0 K, respectively; α is the bandgap reduction coefficient; S represents the electron–phonon coupling factor; ⟨ħω⟩ is the average phonon energy; k_B is the Boltzmann constant; and T is the absolute temperature. This is critical for simulating carrier freeze-out and predicting maximum electric fields (E_{max}) in ultra-wide-bandgap heterojunctions. Carrier transport was computed via self-consistent solutions of Poisson's and electron/hole continuity equations [34,50], including SRH, Auger, and radiative recombination [34,51], along with temperature- and doping-dependent incomplete ionization [34,46] and mobility degradation via the Arora model [34,47]. The depletion width ($W_{p\text{-}n}$) governs junction electrostatics by controlling the space-charge distribution, potential drop, junction capacitance, and internal electric-field profile, directly affecting carrier transport, breakdown, and overall device performance. Junction electrostatics and carrier transport were further evaluated using a

1D self-consistent Poisson–carrier statistics model incorporating temperature- and doping-dependent incomplete ionization [41] (Eq. 2). This framework provides a predictive, physics-based approach for designing high-reliability p-Si/n-β-Ga_2O_3 devices across 77–400 K.

$$\frac{\partial^2\varphi(x,y,z)}{\partial x^2}+\frac{\partial^2\varphi(x,y,z)}{\partial y^2}+\frac{\partial^2\varphi(x,y,z)}{\partial z^2}=-\frac{q\cdot(p-n+N_D^+(T)-N_A^-(T))}{\varepsilon\cdot\varepsilon_0} \tag{2}$$

In this model, ε denotes the material permittivity, and n and p represent the free electron and hole densities, respectively, computed using Fermi–Dirac statistics [28]. The vacuum permittivity is $\varepsilon_0 = 8.85\times10^{-12}$ F·m^{-1}, and φ(x,y,z) is the electrostatic potential. The concentrations of ionized donors ($N_D^+(T)$) and acceptors ($N_A^-(T)$) are treated as temperature-dependent to explicitly capture incomplete ionization, enabling accurate simulation of carrier freeze-out in ultra-wide-bandgap semiconductors like β-Ga_2O_3 [3,26]. The depletion region extends a distance x_p into p-Si and x_n into n-β-Ga_2O_3. Boundary conditions are defined as: Dirichlet condition $\varphi(-x_p)=\varphi_p,\ \varphi(x_n)=\varphi_n$, [21]. Neumann (electric displacement continuity) condition: $\varepsilon_p\left.\frac{d\varphi}{dx}\right|_{x=-x_p}=\varepsilon_n\left.\frac{d\varphi}{dx}\right|_{x=x_n}$ [26]. Here, φ_p and φ_n are the electrostatic potentials at the edges of the depletion region, and ε_p and ε_n are the permittivities of p-Si and n-β-Ga_2O_3, respectively. The total depletion width ($W_{p\text{-}n}$) is then determined from Eq. (2) using these boundary conditions.

$$W_{p-n}(T)=\sqrt{\frac{2\cdot\varepsilon_p\cdot\varepsilon_n\cdot\varepsilon_0\cdot(N_A+N_D)^2\cdot(\varphi_{bi}(T)-U_{p-n})}{q\cdot N_A\cdot N_D\cdot(\varepsilon_p\cdot N_A+\varepsilon_n\cdot N_D)}} \tag{3}$$

Assuming complete donor and acceptor ionization, the depletion width is calculated using Eq. (3), while the junction capacitance (C) is obtained from Eq. (4).

$$C_{p-n}(T)=S\cdot\sqrt{\frac{q\cdot\varepsilon_A\cdot\varepsilon_D\cdot\varepsilon_0\cdot N_A\cdot N_D}{2\cdot(\varepsilon_A\cdot N_A+\varepsilon_D\cdot N_D)\cdot(\varphi_{bi}(T)-U_{p-n})}} \tag{4}$$

However, at low temperatures, Eqs. (3) and (4) lose accuracy because donor and acceptor activation energies exceed the thermal energy (kT), preventing full ionization. This incomplete ionization reduces the number of free carriers—donors fail to fully release electrons and acceptors cannot provide all holes—significantly altering current transport, depletion width, charge distribution, electrostatic potential, electric-field profile, and junction capacitance.

$$W_{p-n}(T)=\sqrt{\frac{2\cdot\varepsilon_p\cdot\varepsilon_n\cdot\varepsilon_0\cdot(N_A^-(T)+N_D^+(T))^2\cdot(\varphi_{bi,eff}(T)-U_{p-n})}{q\cdot N_A^-(T)\cdot N_D^+(T)\cdot(\varepsilon_p\cdot N_A^-(T)+\varepsilon_n\cdot N_D^+(T))}} \tag{5}$$

Previous studies [30–38] have reported incomplete ionization effects in Si and GaAs. Incorporating this behavior, Eqs. (3) and (4) are reformulated as Eqs. (5) and (6) to accurately account for reduced carrier activation.

$$C_{p-n}(T)=S\cdot\sqrt{\frac{q\cdot\varepsilon_A\cdot\varepsilon_D\cdot\varepsilon_0\cdot N_A^-(T)\cdot N_D^+(T)}{2\cdot(\varepsilon_A\cdot N_A^-(T)+\varepsilon_D\cdot N_A^-(T))\cdot(\varphi_{bi,eff}(T)-U_{p-n})}} \tag{6}$$

Eqs. (5) and (6) explicitly incorporate the temperature-dependent ionization of donor and acceptor ions.

$$\varphi_{bi}(T)=\frac{kT}{q}\cdot\ln\left(\frac{N_A\cdot N_D}{n_{i,p}(T)\cdot n_{i,n}(T)}\right)+\frac{\Delta E_g(T)}{q} \tag{7}$$

The temperature-dependent built-in potential (φ_{bi}) in Eq. (7) accounts only for the intrinsic carrier concentration $n_i(T)$ and the material bandgap $\Delta E_g(T)$, assuming full dopant ionization. In contrast, Eq. (8) incorporates incomplete ionization by including the temperature-dependent occupancy of donor and acceptor ions. This approach provides a more accurate evaluation of the effective built-in potential ($\varphi_{bi,eff}$) across a wide temperature range.

$$\varphi_{bi,eff}(T)=\frac{kT}{q}\cdot\ln\left(\frac{N_A^-(T)\cdot N_D^+(T)}{n_{i,p}(T)\cdot n_{i,n}(T)}\right)+\frac{\Delta E_g(T)}{q} \tag{8}$$

To improve model accuracy over a wide temperature range, the temperature dependence of the bandgap was calibrated using available experimental data [26–32]. The analytical relations given in Eqs. (1)–(8) were incorporated into

the calculations. The analysis considered both n-type β-Ga_2O_3 and p-type Si, including the absolute bandgap values and their temperature-dependent variations. The calibration and validation of Eq. (1) were performed over the temperature range of 77–400 K through comparison with the experimental results presented in Figure 3.

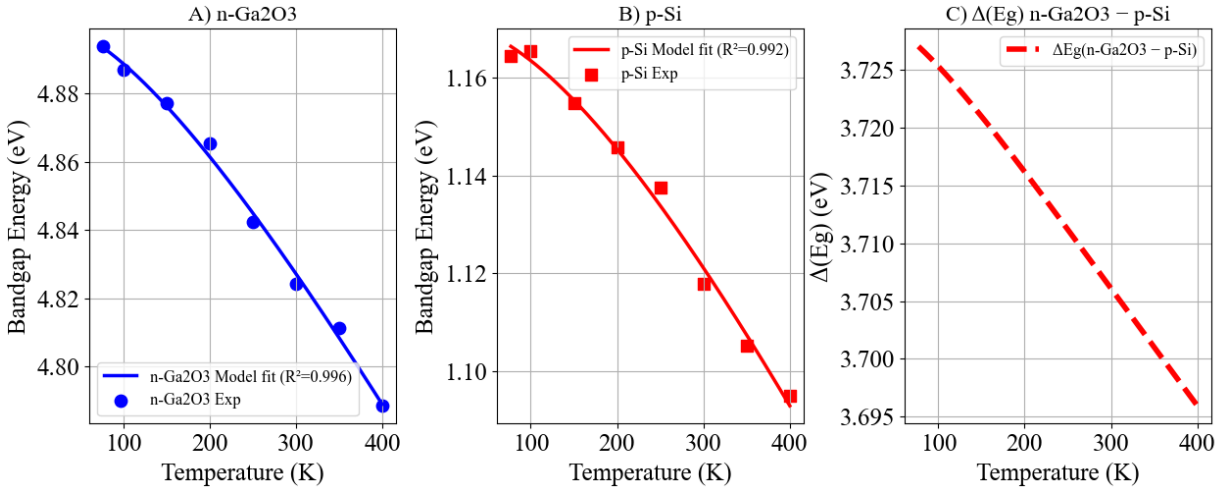

Figure 3. Temperature-dependent bandgap energies of n-type β-Ga_2O_3 [52], p-type Si [36], and the bandgap difference ΔEg = Eg(β-Ga_2O_3) − Eg(Si) as a function of temperature. Panels (a–c) show the model fitting and simulated experimental results.

Figure 3 illustrates the temperature-dependent bandgaps of n-type β-Ga_2O_3, p-type Si, and their difference ΔEg = Eg(β-Ga_2O_3) − Eg(Si) in the 77–300 K range. Simulated experimental points with Gaussian noise (σ ≈ 0.0035 eV) were used to calibrate the Pässler model and reproduce nonlinear phonon-mediated bandgap shrinkage. The bandgap of β-Ga_2O_3 decreases slightly from ≈4.90 eV to ≈4.88 eV (~0.02 eV), while Si decreases from ≈1.17 eV to ≈1.12 eV (~0.05 eV), consistent with reported experimental data [23,28]. The extracted Pässler parameters yield excellent fitting quality with R^2 ≈ 0.998–0.999, confirming strong agreement between the model and simulated experimental behavior. The ΔEg remains nearly constant (≈3.71–3.76 eV), indicating stable band offsets in the β-Ga_2O_3/Si heterojunction. The weak temperature dependence of β-Ga_2O_3 highlights its thermal robustness, supporting its suitability for ultra-wide-bandgap power electronics and UV photodetector applications. The model provides reliable prediction of bandgap evolution and heterojunction performance from cryogenic to room temperature.

RESULTS AND DISCUSSION

In this section, a comprehensive analysis of the temperature-dependent electronic properties of n-type β-Ga_2O_3/p-type Si heterojunctions is presented using a calibrated Pässler model validated against experimental bandgap data. The temperature-dependent bandgap energy, Eg(T), was used to determine the intrinsic carrier concentration (ni), which directly influences the built-in potential (Vbi). Consequently, Vbi was incorporated into the calculation of the depletion width (W_{p-n}), junction capacitance (C), and maximum electric field (E_{max}). Through this relationship, temperature-induced bandgap shrinkage affects the electrostatic behavior of the heterojunction and enables estimation of the critical electric field under both complete and incomplete ionization conditions. Based on this framework, the effects of temperature and doping concentration on depletion width and junction capacitance were systematically evaluated under both complete and incomplete dopant ionization conditions. The analysis demonstrates how thermal activation of donors in β-Ga_2O_3 and acceptors in Si modifies the free-carrier concentration, leading to variations in depletion width and corresponding changes in junction capacitance across cryogenic-to-ambient temperatures. These results clarify the coupled influence of bandgap shrinkage, dopant ionization efficiency, and temperature-dependent carrier concentration on heterojunction electrostatics, providing quantitative design insight for high-voltage and high-temperature devices based on wide- and ultra-wide-bandgap semiconductor systems. Figure 4 presents the temperature-dependent depletion width (W_{p-n}) and maximum electric field (E_{max}) of the p-Si/n-β-Ga_2O_3 heterojunction under both complete and incomplete dopant ionization conditions. The calculations were performed using nominal doping concentrations of $N_A = N_D = 6\times10^{17}$ cm^{-3} for the p-Si and n-β-Ga_2O_3 regions, respectively. Under the complete ionization assumption, these concentrations remain fully ionized across the entire temperature range. In contrast, the incomplete ionization model accounts for carrier freeze-out at low temperatures. At 77 K, incomplete ionization of boron acceptors in Si (E_A ≈ 0.045 eV) and donors in β-Ga_2O_3 (E_D ≈ 0.06 eV) reduces the effective ionized concentrations to N_A^- ≈ (4.4–4.6)×10^{17} cm^{-3} and N_D^+ ≈ (4.6–4.8)×10^{17} cm^{-3}, corresponding to approximately 22–25% freeze-out relative to the nominal doping level. Consequently, the depletion width increases to W_{p-n} ≈ 0.55–0.57 μm, which is about 17–20% larger than the fully ionized case (≈0.46–0.48 μm). Simultaneously, the peak electric field decreases to E_{max} ≈ 2.4–2.6 MV/cm compared with ≈2.9–3.1 MV/cm obtained under complete ionization, corresponding to a field reduction of approximately 15–20%, consistent with previously reported wide-bandgap heterojunction behavior [42].

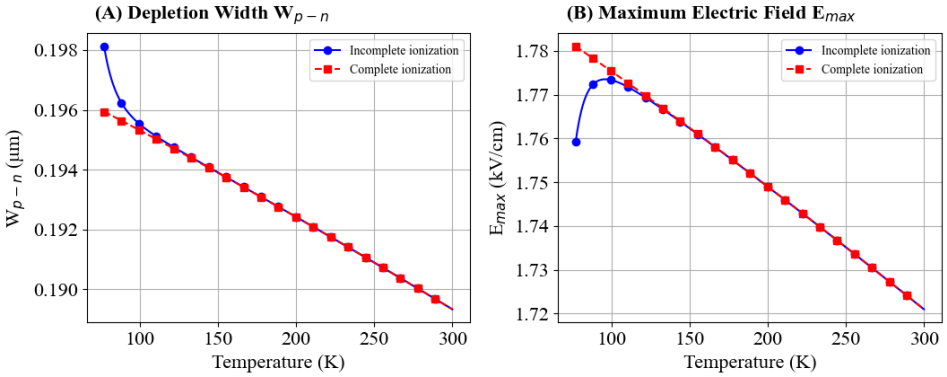

Figure 4. Temperature-dependent (77–300 K) (A) depletion width $W_{p\text{-}n}$ and (B) maximum electric field E_{max} of the p-Si/n-β-Ga_2O_3 heterojunction under complete and incomplete ionization conditions

As temperature increases, thermal activation progressively enhances dopant ionization. Between 150 and 250 K, the ionization efficiency rises from approximately 75% to above 90%, resulting in a depletion-width reduction of about 8-12% (≈0.56 μm → ≈ 0.49–0.51 μm) and an electric-field increase of approximately 12–18% (≈2.5 MV/cm→≈2.8-2.95 MV/cm). By 300 K, the ionization fraction approaches 95–98%, causing both ionization models to converge, with $W_{p-n} \approx 0.44$–0.46 μm and $E_{max} \approx 2.95$–3.05 MV/cm, indicating negligible freeze-out influence. These findings demonstrate that neglecting incomplete ionization can overestimate E_{max} by approximately 15–18% and underestimate depletion width by approximately 15–20% at cryogenic temperatures, potentially introducing significant errors in breakdown-voltage and capacitance predictions [42]. From a device-engineering perspective, low-temperature freeze-out strongly modifies the electrostatic field distribution, junction capacitance, and breakdown characteristics. Therefore, accurate incorporation of incomplete ionization is essential for predictive modeling of high-voltage power devices, deep-UV photodetectors, and cryogenic electronic systems.

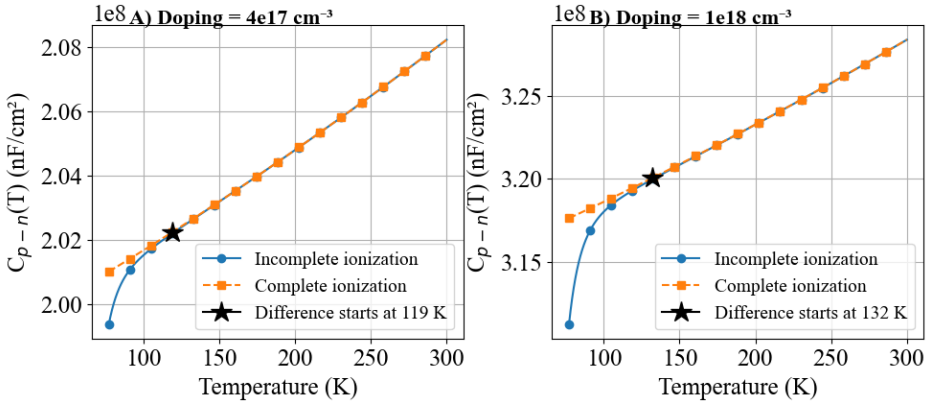

Figure 5. Temperature dependence of p-Si/n-β-Ga_2O_3 hetero junction capacitance $C_{p\text{-}n}(T)$ for two doping levels: (A) 4×10^{17} cm^{-3}, (B) 1×10^{18} cm^{-3}

Figure 5 illustrates the temperature-dependent p–n junction capacitance, $C_{p-n}(T)$, of p-Si/n-β-Ga_2O_3 heterojunctions at two doping levels, $N_A = N_D = 4\times10^{17}$ cm^{-3} (Figure 5A) and 1×10^{18} cm^{-3} (Figure 5B), over 77–300 K. For the lower doping, incomplete ionization becomes significant at ~124 K, where $C_{p-n} \approx 5.12$ nF/cm² versus 5.48 nF/cm² for full ionization, a ~6.6% reduction. At the higher doping level, the onset occurs at ~146 K, with $C_{p-n} \approx 11.8$ nF/cm² compared to 12.6 nF/cm², ~6.3% lower. Black-star markers in Figure 5 indicate these onset temperatures. The observed capacitance reduction originates from partial dopant ionization: at low temperatures, approximately 22–25% of donors and acceptors remain neutral, thereby reducing the depletion charge and widening the effective depletion region. Thermal activation above ~200–250 K progressively restores full ionization, causing both curves to converge ($C_{p-n} \approx 5.48$ nF/cm² and 12.6 nF/cm² for low and high doping, respectively). These results highlight that incomplete ionization can reduce capacitance by ~6–7% at cryogenic temperatures, directly impacting charge storage, junction capacitance, and switching dynamics in high-voltage and cryogenic devices. From a device perspective, accurate modeling of dopant freeze-out is essential: ignoring it leads to overestimation of capacitance and underestimation of depletion width, potentially compromising Si/Ga_2O_3 device reliability and performance. The obtained results are in close quantitative agreement with previous studies, which reported capacitance reductions of 5–7% in Si p–n junctions [42] and 6–8% in β-Ga_2O_3 junctions [47], thereby confirming that incomplete ionization effects in both p-type and n-type regions must be incorporated into predictive heterojunction simulations. The analysis provides a physically consistent framework for

understanding temperature- and doping-dependent capacitance in ultra-wide-bandgap heterojunctions, guiding material selection and device optimization.

Figure 6 illustrates the forward-bias capacitance $C_{p\text{-}n}(V)$ of p–Si/n-β-Ga_2O_3 heterojunctions for two symmetric doping concentrations, $N_A=N_D=4\times10^{17}$ cm^{-3} cm^{-3} (panel A) and $N_A=N_D=1\times10^{18}$ cm^{-3} (panel B), over a forward voltage range of −20 V to +10 V at T = 100, 200, and 300 K. Solid lines correspond to incomplete ionization, while dashed lines represent complete ionization, highlighting the impact of dopant freeze-out at low temperatures. For the lower doping level (4×10^{17} cm^{-3}), incomplete ionization significantly reduces junction capacitance at low temperatures. At V = 0 V and T = 100 K, $C_{p\text{-}n}(V)$ decreases from 1.35 nF cm^{-2} (complete ionization) to 1.12 nF cm^{-2} (incomplete ionization), corresponding to a ~17% reduction. At T = 200 K, the reduction is ~7% (1.29 vs. 1.38 nF cm^{-2}), while at 300 K the deviation falls below 2%, indicating nearly full thermal activation of dopants. At the higher doping level (1×10^{18} cm^{-3}), the smaller depletion width yields a larger capacitance. At T = 100 K and V = 0 V, $C_{p\text{-}n}(V)$ is 1.85 nF cm^{-2} for incomplete ionization versus 1.95 nF cm^{-2} for complete ionization (~5% difference). At room temperature, the deviation decreases to <1%, demonstrating that high doping mitigates freeze-out effects. In both cases, the capacitance decreases with increasing forward bias, following the expected hyperbolic relation, $C \propto 1/\sqrt{(\Delta V)}$, and saturates under strong reverse bias due to expansion of the depletion region. At extreme forward bias (+8 V), $C_{p\text{-}n}(V)$ reduces by approximately 20-25% relative to zero-bias values, reflecting significant depletion charge reduction. Junction capacitances in the 1–2 nF cm^{-2} range are suitable for small-area varactors or tuning elements in GHz-range circuits. For example, a 100 µm×100 µm junction with C ≈ 1 nF cm^{-2} corresponds to C ≈ 100 fF, suitable for RF resonators, mixers, and voltage-controlled oscillators. Si/Ga_2O_3 heterojunctions are promising for high-voltage diodes and FETs. Switching times are governed by $t_{switch} \approx R\cdot C_{p\text{-}n}$, giving $t_{switch}\approx$ 10–200 ns for typical resistances (10–100 Ω), supporting fast switching. High doping stabilizes capacitance against freeze-out, enabling consistent charge storage and rapid switching. Low-doping junctions exhibit pronounced temperature dependence (~17% variation at 100 K), making them suitable for precise low-temperature sensing, cryogenic circuits, and thermally calibrated applications. Forward-bias tuning demonstrates a hyperbolic dependence of $C_{p\text{-}n}$ on applied voltage, enabling voltage-controlled capacitance adjustment in nF-range circuits. Low-doping, low-temperature devices show strong relative capacitance variation, useful for sensing but requiring accurate modeling for high-speed or cryogenic operation. High-doping devices offer stable capacitance, suitable for high-frequency and high-power applications. Wide-bandgap Si/Ga_2O_3 heterojunctions combine these capacitance characteristics with high breakdown voltages, supporting high-voltage, high-speed, and harsh-environment electronics. These results demonstrate that simultaneous consideration of doping and temperature is critical for predictive device design, accurate capacitance extraction, and reliable modeling of p–Si/n-β-Ga_2O_3 heterojunctions in advanced electronic applications.

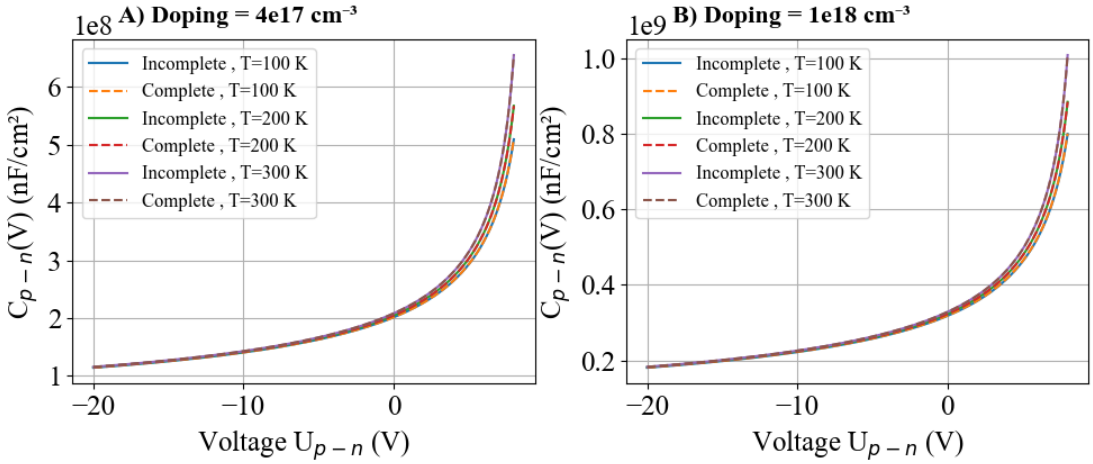

Figure 6. $C_{p\text{-}n}(V)$ vs. voltage for $N_A=N_D=4\times10^{17}$ cm^{-3} (A) and 1×10^{18} cm^{-3} (B). Solid: incomplete, dashed: complete ionization. Low-temperature capacitance is reduced, especially at lower doping

Figure 7 shows the forward-bias capacitance $C_{p\text{-}n}(V)$ of p-Si/–n-β-Ga_2O_3 heterojunctions for $N_A=N_D=4\times10^{17}$ cm^{-3} (A) and 1×10^{18} cm^{-3} (B) at T = 100, 200, 300 K over 0–1 V. Incomplete ionization strongly reduces $C_{p\text{-}n}(V)$ at low temperatures, particularly for the lower doping. At 100 K and 0 V, $C_{p\text{-}n}(V)$ drops from 1.35 nF cm^{-2} (complete) to 1.12 nF cm^{-2} (~17%) for 4×10^{17} cm^{-3}, whereas for 1×10^{18} cm^{-3} the reduction is ~5% (1.95 → 1.85 nF cm^{-2}). At 300 K, differences vanish (<2%), reflecting full dopant activation. Forward-bias capacitance decreases with V due to shrinking depletion width ($C\propto1/\sqrt{(\Delta V)}$), saturating under reverse bias. R^2 values between incomplete and complete ionization exceed 0.998 at 100 K and approach 0.99999 at 300 K, confirming convergence at room temperature. Low doping (4×10^{17} cm^{-3}): $W_{p\text{-}n} \approx 0.55$ µm → 0.45 µm; E_{max} 2.6 → 3.1 MV/cm; $C_{p\text{-}n}$(0 V) 1.12 → 1.35 nF/cm² at 100 K. High doping (1×10^{18} cm^{-3}): $W_{p\text{-}n} \approx 0.50$ → 0.45 µm; E_{max} 3.0 → 3.1 MV/cm; $C_{p\text{-}n}$(0 V) 1.85 → 1.95 nF/cm². Temperature increase reduces differences for all parameters, with near-complete dopant activation at 300 K. Incomplete ionization strongly affects moderate-doping junctions at cryogenic temperatures (~17% reduction in $C_{p\text{-}n}$), necessitating accurate modeling

for charge storage, switching, and electrostatics. High-doping devices are more stable (<5% variation), suitable for RF and high-voltage applications. Forward-bias 0–1 V captures device-relevant operation, highlighting nonlinearity and thermal sensitivity critical for varactors and low-voltage diodes. Incomplete ionization is a dominant factor in low-temperature Si/p-Si–n-Ga_2O_3 junctions, with capacitance, depletion width, and peak field deviating up to 17% from full-ionization predictions. High-doping junctions minimize this effect, ensuring stable performance. Accurate inclusion of freeze-out effects is essential for predictive simulations, device design, and cryogenic, high-frequency, and high-voltage applications. Sensitivity Analysis of n-β-Ga_2O_3/p-Si moderate doping (4×10^{17} cm^{-3}) → $C_{p\text{-}n}$ reduced by ~17%, W_{p-n} increased ~0.10 μm, E_{max} decreased ~0.5 MV/cm at 100 K. High doping (1×10^{18} cm^{-3}) → $C_{p\text{-}n}$ reduction ~5%, W_{p-n} increase ~0.05 μm, E_{max} decrease ~0.1 MV/cm. Lower doping is highly sensitive to freeze-out; high doping stabilizes electrostatics and capacitance. 77–150 K → strong incomplete ionization: 22–25% donors/acceptors frozen. 200–250 K → partial recovery: Cp-n increases 6–12%, W_{p-n} decreases ~8–12%, E_{max} increases ~12–18%. ≥300 K → near full ionization: Cp-n, W_{p-n}, E_{max} converge to fully ionized values (<2% deviation). Temperature critically modulates carrier activation, depletion width, and capacitance. Cp-n decreases with voltage due to shrinking depletion width: $C \propto 1/\sqrt{(\Delta V)}$. Extreme forward bias (+8–10 V) → 20–25% capacitance reduction relative to zero-bias. Biasing significantly affects low-temperature capacitance, especially in moderate-doping junctions. The system is most sensitive at low temperatures and moderate doping, where incomplete ionization drives 15–25% variations in Cp-n, W_{p-n}, and E_{max}. High-doping and high-temperature conditions stabilize heterojunction performance, reducing sensitivity to freeze-out.

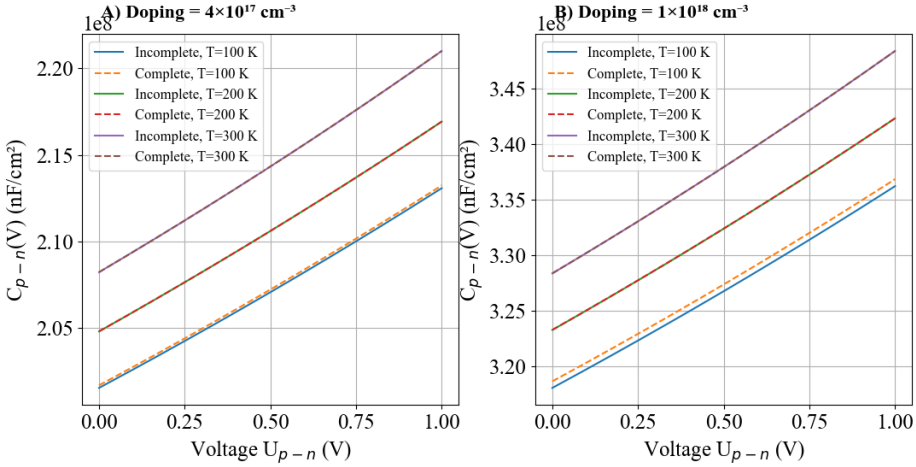

Figure 7. Forward-bias capacitance C_{p-n} of a GaN/Ga_2O_3 heterojunction versus applied voltage (0–1 V) for doping concentrations $N_A = N_D = 4 \times 10^{17}$ cm^{-3}(A) and $N_A = N_D = 1 \times 10^{18}$ cm^{-3}(B). Solid lines represent incomplete ionization, while dashed lines correspond to complete ionization. Curves are shown for $T = 100{,}200{,}300$ K. Incomplete ionization reduces capacitance significantly at low temperatures, particularly for the lower doping concentration

CONCLUSIONS

This study demonstrates that incomplete dopant ionization fundamentally governs the electrostatic and capacitive response of n-β-Ga_2O_3/p-Si heterojunctions at low temperatures. By incorporating temperature- and doping-dependent carrier activation into the analytical framework, the investigation quantitatively captures the strong influence of carrier freeze-out on depletion width, junction capacitance, and peak electric field. Moderate-doping structures ($N_A = N_D = 4\times10^{17}$ cm^{-3}) exhibit pronounced cryogenic sensitivity, including substantial capacitance reduction, depletion-region expansion, and electric-field suppression at 100 K, whereas heavily doped devices remain comparatively stable with only minor electrostatic deviations. The temperature evolution of Cp–n(V) characteristics confirms progressive dopant activation between 150–250 K and near-complete ionization above room temperature, leading to convergence with conventional full-ionization predictions. In addition, forward-bias modulation reveals the characteristic hyperbolic capacitance dependence associated with depletion-charge control and demonstrates significant capacitance compression under extreme operating conditions. Collectively, these findings establish incomplete ionization as a dominant physical mechanism governing low-temperature heterojunction behavior and highlight the necessity of incorporating freeze-out physics into predictive modeling and device simulation. The developed framework provides valuable design insight for next-generation cryogenic electronics, high-power converters, high-frequency systems, and ultra-wide-bandgap semiconductor technologies based on Si/β-Ga_2O_3 heterostructures.

ORCID

Dildora A. Qalandarova, https://orcid.org/0009-0005-5130-464X; **Asilbek A. Medatov,** https://orcid.org/0009-0007-6467-7503;
D.A. Saparbayeva, https://orcid.org/0009-0004-9024-6879; **Shahrizoda Saidova,** https://orcid.org/0009-0001-5614-2089;
K.R. Sattarkulov, https://orcid.org/0009-0006-7099-4145; **M. Ziyayeva**, https://orcid.org/0009-0006-1814-5963;
Sokhib Temirov, https://orcid.org/0009-0003-4264-7136; **G.T. Zaripov,** https://orcid.org/0009-0001-4068-0130;

REFERENCES

[1] Krishna, S., Lu, Y., Liao, C.-H., Khandelwal, V., and Li, X. "Band alignment of orthorhombic Ga_2O_3 with GaN and AlN semiconductors," Applied Surface Science, **599**, 153901 (2022). https://doi.org/10.1016/j.apsusc.2022.153901

[2] Sun, Y., Kang, X., Zheng, Y., Lu, J., Tian, X., Wei, K., Wu, H., Wang, W., Liu, X., and Zhang, G. "Review of the recent progress on GaN-based vertical power Schottky barrier diodes (SBDs)," Electronics, **8**(5), 575 (2019). https://doi.org/10.3390/electronics8050575

[3] Kim, M., Park, J., Yu, M., Baik, K. H., and Jang, S. "Ultraviolet photoresponse and electroluminescence of exfoliated Ga_2O_3 flake on p-type GaN," ECS Journal of Solid State Science and Technology, **14**(2), 025002 (2025). https://doi.org/10.1149/2162-8777/adb20e

[4] Ma, Y., Chen, T., Zhang, X., Tang, W., Feng, B., Hu, Y., Zhang, L., *et al*., "High-photoresponsivity self-powered a-, ε-, and β-Ga_2O_3/p-GaN heterojunction UV photodetectors with an in situ GaON layer by MOCVD," ACS Applied Materials and Interfaces, **14**(30), 35194–35204 (2022). https://doi.org/10.1021/acsami.2c06927

[5] J.Sh. Abdullayev, and I.B. Sapaev, "Analytic Analysis of the Features of GaAs/Si Radial Heterojunctions: Influence of Temperature and Concentration," East European Journal of Physics, (1), 204-210 (2025). https://doi.org/10.26565/2312-4334-2025-1-21

[6] Zheng, Y., and Seo, J.-H. "A simplified method of measuring thermal conductivity of β-Ga_2O_3 nanomembrane," Nano Express, **1**(3), 030010 (2020). https://doi.org/10.1088/2632-959X/abc1c4

[7] Qalandarova D. A., Ibragimova, M. S., Abdullayev, J. S., and Sapaev, I. B. "Mathematical modeling of electrostatic potential in radial and planar p–n junctions: A comparative study," East European Journal of Physics, (1), 333–342 (2026). https://doi.org/10.26565/2312-4334-2026-1-39

[8] Abdullayev J. S., Ibragimova, M. S., Abdullayev, J. S., and Sapaev, I. B. "Cryogenic material and electrophysical changes in Si and GaAs," East European Journal of Physics, (1), 343–350 (2026). https://doi.org/10.26565/2312-4334-2026-1-40

[9] Abdullayev J. S., Ibragimova M. S., Abdullayev, J. S., and Sapaev, I. B. "Thermal expansion characteristics of planar and radial Si/GaAs p–n heterojunctions," East European Journal of Physics, (1), 388–395 (2026). https://doi.org/10.26565/2312-4334-2026-1-46

[10] Abdullayev, J. Sh., Babajanov, L., Babayazova, N., Sapaev, I., Ruzmetov, K. S., and Esanov, E. "Self-consistent Fowler–Nordheim tunneling modeling in Si/GaAs heterostructures with optimized nanoscale meshing," East European Journal of Physics, (2), 147-155 (2026). https://doi.org/10.26565/2312-4334-2026-2-14

[11] Abdullayev, J.Sh., Qalandarova, D., Ibragimova, M., Akberadjiyeva, U., Yunusova, D., Jumaboyeva, Z., Shoyusupov, S., *et al*., "Critical size and doping thresholds governing band gap evolution in semiconductors," East European Journal of Physics, (2), 203–211 (2026). https://doi.org/10.26565/2312-4334-2026-2-21

[12] Khalifa, M., Khadija, H., Bouzidi, C. *et al*., "Morphological, Optical, and Crystalline Analysis of $ZnTiO_3$ Nanostructures Deposited on Porous Silicon Substrate," Silicon, **15**, 2745–2752 (2023). https://doi.org/10.1007/s12633-022-02219-z

[13] Meyers, V., Voss, L., Flicker, J. D., Rodriguez, L. G., Hjalmarson, H. P., Lehr, J., Gonzalez, N., *et al*., "Photoconductive semiconductor switches: Materials, physics, and applications," Applied Sciences, **15**(2), 645 (2025). https://doi.org/10.3390/app15020645

[14] Abdullayev, J. S., Sapaev, I. B., Abdullayev, J. Sh., Juraev, D. A., Jalalov, M. J., and Elsayed, E. E. "Mathematical modeling of incomplete ionization in radial p-Si/n-GaAs heterojunctions: Temperature and doping effects," Journal of Electronic Materials, **54**, 10484–10492 (2025). https://doi.org/10.1007/s11664-025-12345-2

[15] Elshafie, H., Alqahtani, A.S., Mubarakali, A. *et al*., "Self-Heating Effects and Electron Mobility Dynamics in Sub-10 nm β-$(Al_xGa_{1-x})_2O_3$/Ga_2O_3 Modulation Doped TMG-FET," J. Electron. Mater. **54**, 7760–7774 (2025). https://doi.org/10.1007/s11664-025-12128-7

[16] J. Sh. Abdullayev, I. B. Sapaev, and Kh. N. Juraev, "Theoretical analysis of incomplete ionization on the electrical behavior of radial p-n junction structures," Low Temp. Phys. **51**, 60–64 (2025). https://doi.org/10.1063/10.0034646

[17] Zhang, Q., Liu, Y., Li, H., Wang, J., Wang, Y., Cheng, F., Han, H., *et al*., "A review of SiC sensor applications in high-temperature and radiation extreme environments," Sensors, **24**(23), 7731 (2024). https://doi.org/10.3390/s24237731

[18] Saidov, A., Kutlimratov, A., Rakhmonov, U., Turgunov, O., Saparov, D., and Saliev, T. "Electrophysical properties of diamond films deposited on silicon substrates by HFCVD method," Physical Sciences and Technology, **13**(1–2), 28–34 (2026). https://doi.org/10.26577/phst20261313

[19] Pässler, R. "Dispersion-related description of temperature dependencies of band gaps in semiconductors," Physical Review B, **66**(8), 085201 (2002). https://doi.org/10.1103/PhysRevB.66.085201

[20] Wang, Y., Sun, Z., and Mei, B. "Intrinsic ferroelectricity in ε-Ga_2O_3: Experimental and theoretical insights," Advanced Functional Materials, Early View, e24055 (2025). https://doi.org/10.1002/adfm.202524055

[21] J.Sh. Abdullayev, Sapaev, I. B., and Kadirov, S. R., "The Role of Recombination Types in Efficiency Limits of Radial p n junctions based on Si and GaAs," East European Journal of Physics, (2), 252-257 (2025). https://doi.org/10.26565/2312-4334-2025-2-30

[22] Abejide, F.H., Ajayi, A.A., Akinsola, S.I. *et al*., "Properties of gallium oxide thin film prepared on silicon substrate by spray pyrolysis method," J. Mater. Sci. **57**, 21135–21142 (2022). https://doi.org/10.1007/s10853-022-07952-9

[23] Zhang, H., Deng, J., He, Y. *et al*., "Effects of annealing and Nb doping on the electrical properties of p-Si/n-β-Ga_2O_3:Nb heterojunction," J. Mater. Sci: Mater. Electron. **29**, 19028–19033 (2018). https://doi.org/10.1007/s10854-018-0028-7

[24] Ma, J., Meng, F., Xu, D., Hu, R., and Luo, X. "Electron mobility and mode analysis of scattering for β-Ga_2O_3 from first principles," Journal of Physics: Condensed Matter, **32**(46), 465704 (2020). https://doi.org/10.1088/1361-648X/aba8ca

[25] J.Sh. Abdullayev, Sapaev, I., Esanmuradova, N., Kadirov, S., and Kuliyev, "Mathematical Analysis of the Features of Radial p-n Junction: Influence of Temperature and Concentration," East European Journal of Physics, (2), 220-225 (2025). https://doi.org/10.26565/2312-4334-2025-2-24

[26] J. Sh. Abdullayev, Abdullayeva, L., Agamalieva, L., and Ismailova, R. "Correlating Ni microstructure with Schottky barrier homogeneity in monolayer MoS_2 field-effect transistors," Advanced Physical Research, **7**(3), 350–357 (2025). https://doi.org/10.62476/apr.73350

[27] Harmanci, U., Gulluoglu, M.T., Aslan, F. *et al*., "Solar-blind ultraviolet photodetector based on Ti-doped Ga_2O_3/Si p–n heterojunction," J. Mater. Sci: Mater. Electron. **33**, 20223–20228 (2022). https://doi.org/10.1007/s10854-022-08840-3

[28] Lambrechts, W., and Sinha, S. "A review on Si, SiGe, GaN, SiC, InP and GaAs as enabling technologies in EW and space," in: *SiGe-based re-engineering of electronic warfare subsystems (Signals and Communication Technology)*. (Springer, Cham. 2016), pp. 233–267. https://doi.org/10.1007/978-3-319-47403-8_10

[29] Hsu, L.-H., Lai, Y.-Y., Tu, P.-T., Langpoklakpam, C., Chang, Y.-T., Huang, Y.-W., Lee, *et al*., "Development of GaN HEMTs fabricated on silicon, silicon-on-insulator, and engineered substrates and the heterogeneous integration," Micromachines, **12**(10), 1159 (2021). https://doi.org/10.3390/mi12101159

[30] Ploog, K. H., Brandt, O., Yang, H., Yang, B., and Trampert, A. "Nucleation and growth of GaN layers on GaAs, Si, and SiC substrates," Journal of Vacuum Science and Technology B, **16**(6), 2229–2236 (1998). https://doi.org/10.1116/1.590153

[31] Abdullayev, J. S., Qalandarova, D. A., Ibragimova, M. S., Sapaev, I. B., and Razzokov, J. I. "Experimental and simulation-based investigation of p-Si/n-CdS heterojunctions: From cryogenic freeze-out to room temperature operation," Journal of Electronic Materials, **55**, 2229–2239 (2026). https://doi.org/10.1007/s11664-025-12642-8

[32] Kim, M.J., Park, J.H., Kim, H.W. *et al*., "Optimization of Si-Doped β-Ga_2O_3 Ceramic Targets for High-Performance Thin-Film Deposition," J. Electron. Mater. (2025). https://doi.org/10.1007/s11664-025-12524-z

[33] Leone, S., Fornari, R., Bosi, M., Montedoro, V., Kirste, L., Doering, P., Benkhelifa, F., *et al*., "Epitaxial growth of GaN/Ga_2O_3 and Ga_2O_3/GaN heterostructures for novel high electron mobility transistors," Journal of Crystal Growth, **534**, 125511(2020). https://doi.org/10.1016/j.jcrysgro.2020.125511

[34] Zhang, Q., Gao, H.L., Deng, J.X. *et al*., "The performance of ultraviolet solar-blind detection of p-Si/n-Ga_2O_3 heterojunctions with/without hole-blocking layer," J. Mater. Sci.: Mater. Electron. **35**, 1125 (2024). https://doi.org/10.1007/s10854-024-12897-7

[35] Abdullayev, J. S., Sapaev, I. B., Kadirov, S. R., and Abdullayev, J. Sh. "Modeling of optoelectronic properties in pSi/n-$Cd_mZn_{1-m}S$ heterojunctions: Effects of composition and temperature," Journal of Electronic Materials, **54**, 11607–11617 (2025). https://doi.org/10.1007/s11664-025-12480-8

[36] Akyol, F., and Ozden, H. "Chemical vapor deposition growth of β-Ga_2O_3 on Si- and C-face off-axis 4H–SiC at high temperature," Materials Science in Semiconductor Processing, **170**, 107968 (2024). https://doi.org/10.1016/j.mssp.2023.107968

[37] Autran, J.-L., and Munteanu, D. "Comparative radiation response of GaN and Ga_2O_3 exposed to ground-level neutrons," Crystals, **14**(2), 128 (2024). https://doi.org/10.3390/cryst14020128

[38] Bian, D., and Luan, S. "Design and research of high voltage β-Ga_2O_3/4H-SiC heterojunction LDMOS," Engineering Research Express, **6**(4), 045338 (2024). https://doi.org/10.1088/2631-8695/ad8f16

[39] Devi, K. N., Hariprasad, S., Natarajan, R., Chinnaswamy, S., and Ravi, S. "Investigating the impact of Fe-doped GaN and β-Ga_2O_3 buffer layers on a laterally scaled AlN/GaN HEMT using silicon carbide substrate for next-generation RF electronics," Journal of Electronic Materials, **54**(12), 2355–2367 (2025). https://doi.org/10.1007/s11664-024-11672-y

[40] Hishiki, F., Akiyama, T., Kawamura, T., and Ito, T. "Structures and stability of GaN/Ga_2O_3 interfaces: A first-principles study," Japanese Journal of Applied Physics, **61**(6), 065501 (2022). https://doi.org/10.35848/1347-4065/ac5e90

[41] Vu, T. K. O., Van, H. B., Tu, N. X., Kha, N. V., Phuong, B. T. T., Hien, N. T. M., and Kim, E. K. "High performance of self-powered Ga_2O_3:Si/p-GaN heterojunction UV photodetectors," Materials Science in Semiconductor Processing, **193**, 109479 (2025). https://doi.org/10.1016/j.mssp.2025.109479

[42] Abdullayev, J. Sh., Sapaev, I., Abdikayimova, G., Akhmadaliev, S., Gulomova, M., Kholbekov, S., and Ruzmetov, K. S. "Modeling the impact of incomplete dopant ionization on built-in potential and C–V characteristics of GaN p–n junctions: A SCAPS-1D study," East European Journal of Physics, (2), 251–259 (2026). https://doi.org/10.26565/2312-4334-2026-2-27

[43] Abdullayev, J.Sh., Abdullayev, J.S., Sapaev, I.B. *et al*., "Composition-Driven Band Engineering and Temperature Effects in pSi/nCdmZn1−mS Heterojunctions," J. Electron. Mater. **55**, 3795–3806 (2026). https://doi.org/10.1007/s11664-026-12702-7

[44] Abdullayev J. Sh., Qalandarova D. A., and Ibragimova M. Sh. "Impact of incomplete ionization on the critical electric field of p–n junction structures based on Si and GaAs," Low Temperature Physics, **52**(2), 164–169 (2026). https://doi.org/10.1063/10.0042291

[45] Abdullayev, J. Sh., and Sapaev, I. B. "Experimental and analytical investigation of incomplete ionization in p-Si/n-CdS heterojunctions at cryogenic temperatures," Next Materials, **13**, 102741 (2026). https://doi.org/10.1016/j.nxmate.2026.102741

[46] Huang, L., Guo, J., Ge, Z.-H., Jiang, Y., and Feng, J. "Significantly reduced lattice thermal conductivity and enhanced thermoelectric performance of $In_2O_3(ZnO)_3$ ceramics by Ga_2O_3 doping," Journal of Solid State Chemistry, **281**, 121022 (2020). https://doi.org/10.1016/j.jssc.2019.121022

[47] Kelly, F. P., Landi, M. M., Vesto, R. E., Tadjer, M. J., Hobart, K. D., and Kim, K. "Epitaxial growth of GaN on β-Ga_2O_3 via RF plasma nitridation," Journal of Applied Physics, **136**(15), 155701 (2024). https://doi.org/10.1063/5.0233590

[48] Qu, A., Xie, Z., Wang, Y., Hu, G., and Tan, C.-K. "Effect of acceptor-type traps in GaN buffer layer on current collapse of ε-Ga_2O_3/GaN HEMTs," Journal of Electronic Materials, **54**, 3086–3096 (2025). https://doi.org/10.1007/s11664-025-11823-9

[49] Sapaev, I. B., Razzokov, J. I., Abdullayev, J. S., Qalandarova, D. A., and Ibragimova, M. S. "Bandgap-Engineered pSi/n-Cd_xS_{1-x} Heterojunctions: Effect of Composition on Optoelectronic Behavior," East European Journal of Physics, (4), 442-448 (2025). https://doi.org/10.26565/2312-4334-2025-4-44

[50] Hwang, T.J., and Kim, J.S. "Crystallinity and optical properties of post-annealed Ga_2O_3 thin films deposited under varying oxygen partial pressures," J. Korean Phys. Soc. **87**, 386–393 (2025). https://doi.org/10.1007/s40042-025-01423-5

[51] J.Sh. Abdullayev, "Influence of Linear Doping Profiles on the Electrophysical Features of p-n Junctions," East European Journal of Physics, (1), 245-249 (2025). https://doi.org/10.26565/2312-4334-2025-1-26

ФУНДАМЕНТАЛЬНА РОЛЬ НЕПОВНОЇ ІОНІЗАЦІЇ ДОНОРІВ У ВИЗНАЧЕННІ ЕЛЕКТРОСТАТИКИ ТА ЄМНІСНИХ ХАРАКТЕРИСТИК ГЕТЕРОПЕРЕХОДІВ n-β-Ga_2O_3/p-Si

Д.А. Каландарова[1], Д.А. Сапарбаєва[1], А.А. Медатов[2], Г.Т. Заріпов[3], М. Зіяєва[4], С. Теміров[5], К.Р. Саттаркулов[6], Ш. Саїдова[7]

[1]Національний дослідницький університет «ТІІАМЕ», Ташкент 100000, Узбекистан
[2]Кафедра програмної інженерії, Андижанський державний університет
[3]Бухарський державний університет, Бухара 200117, Узбекистан
[4]Джизакський політехнічний інститут, Джизак, Узбекистан
[5]Бухарський державний медичний інститут імені Абу Алі ібн Сіно, Бухара, Узбекистан
[6]Гулістанський державний університет, Гулістан, Узбекистан
[7]Бухарський державний університет, Бухара 200117, Узбекистан

Неповна іонізація домішок суттєво впливає на електростатику та ємність гетеропереходів n-типу β-Ga_2O_3 / p-типу Si, особливо за кріогенних температур. Використовуючи фізично обґрунтовану модель, що враховує температурно- та концентраційно-залежну іонізацію, вирівнювання зон і деградацію рухливості, досліджено вплив мілких і глибоких донорів/акцепторів на ширину збідненого шару, ємність переходу та пікове електричне поле в діапазоні 77–300 К. Для переходів із помірним рівнем легування (N_A=N_D= 4×10^{17} $см^{-3}$) ефект «заморожування» носіїв при 100 К зменшує пряму ємність приблизно на 17%, збільшує ширину збідненого шару приблизно на 0,10 мкм і знижує пікове електричне поле приблизно на 0,5 МВ/см, тоді як у сильно легованих структурах (NA = ND = 1×10^{18} $см^{-3}$) спостерігаються значно менші зміни (<5%). Температурно-залежне моделювання демонструє поступову активацію домішок у діапазоні 150–250 К із майже повною іонізацією вище 300 К, що підтверджує узгодження з моделями повної іонізації. Ємність при прямому зміщенні має гіперболічну залежність від напруги ($C \propto 1/\sqrt{\Delta V}$) та зменшується на 20–25% за екстремальних напруг. Отримані результати дають кількісне уявлення про вплив ефекту заморожування на розподіл носіїв заряду, електростатику та характеристики переходу, забезпечуючи прогностичну основу для проєктування високовольтних, кріогенних та надширокозонних напівпровідникових пристроїв.

Ключові слова: *n-тип β-Ga_2O_3; p-Si гетероперехід; неповна іонізація домішок; електростатика переходу; профілювання ємність–напруга; заморожування носіїв; температурно-залежний транспорт; кріогенна електроніка*

East European Journal of Physics. 3. 516-525 (2026)
DOI:10.26565/2312-4334-2026-3-47 ISSN 2312-4334

GEOMETRY-INDUCED ELECTRIC FIELD ENHANCEMENT IN PLANAR AND RADIAL Si/GaAs HETEROJUNCTIONS UNDER INCOMPLETE IONIZATION

J.Sh. Abdullayev[1,2], B. Uralov[2], M.Sh. Ibragimova[3]*, B. Tadjibaev[4], M.F. Atayeva[5], G. Boymurodov[6], S.Y. Yusupov[7]

[1]*Institute of Fundamental and Applied Research, National Research University "TIIAME", Tashkent 100000, Uzbekistan*
[2]*National Research University TIIAME, Department of Physics and Chemistry, Tashkent, Uzbekistan*
[3]*Urgench State University, Hamid Olimjon Street, 14, Urgench, 220100, Uzbekistan*
[4]*Tashkent State Technical University, Tashkent, Uzbekistan*
[5]*Bukhara State University, Bukhara 200117, Uzbekistan*
[6]*Navoi State University of Mining and Technologies, Navoi 210100, Uzbekistan*
[7]*Department of Traumatology and Neurosurgery, Bukhara State Medical Institute, Bukhara, Uzbekistan*
**Corresponding Author e-mail: madinabonubahodir2024@gmail.com*
Received April 17, 2026; revised June 28, 2026; in final form August 5, 2026; accepted August 6, 2026

This work presents a comprehensive electrostatic and transport analysis of planar and radial Si/GaAs heterojunctions over the cryogenic-to-room-temperature regime (20–300 K) using self-consistent solutions of the Poisson and carrier continuity equations implemented within advanced semiconductor device simulation frameworks. Particular emphasis is placed on the role of incomplete dopant ionization and its coupling with junction geometry in determining electric-field distribution and carrier transport characteristics. The results demonstrate that incomplete ionization significantly alters the electrostatic behavior of the heterojunctions at cryogenic temperatures, whereas its influence progressively diminishes near room temperature due to enhanced dopant activation. For planar heterojunctions under complete ionization, the maximum electric field decreases from approximately $1.55\cdot10^3$ V/cm at 20 K to $8.5\cdot10^2$ V/cm at 300 K. Incorporation of incomplete ionization reduces the peak field by nearly 50–100 V/cm below 50 K, while producing negligible deviations above 200 K. In contrast, radial heterojunctions exhibit pronounced electric-field localization arising from curvature-induced geometric confinement. Under incomplete ionization, the peak electric field remains within $3.2\cdot10^4$–$3.6\cdot10^4$ V/cm, increasing to $4.2\cdot10^4$–$4.6\cdot10^4$ V/cm for fully activated dopants, corresponding to a geometry-enhanced field amplification of approximately 28–38%. Carrier transport analysis further reveals strong temperature sensitivity of minority carrier injection, which increases by nearly seven orders of magnitude, from 10^2 cm^{-3} at 50 K to 10^9 cm^{-3} at 300 K, whereas majority carrier concentration remains nearly constant at 10^{16} cm^{-3}. The radial architecture additionally produces localized depletion-field enhancement near the cylindrical interface, indicating superior electrostatic confinement compared with conventional planar configurations. These findings establish the coupled influence of geometry, dopant activation, and temperature-dependent transport mechanisms on Si/GaAs heterojunction performance and provide a rigorous framework for the optimization of cryogenic optoelectronic, nanoelectronic, and high-field semiconductor devices.
Keywords: *Si/GaAs heterojunctions; Field distribution; Incomplete dopant ionization; Cryogenic temperatures; Depletion region*

INTRODUCTION

Semiconductor devices constitute the foundation of modern information processing, energy conversion, and photonic technologies [1–3]. Among available material platforms, silicon (Si) has maintained technological dominance due to its scalability, long-term reliability, and compatibility with mature complementary metal–oxide–semiconductor fabrication processes [4–7]. In contrast, gallium arsenide (GaAs) offers distinct advantages, including high electron mobility, a direct bandgap, and strong optical absorption and emission efficiency, making it indispensable for high-speed and optoelectronic applications [8–12]. Owing to these complementary properties, Si and GaAs have become key materials in advanced devices such as radio-frequency transistors, infrared photodetectors, multijunction solar cells, and hybrid optoelectronic systems [13–18].

The integration of Si's cost-effectiveness with GaAs's superior optoelectronic performance has therefore attracted sustained research interest in Si/GaAs heterojunction architectures [19–22]. Recent advances in epitaxial growth, wafer bonding, and interface passivation have significantly improved the structural integrity and electrical stability of Si/GaAs heterostructures [23–27]. Electrical characterization using current–voltage (I–V) and capacitance–voltage (C–V) techniques has further clarified dominant transport mechanisms and junction properties [28–31]. Nevertheless, intrinsic challenges remain. Lattice mismatch, thermal expansion asymmetry, and interface defect states continue to limit device performance, particularly under non-ambient operating conditions [32–35].

These limitations become increasingly severe at low temperatures, where incomplete dopant ionization, carrier freeze-out, and defect-assisted trapping substantially modify electrostatic profiles and transport behavior [36–39]. Reduced ionized dopant density at cryogenic temperatures alters space-charge distributions, suppresses built-in electric fields, and affects breakdown characteristics—issues that are especially critical for space electronics, radiation detectors, and low-noise optoelectronic systems [40–43]. Accurate modeling of such devices therefore requires explicit

Cite as: J.Sh. Abdullayev, B. Uralov, M.Sh. Ibragimova, B. Tadjibaev, M. F. Atayeva,G. Boymurodov, S. Y. Yusupov, East Eur. J. Phys. 3, 516 (2026), https://doi.org/10.26565/2312-4334-2026-3-47

consideration of temperature-dependent dopant activation, which is often neglected in simplified junction analyses [44-46].

To address these challenges, various material and processing strategies—including surface passivation, plasma-assisted bonding, and advanced substrate engineering using liquid-encapsulated Czochralski (LEC), vertical gradient freeze (VGF), and molecular beam epitaxy (MBE)—have been widely explored [47–50]. While these approaches have led to notable improvements in planar Si/GaAs heterojunctions, alternative device geometries remain comparatively underinvestigated. In particular, radial heterojunction configurations offer inherent advantages such as enhanced electric-field localization, increased effective junction area, and improved tolerance to dopant freeze-out effects, yet their electrostatic behavior has not been systematically examined [15,17,32,45].

In this work, a comprehensive comparative analysis of planar and radial Si/GaAs heterojunctions is presented over the temperature range of 20–300 K. The methodology combines analytical solutions of coupled Poisson and carrier continuity equations with calibrated numerical simulations, explicitly incorporating incomplete dopant ionization. By evaluating space-charge density, electrostatic potential, and electric-field distributions, this study elucidates how junction geometry governs low-temperature electrostatics. The results provide quantitative design guidelines for optimizing Si/GaAs heterostructures in cryogenic, radiation-hardened, and high-performance optoelectronic and nanoelectronic applications.

METHODS AND MATERIAL

The Si/GaAs heterojunction was modeled with a p–n junction as the fundamental active element. In the considered structures, boron (B) was adopted as the acceptor dopant for p-type Si, while silicon (Si) was employed as the donor species for n-type GaAs. The parameter set was extracted from established semiconductor databases and experimental reports [26], ensuring consistency with the physical behavior of Si and GaAs. A summary of the parameters employed in the modeling is provided in Table 1.

Table 1. Summary of the electrophysical parameters of Si and GaAs employed in the modeling of the p–n heterostructure in this work at 300 K [45].

Materials	$Eg\,(eV)$	$E_A,\ E_D\,(meV)$	$N_C\left(cm^{-3}\right)$	$N_V\,(cm^{-3})$	$n_i\left(cm^{-3}\right)$	$g_{A,}g_D$	ε	β_p,β_n
Si	1.12	45	$2.8{\cdot}10^{19}$	$1.04{\cdot}10^{19}$	$1.5{\cdot}10^{10}$	4	11.7	1
GaAs	1.42	5	$4.7{\cdot}10^{17}$	$7.0{\cdot}10^{18}$	$1.8{\cdot}10^{6}$	2	12.9	1

The device simulations incorporated the essential electrophysical parameters of Si and GaAs, including bandgap energy (Eg), donor and acceptor ionization energies (E_D, E_A), effective density of states in the conduction and valence bands (Nc, Nv), intrinsic carrier concentration $n_i(T)$, degeneracy factors of donor and acceptor states (g_D, g_A), relative dielectric constant ε, and electron and hole capture coefficients (βn, βp). All simulations were carried out by solving the coupled Poisson and carrier continuity equations, with explicit treatment of incomplete dopant ionization across the 20–300 K temperature range. Beyond material parameters, device geometry critically influences electrophysical behavior. To enable direct comparison, both planar and radial Si/GaAs heterojunctions were modeled. The adopted dimensions and boundary conditions are summarized in Figure 1, which schematically depicts the investigated structures.

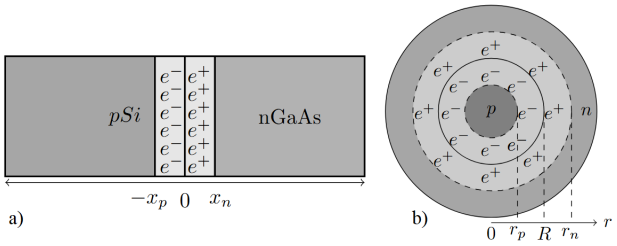

Figure 1. Two-dimensional schematics of the investigated Si/GaAs heterojunctions: (a) planar and (b) radial geometries. The junction comprises p-type Si and n-type GaAs with well-defined depletion regions (x_p, x_n for planar and r_p, r_n for radial configurations). Fixed charges are represented by ionized acceptors $e-$ and donors $e+$, while R denotes the core radius in the radial. These structural configurations serve as the foundation for the analytical and numerical modeling of electric field distribution, depletion width, and breakdown behavior across varying doping levels and temperatures.

In the analysis of the electrophysical distributions of the heterojunctions depicted in Figure 1 (a) planar and (b) radial the governing Poisson equation is solved within distinct coordinate frameworks: Cartesian coordinates for the planar configuration and cylindrical coordinates for the radial configuration. In earlier studies [23,24], analytical expressions for planar (Eq. 1) and radial (Eq. 2) heterojunctions have been widely utilized to describe the resulting electrostatic distributions.

Figure 2 shows excellent agreement is achieved between model and experiment, with coefficients of determination $R^2 = 0.9860$ (Si) and $R^2 = 0.9728$ (GaAs), confirming deviations remain within 0.01 eV across 180–380 K. For Si, the model predicts a bandgap energy of 1.124 eV at 300 K, in close agreement with the experimental value of 1.122 eV ($\Delta \approx 0.002$ eV). For GaAs, the calculated bandgap energy is 1.422 eV, compared with the experimental value of 1.424 eV

($\Delta \approx 0.002$ eV). These results validate the calibration of our temperature-dependent model and confirm its reliability for device-level simulations and predictive analyses.

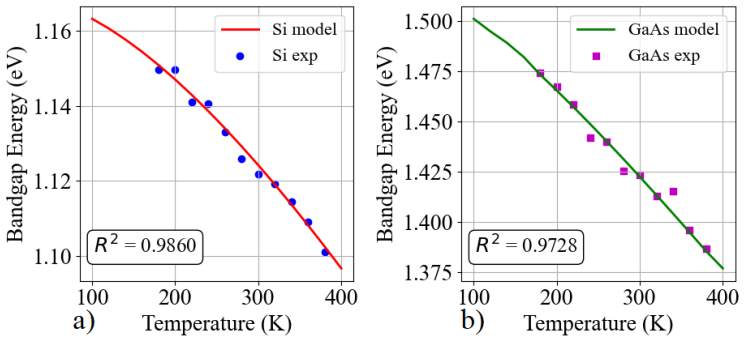

Figure 2. Temperature dependence of the bandgap energy for (a) Si and (b) GaAs, showing comparison between model (solid lines) and experimental data (symbols) [45,46].

$$\frac{d^2\varphi(x)}{dx^2} = \begin{cases} -\dfrac{qN_A}{\varepsilon_{Si}\cdot\varepsilon_0}, & \text{for} \quad -x_p \le x \le 0 \quad (p\text{-Si}) \\ \dfrac{qN_D}{\varepsilon_{GaAs}\cdot\varepsilon_0}, & \text{for} \quad 0 \le x \le x_n \quad (n\text{-GaAs}) \\ 0, & (\text{neutral region}) \end{cases} \tag{1}$$

However, these conventional formulations typically neglect the influence of temperature and applied external bias, factors that can substantially alter the electrostatic behavior of the junction. As a result, their omission may lead to significant inaccuracies when modeling or analyzing devices operating across broad temperature ranges or under both forward and reverse bias conditions.

$$\frac{1}{r}\frac{d}{dr}\left(r\frac{d\varphi(r)}{dr}\right) = \begin{cases} -\dfrac{qN_A}{\varepsilon_{Si}\cdot\varepsilon_0}, & \text{for} \quad r_p \le r \le R \quad (p\text{-Si}) \\ \dfrac{qN_D}{\varepsilon_{GaAs}\cdot\varepsilon_0}, & \text{for} \quad R \le r \le r_n \quad (n\text{-GaAs}) \\ 0, & (\text{neutral region}) \end{cases} \tag{2}$$

In analyzing the electrophysical distributions of heterojunctions (Figure 1), the Poisson equation is solved in Cartesian coordinates for planar and cylindrical coordinates for radial configurations. While conventional formulations (Eqs. 1 and 2) have been widely applied, they often neglect temperature and external bias, leading to inaccuracies across broad operating conditions. Experimental and numerical studies confirm that variations in temperature and applied voltage significantly affect space-charge density, potential, and electric-field profiles. To overcome these limitations, temperature-dependent effects such as self-heating at high temperatures and incomplete ionization at low temperatures were incorporated. The reformulated models introduce additional terms for material parameters, dopant activation energies, carrier distributions, and quantum contributions, yielding new analytical expressions (Eqs. 3 and 4) with improved predictive accuracy.

$$\frac{d^2\varphi(x)}{dx^2} = \begin{cases} -\dfrac{qN_A}{\varepsilon_{Si}\cdot\varepsilon_0\cdot\left(1+\dfrac{g_A\cdot p_p}{\beta_p\cdot N_V(T)}\cdot\exp\left(\dfrac{\Delta E_A}{kT}\right)\right)}, & \text{for} \quad -x_p \le x \le 0 \quad (p\text{-Si}) \\ \dfrac{qN_D}{\varepsilon_{GaAs}\cdot\varepsilon_0\cdot\left(1+\dfrac{g_D\cdot n_n}{\beta_n\cdot N_C(T)}\cdot\exp\left(\dfrac{\Delta E_D}{kT}\right)\right)}, & \text{for} \quad 0 \le x \le x_n \quad (n\text{-GaAs}) \\ 0, & (\text{neutral region}) \end{cases} \tag{3}$$

Space-charge density, electrostatic potential, and electric-field distributions were systematically evaluated across a broad temperature range by comparing the conventional formulations (Eqs. 1 and 2) with the newly derived models (Eqs 3 and 4).

$$\frac{1}{r}\frac{d}{dr}\left(r\frac{d\varphi(r)}{dr}\right)=\begin{cases}-\dfrac{qN_A}{\varepsilon_{Si}\cdot\varepsilon_0\cdot\left(1+\dfrac{g_A\cdot p_p}{\beta_p\cdot N_V(T)}\cdot\exp(\dfrac{\Delta E_A}{kT})\right)}, & \text{for } r_p\le r\le R \quad (p\text{-Si})\\ \dfrac{qN_D}{\varepsilon_{GaAs}\cdot\varepsilon_0\cdot\left(1+\dfrac{g_D\cdot n_n}{\beta_n\cdot N_C(T)}\cdot\exp(\dfrac{\Delta E_D}{kT})\right)}, & \text{for } R\le r\le r_n \quad (n\text{-GaAs})\\ 0, & \text{(neutral region)}\end{cases} \tag{4}$$

The graphical analyses reveal pronounced differences in device behavior and demonstrate the superior predictive capability of the revised models. To obtain these solutions, Neumann boundary conditions were imposed by specifying zero electric field at the domain boundaries, $E(r_n)=0$ and $E(r_p)=0$. Dirichlet boundary conditions fixing the electrostatic potential at the contacts were applied in conjunction with appropriate initial conditions, as schematically illustrated in Figure 1 $\varphi(r_p)=0$ $\varphi(r_n)=\varphi_k(T)$. N_D, N_A — total concentration of donors and acceptors, E_f — Fermi level, E_D, E_A — donor and acceptor energy levels, kT — thermal energy.

$$E(x)=\begin{cases}-\dfrac{q\cdot N_A}{\varepsilon_{Si}\cdot\varepsilon_0}\cdot\left(x_p+x\right), & \text{for } -x_p<x<0 \quad (\text{p-Si})\\ \dfrac{q\cdot N_D}{\varepsilon_{GaAs}\cdot\varepsilon_0}\cdot\left(x_n-x\right), & \text{for } 0<x<x_n \quad (\text{n-GaAs})\\ 0, & \text{(neutral region)}\end{cases} \tag{5}$$

In the case of the planar p–n junction, expression (5) lacks explicit dependence on both temperature and external bias voltage. This limitation leads to increasing discrepancies in the calculated results, particularly when the model is applied across a broad temperature range.

$$E(r)=\begin{cases}-\dfrac{qN_A}{\varepsilon_{Si}\cdot\varepsilon_0}\cdot\left[r-\dfrac{r_p^2}{r}\right], & \text{for } r_p\le r\le R \quad (p\text{-Si})\\ \dfrac{qN_D}{\varepsilon_{GaAs}\cdot\varepsilon_0}\cdot\left[r-\dfrac{r_n^2}{r}\right], & \text{for } R\le r\le r_n \quad (n\text{-GaAs})\\ 0, & \text{(neutral region)}\end{cases} \tag{6}$$

In the case of the radial p–n junction, expression (6) does not explicitly account for temperature or external bias voltage. Consequently, the model exhibits increasing deviations from the actual electrostatic behavior when applied over broad temperature ranges or under varying bias conditions.

$$E(x,T)=\begin{cases}-\dfrac{q\cdot N_A}{\varepsilon_{Si}\cdot\varepsilon_0\cdot\left(1+\dfrac{g_A\cdot p_p}{\beta_p\cdot N_V(T)}\cdot\exp(\dfrac{\Delta E_A}{kT})\right)}\cdot\left(x_p+x\right), & \text{for } -x_p<x<0 \quad (\text{p-Si})\\ \dfrac{q\cdot N_D}{\varepsilon_{GaAs}\cdot\varepsilon_0\cdot\left(1+\dfrac{g_D\cdot n_n}{\beta_n\cdot N_C(T)}\cdot\exp(\dfrac{\Delta E_D}{kT})\right)}\cdot\left(x_n-x\right), & \text{for } 0<x<x_n \quad (\text{n-GaAs})\\ 0, & \text{(neutral region)}\end{cases} \tag{7}$$

The proposed expression (7) for planar p–n junctions incorporates the effects of temperature, dopant activation energy, doping concentration, and material properties, thereby providing a more accurate description of their electrostatic behavior.

The proposed expressions (7) and (8) extend the applicability of analytical models for planar and radial p–n junctions by incorporating temperature dependence, dopant activation energy, doping concentration, and material-specific parameters. Electric field distributions were evaluated under both complete and incomplete ionization, with the latter

modeled using Fermi–Dirac statistics. Incomplete ionization reduces the effective space-charge density and lowers the maximum electric field in the depletion region. The results obtained from expressions (5) and (7) for planar junctions and expressions (6) and (8) for radial junctions are presented for Si/GaAs heterojunction structures in the following section.

$$E(r,T)=\begin{cases}-\dfrac{qN_A}{\varepsilon_{Si}\cdot\varepsilon_0\cdot\left(1+\dfrac{g_A\cdot p_p}{\beta_p\cdot N_V(T)}\cdot\exp(\dfrac{\Delta E_A}{kT})\right)}\cdot\left[r-\dfrac{r_p^2}{r}\right], & \text{for } r_p\le r\le R \quad (p\text{-Si})\\ \dfrac{qN_D}{\varepsilon_{GaAs}\cdot\varepsilon_0\cdot\left(1+\dfrac{g_D\cdot n_n}{\beta_n\cdot N_C(T)}\cdot\exp(\dfrac{\Delta E_D}{kT})\right)}\cdot\left[r-\dfrac{r_n^2}{r}\right], & \text{for } R\le r\le r_n \quad (n\text{-GaAs})\\ 0, & \text{(neutral region)}\end{cases} \tag{8}$$

RESULTS AND DISCUSSION

This section presents the electrostatic characteristics of planar and radial p–n junctions in Si/GaAs heterostructures. Results obtained from the conventional models (5) and (6) are compared with the proposed formulations (7) and (8) under both complete and incomplete ionization conditions. The analysis highlights their influence on space-charge distribution, electric field profiles, and overall junction behavior across varying operating regimes. The injection characteristics of electrons into the p-side and holes into the n-side of the Si/GaAs heterojunction (Fig. 3) exhibit a strong temperature dependence. At 50 K, minority carrier densities are limited to ~10^2–10^3 cm^{-3} due to incomplete ionization. With increasing temperature, the densities rise progressively: ~ 10^4–10^5 cm^{-3} at 100 K, ~10^6–10^7 cm^{-3} at 200 K, and ~10^8–10^9 cm^{-3} at 300 K.

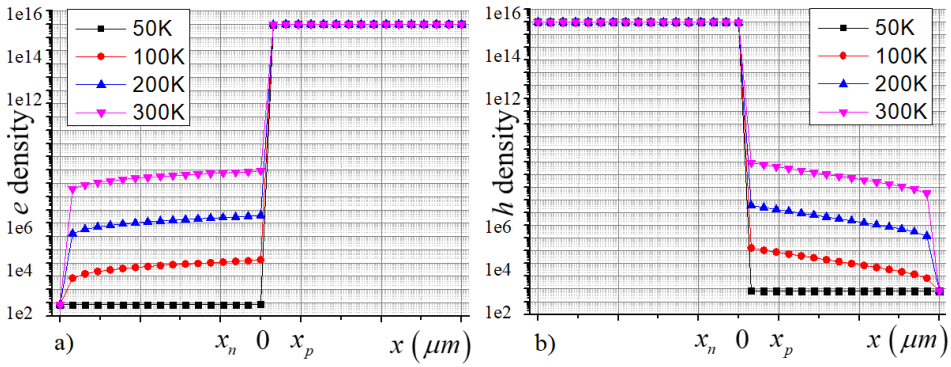

Figure 3. Temperature-dependent injection of (a) electrons into the p-side and (b) holes into the n-side of the Si/GaAs hetero p–n junction. Carrier concentrations are presented for 50 K, 100 K, 200 K, and 300 K.

This nearly seven-order-of-magnitude increase underscores the decisive role of dopant activation in governing injection efficiency. In contrast, majority carrier densities remain fixed at ~10^{16} cm^{-3}, reflecting the imposed doping concentrations. The sharp transition at the metallurgical junction confirms strong electrostatic confinement, while the extended injection profiles reveal the thermal modulation of minority carrier availability. A slight asymmetry is observed, with electrons injected into the p-side (Fig. 3a) exceeding hole injection into the n-side (Fig. 3b), reflecting transport differences across the Si/GaAs interface. Minority carrier injection critically shapes the electrostatic potential and electric field within the depletion region: at low temperatures, dopant freeze-out weakens the built-in field and limits current transport, whereas at higher temperatures, enhanced injection strengthens charge separation but also increases recombination.

Temperature-dependent injection has direct implications for device performance. In solar cells, carrier injection rises from ~10^2 cm^{-3} at 50 K to ~10^9 cm^{-3} at 300 K (a ~7-order increase), strengthening charge separation but also raising recombination at high T. In LEDs and lasers, the observed asymmetry of electrons injected into the p-side reaching up to 10× higher densities than holes in the n-side can reduce radiative efficiency. For photodetectors, injection suppression at low T lowers responsivity by several orders of magnitude, critical for cryogenic or space operation. In high-power/high-frequency devices, variations in space-charge density from ~10^{16} cm^{-3} (majorities) to as low as 10^2 cm^{-3} (minorities at 50 K) significantly alter the built-in potential and field, impacting breakdown and reliability. Injection varying by up to seven orders of magnitude directly links microscopic carrier dynamics with macroscopic device efficiency.

Figure 4 depicts the evolution of the electric-field distribution in planar Si/GaAs heterojunctions as a function of temperature under different ionization assumptions. At 20 K, the maximum electric field reaches approximately

1.55×10^3 V/cm when full dopant activation is assumed, whereas partial ionization limits the peak field to about 1.45×10^3 V/cm. As temperature increases, E_{max} exhibits a monotonic decline in both cases, decreasing to roughly 1.25×10^3 V/cm (complete ionization) and 1.10×10^3 V/cm (incomplete ionization) at 50 K, followed by values near 1.05×10^3/9.5×10^2 V/cm at 100 K, 9.5×10^2/8.7×10^2 V/cm at 200 K, and finally converging to approximately 8.5×10^2/8.0×10^2 V/cm at 300 K. Overall, the reduction in peak field amounts to ~45% for the fully ionized case and ~40% when incomplete ionization is considered.

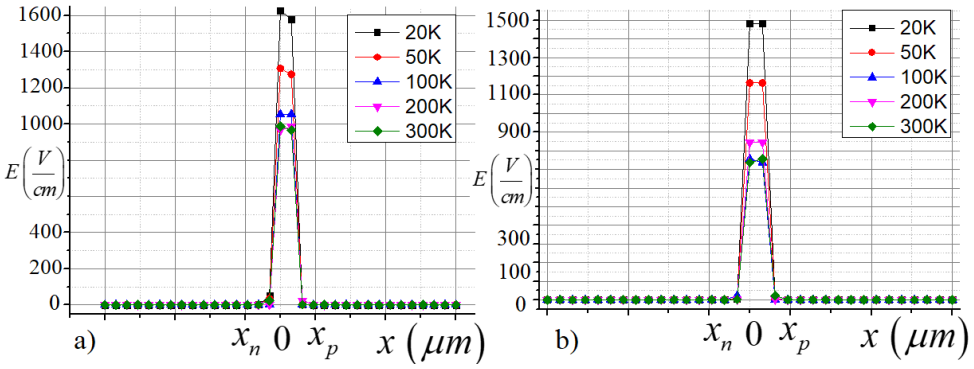

Figure 4. Simulated electric-field profiles for planar Si/GaAs hetero p–n junctions assuming (a) complete dopant ionization and (b) incomplete ionization, evaluated over the temperature range from 20 to 300 K.

The disparity between the two ionization models is most pronounced at cryogenic temperatures, where the difference in E_{max} approaches ~100 V/cm at 20 K due to limited dopant activation. This gap progressively diminishes with increasing temperature and reduces to ~50 V/cm near room temperature, reflecting near-complete ionization of dopants. These trends indicate that incomplete ionization substantially alters junction electrostatics at low temperatures by reducing the built-in potential and suppressing the electric field, while its influence becomes marginal at elevated temperatures. Accurate inclusion of temperature-dependent ionization effects is therefore essential for predictive device modeling and optimization. In cryogenic radiation detectors and space-borne electronics, suppressed electric fields can degrade charge-separation efficiency and timing performance. Similarly, in photovoltaic devices and photodetectors, the temperature-induced reduction of E_{max} directly affects carrier collection efficiency and achievable open-circuit voltage. Incorporating realistic ionization dynamics also improves the reliability of electric-field predictions, aiding in the mitigation of premature breakdown and the optimization of doping profiles. A rigorous understanding of temperature- and ionization-dependent electrostatics thus forms a critical basis for the design of robust, high-efficiency Si/GaAs optoelectronic devices.

Figure 5 illustrates the spatial variation of the radial electric field in Si/GaAs heterojunctions for three different junction radii (R = 0.5, 1.0, and 1.5 μm), highlighting the impact of dopant ionization. In all cases, the electric field reaches its maximum near the depletion boundaries. Under incomplete ionization conditions (case A), peak field values fall within the range of 3.2×10^4–3.6×10^4 V/cm, whereas full dopant activation (case B) increases the peak field to approximately 4.2×10^4–4.6×10^4 V/cm, corresponding to an enhancement of roughly 30–38%. The lower E_{max} observed for incomplete ionization is attributed to the reduced concentration of ionized impurities, which expands the depletion region and consequently weakens the local electric field.

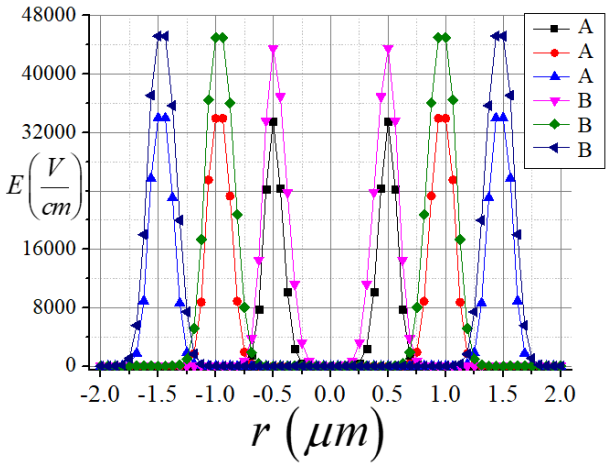

Figure 5. Radial electric field profiles, E(r), calculated for a Si/GaAs hetero p–n junction with cylindrical symmetry. Simulations are shown for device radii of R = 0.5, 1.0, and 1.5 μm. Curves labeled A correspond to partial dopant ionization, whereas curves labeled B represent the fully ionized case.

Table 2. Extracted maximum radial electric field values, E_{max} (V/cm), for Si/GaAs radial p–n junctions under incomplete (A) and complete (B) dopant ionization conditions at different junction radii (R, μm). The relative percentage increase in E_{max} resulting from full dopant activation is also reported.

Radius R (μm)	E_{max} B (V/cm)	E_{max} A (V/cm)	Increase B vs A (%)
0.5	44,000	32,000	37.5
1.0	42,000	32,000	31.3
1.5	46,000	36,000	27.8

In radial architectures, the cylindrical coordinate system intrinsically amplifies the electric field toward the inner radius, whereas the Si/GaAs heterointerface modifies the depletion balance through the contrast in dielectric permittivity between the two semiconductors. As a result, the combined effects of dopant activation, junction radius, and material parameters play a decisive role in shaping the radial electric-field profile. These factors directly impact charge separation efficiency, low-temperature device operation, and susceptibility to high-field phenomena such as premature breakdown in photodetectors and photovoltaic cells. Electric-field maps for planar and radial Si/GaAs hetero p–n junctions under complete and incomplete dopant ionization are shown in Figures 4 and 5.For planar junctions with fully ionized dopants, the maximum electric field E_{max} decreases steadily with temperature, falling from approximately 1.55×10^3 V/cm at 20 K to about 8.5×10^2 V/cm at 300 K. When incomplete ionization is considered, E_{max} is further suppressed by roughly 50–100 V/cm at cryogenic temperatures, reflecting the reduced density of ionized impurities. In contrast, radial heterojunctions develop much stronger electric fields, with peak values of 3.2×10^4–3.6×10^4 V/cm under partial ionization and 4.2×10^4–4.6×10^4 V/cm assuming full activation, corresponding to a relative increase of approximately 28–38%. This enhancement originates from geometric field convergence near the depletion boundary, whereas planar structures distribute the electric field more evenly across the junction region. Across both geometries, partial dopant ionization at low temperatures lowers the effective space-charge concentration, increases the depletion width, and consequently reduces E_{max} These observations emphasize the necessity of incorporating temperature-dependent dopant activation in electrostatic simulations. Overall, radial Si/GaAs heterojunctions enable highly localized electric fields that improve carrier separation and collection, while planar junctions mitigate peak-field stress through more uniform field profiles, highlighting how geometry and ionization physics jointly define device performance.

CONCLUSIONS

In this study, the electrostatic and transport characteristics of planar and radial Si/GaAs heterojunctions were systematically investigated under both complete and incomplete dopant ionization conditions across the temperature range of 20–300 K. By employing self-consistent numerical solutions of the Poisson and carrier continuity equations, the analysis clarifies the coupled effects of junction geometry, dopant activation, and temperature-dependent carrier dynamics on electric-field formation and charge transport. The results reveal that incomplete ionization plays a critical role in determining the low-temperature electrostatic response of the heterojunctions. For planar structures under full dopant activation, the maximum electric field decreases from approximately $1.55 \cdot 10^3$ V/cm at 20 K to $8.5 \cdot 10^2$ V/cm at 300 K. When incomplete ionization is incorporated, the peak field is reduced by approximately 50–100 V/cm at cryogenic temperatures owing to suppressed dopant activation, while the discrepancy becomes negligible above approximately 200 K as thermal ionization approaches completion. Radial heterojunctions exhibit substantially stronger electric-field enhancement than their planar counterparts due to curvature-driven electrostatic confinement. Under incomplete ionization, the maximum electric field remains within $3.2 \cdot 10^4$–$3.6 \cdot 10^4$ V/cm, increasing to $4.2 \cdot 10^4$–$4.6 \cdot 10^4$ V/cm under complete ionization, corresponding to a field amplification of approximately 28–38%. The cylindrical geometry induces pronounced electric-field localization near the depletion boundary, whereas planar heterojunctions maintain comparatively uniform field distributions. Furthermore, a moderate increase in field intensity is observed for smaller junction radii R = 0.5 μm relative to larger radii R = 1.5 μm, consistent with geometric field-focusing effects inherent to radial architectures. The numerical model was further validated through temperature-dependent bandgap calibration against experimental data. Excellent agreement was obtained for both semiconductor materials, with coefficients of determination of R^2 =0.9860 for Si and R^2 =0.9728 for GaAs, while absolute deviations remained below 0.01 eV throughout the 180–380 K interval. At 300 K, the calibrated model predicts bandgap energies of 1.124 eV for Si and 1.422 eV for GaAs, with deviations of approximately 0.002 eV relative to reported experimental values. These results confirm the robustness and physical consistency of the proposed modeling framework. The present study demonstrates that the interplay between incomplete dopant ionization and junction geometry fundamentally governs electric-field distribution, carrier separation efficiency, and transport behavior in Si/GaAs heterostructures. The pronounced electrostatic enhancement observed in radial configurations highlights their potential for next-generation cryogenic optoelectronic, high-field, and nanoscale semiconductor applications. The developed framework further provides a scalable foundation for future investigations involving quantum confinement, interface-state effects, and nonequilibrium transport phenomena in complex heterojunction architectures.

ORCID

Jo'shqin Sh. Abdullayev, https://orcid.org/0000-0001-6110-6616; **M.Sh. Ibragimova,** https://orcid.org/0009-0004-7867-7086
Bakhtiyor Uralov, https://orcid.org/0000-0001-9371-5563;

REFERENCES

[1] Cariou, R., Benick, J., Feldmann, F., Höhn, O., Hauser, H., Beutel, P., and Dimroth, F. "III–V-on-silicon solar cells reaching 33% photoconversion efficiency," Nature Energy, **3**, 326–333 (2018). https://doi.org/10.1038/s41560-018-0131-4

[2] Yao, Z., Yang, G., Han, C., Moya, P. P., Ozkol, E., Yen, J., and Isabella, O. "Poly-SiOx passivating contacts with plasma-assisted N_2O oxidation," Solar RRL, **7**(18), 2300186 (2023). https://doi.org/10.1002/solr.202300186

[3] Mandal, N. C., Biswas, S., Acharya, S., Panda, T., Sadhukhan, S., Sharma, J. R., *et al*., "Properties of SiOx layers for passivation in TOPCon solar cells," Materials Science in Semiconductor Processing, **119**, 105163 (2020). https://doi.org/10.1016/j.mssp.2020.105163

[4] Kang, D., Sio, H. C., Stuckelberger, J., Yan, D., Phang, S. P., Liu, R., and Nguyen, H. T. "Firing stability of p- and n-type polysilicon passivating contacts," Progress in Photovoltaics, **30**(8), 970–980 (2022). https://doi.org/10.1002/pip.3521

[5] Verma, M., Routray, S., Sahoo, G. S., and Mishra, G. P. "Optimization of a-Si thin film solar cell with passivation and c-Si cap layer," Physica Status Solidi (A), **220**(18), 2300213 (2023). https://doi.org/10.1002/pssa.202300213

[6] Saini, A., Srivastava, S.K., Misra, P., and Dutta, M. "Fabrication Techniques of Silicon Microwire Arrays and Realization of Radial Junction Silicon Microwire Solar Cells," in: *Photon to Power. Progress in Optical Science and Photonics*, edited by Ravindran, P., K. G., D., Asok, A., Shankar, D., Ahmed, A.J. (eds) vol 32. (Springer, Singapore, 2025). https://doi.org/10.1007/978-981-96-5914-2_19

[7] Verma, M., and Mishra, G. P. "Electrical analysis of Ta_2O_5 vs SiO_2 tunneling oxides in passivated c-Si cells," International Journal of High Speed Electronics and Systems, **30**(1–2), 2140002 (2022). https://doi.org/10.1142/S0129156421400028

[8] Sahoo, G. S., Harini, C., Mahadevi, N., Nethra, P. S., Tripathy, A., Verma, M., and Mishra, G. P. "CuO film as recombination blocking layer in Si solar cells," Silicon, **15**, 4039–4048 (2023). https://doi.org/10.1007/s12633-023-02701-x

[9] Lepkowski, D. L., Garassman, T. J., Boyer, J. T., Chmielewski, D. J., Yi, C., Juhl, M. K., and Ringel, S. A. "23.4% monolithic epitaxial GaAsP/Si tandem solar cell," Solar Energy Materials and Solar Cells, **230**, 111299 (2021). https://doi.org/10.1016/j.solmat.2021.111299

[10] Li, D., Luo, C., Wang, H., Ling, F., and Yao, J. "Active control of plasmon-induced transparency based on a GaAs/Si heterojunction in the terahertz range," Optical Materials, **114**, 111609 (2021). https://doi.org/10.1016/j.optmat.2021.111609

[11] Hasan, M. N., Zheng, Y., Lai, J., Swinnich, E., Licata, O. G., Baboli, M. A., Mazumder, B., *et al*., "Influences of native oxide on the properties of ultrathin Al_2O_3-interfaced Si/GaAs heterojunctions," Advanced Materials Interfaces, **9**(13), 2101531 (2022). https://doi.org/10.1002/admi.202101531

[12] Jurisch, M., Börner, F., Bünger, T., Eichler, S., Flade, T., Kretzer, U., Köhler, A., Stenzenberger, J., and Weinert, B. "LEC- and VGF-growth of SI GaAs single crystals—Recent developments and current issues," Journal of Crystal Growth, **275**(1–2), 283-291 (2005). https://doi.org/10.1016/j.jcrysgro.2004.10.092

[13] Herfort, J., Schönherr, H.-P., and Ploog, K. H. "Epitaxial growth of hybrid structures," Applied Physics Letters, **83**(18), 3912-3914 (2003). https://doi.org/10.1063/1.1625426

[14] Abdullayev, J. Sh. "Influence of linear doping profiles on the electrophysical features of p-n junctions," East European Journal of Physics, (1), 245–249 (2025). https://doi.org/10.26565/2312-4334-2025-1-26

[15] Heun, S., Sugiyama, M., Maeyama, S., Watanabe, Y., Wada, K., and Oshima, M. "Growth of Si on different GaAs surfaces: A comparative study," Physical Review B, **53**, 13534–13541 (1996). https://doi.org/10.1103/PhysRevB.53.13534

[16] Saxena, P. K., Srivastava, P., and Srivastava, A. "Defect analysis of MBE reactor-grown HgCdTe on Si, GaAs, GaSb, and CZT substrates through the TNL-Epigrow simulator," Journal of Electronic Materials, **53**, 5803–5812 (2024). https://doi.org/10.1007/s11664-024-11082-0

[17] Bardhan Roy, A., Rasulji Valiji, N. H., Mohammad, R., Giridhar, P., and Mondal, P. "Performance enhancement of Si/GaAs based heterojunction solar cells by opto-electronics modeling and optimization," in: *2024 International Conference on Recent Advances in Electrical, Electronics, Ubiquitous Communication, and Computational Intelligence (RAEEUCCI)*, (IEEE, 2024), pp. 1–6. https://doi.org/10.1109/RAEEUCCI61380.2024.10547792

[18] Piriyev, M., Loget, G., Léger, Y., Chen, L., Létoublon, A., Rohel, T., Levallois, C., *et al*., "Dual bandgap operation of a GaAs/Si photoelectrode," Solar Energy Materials and Solar Cells, **251**, 112138 (2023). https://doi.org/10.1016/j.solmat.2022.112138

[19] Jarndal, A., Rakib, F.R. and Alim, M.A. On efficient modeling of drain current for designing high-power GaN HEMT-based circuits. J. Comput. Electron. **23**, 1355–1367 (2024). https://doi.org/10.1007/s10825-024-02225-x

[20] Alanis, J., Gutiérrez-Ojeda, S. J., Méndez-Camacho, R., and Cruz-Hernández, E. "Theoretical investigation of the growth of GaAs on Si(001), Si(110), Si(111), Si(113), and Si(331)," Surfaces and Interfaces, **44**, 103792 (2024). https://doi.org/10.1016/j.surfin.2023.103792

[21] Huang, R., Wang, Q., Guo, Y., and Wang, Z. "Comparative study on GaAs/Si heterojunction fabricated by nitrogen and oxygen plasma activated bonding," Vacuum, **208**, 111735 (2023). https://doi.org/10.1016/j.vacuum.2022.111735

[22] Yamaguchi, M., Takamoto, T., Juso, H., Nakamura, K., Ozaki, R., and Kojima, N. "33.7% efficiency Si tandem solar cell modules," in: *Proceedings of the 2024 IEEE 52nd Photovoltaic Specialist Conference (PVSC)*, (IEEE, 2024). https://doi.org/10.1109/PVSC57443.2024.10749502

[23] Liang, J., Chai, L., Nishida, S., Morimoto, M., and Shigekawa, N. "Investigation on the interface resistance of Si/GaAs heterojunctions fabricated by surface-activated bonding," Japanese Journal of Applied Physics, **54**(3), 030211 (2015). https://doi.org/10.7567/JJAP.54.030211

[24] Haris, M., Loan, S. A., and Mainuddin. "Si/GaAs hetero junction tunnel FET: Design and investigation," Journal of Nanoelectronics and Optoelectronics, **14**(10), 1434–1444 (2019). https://doi.org/10.1166/jno.2019.2575

[25] Liang, J., Miyazaki, T., Morimoto, M., Nishida, S., Watanabe, N., and Shigekawa, N. "Electrical properties of p-Si/n-GaAs heterojunctions by using surface-activated bonding," Applied Physics Express, **6**(2), 021801 (2013). https://doi.org/10.7567/APEX.6.021801

[26] Strzelecka, S., Pawlowska, M., Hruban, A., Gladysz, M., Wegner, E., Gladki, A., and Orlowski, W. "Investigation of As-precipitates in SI GaAs," in: *Solid State Crystals: Growth and Characterization*, edited by J. Zmija, A. Majchrowski, J. Rutkowski, and J. Zielinski, vol. 3178, (SPIE, 1997). pp. 238–241. https://doi.org/10.1117/12.280741

[27] Sapaev, I. B., Razzokov, J. I., Abdullayev, J. S., Qalandarova, D. A., and Ibragimova, M. S. "Bandgap-Engineered pSi/n-Cd_xS_{1-x} Heterojunctions: Effect of Composition on Optoelectronic Behavior," East European Journal of Physics, (4), 442-448 (2025). https://doi.org/10.26565/2312-4334-2025-4-44

[28] Abdullayev, J.S., Qalandarova, D.A., Ibragimova, M.S. *et al*., "Experimental and Simulation-Based Investigation of p-Si/n-CdS Heterojunctions: From Cryogenic Freeze-Out to Room Temperature Operation," J. Electron. Mater. **55**, 2229–2239 (2026). https://doi.org/10.1007/s11664-025-12642-8

[29] Yu, T., Zhang, H., Li, D., and Lu, Y. "Electronic and optical properties of silicene on GaAs(111) with hydrogen intercalation: A first-principles study," RSC Advances, **11**, 16040–16050 (2021). https://doi.org/10.1039/D1RA01959G

[30] Sushkov, A. A., Pavlov, D. A., Andrianov, A. I., Shengurov, V. G., Denisov, S. A., Chalkov, V. Y., Kriukov, R. N., *et al*., "Comparison of III–V heterostructures grown on Ge/Si, Ge/SOI, and GaAs," Semiconductors, **56**, 122–133 (2022). https://doi.org/10.1134/S106378262201012X

[31] Huang, R., Wang, Z., Wu, K., Xu, H., Wang, Q., and Guo, Y. "Hybrid bonding of GaAs and Si wafers at low temperature by Ar plasma activation," Journal of Semiconductors, **45**(4), 042701 (2024). https://doi.org/10.1088/1674-4926/45/4/042701

[32] Seaford, M.L., Tomich, D.H., Eyink, K.G. *et al.*, "Comparison of GaAs grown on standard Si (511) and compliant SOI (511)," J. Electron. Mater. **29**, 906–908 (2000). https://doi.org/10.1007/s11664-000-0179-0

[33] Abdullayev, J.S., Sapaev, I.B., Abdullayev, J.S. *et al.,* "Mathematical Modeling of Incomplete Ionization in Radial *p*-Si/*n*-GaAs Heterojunctions: Temperature and Doping Effects," J. Electron. Mater. **54**, 10484–10492 (2025). https://doi.org/10.1007/s11664-025-12391-8

[34] Baruah, S., Borah, J., Bora, J. *et al.* "Optical modelling of a GaAs/GaSb core–shell cone-topped octagonal-faced nanopillar array with periodic trapezoidal textured cut for high photon trapping efficiency," J. Comput. Electron. **21**, 882–894 (2022). https://doi.org/10.1007/s10825-022-01898-6

[35] Ćalasan, M. Mathematical modeling of solar cells: novel approaches based on Special Trans Function Theory. J. Comput. Electron. **23**, 1137–1147 (2024). https://doi.org/10.1007/s10825-024-02190-5

[36] Ramnarayan, Singh, R., Yadav, P. *et al.* "Numerical modelling of the surface plasmon modes of a circular cylindrical three-layer graphene waveguide," J. Comput. Electron. **24**, 15 (2025). https://doi.org/10.1007/s10825-024-02250-w

[37] Abdullayev J. Sh., Qalandarova D. A., and Ibragimova M. Sh. "Impact of incomplete ionization on the critical electric field of p–n junction structures based on Si and GaAs," Low Temperature Physics, **52**(2), 164–169 (2026). https://doi.org/10.1063/10.0042291

[38] Abdukarimov, A., Rakhmonov, U. S., and Turaev, F. Z. "Dynamic response of the system to external influences," in: *AIP Conference Proceedings* (Vol. 2612, Issue 1, Article 030017). https://doi.org/10.1063/5.0117527

[39] Rakhmonov, U. S., and Matyakubov, Z. K. "Carleman's formula for the matrix domains of Siegel," Chebyshevskii Sbornik, **23**(4), 126–135 (2022). https://doi.org/10.22405/2226-8383-2022-23-4-126-135

[40] Matyakubov, Z. K., Rakhmonov, U. S., Abdullayev, J. S., and Kuromboev, K. "On the Carleman formula for an unbounded matrix domain associated with the classical domain of the second type," Boletim da Sociedade Paranaense de Matematica, **44**(3), 1–8 (2026). https://doi.org/10.5269/bspm.79871

[41] Alanis, J., Gutiérrez-Ojeda, S. J., Méndez-Camacho, R., and Cruz-Hernández, E. (2024). "Theoretical investigation of the growth of GaAs on Si(001), Si(110), Si(111), Si(113) and Si(331)," Surfaces and Interfaces, **44**, 103792. https://doi.org/10.1016/j.surfin.2023.103792

[42] Jahromi, H. D., Zeiri, N., and Lotfiani, A. "CMOS-integrated UV phototransistor utilizing a novel p-GaAs/p-Si staggered heterojunction," Journal of Science: Advanced Materials and Devices, **10**(3), 100891 (2025). https://doi.org/10.1016/j.jsamd.2025.100891

[43] Kumar, T.R., and Priya, G.L. "Temperature and interface trap-induced variations in RF analog and linearity performance of a drain-scaled Si/GaAs uniform tunnel FET dengue nano-biosensor," Microsyst. Technol. **32**, 21 (2026). https://doi.org/10.1007/s00542-025-05976-0

[44] Abdullayev, J. Sh., and Sapaev, I. B. "Experimental and analytical investigation of incomplete ionization in p-Si/n-CdS heterojunctions at cryogenic temperatures," Next Materials, **13**, 102741 (2026). https://doi.org/10.1016/j.nxmate.2026.102741

[45] Geng, P., Li, W., Zhang, X., Zhang, X., Deng, Y., and Kou, H. "A novel theoretical model for the temperature dependence of band gap energy in semiconductors," Journal of Physics D: Applied Physics, **50**(40), 40LT02(2017). https://doi.org/10.1088/1361-6463/aa85ad

[46] Pässler, R. "Semi-empirical descriptions of temperature dependences of band gaps in semiconductors," Physica Status Solidi (b), **236**(3), 710–728 (2003). https://doi.org/10.1002/pssb.200301752

[47] Perera, M. M., Lin, M.-W., Chuang, H.-J., Chamlagain, B. P., Wang, C., Tan, X., Cheng, M. M.-C., *et al*., "Improved Carrier Mobility in Few-Layer MoS2 Field-Effect Transistors with Ionic-Liquid Gating," ACS Nano, **7**(5), 4449–4458 (2013). https://doi.org/10.1021/nn401053g

[48] Musolino, M., Tahraoui, A., Treeck, D. van, Geelhaar, L., and Riechert, H. "A modified Shockley equation taking into account the multi-element nature of light emitting diodes based on nanowire ensembles," Nanotechnology, **27**(27), 275203 (2016). https://doi.org/10.1088/0957-4484/27/27/275203

[49] Han, D.-P., Shin, D.-S., Shim, J.-I., Kamiyama, S., Takeuchi, T., Iwaya, M., and Akasaki, I. "Modified Shockley Equation for GaInN-Based Light-Emitting Diodes: Origin of the Power- Efficiency Degradation Under High Current Injection," IEEE Journal of Quantum Electronics, **55**(4), 1–11 (2019). https://doi.org/10.1109/JQE.2019.2917180

[50] Ali, N. M., Allam, N. K., Abdel Haleem, A. M., and Rafat, N. H. "Analytical modeling of the radial pn junction nanowire solar cells," Journal of Applied Physics, **116**(2), (2014). https://doi.org/10.1063/1.4886596

ГЕОМЕТРИЧНО ЗУМОВЛЕНЕ ПІДСИЛЕННЯ ЕЛЕКТРИЧНОГО ПОЛЯ В ПЛАНАРНИХ І РАДІАЛЬНИХ Si/GaAs ГЕТЕРОПЕРЕХОДАХ ЗА НЕПОВНОЇ ІОНІЗАЦІЇ

Дж.Ш. Абдуллаєв[1,2], Б. Уралов[2], М.Ш. Ібрагімова[3], Б. Таджибаєв[4], М.Ф. Атаєва[5], Г. Боймуродов[6], С.Й. Юсупов[7]

[1]Інститут фундаментальних та прикладних досліджень, Національний дослідницький університет «ТІІАМГ», Ташкент 100000, Узбекистан

[2]Національний дослідницький університет ТІІАМЕ, кафедра фізики та хімії, Ташкент, Узбекистан

[3]Ургенчський державний університет, вулиця Хаміда Олімджона, 14, Ургенч, 220100, Узбекистан

[4]Ташкентський державний технічний університет, Ташкент, Узбекистан

[5]Бухарський державний університет, Бухара 200117, Узбекистан

[6]Навойський державний гірничо-технологічний університет, Навої 210100, Узбекистан

[7]Кафедра травматології та нейрохірургії, Бухарський державний медичний інститут, Бухара, Узбекистан

Ця робота представляє комплексний електростатичний і транспортний аналіз планарних та радіальних Si/GaAs гетеропереходів у температурному діапазоні від кріогенних до кімнатних температур (20–300 K) із використанням самозгодженого розв'язання рівняння Пуассона та рівнянь неперервності носіїв заряду, реалізованих у сучасних програмних середовищах моделювання напівпровідникових приладів. Особливу увагу приділено ролі неповної іонізації домішок та її взаємозв'язку з геометрією переходу у формуванні розподілу електричного поля та транспортних характеристик носіїв заряду. Отримані результати демонструють, що неповна іонізація суттєво впливає на електростатичну поведінку гетеропереходів за кріогенних температур, тоді як її вплив поступово зменшується поблизу кімнатної температури внаслідок посилення активації домішок. Для планарних гетеропереходів за умови повної іонізації максимальне електричне поле зменшується приблизно від 1.55×10^3 В/см при 20 K до 8.5×10^2 В/см при 300 K. Урахування неповної іонізації призводить до зниження пікового поля приблизно на 50–100 В/см нижче 50 K, тоді як вище 200 K відхилення стають практично незначними. На відміну від цього, радіальні гетеропереходи характеризуються вираженою локалізацією електричного поля, зумовленою геометричним обмеженням, пов'язаним із кривизною структури. За умов неповної іонізації пікове електричне поле перебуває в межах 3.2×10^4–3.6×10^4 В/см, збільшуючись до 4.2×10^4–4.6×10^4 В/см у випадку повністю активованих домішок, що відповідає геометрично зумовленому підсиленню поля приблизно на 28–38%. Аналіз транспорту носіїв також виявив високу температурну чутливість інжекції неосновних носіїв, концентрація яких зростає майже на 7 порядків — від $\sim1\times10^2$ см$^{-3}$ при 50 K до $\sim1\times10^9$ см$^{-3}$ при 300 K, тоді як концентрація основних носіїв залишається майже сталою на рівні $\sim1\times10^{16}$ см$^{-3}$. Радіальна архітектура додатково забезпечує локалізоване підсилення поля в області збіднення поблизу циліндричного інтерфейсу, що свідчить про ефективніше електростатичне обмеження порівняно з традиційними планарними конфігураціями. Отримані результати встановлюють комплексний взаємозв'язок між геометрією структури, активацією домішок та температурно-залежними механізмами транспорту під час формування характеристик Si/GaAs гетеропереходів і забезпечують надійну основу для оптимізації кріогенних оптоелектронних, наноелектронних та високопольових напівпровідникових пристроїв.

Ключові слова: *гетеропереходи Si/GaAs; розподіл електричного поля; неповна іонізація домішок; кріогенні температури; область збіднення*

East European Journal of Physics. 3. 526–538 (2026)
DOI: 10.26565/2312-4334-2026-3-48 ISSN 2312-4334

THEORETICAL AND EXPERIMENTAL ANALYSIS OF RAYLEIGH–TAYLOR INSTABILITY AND MARANGONI CONVECTION IN COPPER FOIL UNDER LASER IRRADIATION

M.M. Akhmedov[1*], **J.O. Sadullayev**[1], **M.E. Vapayev**[1], **N.P. Babayazova**[1], **A.R. Matnazarov**[2], **I.Y. Davletov**[1], **M. Jumaniyazova**[3], **R.O. Ozodov**[4], **B. Ismatov**[5], **F.J. Matchanova**[6]

[1]*Deparment of Technique, Urgench State University named after Abu Raykhan Beruni, Urgench, 220100, Uzbekistan*
[2]*Urgench Innovation University, st. Town Independence MFY, 2nd House, Urgench, 220100,Uzbekistan*
[3]*Department of Physics and Astronomy, Urgench State Pedagogical Institute, 1-A, Gurlan Str., Urgench city, 220100, Uzbekistan*
[4]*Department of Biophysics, Physical Culture and Sports, Urgench State Medical Institute, Al Khorezmi Street 2, Urgench city, 220100, Uzbekistan*
[5]*"Tashkent Institute of Irrigation and Agricultural Mechanization Engineers" National Research University, Kori Niyoziy 39, Tashkent, 100000, Uzbekistan*
[6]*Khiva district general secondary school No. 10 Sakhovat Street 98, Khiva district, 220900, Uzbekistan*
[*]*Corresponding Author e-mail: munisbek95@urdu.uz*
Received April 24, 2026; revised July 31, 2026; accepted August 3, 2026

This study investigates the physical phenomena occurring on the surface of copper foil under high-intensity pulsed irradiation of a Nd: YAG laser (λ = 1064 nm, τ = 28 ps), with particular focus on plasma formation, Rayleigh–Taylor (RT) instability, and the influence of Marangoni convection on crater morphology. The plasma temperature and electron density are determined using experimental methods through spectral emission lines. These parameters evaluate the pressure gradient in the plasma, temperature variations, and changes in surface tension. The RT instability is modeled based on density contrasts arising under strong pressure differentials, while Marangoni convection is described as a mechanism for surface flow formation driven by temperature gradients. The paper analyzes the interplay between these two instabilities, their role in material redistribution, and their influence on the final geometric shape of the laser-induced crater, supported by theoretical calculations and spectroscopic measurements. The results contribute to a deeper understanding of the complex thermohydrodynamic processes involved in laser ablation.

Keywords: *Rayleigh–Taylor instability; Marangoni convection; Laser ablation; Copper plasma; Surface morphology; Electron density; Spectroscopic diagnostics*

1. INTRODUCTION

Laser–matter interaction is one of modern science's most actively developing fields, particularly within high-energy physics, materials science, and nanophotonics [1–3]. In particular, the use of ultrashort pulsed lasers (in the femtosecond and picosecond ranges) has attracted significant attention due to their ability to induce localized heating, melting, and vaporization of material surfaces, leading to plasma formation as well as the generation of craters and nano/micro-scale surface structures [4–9]. Extreme temperature gradients, pressure differences, and dynamic instabilities such as Rayleigh-Taylor and Marangoni types that arise during these processes significantly alter the surface morphology. The Rayleigh–Taylor (RT) instability occurs when high-pressure plasma layers interact with the denser metallic layer beneath them [10], leading to nonuniform material displacement at the bottom of the crater. On the other hand, Marangoni convection refers to surface fluid flows caused by surface tension gradients induced by temperature differences. The intensity of these flows is characterized by the Marangoni number (Ma), defined as:

$$\mathrm{Ma} = \frac{\left|\frac{d\sigma}{dT}\right| \cdot \Delta T \cdot L}{\mu \cdot \alpha} \tag{1}$$

where $\frac{d\sigma}{dT}$ is the temperature dependence of surface tension [N/(m·K)], ΔT is the temperature difference [K], L is the characteristic length scale [m], μ is the dynamic viscosity [Pa·s], and α is the thermal diffusivity [m²/s]. A high Marangoni number indicates the presence of strong convective flows [11], which drive the motion of molten material toward the periphery in the liquid metal layer. In recent years, several theoretical and experimental studies [12, 13, 16–22] have focused on how these instabilities affect the shape, depth, and peripheral material redistribution of laser-induced craters. Moreover, the development of spectroscopic techniques has enabled determination of plasma parameters such as temperature, electron density, and pressure gradients under realistic experimental conditions, thereby enabling more accurate modeling of the instabilities involved [23–32].

Cite as: M.M. Akhmedov, J.O. Sadullayev, M.E. Vapayev, N.P. Babayazova, A.R. Matnazarov, I.Y. Davletov, M. Jumaniyazova, R.O. Ozodov,Bakhtiyor Ismatov,F.J. Matchanova, East Eur. J. Phys. 3, 526 (2026), https://doi.org/10.26565/2312-4334-2026-3-48

In this study, for the first time, the physical processes occurring on the surface of copper foil under picosecond Nd: YAG laser irradiation are comprehensively investigated in the context of both Rayleigh–Taylor instability and Marangoni convection. Although previous studies have predominantly analyzed these phenomena separately [11–13], this article presents a unified theoretical and experimental approach. Based on the spectral characteristics of the generated plasma, a combined analysis of RT instability and Marangoni convection is carried out. The interrelations among temperature gradients, surface flows, pressure differences, and crater morphology are identified and illustrated through graphical data and experimental observations.

Besides laser irradiation, similar crater formation mechanisms have also been reported under other pulsed energy deposition techniques. Bryukhovetsky et al. [14] investigated crater formation on AA6111 aluminum alloy irradiated by a high-current pulsed electron beam and demonstrated that crater geometry is governed by non-uniform solidification of the remelted layer and the heterogeneous distribution of alloying elements. Their results indicate that material composition and crystallization dynamics strongly affect the final crater morphology. Likewise, Zhong et al. [15] studied crater formation under intense pulsed ion beam irradiation and revealed that inclusions exposed on the target surface significantly modify the melt flow through differences in the surface tension coefficient between the molten inclusion and the surrounding molten matrix. Their numerical simulations showed that thermocapillary flow driven by surface-tension differences represents the dominant mechanism responsible for crater evolution. These studies demonstrate that although the energy deposition mechanisms differ between laser, electron-beam, and ion-beam irradiation, crater formation is fundamentally governed by coupled thermal, hydrodynamic, and solidification processes.

2. EXPERIMENTAL METHODS

The experiments were carried out using commercially available high-purity copper foil (99.99 wt.% Cu) with a thickness of 63.1 μm. The high purity of the material was selected to minimize the influence of impurities on plasma formation, molten-layer dynamics, and surface-tension gradients during laser irradiation. A picosecond Nd:YAG laser (λ = 1064 nm, τ = 28 ps) operating at a laser fluence of 16 J/cm^2 was employed to irradiate the copper surface. The laser beam was focused onto the sample using a lens with a focal length of f = 25 cm. The primary objective of the experiment was to determine the plasma parameters generated during laser–matter interaction through spectroscopic diagnostics and to investigate the associated Rayleigh–Taylor instability and Marangoni convection by combining experimental observations with theoretical analysis.

Spectral analyses were performed using an Ocean Optics HR-4000 optical spectrometer. The plasma's electron density was estimated from Stark broadening of optical emission lines, while the electron temperature was determined using the Boltzmann distribution method. The crater morphology was investigated using a CX-200 scanning electron microscope (SEM), capable of magnifying up to 300,000×, allowing for high-resolution analysis of crater geometry.

During the experiment, the distribution of laser energy, spot radius, pulse repetition rate, and the optical and thermophysical properties of the material were taken into account. Figure 1 presents the experimental setup, in which the diameter of the ablated region under laser irradiation was evaluated both theoretically and experimentally.

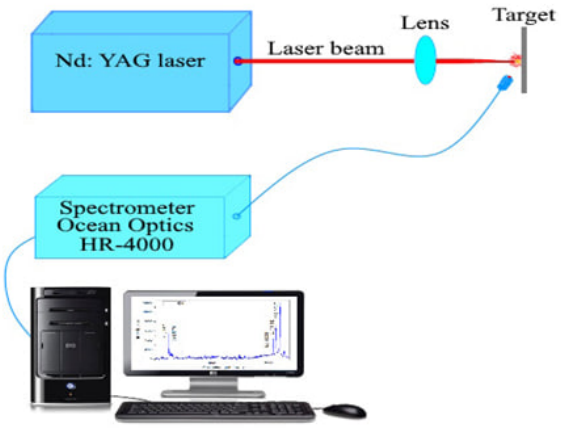

Figure 1. Schematic of the experimental setup

In future studies, expanding the experimental configuration with time-resolved diagnostics, such as gated ICCD or streak cameras, would allow detailed tracking of plasma evolution dynamics. This would provide a deeper understanding of how picosecond pulses drive fast ionization and relaxation mechanisms. Moreover, implementing environmental control (e.g., vacuum chambers or inert atmospheres) could isolate plasma effects from ambient air interactions, improving the repeatability and accuracy of results. Experiments on a broader range of materials, such as semiconductors and

dielectrics, will further contextualize copper's behavior and support a comparative analysis of ablation thresholds and plasma generation efficiency under similar laser parameters.

3. RESULTS AND DISCUSSION

Neutral atomic transition lines of Cu I were identified in the plasma spectrum, and the free electron concentration was calculated using the Stark broadening method. This technique enables the determination of electron density and temperature by analyzing the broadening and shifting of spectral lines under the influence of electric fields within the plasma.The formed crater was also subjected to spectral analysis to evaluate the presence and influence of Rayleigh–Taylor instability and Marangoni convection.

3.1. Determination of electron density and temperature

In the plasma spectrum generated on the surface of the copper foil under laser irradiation, the characteristic atomic transitions of the neutral copper atoms (Cu I) were identified (FIG 2). The identification of atomic emission lines corresponding to the plasma spectrum was carried out using data from the NIST atomic spectra database [33].

Determining the electron density is of critical importance in the study of plasma formed under laser irradiation. This work employed the Stark broadening method to estimate the electron density. Stark broadening refers to the widening and shifting of spectral lines caused by electric fields within the plasma, and it serves as a key phenomenon that enables the quantitative evaluation of free electron density.

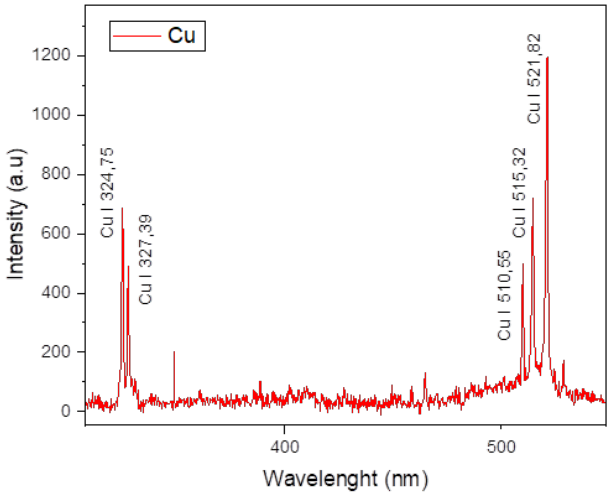

Figure 2. Plasma emission spectra of copper foil

The analysis of neutral copper atomic transition lines enabled precise characterization of plasma parameters, thereby providing a deeper understanding of laser ablation and its associated processes. For non-hydrogen-like atoms, the relationship between electron density and spectral lines' full width at half maximum (FWHM) is determined through Stark broadening [34].

$$\Delta\lambda_{\frac{1}{2}} = 2W\left(\frac{n_e}{10^{16}}\right)\text{Å}, \tag{2}$$

Here, $\Delta\lambda_{1/2}$=FWHM denotes the full width at half maximum of the spectral line, n_e is the electron density, and W is the electron impact parameter. Electron densities were determined using the spectral wavelengths corresponding to Cu I atomic transitions via the Stark broadening method (Table 1). The FWHM values were obtained by fitting the spectral line profiles to a Voigt function (Fig. 3). Closely spaced atomic transitions were resolved and analyzed separately. Using the electron impact parameter W as reported in [35], the electron density n_e was calculated accordingly.

In the plasma field, the electron temperature is typically determined under the Local Thermodynamic Equilibrium (LTE) assumption. For a plasma in LTE, the population of particles' energy levels (excited states) follows the Boltzmann distribution law. According to the LTE condition, the Boltzmann plot method is expressed as follows [36, 37].

$$\ln\left(\frac{I_\lambda}{gA}\right) = -\frac{E_u}{k_B T_e} + \text{const}$$

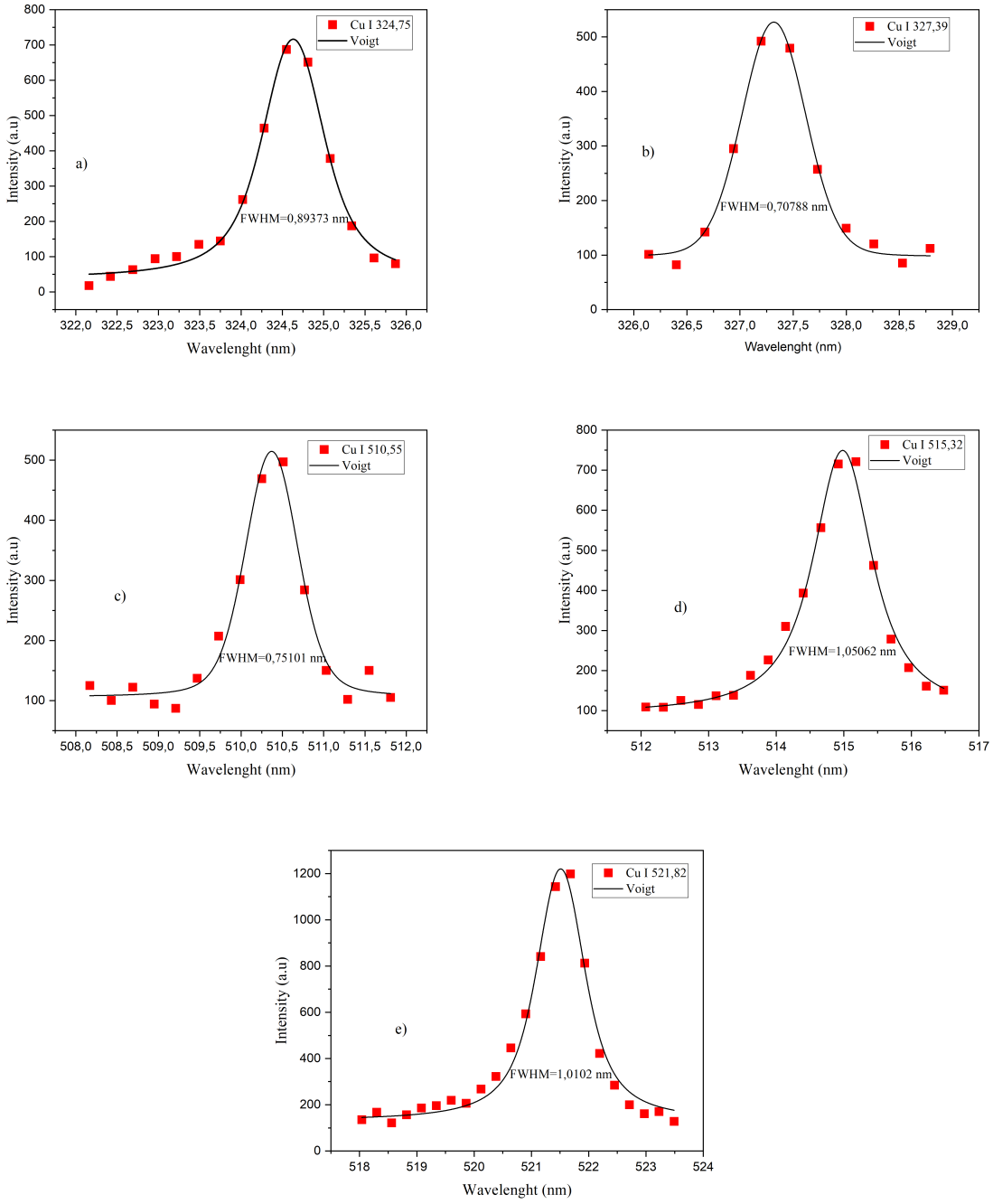

Figure 3. Voigt fitting of spectral lines in the plasma formed on the Cu surface: a) $\lambda = 324.75nm$, b) $\lambda = 327.39nm$, c) $\lambda = 510.55nm$, d) $\lambda = 515.32nm$, e) $\lambda = 521.82nm$.

Table 1. Experimental data table for Copper (Cu) element

Atom/ion	λ (nm)	FWHM (nm)	T (K)	w (Å)	n_e (10^{18} cm^{-3})
Cu I	324.75	0.89		0.003	14.84
Cu I	327.39	0.70		0.003	11.76
Cu I	510.55	0.75	8825	0.043	0.87
Cu I	515.32	1.05		0.19	0.27
Cu I	521.82	1.01		0.22	0.23

The intensity of the spectral line (I), wavelength (λ), statistical weight of the upper level (g), Einstein coefficient (A), energy of the upper level (E_u), Boltzmann constant (k_B), and electron temperature of the plasma (T_e) are the main parameters involved. The values of the parameters required to determine the electron temperature are taken from the

NIST [33] database, as presented in Table 2.

Atom	$\lambda_{ki,Z}$ (nm)	**Upper Level Energy** E_k (cm^{-1})	**Upper-state degeneracy** g_k	**Einstein coefficients**A_{ki} (s^{-1})
Cu I	324.75	30783.697	4	1.39×10^8
Cu I	327.39	30535.324	2	1.376×10^8
Cu I	510.55	30783.697	4	2×10^6
Cu I	515.32	49935.195	4	6×10^7
Cu I	521.82	49942.051	6	7.5×10^7

Table 2. Experimental Data Table for Copper (Cu) Element

The left-hand side of the linear equation based on the Boltzmann distribution is given by $\ln\left(\frac{I\lambda}{gA}\right)$. When several transitions to higher energy levels are considered for particles in the same ionization stage (Z), the left-hand side becomes proportional to the inverse of the electron temperature, $-1/(k_B T_e)$. This method, which relies on spectroscopic data, provides high accuracy in determining the plasma state, particularly the electron temperature. In plasma diagnostics, the electron temperature is not merely a numerical value; rather, it is a key parameter that characterizes the internal energy state of the plasma. Accurate temperature determination allows for precise conclusions regarding the plasma properties, such as the degree of ionization, charge carrier density, and other dynamic characteristics.

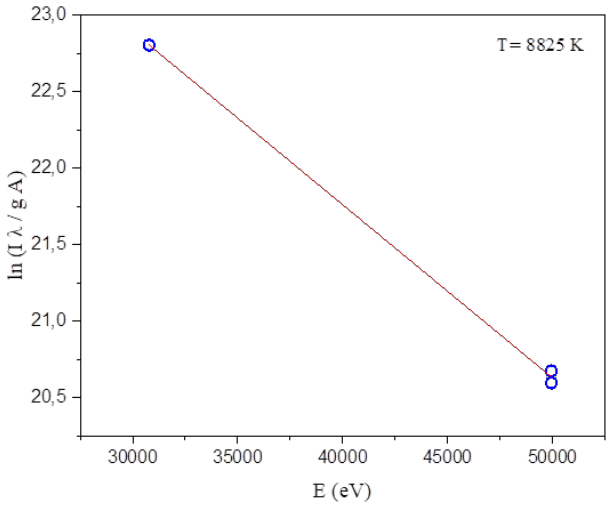

Figure 4. Emission spectral lines of neutral copper atom (Cu I) transitions plotted on a Boltzmann distribution graph

The plasma temperature was estimated using the Boltzmann plot method based on the intensities and energy levels of various Cu I spectral lines. The determined plasma temperature was approximately 8825 K. The electron density was observed to range from 0.23×10^{18} cm^{-3} to 14.84×10^{18} cm^{-3}, with the highest value corresponding to the spectral line at 324.75 nm (Fig. 4).

3.2. Crater morphology

The image of the crater formed as a result of laser ablation was obtained using a Scanning Electron Microscope (SEM). The laser radiation with a wavelength of 1064 nm (infrared) is significantly absorbed by the copper (Cu) foil. The pulse duration of 28 picoseconds (ps) is extremely short, meaning the metal heats rapidly under laser exposure, leading to vaporization. A laser fluence of 16 J/cm^2 is sufficient to initiate local melting and vaporization on the surface of the foil.

When the laser radiation interacts with the foil surface, the outer electrons of copper atoms transition to higher energy states, resulting in localized heating. Due to the laser energy being concentrated in a very small area, the material melts rapidly. The short pulse duration limits thermal diffusion into the bulk material, causing heat to accumulate primarily at the surface. This process is associated with hot electron diffusion, which confines thermal energy within the near-surface region.

If the laser energy is sufficiently high, the copper layer melts and part of it immediately vaporizes. At high vaporization rates, a plasma regime is established. The vaporized particles expand from the surface, interact with ambient air molecules, and cool and condense. As a result of these processes, a crater is formed on the Cu foil surface (Fig 5).

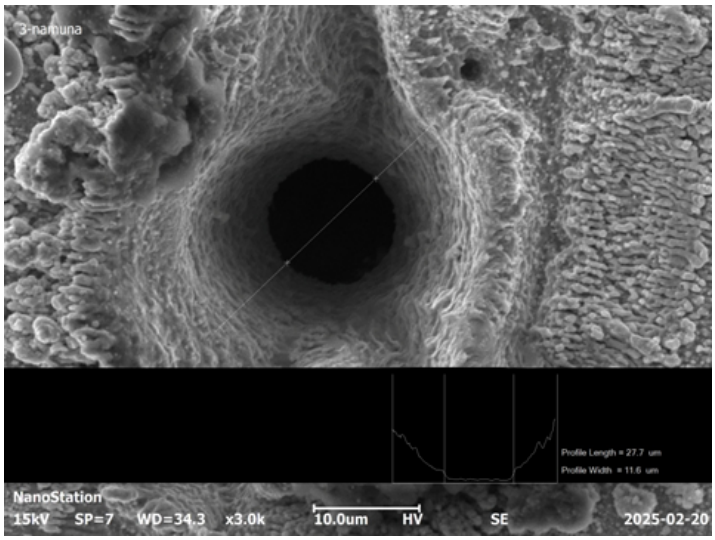

Figure 5. Scanning Electron Microscope (SEM) image of a crater formed on a copper foil surface (crater depth: 11.6 μm)

A model based on the Gaussian intensity profile of the laser beam is considered to estimate the crater diameter or the expansion of the ablated region during laser ablation. In this profile, the laser intensity is maximal at the center and decays exponentially with radial distance [38].

The spatial distribution of laser intensity follows a Gaussian profile:

$$I(r) = I_0 \cdot \exp\left(-\frac{2r^2}{\omega^2}\right), \tag{3}$$

where I_0 is the peak intensity at the center ($r = 0$), ω is the beam radius at $1/e^2$ intensity level, and r is the radial distance from the center.

Ablation occurs only when the local fluence exceeds a threshold value E_0. Solving for the radial position r where $E(r) = E_0$, the ablated diameter D can be expressed as:

$$D = a \cdot \omega \cdot \sqrt{2 \ln\left(\frac{E}{E_0}\right)}, \tag{4}$$

where a is an empirical correction factor close to 1, accounting for beam geometry and experimental conditions.

This model reveals that the relationship between laser fluence and crater diameter is not linear but logarithmic. Hence, doubling the laser energy fluence does not double the crater diameter; the growth is proportional to $\ln(E)$.

Two key effects are considered in understanding the morphology of the crater and its surrounding surface texture. Circular-shaped craters were observed to form, and the laser fluence and pulse duration directly influenced their dimensions and geometries. The ablation radius was calculated based on the logarithmic relationship between fluence and the ablation threshold, in agreement with previously published studies [39]. The crater rim exhibits signs of resolidification and material redistribution, driven by thermal gradients and recoil pressure.

3.3. Quantitative analysis of molten-layer dynamics and Rayleigh–Taylor instability

When intense picosecond laser radiation interacts with a metallic foil, rapid energy deposition leads to surface vaporization and plasma formation. In the central region of the laser spot, where the local fluence is maximal, material removal is dominated by explosive ablation. In contrast, in the peripheral region of the spot the fluence decreases below the ablation threshold, resulting primarily in transient surface melting accompanied by lateral molten flow. Under such conditions, the appearance of periodic ripple-like or finger-shaped structures at the crater edge is commonly attributed to hydrodynamic instabilities developing within the molten layer, most notably the Rayleigh–Taylor instability (RTI) [40,41].

The Rayleigh–Taylor instability arises at an interface between two media of different densities when the denser layer is accelerated toward the lighter one. In the case of laser ablation, this configuration naturally occurs at the molten metal–plasma (or vapor) interface, where the dense molten copper layer is subjected to a strong outward acceleration driven by the plasma pressure gradient. Small perturbations at this interface may therefore grow in time, leading to characteristic ripple or finger-like morphologies upon resolidification.

3.3.1. Experimental input parameters Plasma parameters were determined using optical emission spectroscopy. The electron temperature was found to be $T_e \approx 8825$ K, while the electron density varied in the range $n_e = (0.23\text{–}14.84) \times 10^{18}$ cm^{-3}, depending on the selected Cu I emission line. Assuming local thermodynamic equilibrium and using the ideal gas approximation, the plasma pressure corresponding to each spectral line was calculated as

$$P = n_e k_B T_e. \tag{5}$$

Among the analyzed transitions, the Cu I line at 324.75 nm yielded the highest pressure, $P = 1.88 \times 10^6$ Pa, which was adopted as a representative value characterizing the maximum plasma loading acting on the molten surface. High-resolution SEM observations of the crater periphery revealed a well-defined periodic surface modulation. Statistical analysis over a 10 μm field of view containing multiple periods yielded a dominant wavelength

$$\lambda = (0.91 \pm 0.10)\ \mu\text{m}, \tag{6}$$

corresponding to a perturbation wavenumber

$$k = \frac{2\pi}{\lambda} \approx 6.9 \times 10^6\ \text{m}^{-1}. \tag{7}$$

3.3.2. Molten-layer thickness and lifetime estimation In the picosecond laser irradiation regime, the extremely short pulse duration confines heat transport to a narrow near-surface region, thereby suppressing significant thermal diffusion into the bulk material. As a result, laser energy deposition leads to the formation of a transient molten layer characterized by an effective thickness L. The temporal evolution and persistence of this molten phase are primarily governed by thermal diffusion and can be estimated using a characteristic diffusion timescale,

$$t_{\text{eff}} \sim \frac{L^2}{\alpha}, \tag{8}$$

where α denotes the thermal diffusivity of copper, taken as $\alpha \approx 1.0 \times 10^{-4}$ m^2 s^{-1}.

Assuming a physically realistic molten-layer thickness in the range $L = 1\text{–}5$ μm, the corresponding molten-layer lifetime is estimated to fall within

$$t_{\text{eff}} \sim 10\text{–}250\ \text{ns}. \tag{9}$$

This nanosecond-scale lifetime significantly exceeds the laser pulse duration and establishes a well-defined temporal window during which the molten layer remains dynamically active. Such a timescale is sufficient to permit the initiation and growth of interfacial hydrodynamic instabilities at the molten metal–plasma interface, thereby providing favorable conditions for the emergence of instability-driven surface modulations and complex crater-edge morphologies (Fig 6).

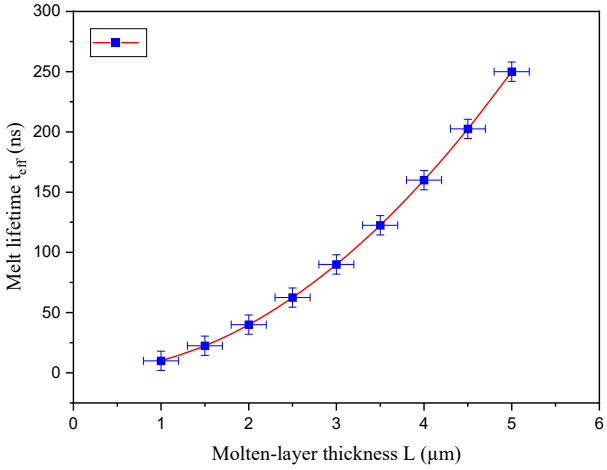

Figure 6. Dependence of the molten-layer lifetime t_{eff} on the molten-layer thickness L. The experimental data with error bars are well fitted by a quadratic function, indicating a diffusion-controlled thermal relaxation process governing the transient molten phase.)

3.3.3. Rayleigh–Taylor instability growth For a molten layer of finite thickness, the growth rate of the Rayleigh–Taylor instability can be expressed as [40, 41]

$$\gamma_{\mathrm{RTI}} = \sqrt{\frac{A g_{\mathrm{eff}} k}{1 + Ak L}}, \tag{10}$$

where $A = (\rho_1 - \rho_2)/(\rho_1 + \rho_2)$ is the Atwood number, k is the perturbation wavenumber, and g_{eff} is the effective acceleration acting at the interface. Since the density of molten copper is several orders of magnitude larger than that of the plasma or vapor phase, the Atwood number can be reasonably approximated as $A \approx 1$.

The effective acceleration is governed by the plasma-induced pressure gradient acting on the molten layer and may be estimated as

$$g_{\mathrm{eff}} \simeq \frac{\Delta P}{\rho_h L}, \tag{11}$$

where $\rho_h \approx 8000\ \mathrm{kg\,m^{-3}}$ is the density of molten copper.

Using the experimentally determined plasma pressure and the measured perturbation wavelength, the characteristic RTI growth time, $\tau_{\mathrm{RTI}} = \gamma^{-1}$, is found to lie in the range

$$\tau_{\mathrm{RTI}} \sim 70\text{–}330\ \mathrm{ns}, \tag{12}$$

depending on the assumed molten-layer thickness.

3.3.4. Physical interpretation and role of thermal gradients The close correspondence between the characteristic growth time of the Rayleigh–Taylor instability, τ_{RTI}, and the effective lifetime of the molten layer, t_{eff}, provides compelling evidence that RTI can fully evolve within the transient molten phase generated by picosecond laser irradiation. This temporal compatibility is not merely qualitative but quantitatively confirms that the molten copper layer persists long enough for interfacial perturbations to amplify under the action of an effective acceleration field. Consequently, the experimentally observed sub-micrometer ripple patterns and finger-like protrusions formed at the crater periphery can be consistently attributed to RTI-driven deformation at the liquid–solid interface during the molten stage.

Beyond the pressure-induced instability mechanism, the laser–matter interaction inherently establishes an extreme thermal gradient between the hot laser-induced plasma and the comparatively cold bulk material beneath the surface. This gradient may be estimated using

$$\nabla T = \frac{T_{\mathrm{plasma}} - T_{\mathrm{ambient}}}{\Delta x}, \tag{13}$$

where the plasma temperature can be reasonably approximated by the electron temperature ($T_{\mathrm{plasma}} \approx T_e$), the ambient temperature is taken as $T_{\mathrm{ambient}} \approx 300$ K, and Δx denotes the characteristic depth over which the temperature drop occurs. In the picosecond regime, where thermal diffusion is strongly confined to the near-surface region, this depth can be safely approximated by the molten-layer thickness, such that $\Delta x \approx L$.

Under these conditions, the resulting temperature gradient reaches values on the order of 10^9–$10^{10}\ \mathrm{K\,m^{-1}}$, signifying the presence of extremely strong thermocapillary forces at the molten surface. Such gradients are sufficient to drive intense Marangoni convection, promoting lateral melt flow and additional redistribution of molten material. Although these thermally driven flows are not explicitly included in the analytical formulation of the RTI growth rate-where the dominant contribution arises from the pressure-induced effective acceleration-they are expected to play a complementary role. Specifically, Marangoni convection can act synergistically with RTI by modifying the local melt thickness and enhancing the nonlinear evolution of interfacial perturbations.

Taken together, these results suggest that the final surface morphology observed after resolidification is governed by the combined action of pressure-driven Rayleigh–Taylor instability and thermocapillary melt flow. While RTI provides the primary mechanism for pattern initiation and wavelength selection, the strong temperature-gradient-induced Marangoni convection contributes to the amplification and lateral modulation of surface features, leading to the complex crater-edge structures observed experimentally [42–44].

3.4. Marangoni convection

When a solid metal surface is exposed to high-power picosecond laser irradiation, the deposited energy is absorbed within an extremely shallow near-surface region, leading to an ultrafast and highly localized temperature rise. Under these conditions, the surface layer rapidly enters a molten state and may partially ionize, resulting in the formation of a laser-induced plasma above the target. Owing to the short pulse duration and the correspondingly limited thermal diffusion length, heat transport into the bulk material is strongly suppressed. As a consequence, the temperature field within the molten metal layer becomes highly nonuniform, exhibiting steep thermal gradients between the intensely heated central region and the cooler peripheral zones.

Such pronounced thermal inhomogeneity naturally gives rise to Marangoni convection, a thermocapillary-driven flow mechanism originating from spatial variations in surface tension along the molten surface [11, 13]. In metallic melts, surface tension generally decreases with increasing temperature, implying that temperature gradients are directly converted

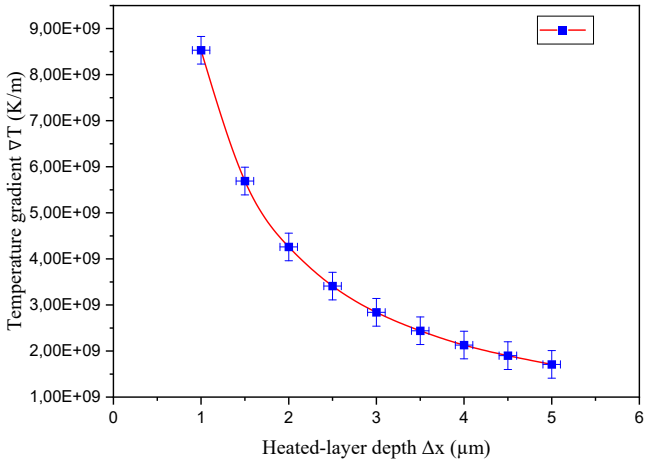

Figure 7. Dependence of the temperature gradient ∇T on the heated-layer depth Δx. The experimental data with error bars are well described by an inverse relationship, $\nabla T \propto 1/\Delta x$, indicating the presence of a steep thermal gradient within the laser-heated near-surface region.)

into surface-tension gradients. As a result, molten material is driven from regions of lower surface tension (hot zones) toward regions of higher surface tension (cooler zones), leading to an efficient lateral redistribution of the melt during the laser–matter interaction [45].

The thermocapillary driving force associated with Marangoni convection can be expressed as

$$\nabla\sigma = \frac{d\sigma}{dT}\,\nabla T, \tag{14}$$

where $\nabla\sigma$ denotes the surface-tension gradient, $\frac{d\sigma}{dT}$ is the temperature coefficient of surface tension, and ∇T represents the temperature gradient across the molten layer. For molten copper, the temperature coefficient of surface tension is negative, $\frac{d\sigma}{dT} \approx -0.3 \times 10^{-3}\ \mathrm{N\,m^{-1}\,K^{-1}}$, indicating that the thermocapillary flow is directed radially outward from the laser-heated center toward the cooler periphery.

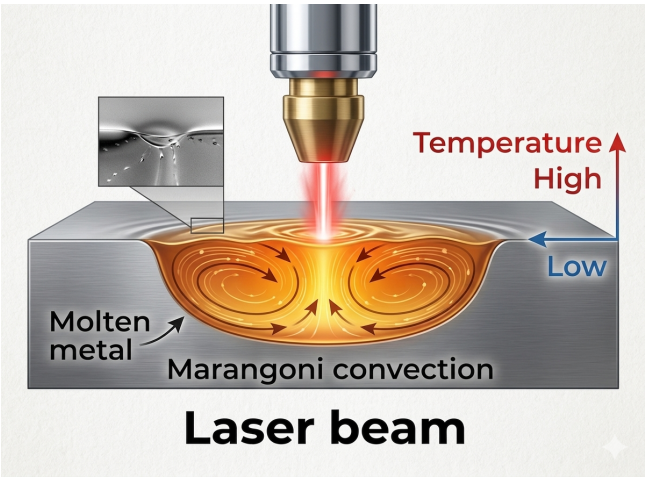

Figure 8. Schematic illustration of Marangoni convection induced by strong temperature gradients on the molten metal surface during picosecond laser irradiation.

Figure 8 schematically illustrates the development of Marangoni convection during laser irradiation. As the surface temperature gradient increases, the associated surface-tension gradient becomes stronger, giving rise to more intense thermocapillary flow. This flow substantially modifies the melt-pool geometry and plays an important role in determining the final crater morphology after resolidification, which may range from nearly axisymmetric to strongly distorted depending on the balance between convective transport and solidification dynamics.

The relative importance of Marangoni convection can be quantitatively assessed using the dimensionless Marangoni number (Ma), which characterizes the ratio of thermocapillary driving forces to viscous dissipation:

$$Ma = \frac{\left|\frac{d\sigma}{dT}\right| \Delta T\, L}{\mu\, \alpha}, \tag{15}$$

where ΔT is the characteristic temperature difference across the molten layer, L is the effective molten-layer thickness, μ is the dynamic viscosity of the molten metal, and α is the thermal diffusivity.

The importance of the surface-tension coefficient in determining crater morphology has also been confirmed under other pulsed irradiation techniques. Zhong et al. [15] demonstrated that differences in the surface-tension coefficient between molten inclusions and the surrounding molten matrix generate strong thermocapillary flow, ultimately controlling crater evolution during intense pulsed ion beam irradiation. Although the present study employed high-purity copper foil, where impurity effects are expected to be minimal, the reported mechanism emphasizes that even small compositional variations may alter Marangoni convection through local changes in the temperature coefficient of surface tension ($d\sigma/dT$). Therefore, the purity of the target material should be regarded as an important parameter affecting crater morphology.

Based on experimentally inferred plasma and surface temperatures, the peak temperature in the laser-irradiated region reaches approximately $T_{\text{plasma}} \approx 8.8 \times 10^3$ K, while the surrounding material remains close to ambient conditions, $T_{\text{ambient}} \approx 300$ K. This yields a temperature difference of $\Delta T \approx 8.5 \times 10^3$ K. Taking a molten-layer thickness consistent with the RTI analysis, L = 1–5 μm, together with a dynamic viscosity of molten copper $\mu \approx 4.3 \times 10^{-3}$ Pa·s and a thermal diffusivity $\alpha \approx 1.1 \times 10^{-5}$ m^{2}s^{-1}, the Marangoni number is estimated to lie in the range

$$Ma \sim (5 \times 10^4)\text{–}(3 \times 10^5). \tag{16}$$

This relatively large Marangoni number indicates that thermocapillary convection plays a dominant role compared to purely diffusive heat transport within the molten layer. Under such conditions, surface-driven flows are expected to redistribute molten material on nanosecond time scales, thereby significantly influencing melt-pool dynamics and the resulting surface morphology. Similar ranges of Marangoni numbers have been reported in previous experimental and numerical studies of laser-induced melt flows in metals, confirming that Marangoni convection constitutes a key mechanism governing crater-edge accumulation and material redistribution in pulsed laser ablation [46].

Furthermore, the interaction between Marangoni convection and other hydrodynamic instabilities, such as the Rayleigh–Taylor instability, further enhances the complexity of molten-layer dynamics. While RTI primarily governs the vertical deformation of the molten interface under plasma-induced effective acceleration, Marangoni convection introduces strong lateral transport. Together, these mechanisms act synergistically to shape the final resolidified surface features observed experimentally.

A comparison with previous investigations suggests that the physical mechanisms governing crater formation are largely independent of the irradiation source. Bryukhovetsky et al. [14] attributed crater formation under pulsed electron-beam irradiation to non-uniform crystallization of the remelted surface layer, whereas Zhong et al. [15] emphasized the role of impurity-induced surface-tension differences during pulsed ion beam irradiation. In contrast, the present work demonstrates that for high-purity copper irradiated by picosecond laser pulses, crater morphology is mainly controlled by the combined action of Rayleigh–Taylor instability and Marangoni convection. Thus, while the dominant driving force varies depending on the irradiation technique and material characteristics, hydrodynamic melt flow remains the key factor governing crater evolution.

4. CONCLUSIONS

Within the scope of this study, the physical phenomena induced by laser irradiation on metallic surfaces were systematically investigated. In particular, processes such as plasma formation under laser pulse exposure, surface flows within the molten layer, instabilities, and crater formation were analyzed theoretically and experimentally in depth. Key parameters such as laser power, pulse duration, spot radius, and material properties (e.g., viscosity and thermal diffusivity) were carefully considered.

Based on the analysis of plasma spectra using the Voigt profile, the temperature was estimated as $T \approx 8825$ K, and the electron densities derived from several spectral lines were found to be on the order of $n_e \sim 10^{18}$ cm^{-3}, indicating a dense and high-energy plasma state. This suggests a high intensity of energy exchange in the laser–material interaction.

The temperature gradients formed at the plasma–melt interface are strongly associated with the temperature dependence of surface tension, which leads to pronounced Marangoni convection. According to calculations, the Marangoni number was approximately $Ma \approx 5.4 \times 10^5$, implying that convective transport dominates surface diffusion. These flows play a crucial role in redistributing the molten metal from the center to the periphery, thereby shaping the crater geometry.

Furthermore, the density differences induced within the material by laser irradiation triggered Rayleigh–Taylor instability. This instability leads to the emergence of irregular internal structures, concentration gradients, and an unstable evolution of the surface morphology. As a result of the combination of such instabilities and convective flows, the crater shape, depth, and radius formed by laser irradiation exhibit complex variability.

Comparison with previous studies employing pulsed electron and ion beams further confirms that crater formation is a universal consequence of coupled thermal transport, melt hydrodynamics, and solidification processes. However, the dominant mechanism may vary depending on material purity, alloy composition, irradiation source, and energy deposition conditions.

In conclusion, the research confirms the intricate nature of the processes occurring on metal surfaces under laser irradiation and highlights the importance of accurate modeling. The findings demonstrate that energy absorption, plasma dynamics, temperature gradients, instabilities, and internal flows influence crater formation. These results are essential for enhancing precision and quality in forming surface structures and craters using laser technologies.

ORCID

M.M. Akhmedov, https://orcid.org/0000-0003-1208-1736; **J.O. Sadullayev**, https://orcid.org/0000-0002-5577-2644;
M.E. Vapayev, https://orcid.org/0009-0007-5194-131X; **N.P. Babayazova**, https://orcid.org/0009-0006-7877-2459;
A.R. Matnazarov, https://orcid.org/0009-0000-7420-8742; **I.Y. Davletov**, https://orcid.org/0009-0006-5971-7649;
M. Jumaniyazova, https://orcid.org/0009-0001-9809-3086; **R.O. Ozodov**, https://orcid.org/0009-0002-4878-6519;
B. Ismatov, https://orcid.org/0000-0003-1283-8970; **F.J. Matchanova**, https://orcid.org/0009-0005-5194-5439

REFERENCES

[1] Japakov A. I. *et al*. "The impact of laser radiation frequency on the formation of the main characteristics of ions in a mono-element laser plasma," EPJ Web of Conferences, EDP Sciences, **318**, 05002 (2025). https://doi.org/10.1051/epjconf/202531805002

[2] Japakov A. I. *et al*. "Spectra of multiply charged ions in laser plasma formed from gas-containing targets,"East European Journal of Physics, (3), 490-494 (2023). https://doi.org/10.26565/2312-4334-2023-3-55

[3] Ruziev Z. *et al*. "Surface ionization of diamond by femtosecond laser pulses: A comparative study of analytical models," Results in Optics, **23**, 100942 (2026). https://doi.org/10.1016/j.rio.2025.100942

[4] Lian B. *et al*. "Research and experimentation on acoustic monitoring technology for laser drilling penetration," Micromachines, **16**(4), 475 (2025). https://doi.org/10.3390/mi16040475

[5] Hayasaki Y., and Miura T. "Femtosecond laser drilling controlled with laser-generated ultrasound pressure," Applied Physics B, **130**(12), 220 (2024). https://doi.org/10.1007/s00340-024-08355-1

[6] Sheng L. et al. "Investigation on cutting of CFRP composite by nanosecond short-pulsed laser with rotary drilling method," Science and Engineering of Composite Materials, **32**(1), 20240047 (2025). https://doi.org/10.1515/secm-2024-0047

[7] Boltaev G. S. *et al*. "Impact of plasma conditions on the shape of femtosecond laser-induced surface structures of Ti and Ni," Applied Physics A, **128**(6), 488 (2022). https://doi.org/10.1007/s00339-022-05614-w

[8] Eshchanov B. X. *et al*. "Ultrafast laser nanostructured silicon coated with silver nanoparticles for efficient SERS detection of R6G," Applied Physics A, **132**(2), 111 (2026). https://doi.org/10.1007/s00339-025-09179-2

[9] Vapaev M. E. *et al*. "Laser fluence-dependent LIPSS formed on the surface of niobium alloys," EPJ Web of Conferences. – EDP Sciences, **318**, 05005 (2025). https://doi.org/10.1051/epjconf/202531805005

[10] S. Singh, B. Vidhani, S. Yogi, A. Tyagi, S. Kumar, and S.K. Meena, *Plasma waves and Rayleigh–Taylor instability: Theory and application, Plasma Science-Recent Advances, New Perspectives and Applications*, (IntechOpen, 2023). https://doi.org/10.5772/intechopen.109965

[11] Hu K. *et al*., "Thermal-fluid modeling and physics-informed machine learning for predicting molten pool depth in single-layer multi-track fiber laser cladding," The International Journal of Advanced Manufacturing Technology, **135**(7), 3591-3613 (2024). https://doi.org/10.1007/s00170-024-14706-1

[12] Zheng G. *et al*. "A linearized hydrodynamic code for laser ablation and its application to laser pulse shaping for direct-drive fusion," Physics of Plasmas, **31**(10), 102705 (2024). https://doi.org/10.1063/5.0225382

[13] Dai D. *et al*. "Role of angular velocity on Marangoni convection shifting, heat accumulation, and microstructure evolution using laser directed energy deposition," Journal of Applied Physics, **135**, 053105 (2024). https://doi.org/10.1063/5.0187045

[14] Bryukhovetsky V. V. *et al*. "Formation mechanism of craters on the surface of AA6111 aluminum alloy irradiated by quasi-relativistic high-current electron beam," Vacuum, **215**, 112263 (2023). https://doi.org/10.1016/j.vacuum.2023.112263

[15] Zhong H. *et al*. "Dynamic mechanism of crater formation induced by inclusion during intense pulsed ion beam irradiation," Vacuum, **179**, 109541 (2020). https://doi.org/10.1016/j.vacuum.2020.109541

[16] Tojinazarov F. *et al*. "Picosecond laser drilling grids in aluminium foil at 532 and 355 nm wavelengths," Engineering Research Express, **6**(1), 015050 (2024). https://doi.org/10.1088/2631-8695/ad1ea3

[17] Akhmedov M. *et al*. "Picosecond-pulsed laser ablation of aluminum foils: crater morphology and plasma parameters," Engineering Research Express, **7**(3), 035362 (2025). https://doi.org/10.1088/2631-8695/ae0092

[18] Akhmedov M. et al. "Effects of picosecond pulsed laser radiation on crater formation on copper foil surfaces," Engineering Research Express, **8**(3), 035401 (2026). https://doi.org/10.1088/2631-8695/ae3b9d

[19] Akhmedov M. *et al*. "Self-regulated crater formation governed by electron density in picosecond Nd: YAG laser-induced molybdenum plasma," Journal of Russian Laser Research, 1-15 (2026). https://doi.org/10.1007/s10946-026-10318-0

[20] Sadullayev J. O. *et al*. "Modeling of Thermal Effects in a Polyimide Target Under Pulsed Laser Irradiation," East European Journal of Physics, (1), 274-280 (2026). https://doi.org/10.26565/2312-4334-2026-1-31

[21] Sadullayev J. O. *et al*. "Finite Element Modeling of Scanning Speed Effects in Femtosecond Laser-Induced Graphene Fabrication," East European Journal of Physics, (2), 352-360 (2026). https://doi.org/10.26565/2312-4334-2026-2-37

[22] Ajith A. et al. "Comprehensive analysis of copper plasma: A laser-induced breakdown spectroscopic approach," Photonics, MDPI, 10(2), 199 (2023). https://doi.org/10.3390/photonics10020199

[23] Isaev M. S. *et al*. "The Surface Layer Morphology of Si¡ Cr¿ Samples," East European Journal of Physics, (4), 297-300 (2024). https://doi.org/10.26565/2312-4334-2024-4-32

[24] Isaev M. S. *et al*. "Study of the Inhomogeneities of Overcompensed Silicon Samples Doped with Manganese," East European Journal of Physics, (2), 341-344 (2024). https://doi.org/10.26565/2312-4334-2024-2-40

[25] Mamadalimov A. T. *et al*. "Study of Silicide Formation in Large Diameter Monocrystalline Silicon," East European Journal of Physics, (2), 366-371 (2024). https://doi.org/10.26565/2312-4334-2024-2-45

[26] Mustafoqulov A. *et al*. "Angular displacement measurement and control sensors of agricultural robot-manipulators," BIO Web of Conferences. – EDP Sciences, **105**, 03003 (2024). https://doi.org/10.1051/bioconf/202410503003

[27] Boboev A. Y. *et al*. "SRIM simulation of irradiation damage by protons in ZnO: S compound," Journal of Ovonic Research, **21**6, 781–788 (2025). https://doi.org/10.15251/JOR.2025.216.781

[28] Boboev, A. Y., Karimberdiev, U., Kadirov, S., Yunusaliyev, N. Y. "Growth of Solid Solutions $(Ge_2)(GaAs_{1-\delta}Bi_\delta)_x(ZnSe)_y$ on Silicon Substrates by Liquid Phase Epitaxy," Chalcogenide Letters, **22**(11), 951-957 (2025). https://doi.org/10.15251/CL.2025.2211.951

[29] Mamadalimov A. T. *et al*. "Comparative Analysis of the Properties of Manganese Silicide," Journal of Nano- and Electronic Physics, **17**(5), 05011 (2025). https://doi.org/10.21272/jnep.17(5).05011

[30] Qodirov S. R. U., and Davletov I. Y. "Improving thinking and imagining skills in school students by training the physics using simulations," AIP Conference Proceedings, **3268**(1), 060006 (2025). https://doi.org/10.1063/5.0257234

[31] Davletov I. *et al*. "Soft start of induction electric motors using rezistor and denistor devices," E3S Web of Conferences. – EDP Sciences, **461**, 01066 (2023). https://doi.org/10.1051/e3sconf/202346101066

[32] Davletov I. Y. *et al*. "Increasing the Efficiency of Asynchronous Motors by Improving the Quality of the Electric Current," in: *2023 IEEE XVI International Scientific and Technical Conference Actual Problems of Electronic Instrument Engineering (APEIE)*, (IEEE, 2023). pp. 1820-1824. https://doi.org/10.1109/APEIE59731.2023.10347842

[33] Kramida A., Ralchenko Y., and Reader J. "National Institute of Standards and Technology (NIST)," Atomic Spectra Database. 2022. https://physics.nist.gov/PhysRefData/ASD/lines_form.html

[34] Griem H. R. "Plasma spectroscopy in inertial confinement fusion and soft x-ray laser research," Physics of Fluids B: Plasma Physics, **4**(7), 2346-2361 (1992). https://doi.org/10.1063/1.860205

[35] Sahal-Bréchot S., Dimitrijević M. S., and Ben Nessib N. "Widths and shifts of isolated lines of neutral and ionized atoms perturbed by collisions with electrons and ions: An outline of the semiclassical perturbation (SCP) method and of the approximations used for the calculations," Atoms, **2**(2), 225-252 (2014). https://doi.org/10.3390/atoms2020225

[36] Harilal S. S. *et al*. "Optical diagnostics of laser-produced plasmas," Reviews of modern Physics, **94**(3), 035002 (2022). https://doi.org/10.1103/RevModPhys.94.035002

[37] Fikry M., Tawfik W., and Omar M. M. "Investigation on the effects of laser parameters on the plasma profile of copper using picosecond laser induced plasma spectroscopy," Optical and Quantum Electronics, **52**(5), 249 (2020). https://doi.org/10.1007/s11082-020-02381-x

[38] Zhang Z. *et al*. "Rule of the pulse energy from ground-based lasers for the laser ablation propulsion in space," Optics Express, **33**(6), 13439-13454 (2025). https://doi.org/10.1364/OE.554720

[39] Mohajan S., Beier N. F., and Hussein A. E. "Investigating crater formation in nanosecond laser ablation of aluminum foils," Journal of Applied Physics, **136**(2), 023102 (2024). https://doi.org/10.1063/5.0212660

[40] Suchandra P., and Ranjan D. "Dynamics of multilayer Rayleigh–Taylor instability at moderately high Atwood numbers," Journal of Fluid Mechanics, **974**, A35 (2023). https://doi.org/10.1017/jfm.2023.689

[41] Zhou Y. "Rayleigh–Taylor and Richtmyer–Meshkov instability induced flow, turbulence, and mixing. II," Physics Reports, **723**, 1-160 (2017). https://doi.org/10.1016/j.physrep.2017.07.008

[42] Xi C., and Xin T. "Heat transfer to a particle exposed to a rarefied plasma with a great temperature gradient," Journal of Thermal Science, **2**(2), 135-142 (1993). https://doi.org/10.1007/BF02718269

[43] Sun W. *et al*. "Numerical study of the effect of a magnetic field on Rayleigh-Taylor instability with different density disturbances," Frontiers in Physics, **11**, 1203081 (2023). https://doi.org/10.3389/fphy.2023.1203081

[44] Martins I. T., Gómez L. C., and Alvariño P. F. "Parametric investigation of Rayleigh–Taylor instability under experimental conditions with the lattice Boltzmann method," Physics of Fluids, **37**(2), 024131 (2025). https://doi.org/10.1063/5.0256018

[45] Onoda K., and Nanzai B. "Marangoni Convection Velocity in Nonlinear Hanging-Droplet Vibration Phenomena," Processes, **12**(3), 609 (2024). https://doi.org/10.3390/pr12030609

[46] Lin F. *et al*. "Marangoni convection-driven laser fountains on free surfaces of liquids," Materials Today Physics, **21**, 100558 (2021). https://doi.org/10.1016/j.mtphys.2021.100558

ТЕОРЕТИЧНИЙ ТА ЕКСПЕРИМЕНТАЛЬНИЙ АНАЛІЗ НЕСТАБІЛЬНОСТІ РЕЛЕЯ — ТЕЙЛОРА ТА КОНВЕКЦІЇ МАРАНГОНІ В МІДНІЙ ФОЛЬЗІ ПІД ДІЄЮ ЛАЗЕРНОГО ВИПРОМІНЮВАННЯ

М.М. Ахмедов[1], **Дж.О. Садуллаєв**[1], **М.Є. Вапаєв**[1], **Н.П. Бабаязова**[1], **А.Р. Матназаров**[2], **І.Й. Давлетов**[1], **М. Джуманіязова**[3], **Р.О. Озодов**[4], **Б. Ісматов**[5], **Ф.Дж. Матчанова**[6]

[1]*Кафедра техніки, Ургенчський державний університет імені Абу Райхана Беруні, Ургенч, 220100, Узбекистан*

[2]*Ургенчський інноваційний університет, вул. Міської Незалежності, 2-й будинок, Ургенч, 220100, Узбекистан*

[3]*Кафедра фізики та астрономії, Ургенчський державний педагогічний інститут, вул. Гурлан, 1-А, Ургенч, 220100, Узбекистан*

[4]*Кафедра біофізики, фізичної культури та спорту, Ургенчський державний медичний інститут. вул. Аль-Хорезмі, 2, Ургенч, 220100, Узбекистан*

[5]*Національний дослідницький університет "Ташкентський інститут інженерів іригації та механізації сільського господарства". Kori Niyoziy 39, Ташкент, 100000, Uzbekistan*

[6]*Хівська районна загальноосвітня середня школа № 10, вул. Саховат, 98, Хівський район, 220900, Узбекистан*

У цьому дослідженні вивчаються фізичні явища, що виникають на поверхні мідної фольги під дією високоінтенсивного імпульсного випромінювання Nd:YAG-лазера ($\lambda = 1064$ нм, $\tau = 28$ пс), з особливим акцентом на утворенні плазми, нестабільності Релея — Тейлора (РТ) та впливі конвекції Марангоні на морфологію кратера. Температура плазми та електронна концентрація визначаються експериментальними методами за спектральними лініями випромінювання. Ці параметри дозволяють оцінити градієнт тиску в плазмі, температурні варіації та зміни поверхневого натягу. Нестабільність РТ моделюється на основі контрастів густини, що виникають за сильних перепадів тиску, тоді як конвекція Марангоні описується як механізм формування поверхневих потоків, зумовлених градієнтами температури. У роботі аналізується взаємодія між цими двома видами нестабільностей, їхня роль у перерозподілі матеріалу та вплив на кінцеву геометричну форму кратера, утвореного лазером, що підкріплюється теоретичними розрахунками та спектроскопічними вимірюваннями. Результати сприяють глибшому розумінню складних термогідродинамічних процесів, що супроводжують лазерну абляцію.

Ключові слова: *нестабільність Релея — Тейлора; конвекція Марангоні; лазерна абляція; мідна плазма; морфологія поверхні; електронна концентрація; спектроскопічна діагностика*

East European Journal of Physics. 3. 539-549 (2026)
DOI:10.26565/2312-4334-2026-3-49 ISSN 2312-4334

PHOTON-INDUCED FERMI LEVEL SHIFTS AND ENERGETIC MODULATION OF RESONANT STATES IN DOUBLE-BARRIER RESONANT TUNNELING NANOSTRUCTURES

Shokhjakhon O. Mamadaliev[1], Mukhammadjon G. Dadamirzaev[1], Munirakhon K. Uktamova[1], Sobirjon R. Boidedaev[1], Kudiratulla B. Umarov[1], Yusuf Usmanov[2]
[1]Namangan State Technical University, Namangan, Uzbekistan
[2]Tashkent Institute of Irrigation and Agricultural Mechanization Engineers, National Research University, Tashkent, Uzbekistan
**Corresponding author e-mail: shoxjaxonmamadaliyev371@gmail.com*
Received April 2, 2026; revised July 24, 2026; accepted August 10, 2026

This paper presents a theoretical analysis of quantum tunneling mechanisms under photon energy excitation within the framework of the Landauer–Büttiker formalism. The study considers the effects of photon absorption during resonant tunneling, leading to modifications of the Fermi–Dirac distribution and shifts in the chemical potentials. It is shown that photogeneration processes induced by optical excitation enhance the tunneling probability, cause an energy broadening of the transmission function, and result in a shift of the resonant peak in the current–voltage (I–V) characteristics. Based on the proposed model, a nonlinear dependence of quantum conductance on photon energy is established, and it is theoretically demonstrated that an increase in photon energy leads to enhanced tunneling conductance. The developed approach provides a deeper insight into optically excited quantum transport phenomena and establishes a new theoretical basis for the design of light-controlled transport systems in nanoelectronic devices.
Keywords: *Landauer–Büttiker formalism; Quantum tunneling; Photon energy; Fermi–Dirac distribution; Transmission function; Chemical potential shift; Nonlinear conductance*

INTRODUCTION

Resonant tunneling diodes (RTDs) are semiconductor nanostructures based on quantum-mechanical transport phenomena and play a crucial role in the development of high-speed electronic and optoelectronic devices [1, 2]. These structures operate on the principle of a double-barrier quantum well (DBQW) and are characterized by a distinctive N-shaped current–voltage (I–V) characteristic associated with the presence of negative differential resistance (NDR) [3]. In RTD structures, resonant tunneling of electrons through potential barriers significantly enhances the transmission probability, leading to the formation of the NDR region [1, 3, 5]. Experimental studies performed by Romeira and co-authors (2013) on resonant tunneling diode photodetectors (RTD-PDs) revealed pronounced modifications of the I–V characteristics under optical illumination [5]. In particular, an increase in light intensity resulted in a shift of the resonance peak and a substantial enhancement of the photocurrent. These findings experimentally demonstrate the high sensitivity of RTD-PD devices to optical signals and the efficient modulation of quantum electron transport under optical excitation [4]. However, the theoretical mechanisms underlying these effects, including the shift of Fermi levels, the modification of the transmission function, and the generation of photocurrent under illumination, have not yet been fully explained within the framework of the Landauer–Büttiker formalism [6, 7]. In recent years, RTDs and RTD-based nanostructured devices have attracted growing attention as key components of high-speed electronic and optoelectronic systems. In particular, RTDs have been widely explored for applications in terahertz (THz) frequency generators, high-speed signal modulators, and light-sensitive quantum devices. Scientific studies published between 2018 and 2026 have focused on advancing the materials platforms, understanding quantum transport mechanisms, and investigating optical effects in RTD technologies. Improving RTD performance is primarily associated with enhancing the quality of the resonance peak and the NDR region. For instance, graphene-based RTDs have demonstrated high peak-to-valley current ratios, highlighting the potential of two-dimensional materials for significantly improving RTD efficiency [8]. Strong NDR and stable resonant tunneling regimes have also been reported in WSe_2/h-BN/WSe_2 heterostructures and related low-dimensional systems [9]. One of the major factors limiting RTD performance in practical devices is interface roughness and structural imperfections. Recent theoretical and numerical studies have shown that correlated interface roughness strongly affects resonant energy levels and tunneling current characteristics, emphasizing the need for nanometer-scale technological control in RTD fabrication [10]. Significant progress has also been achieved in high-frequency RTD applications, particularly in the development of THz oscillators based on optically coupled RTD arrays, demonstrating improved output power and stability [11]. From a theoretical perspective, the Landauer–Büttiker formalism remains one of the most powerful approaches for describing quantum transport in RTD systems. This framework has been successfully applied to model optical transport in graphene-based devices and resonant tunneling structures [12]. Moreover, external influences such as bias voltage, mechanical strain, and electromagnetic fields have been shown to effectively control the tunneling transmission function, as demonstrated in piezotronic resonant tunneling junctions [13].

Cite as: Sh.O. Mamadaliev, M.G. Dadamirzaev, M.K. Uktamova, S.R. Boidedaev, K.B. Umarov, Y. Usmanov, East Eur. J. Phys. 3, 539 (2026), https://doi.org/10.26565/2312-4334-2026-3-49

Resonant tunneling of electrons and holes in complex heterostructures, including AlGaAs/GaAsBi/AlGaAs systems, further confirms the possibility of engineering resonant energy levels through material and structural design [14-17]. Additionally, symmetric doping-free resonant tunneling phenomena in polar heterostructures have recently been investigated both experimentally and theoretically [18-21]. Recent review studies on quantum transport under external perturbations, including time-dependent electromagnetic fields, highlight the crucial role of photon–matter interactions in RTDs and related nanostructures [22, 23]. Nevertheless, in most existing works, the light-induced shift of I–V characteristics, redistribution of Fermi levels, and photocurrent generation in RTD-PD devices are often interpreted using optical or simplified approaches. Therefore, a consistent theoretical model that provides an integral description of optically excited quantum transport in RTD-PD structures within the Landauer–Büttiker formalism is still lacking. This work aims to fill this gap by providing a comprehensive theoretical analysis of photon-induced quantum transport mechanisms in RTD-PD devices based on the Landauer–Büttiker approach, relying on recent scientific results published between 2018 and 2026.

METHODS

A resonant tunneling diode (RTD) is a semiconductor device based on quantum-mechanical phenomena, whose primary operating principle relies on the resonant tunneling of electrons through a potential barrier [1, 2]. In this work, the following parameters of the resonant tunneling diode are theoretically investigated: the dark current I_{dark}, the total current under illumination I_{light}, the photocurrent defined as the difference between illuminated and dark currents, the current–voltage (I–V) characteristics, the photon energy in the heterostructures −hν, the transmission function T(E, hν) and the Fermi–Dirac distribution functions at the contacts, $f_p(E)$ and $f_n(E)$. The calculations are performed using current expressions derived from the Landauer–Büttiker formalism, and numerical computations are carried out using the Maple software package. To describe the current flow in the RTD, the Landauer–Büttiker theoretical approach is employed [6, 7]. Within this framework, the electric current arises from the quantum-mechanical tunneling of electrons through the potential barrier, where electrons exhibit wave-like behavior during transmission. The general expression for the current is given by

$$J(V) = \frac{2q}{h}\int_{-\infty}^{\infty} T(E)[f_p(E) - f_n(E)]dE \tag{1}$$

Here, $-T(E)$ denotes the transmission function of the structure, while $f_p(E)$ and $f_n(E)$ are the Fermi–Dirac distribution functions of the p- and n-type electrodes, respectively. This expression serves as the basis for determining the dark current in RTD devices. The electron tunneling process through the double-barrier potential structure described by Eq. (1) is illustrated schematically in Figure 1.

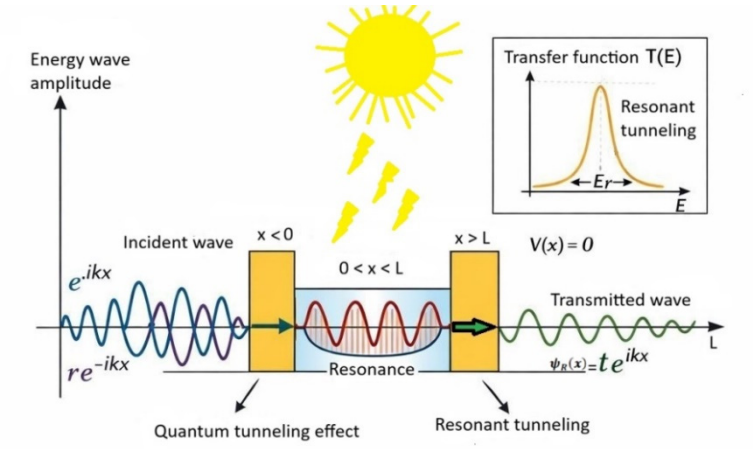

Figure 1. The electron tunneling process through a quantum structure consisting of two potential barriers is illustrated

As a result of quantum tunneling, electrons exhibit a high transmission probability at specific resonance energies, leading to the observation of the resonant tunneling effect. Using the Schrödinger equation,

$$-\frac{\hbar^2}{2m}\frac{d^2\psi(x)}{d(x)^2} + V(x)\psi(x) = E\psi(x). \tag{2}$$

The electron transport through a double-barrier quantum well (DBQW) structure is analyzed. For the left ($x < 0$) and right ($x > L$) contact regions, the potential is taken as $V(x) = 0$, corresponding to free electrons. The transmission coefficient $T(E)$is obtained from the corresponding wave functions. In the left contact region, the wave function is expressed as $\psi_L(x) = e^{ikx} + re^{-ikx}$ representing the incident and reflected electron waves, where (r) is the reflection amplitude. In the right contact region, the transmitted wave function takes the form $\psi_R(x) = te^{ikx}$ where (t) denotes the

transmission amplitude. Inside the quantum well region $(0 < x < L)$, the electron wave function in the resonant state is written as $\psi_w(x) = A\phi(x)$, with (A) being the amplitude inside the well. The continuity conditions for the wave function and its derivative at the interfaces,$\psi_L(0) = \psi w(0);\ \ \psi'_L(0) = \psi'_w(0); \psi_w(L) = \psi_R(L);\ \ \psi'_w(L) = \psi'_R(L)$ lead to a linear system of equations for the coefficients (r), (t), and (A) [28, 29].

For an open quantum system, the discrete energy level in the quantum well becomes a metastable resonant state due to coupling with the left and right contacts. As a result, the resonant energy acquires a complex form,

$$\widetilde{E_r} = E_r - i\frac{\Gamma}{2},\ \Gamma = \Gamma_p + \Gamma_n \tag{3}$$

$\widetilde{E_r}$–is the resonance energy, that is, the energy at which an electron forms a temporarily bound state within the quantum well which physically corresponds to an electron being temporarily confined in the well before tunneling out through the barriers. The transmission probability can be conveniently expressed using the Green's function formalism. The retarded Green's function is given by

$$G^r(E) = \frac{1}{E - E_r + i\frac{\Gamma}{2}} \tag{4}$$

The energy-dependent transmission function then takes the Lorentzian form

$$T(E) = \frac{\Gamma_p\,\Gamma_n}{(E-E_r)^2 + \left(\frac{\Gamma p + \Gamma n}{2}\right)^2} \tag{5}$$

The Lorentzian transmission function arises naturally from the retarded Green's function description of a single resonant state coupled to two contacts. In the resonant tunneling regime, the finite coupling between the quantum well state and the contacts leads to an energy broadening characterized by Γ_p and Γ_n. Consequently, the transmission probability exhibits a Lorentzian line shape centered at the resonant energy Er. This result is well established in resonant tunneling theory and quantum transport calculations [1, 29].

Here, Γ_p and Γ_n represent the coupling (broadening) strengths associated with the *p* and *n* type contacts, respectively, and E_r denotes the resonant energy level.

For InGaAs/AlAs nanostructures, the lowest resonant energy typically lies in the range $E_r \sim 0.1 - 0.3\ eV$. The resonance peak is centered at the resonant energy E_r =0.2 eV, illustrating the transmission characteristics of the InGaAs/AlAs double-barrier structure. The corresponding Lorentzian transmission probability calculated from Eq. (5) is plotted in Figure 2.

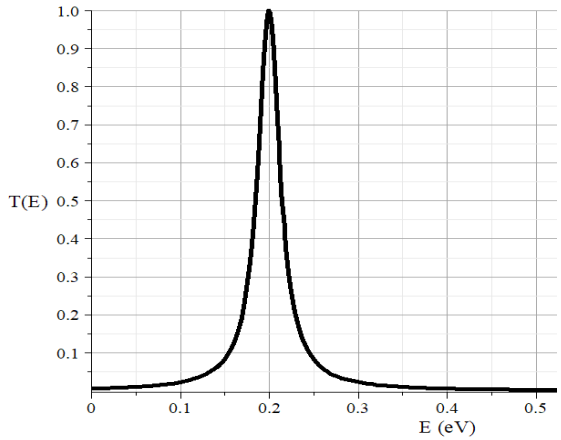

Figure 2. Energy dependence of the Lorentzian transmission probability T(E) calculated using Eq. (5) for an ideal resonant tunneling diode

RESULTS

At finite temperatures, electrons can occupy not only energy states below the chemical potential μ but also states with energies higher than μ. This occurs because thermal excitation allows electrons to transition from lower-energy states to higher-energy states. Under these conditions, the probability that an electron occupies an energy state at the Fermi level is equal to ½, while the probability of occupying states above the Fermi level is nonzero. Since the function $f(E)$ represents the probability that an electron occupies a given energy state, the complementary probability that this energy state is unoccupied by electrons is given by

$$f'(\varepsilon) = 1 - f(\varepsilon) \tag{6}$$

This expression therefore describes the probability that a given energy state is empty of electrons. For an energy level with degeneracy g_i, of which n_i states are occupied by electrons, the Fermi–Dirac distribution function can be written as

$$f(E) = \frac{n_i}{g_i} = \frac{1}{e^{\frac{\varepsilon-\mu}{kT}}+1} \tag{7}$$

Accordingly, the probability of hole occupation, corresponding to an unoccupied electronic state with energy (E), is expressed as

$$f(E) = \frac{n_i}{g_i} = \frac{1}{e^{\frac{\mu-\varepsilon}{kT}}+1} \tag{8}$$

This function represents the probability that an energy state with energy E is occupied by a hole. In semiconductors, mobile holes obey this distribution function. The resulting band diagram, showing the conduction and valence bands, the Fermi level, and electron and hole occupations, is presented in Figure 3.

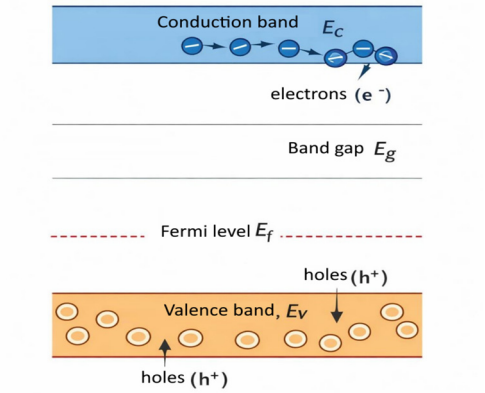

Figure 3. Schematic energy-band diagram illustrating the conduction band, valence band, Fermi level, and electron–hole occupation in a semiconductor

$$f'_p(E) = \frac{1}{e^{-\frac{\mu-\varepsilon}{kT}}+1} \tag{9}$$

Here, -$\mu_p$enotes the Fermi level of the *p-contact,* -k, is the Boltzmann constant, and -T, is the absolute temperature. This expression is particularly relevant for regions with a high concentration of acceptor impurities, where hole transport dominates:

In the n-contact, where donor impurities dominate, and electrons are the majority charge carriers, the Fermi–Dirac distribution function describing the energy-dependent occupation probability of electrons is used. In this case, the distribution function is given by [8, 9]:

$$f_n(E) = \frac{1}{1+e^{\left(\frac{E-\mu_n}{kT}\right)}} \tag{10}$$

Here,$-\mu_n$ denotes the Fermi level of the n-contact. This distribution function describes the probability that an electronic state with energy (E) is occupied by an electron in the n-type semiconductor region:

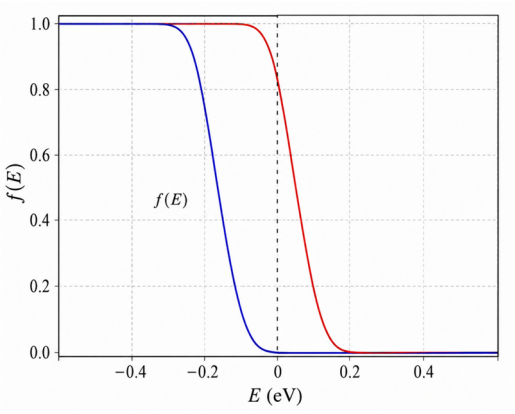

Figure 4. Illustration of the overlap between the Fermi–Dirac distributions of the p- and n-contacts, indicating the energy region where resonant tunneling is expected to occur

By combining the Fermi–Dirac distribution functions of the p- and n-contacts, an energy window can be identified in which resonant electron tunneling occurs [10, 11]. This overlap region defines the range of energies for which charge carriers can effectively tunnel through the double-barrier structure and contribute to the resonant transport process. This overlap of the Fermi-Dirac distributions of the p- and n-contacts is shown in Figure 4.

Using the generalized current expression given in Eq. (1), the current–voltage (I–V) characteristics of the resonant tunneling diode can be obtained [12–14]. In particular, the dark current (J_{dark}) is calculated by integrating the transmission function over the energy range defined by the Fermi–Dirac distributions of the contacts.

The dark current of the resonant tunneling diode is expressed as:

$$J_{dark}(V) = \frac{2q}{h}\int_{\mu_p}^{\mu_n+qV} \frac{\Gamma_p\,\Gamma_n}{(E-E_r)+\left(\frac{\Gamma p+\Gamma n}{2}\right)^2}\cdot\left[\frac{1}{1+e^{\left(\frac{E-\mu_p}{kT}\right)}}-\frac{1}{1+e^{\left(\frac{E-\mu_n+qV}{kT}\right)}}\right]dE \tag{11}$$

This expression describes the current–voltage (I–V) characteristics associated with resonant electron tunneling through the double-barrier structure and is valid for the ideal equilibrium (dark) condition.

When optical illumination is applied, the quasi-Fermi levels of electrons and holes shift due to nonequilibrium carrier generation. This effect can be expressed as

$$\mu_p, \mu_n \rightarrow \mu_p + \Delta\mu_p, \mu_n + \Delta\mu_n \tag{12}$$

Under illumination, electron–hole pairs are generated in the material, disturbing the equilibrium and leading to shifts in the quasi-Fermi levels [18]. The resulting Fermi-level shift can be approximated by:

$$\Delta\mu \approx kT\ \ln\left(1+\frac{G\,\tau}{n_0}\right) \tag{13}$$

Where, $G-$ is the photogeneration rate, τ- is the carrier lifetime, and, $n_0$is the equilibrium sheet carrier density. For InGaAs/AlAs RTD-PD structures, typical values lie in the range $n_0 \sim 1\cdot 10^{11} - 1\cdot 10^{12} cm^{-2}$ .The magnitude of Δμdepends on the illumination intensity and material parameters and directly reflects the increase in current under optical excitation.

The photogeneration rate is defined as

$$G = \int_{E_g}^{\infty} \phi(E)[1-\omega\alpha(E)]\,dE \tag{14}$$

Here, (G) is the photogeneration rate. It represents the number of electron–hole pairs generated per unit volume (or per unit area) per second. This formula incorporates the following processes: photons incident over the spectral distribution $-\phi(h\nu)$,their absorption probability $-(\alpha(E)\omega)$,as well as the forbidden bandgap energy of the InGaAs material, which is approximately $E_g \sim 0.75\ eV$. Here, ω denotes the effective optical path length (or effective absorption thickness) of the active region in the RTD structure. For InGaAs/AlAs resonant tunneling nanostructures, $\omega -$ is taken to be on the order of 1-2 nm. In the present calculations, a representative value of $\omega = 2\ 10^{-9} m$ is used [22-24, 27].

The absorption coefficient is given by

$$\alpha(E) = \begin{cases} \left(\alpha_0 + \beta_0 \frac{h\nu}{E_g}\right)\cdot\sqrt{\frac{h\nu}{E_g}-1} & \begin{matrix} h\nu \geq E_g; \\ h\nu \leq E_g \end{matrix} \\ 0 \end{cases} \tag{15}$$

The absorption coefficient $-\alpha(h\nu)$ is an optical parameter that characterizes the intensity of photon absorption in a semiconductor material [25, 26]. For InGaAs/AlAs nanostructures, this parameter corresponds to barrier layers with thicknesses of, 1–2 nm. The values are taken as $\alpha_0 = 1\cdot 10^9\ m^{-1}, \beta_0 = 1\cdot 10^9 m^{-1}$.

The photon flux is defined as

$$\phi(h\nu) = \begin{cases} \left(\phi_0 e^{[-\eta(h\nu-E_g)]}\right) & \begin{matrix} h\nu \geq E_g \\ h\nu < E_g \end{matrix} \\ 0 \end{cases} \tag{16}$$

Here,$-\phi(h\nu)$ denotes the photon flux density, that is, the number of photons with energy $-(h\nu)$ incident on a unit area per unit time. The parameter $-\eta$ is the decay coefficient, which determines how rapidly the photon flux decreases as the photon energy increases. In theoretical models of photon-assisted tunneling, $\eta \sim 0.01\ (10^{-2})$. Under strong illumination conditions, $\eta \sim 0.05$,The parameter ϕ_0 represents the initial photon flux and corresponds to its maximum value. If $h\nu < E_g$ i.e., when the photon energy is smaller than the forbidden bandgap energy, no electron–hole pairs are generated. When $h\nu \geq E_g$ this condition is satisfied and electron–hole pair generation occurs [28]. Illustrating the formation of electron–hole pairs and the competition between photogeneration and recombination processes. In this case, by combining Eqs. 13, 14, 15, 16, the shift of the chemical potentials under illumination can be written as

$$\Delta\mu \approx kT\ \ln\left(1+\frac{\tau}{n_0}\int_{E_g}^{\infty}\phi_0 e^{[-\eta(h\nu-E_g)]}\left[1-e^{\left(-\omega\left(\alpha_0+\beta_0\frac{h\nu}{Eg}\right)\cdot\sqrt{\frac{h\nu}{Eg}-1}\right)}\right]dE\right) \tag{17}$$

The resulting dependence of the quasi-Fermi level shift on photon frequency, obtained from Eq. (17), is shown in Figure 5.

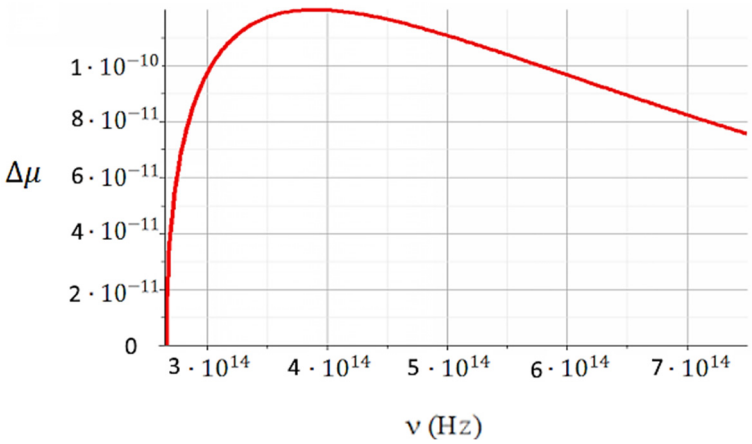

Figure 5. Dependence of the quasi-Fermi level shift ($\Delta\mu$) on the photon frequency under optical illumination

Next, we analyze the influence of optical absorption on the transport characteristics. According to expression (5), the coupling parameters Γ_p and Γ_n which describe the interaction between the contacts and the resonant state, are affected by photon absorption processes. Under optical excitation, photon absorption and emission enhance the contact–resonance coupling, leading to an increase in the total broadening parameter -Γ. As a result, the resonance width becomes larger. For convenience, the photon energy is expressed as $E=\hbar\omega$ and the parameter -Γ, is commonly modeled as a function of the photon energy. The light-induced broadening of the resonant level can be written as,

$$\Gamma_{L,R} = \eta_{L,R} I_{ph} \delta(E_0 \pm \hbar\omega - E) \tag{18}$$

or, in a simplified form,

$$\Gamma_{L,R} = \Gamma_{L,R}{}^{(0)} \left[1 + \eta_{L,R} \frac{I_{ph}}{(\hbar\omega)^2}\right] \tag{19}$$

Here, $-\hbar\omega$ is the photon energy, $-I_{ph}$ denotes the light intensity, and, $-\eta_{L,R}$ is the electron–photon interaction coefficient. The parameter $(-\eta_{L,R}\ is\ taken\ to\ be\ approximately\ 0.01)$. Thus, in order to account for the effect of optical excitation on the resonance energy broadening, the transmission function can be written in the following form:

$$T(E) = \frac{\Gamma_L(\hbar\omega)\Gamma_R(\hbar\omega)}{(E-E_0)^2 + \left[\frac{\Gamma_L(\hbar\omega)+\Gamma_R(\hbar\omega)}{2}\right]^2} \tag{20}$$

In this case, the electron tunnels not only at the resonant energy $-E_0$ but also at energies shifted by $E_0 \pm (\hbar\omega)$.

In the absence of light (dark condition), the transmission spectrum exhibits a Lorentzian resonance profile, whereas under optical illumination the resonance evolves into an asymmetric Fano line shape.

Under illumination, the carrier lifetime changes due to electron–photon interactions. Therefore, both illuminated and non-illuminated cases are considered. The carrier lifetime is given by

$$\tau = \frac{\hbar}{\Gamma_p + \Gamma_n} \tag{21}$$

In the absence of external influence, the Lorentzian resonance appears as shown in Figure 6(a), whereas the Fano resonance emerges under illumination, as illustrated in Figure 6(b).

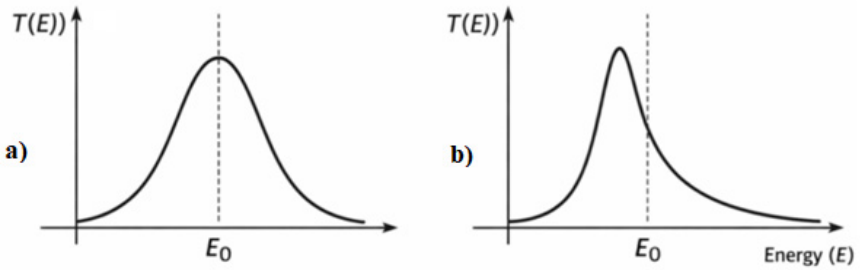

Figure 6. Panels (a) and (b) illustrate the transmission spectra in the absence and presence of optical illumination, respectively

When light is incident on the structure, charge carriers can absorb or emit photons, which modifies their lifetime. In this case, the electron acquires additional energy,

$$E_{ph} = \hbar\omega \tag{22}$$

allowing it to overcome the potential barrier more easily. Accordingly, the partial broadening parameters are expressed as

$$\Gamma_p = \Gamma_p^{(0)} + \Gamma_p^{(ph)} \tag{23}$$

$$\Gamma_n = \Gamma_n^{(0)} + \Gamma_n^{(ph)} \tag{24}$$

Here, $\Gamma^{(ph)}$ denotes the light-induced contribution to the resonance broadening. According to Eq. (21), under optical illumination the lifetime of charge carriers takes the following form:

$$\tau = \frac{\hbar}{\left(\Gamma_p^{(0)}+\Gamma_p^{(ph)}(\hbar\omega)\right)+\left(\Gamma_n^{(0)}+\Gamma_n^{(ph)}(\hbar\omega)\right)} \tag{25}$$

In this expression, the total (effective) lifetime of the charge carriers is obtained by taking into account both the intrinsic and light-induced broadening contributions. As a result, an additional quasi-potential emerges, which allows us to understand how the transmission probability (T(E)) is modified under illumination. Consequently, we obtain an additional impurity potential, which allows us to understand how the transmission probability changes. In the absence of light: a) In the figure, there is no change in the impurity potential, and the transparency also remains unchanged. In the presence of light: b) In the figure, due to illumination, electron-hole pairs are generated, which modifies the tunneling process. As a result, the transmission profile changes toward a Fano resonance, as illustrated in Fig. 7. Schematically illustrates that, due to the generation of additional charge carriers and the resulting shift , extra tunneling channels appear. These additional channels give rise to interference effects, causing the transparency to evolve from a Lorentzian profile to a Fano resonance under optical excitation.

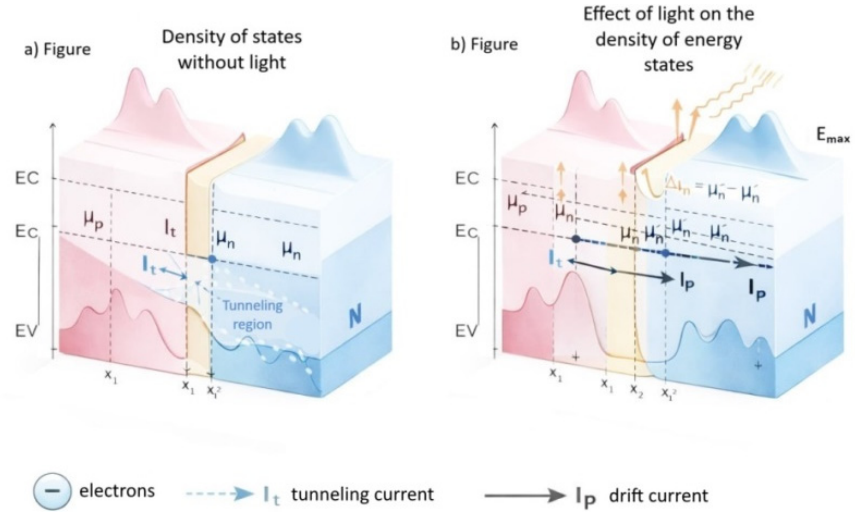

Figure 7. Schematic representation of the density of localized states and charge-carrier transport mechanisms: (a) in the dark, showing tunneling current, and (b) under illumination, showing photoinduced changes in the density of states and drift current

In the absence of illumination, the Fermi levels are taken as, μ_p=0.2 eV and μ_n=0.1 eV. Under optical illumination, the shifts, $\Delta\mu_p$=0.3 eV and $\Delta\mu_n$=0.2 eV occur. These shifts arise due to the photogeneration of charge carriers and lead to a modification of the Fermi energy. The photocurrent under illumination is given by the following expression:

$$J_{light}(V) = \frac{2q}{h}\int_{\mu_p+\Delta\mu_p}^{\mu_n+\Delta\mu_n+qV} \frac{\Gamma_p\,\Gamma_n}{(E-E_r)+\left(\frac{\Gamma_p+\Gamma_n}{2}\right)^2}\left[\frac{1}{1+e^{\left(\frac{E-\mu_p+\Delta\mu_p}{kT}\right)}} - \frac{1}{1+e^{\left(\frac{E-\mu_n+\Delta\mu_n+qV}{kT}\right)}}\right]dE \tag{26}$$

From Eq. (26), only the current generated under optical illumination can be obtained. If the total (net) current is required, it can be written as $J_{net}(V) = J_{light}(V) - J_{dark}(V)$ where the resulting net current represents exclusively the contribution induced by illumination [18, 30-32]. By combining Eq. (26) with Eq. (11) and analyzing the results separately, the illuminated and non-illuminated cases can be directly compared. The corresponding behaviors are illustrated in the graphs presented below. When light is incident on the device, photogeneration leads to a shift of the quasi-Fermi levels, which increases the tunneling probability and results in a higher total current J_{light} compared to the dark current J_{dark}. The difference between these two currents represents the pure photocurrent.

The calculated current–voltage (J–V) characteristics of the resonant tunneling structure under dark and illuminated conditions are shown in Figure 8.

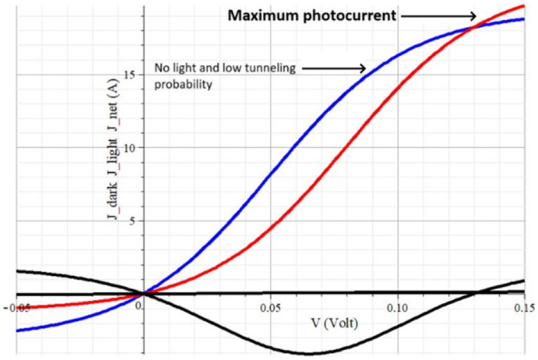

Figure 8. Current–voltage (J–V) characteristics of the resonant tunneling structure under dark and illuminated conditions.

The red curve $-J_{light}(V)$, represents the total current under illumination. When light is incident on the semiconductor, photogeneration occurs in the active region, leading to the formation of additional electron–hole pairs. As a result, the quasi-Fermi levels (μ_p, μ_n) shift, the tunneling probability increases, and consequently the total current is enhanced. This explains why the red curve is located at the highest level.

The blue curve corresponds to the dark current $-J_{dark}$ which represents the current prior to illumination. In the absence of photogeneration, the Fermi energy levels do not shift, the tunneling probability remains low, and therefore the current is smaller. As a result, the blue curve lies below the red one.

The black curve denotes the net current $-J_{net}(V)$defined as the difference $J_{net}(V) = J_{light}(V) - J_{dark}(V)$ which corresponds to the additional current generated exclusively by illumination, commonly referred to as the photocurrent. This curve is not shown as a current flowing "below" the others; instead, it is presented as a differential quantity, representing the amplitude of the photocurrent. From a physical point of view, this indicates that electron transport and photogeneration occur simultaneously, while the plotted net current reflects only the contribution induced by optical excitation.

A pronounced modification of the I–V characteristics under illumination is observed. When light is absorbed, electron–hole pairs are generated, which induces a shift of the chemical potentials (Fermi levels) at the heterojunctions. As a consequence of this Fermi level shift, the energy range favorable for electron tunneling is broadened, and the resonant current peak is shifted toward higher values (Fig. 8). As a result, the photocurrent in the RTD structure increases under illumination, providing clear evidence of light-controlled resonant tunneling. Furthermore, in comparison with the dark condition, a broadening of the N-shaped resonant peak is observed in the current–voltage characteristics. This behavior can be consistently explained by the photogeneration rate described by Eq. (14) and the chemical potential shift given by Eq. (13).

Therefore, the obtained results indicate the following:

1. Resonant tunneling is significantly enhanced under illumination.
2. The shift of the chemical potentials ($\Delta\mu$) directly leads to an increase in the tunneling current.
3. RTD structures can be utilized as highly sensitive nano-photodetectors or photomodulators for optoelectronic applications.

Thus, the investigated model enables a detailed analysis of the resonant tunneling mechanism under illumination and provides a theoretical basis for predicting photoinduced currents in semiconductor tunnel diodes.

For comparison with the theoretical results, the experimentally observed photocurrent characteristics reported by Romeira et al. are shown in Figure 9.

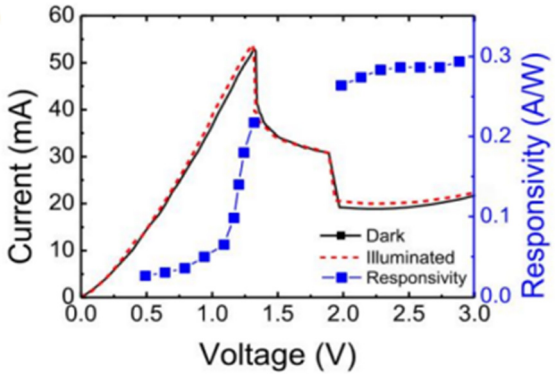

Figure 9. Experimentally observed variation of the photocurrent reported by Romeira et al. (2013).

According to the experimental results presented by Romeira et al. [5], a resonant tunneling diode photodetector (RTD-PD) based on an InGaAs/AlAs heterostructure was systematically investigated. In their study, when optical radiation with a wavelength of 1.55 μm was incident on the RTD-PD structure, pronounced modifications were observed in the current–voltage (I–V) characteristics. These experimental observations are illustrated in Fig. 9.

In particular, with increasing light intensity, the resonant peak voltage was found to shift by approximately $\Delta V_{peak} \approx 0.3$ V accompanied by a significant increase in the photocurrent. These results clearly demonstrate the light-sensitive transport behavior of the RTD-PD device. The theoretical model developed in this work provides a consistent explanation of this phenomenon through the following relation:

$$V_P = \frac{\Delta\mu_p - \Delta\mu_n}{q} \tag{27}$$

Where $\mu_p$and μ_n, denote the light-induced shifts of the chemical potentials at the *p* and *n* contacts, respectively, and q is the elementary charge.

As a result of photogeneration, electron–hole pairs are created, leading to a modification of the potential profile near the contacts. Consequently, the resonant energy level involved in the tunneling process is shifted. This shift of the resonant level results in an increase of the peak voltage toward higher values, which is in excellent agreement with the experimentally observed shift of approximately 0.3 V reported in Ref. [5]. The close correspondence between the theoretical predictions and experimental data confirms the validity of the proposed photogeneration-assisted resonant tunneling model. Thus, under illumination, the transmission function T(E) broadens as a result of the light-induced shift of the Fermi levels, leading to an increase in the current ($I_{light} > I_{dark}$) and an upward shift of the resonant energy state. In this way, the proposed theoretical model provides a consistent physical explanation for the experimentally observed I-V peak shift and photocurrent enhancement reported by Bruno Romeira et al. [5].

1. The transport processes in the RTD structure were comprehensively analyzed within the framework of the Landauer–Büttiker formalism. While previous studies mainly applied this approach to purely electrical transport, in this work it is implemented in an integral form to describe resonant tunneling processes modified by optical excitation.
2. In the theoretical model of the RTD device, the photogeneration process, the light-induced shift of the Fermi levels, and the photon-energy dependence of the transmission function are integrated into a unified analytical formulation. Although these components have been treated separately in earlier studies, their combined analysis within a single generalized framework is demonstrated here for the first time.
3. A new analytical expression is proposed to describe the variation of the resonant tunneling probability and the shift of the resonant peak in the current–voltage (I–V) characteristics with increasing photon energy. Using this expression, the nonlinear dependence of the light-controlled photocurrent on illumination intensity is theoretically established.
4. The proposed model identifies the mechanism of light-induced chemical potential shifts in RTD structures and enables a combined analysis of resonant tunneling and photogeneration processes.

CONCLUSIONS

In this study, quantum transport processes occurring under illumination in a resonant tunneling diode (RTD) device were theoretically analyzed using the Landauer–Büttiker formalism. The results show that electron–hole pairs generated due to photon absorption lead to shifts in the Fermi levels, which enhance the tunneling probability and cause an upward shift of the resonant peak in the current–voltage (I–V) characteristics.

Using the proposed theoretical model, the Fermi–Dirac distribution, photogeneration rate, and transmission function were analyzed in an integral and self-consistent manner, and the nonlinear dependence of the photocurrent on light intensity was theoretically demonstrated.

The theoretical predictions are in good qualitative agreement with the experimental observations reported by Romeira et al. (2013). In particular, both studies demonstrate resonant tunneling behavior, nonlinear current-voltage characteristics, and enhanced photocurrent under optical illumination. The remaining differences can be attributed to real-device effects, such as contact heating, structural imperfections, series resistance, and other non-ideal parameters that are not included in the present theoretical model. Overall, the proposed model enables the analysis of light-controlled chemical potential shifts in RTD structures and establishes a new theoretical basis for the design of nano-photodetectors and optoelectronic sensors.

ORCID

M.G. Dadamirzaev, https://orcid.org/0000-0001-8258-4617; **M.K. Uktamova,** https://orcid.org/0009-0005-7562-2677
Y. Usmanov, https://orcid.org/0000-0002-0509-999X

REFERENCES

[1] S. Datta, *Quantum Transport: Atom to Transistor*, (Cambridge University Press, Cambridge, 2005).
[2] L.L. Chang, L. Esaki, and R. Tsu, "Resonant tunneling in semiconductor double barriers," Applied Physics Letters, **24**(12), 593-595 (1974). https://doi.org/10.1063/1.1655067
[3] S.M. Sze, Y. Li, and K.K. Ng, *Physics of Semiconductor Devices*, 4th Edition, (Wiley, 2021).
[4] K. Xu, E. Wynne, and W. Zhu, "Resonant Tunneling and Negative Differential Resistance in Black Phosphorus Vertical Heterostructures," Advanced Electronic Materials, **6**(8), 2000318 (2020). https://doi.org/10.1002/aelm.202000318

[5] B. Romeira, L.M. Pessoa, H.M. Salgado, C.N. Ironside, and J.M.L. Figueiredo, "Photo-Detectors Integrated with Resonant Tunneling Diodes," Sensors, **13**(7), 9464–9482 (2013). https://doi.org/10.3390/s130709464
[6] A.C. Seabaugh, and Q. Zhang, "Low-Voltage Tunnel Transistors for Beyond CMOS Logic," Proceedings of the IEEE, **98**(12), 2095–2110 (2010). https://doi.org/10.1109/JPROC.2010.2070470
[7] R. Landauer, "Electrical resistance of disordered one-dimensional lattices," Philosophical Magazine, **21**(172), 863–867 (1970). https://doi.org/10.1080/14786437008238472
[8] M. Büttiker, "Four-terminal phase-coherent conductance. Physical Review Letters," **57**(14), 1761–1764 (1986). https://doi.org/10.1103/PhysRevLett.57.1761
[9] P. Acharya, N. Kumar, A. Dixit, J. Lee, and V. Georgiev, "Impact of interface roughness correlation on resonant tunnelling diode variation," Scientific Reports, **15**, 26815 (2025). https://doi.org/10.1038/s41598-025-07720-0
[10] M. Van Ta, *et al.,* "Terahertz resistor-coupled arrayed resonant-tunneling-diode oscillators with high DC-to-RF efficiency using metal-insulator-metal capacitor," REV Journal on Electronics and Communications, **14**(3), 39–43 (2024). https://doi.org/10.21553/rev-jec.377
[11] M. Sun, *et al.,* "High-frequency resonant tunneling diodes," IEEE Trans. Electron Devices, **60**, 3077–3083 (2013). https://doi.org/10.1109/TED.2013.2274479
[12] K. Kinoshita, *et al.,* "Negative Differential Resistance Device with High Peak-to-Valley Ratio Realized by Subband Resonant Tunneling of Γ-Valley Carriers in WSe_2/h-BN/WSe_2 Junctions," ACS Nano, **18**(42), 28968–28976 (2024). https://doi.org/10.1021/acsnano.4c09569
[13] Z. Zhang, *et al.,* "Toward High-Peak-to-Valley-Ratio Graphene Resonant Tunneling Diodes," Nano Letters, **23**(17), 8132–8139 (2023). https://doi.org/10.1021/acs.nanolett.3c02281
[14] J. Encomendero, V. Protasenko, D. Jena, and H.G. Xing, "Defeating broken symmetry with doping: Symmetric resonant tunneling in noncentrosymmetric heterostructures," Physical Review B, **107**, 125301 (2023). https://doi.org/10.1103/PhysRevB.107.125301
[15] F.A. Giyasova, and M.A. Yuldoshev, "Investigation of temporal characteristics of photosensitive heterostructures based on gallium arsenide and silicon," Chalcogenide Letters, **22**(2), 123–129 (2025). https://doi.org/10.15251/CL.2025.222.123
[16] Sh.B. Utamuradova, F.A. Giyasova, K.N. Bakhronov, M.A. Yuldoshev, M.R. Bekchanova, and B. Ismatov. "Current Transfer Mechanism in A Thin-Based Heterosystem Based on A^2B^6 Compounds," East Eur. J. Phys. (3), 325 (2025). https://doi.org/10.26565/2312-4334-2025-3-31
[17] F.A. Giyasova, A.Z. Rakhmatov, Kh.N. Bakhronov, M.A. Yuldoshev, F.A. Giyasov, A.N. Olimov, and N.A. Sattarov, "Physical Principles of Photocurrent Generation in a Silicon-Based Photodiode Structure with a Schottky Barrier," East Eur. J. Phys. (4), 397 (2025). https://doi.org/10.26565/2312-4334-2025-4-38
[18] M. Uktamova, and Sh. Mamadaliev, "Three-dimensional modeling of the relationship between static tunneling and the optical absorption coefficient in tunnel diodes," Results in Optics, **22**, 100950 (2026). https://doi.org/10.1016/j.rio.2025.100950
[19] Sh. B. Utamuradova, F. A. Giyasova, M. S. Paizullakhanov, S. Yu. Gerasimenko, M. A. Yuldoshev, S. R. Boydedayev, M. R. Bekchanova, "Investigation of the functional capability of modified silicon-based photodiodes structure," Chalcogenide Letters **22**(8), 753 – 764 (2025). https://doi.org/10.15251/CL.2025.228.753
[20] Z.T. Azamatov, Sh.B. Utamuradova, M.A. Yuldoshev, and N.N. Bazarbaev, "Some properties of semiconductor-ferroelectric structures," East Eur. J. Phys. (2), 187-190 (2023). https://doi.org/10.26565/2312-4334-2023-2-19
[21] F.A. Giyasova, Kh.N. Bakhronov, M.A. Yuldoshev, I.B. Sapaev, R.G. Ikramov, F.A. Giyasov, M.R. Bekchanova, et al., "Study of the influence of temperature on the transitions of the CdS/Si/CdTe heterosyste," East Eur. J. Phys. (4), 461 (2025). https://doi.org/10.26565/2312-4334-2025-4-47
[22] M.G. Dadamirzaev, M.K. Uktamova, Sh. Rakhmanova, and G.A. Ibadullayev, "Simulation of tunnel diode I-V Characteristics with photocurrent and phonon-assisted processes," East Eur. J. Phys. (4), 675-681 (2025). https://doi.org/10.26565/2312-4334-2025-4-73
[23] M. Acciai, L. Arrachea, and J. Splettstoesser, "Quantum transport phenomena induced by time-dependent fields," La Rivista del Nuovo Cimento, **48**(10), 653–798 (2025). https://doi.org/10.1007/s40766-025-00074-3
[24] G. Platero, R. Aguado, "Photon-assisted transport in semiconductor nanostructures," Physics Reports, **395**(1–2), 1–157 (2004). https://doi.org/10.1016/j.physrep.2004.01.004
[25] B. Kaestner, and V. Kashcheyevs, "Non-adiabatic quantized charge pumping with tunable-barrier quantum dots: A review of current progress," Reports on Progress in Physics, **78**(10), 103901 (2015). https://doi.org/10.1088/0034-4885/78/10/103901
[26] A. Rogalski, P. Martyniuk, and M. Kopytko, "Type-II superlattice photodetectors versus HgCdTe photodiodes," Progress in Quantum Electronics, **68**, 100228 (2019). https://doi.org/10.1016/j.pquantelec.2019.100228
[27] Gulyamov, G., Dadamirzayev, M. G., Uktamova, K. M., & Mislidinov, B. Z. "The effect of a heated electron on the VAX of a tunnel diode," AIP Conference Proceedings, **2700**(1), 050007 (2023). https://doi.org/10.1063/5.0126516
[28] G. Gulyamov, S.B. Utamuradova, M.G. Dadamirzaev, N.A. Turgunov, M.K. Uktamova, K.M. Fayzullaev, A.I. Khudayberdiyeva, and A.I. Tursunov, East Eur. J. Phys. (2), 221 (2023). https://doi.org/10.26565/2312-4334-2023-2-24
[29] M.G. Dadamirzaev, M.K. Uktamova, S.R. Boydedayev, M.A. Yuldoshev, and S.H. Mamadaliev, "Theoretical Analysis of Photon-Energy-Controlled Quantum Tunneling Mechanisms Based on the Landauer–Büttiker Formalism," Physics AUC, **35**, 76-84 (2025). https://share.google/EqKveBzVq9UCc2Ndc
[30] P.R. Berger, G. Gulyamov, M.G. Dadamirzaev, M.K. Uktamova, and S.R. Boidedaev, "Influence of Microwave and Magnetic Fields on the Electrophysical Parameters of a Tunnel Diode," Romanian Journal of Physics, **69**(3–4), Article 609 (2024). https://doi.org/10.59277/RomJPhys.2024.69.609
[31] U.I. Erkaboev, and R.G. Rakhimov, "Determination of the Dependence of Transverse Electrical Conductivity and Magnetoresistance Oscillations on Temperature in Heterostructures Based on Quantum Wells," e-Journal of Surface Science and Nanotechnology, **22**(2), 98–106 (2024). https://doi.org/10.1380/ejssnt.2023-070

[32] U.I. Erkaboev, R.G. Rakhimov, “Oscillations of Transverse Magnetoresistance in the Conduction Band of Quantum Wells at Different Temperatures and Magnetic Fields,” Journal of Computational Electronics, **23**(2), 279–290 (2024). https://doi.org/10.1007/s10825-024-02130-3

ФОТОІНДУКОВАНІ ЗСУВИ РІВНЯ ФЕРМІ ТА ЕНЕРГЕТИЧНА МОДУЛЯЦІЯ РЕЗОНАНСНИХ СТАНІВ У ДВОБАР'ЄРНИХ РЕЗОНАНСНО-ТУНЕЛЬНИХ НАНОСТРУКТУРАХ

Шохжахон О. Мамадалієв[1], Мухаммаджон Г. Дадамірзаєв[1], Мунірахон К. Уктамова[1], Собіржон Р. Бойдедаєв[1], Кудіратулла Б. Умаров[1], Юсуф Усманов[2]

[1]Наманганський державний технічний університет, Наманган, Узбекистан

[2]Ташкентський інститут інженерів іригації та механізації сільського господарства, Національний дослідницький університет, Ташкент, Узбекистан

У цій роботі представлено теоретичний аналіз механізмів квантового тунелювання під впливом збудження енергією фотонів у межах формалізму Ландауера–Бюттікера. Дослідження розглядає ефекти поглинання фотонів під час резонансного тунелювання, що призводять до модифікації розподілу Фермі–Дірака та зсувів хімічних потенціалів. Показано, що процеси фотогенерації, індуковані оптичним збудженням, підвищують ймовірність тунелювання, спричиняють енергетичне розширення функції проходження та призводять до зсуву резонансного піка на вольт-амперних характеристиках (ВАХ). На основі запропонованої моделі встановлено нелінійну залежність квантової провідності від енергії фотонів, а також теоретично доведено, що підвищення енергії фотонів призводить до посилення тунельної провідності. Розроблений підхід забезпечує глибше розуміння явищ квантового транспорту під впливом оптичного збудження та створює нове теоретичне підґрунтя для проєктування систем транспорту з оптичним керуванням у пристроях наноелектроніки.

Ключові слова: *формалізм Ландауера–Бюттікера; квантове тунелювання; енергія фотонів; розподіл Фермі–Дірака; функція проходження; зсув хімічного потенціалу; нелінійна провідність*

EAST EUROPEAN JOURNAL OF PHYSICS. 3. 550-563 (2026)
DOI:10.26565/2312-4334-2026-3-50 ISSN 2312-4334

MULTI-FIELD MODULATION OF TUNNELING CURRENT, DIFFERENTIAL RESISTANCE AND NOISE IN n^+–GaAs/AlGaAs TUNNEL DIODES

Mukhammadjon G. Dadamirzaev[1], Munirakhon K. Uktamova[1,2]*, Nosirbek A. Sattarov[3], Sobir Ruziboyev[4], Arofat I. Khudayberdieva[5]
[1]*Namangan State Technical University, Namangan, Uzbekistan*
[2]*University of Business and Science, Tashkent, Uzbekistan*
[3]*Kimyo International University in Tashkent, Uzbekistan*
[4]*Tashkent Institute of Irrigation and Agricultural Mechanization Engineers, National Research University, Uzbekistan*
[5]*Tashkent Institute of Chemical Technology (TICT)*
**Corresponding Author e-mail: umk9391@gmail.com*
Received March26, 2026; revised June 22, 2026; in final form July 20, 2026; accepted August 6, 2026

This work presents a theoretical study of differential resistance and noise in tunnel diodes under combined optical, magnetic, and high-frequency electromagnetic fields. The tunneling current is modeled using the Tsu–Esaki approach with WKB approximation, while magnetic field effects are introduced via Landau quantization. Optical excitation leads to quasi-Fermi-level splitting and enhances the tunneling current, thereby modulating and smoothing the negative differential resistance (NDR) region. High-frequency fields further modify the barrier transparency, thereby affecting the device's dynamic behavior. Noise analysis based on shot noise and Fano factor shows that a high signal-to-noise ratio (SNR) can be maintained under external perturbations. A generalized multi-field model for n^+–GaAs/AlGaAs heterostructures is proposed, demonstrating controllable tunneling dynamics, low noise, and stable operation in the sub-THz range. The results indicate strong potential for applications in high-speed optoelectronics and radiation-resistant space electronics.
Keywords: *Tunnel diode; Negative differential resistance; Tsu–Esaki model; WKB approximation; Landau quantization; Shot noise; GaAs/AlGaAs heterostructure; Quasi-Fermi level; High-frequency fields; Optical excitation; Magnetic field effects*

INTRODUCTION

The investigation of quantum tunneling phenomena in semiconductor heterostructures remains an important research area due to its relevance for high-speed and high-frequency electronic devices [1-4]. Tunnel diodes constitute a prominent class of such devices, operating through charge-carrier tunneling across a narrow potential barrier. A tunnel diode is a semiconductor device that operates based on the quantum mechanical tunneling phenomenon [5-7]. This effect was first experimentally observed and theoretically explained by Leo Esaki, who demonstrated negative differential resistance (NDR) in heavily doped p–n junctions [8]. The unique current–voltage (I–V) characteristics of tunnel diodes enable their application in high-speed switching, oscillators, and microwave and terahertz electronic devices. The tunneling process is inherently a quantum mechanical effect in which charge carriers penetrate potential barriers that would be forbidden in classical physics. This phenomenon is typically described using the WKB approximation, which provides an analytical expression for the tunneling probability through a potential barrier [9]. Furthermore, the current in tunnel diodes is commonly modeled using the Tsu–Esaki formalism, which integrates the tunneling probability with the Fermi–Dirac distribution of carriers [1, 10]. The concept of resonant tunneling was later introduced in double-barrier quantum structures by Raphael Tsu and Leo Esaki, leading to the development of resonant tunneling diodes (RTDs) [10, 11]. These devices exhibit extremely fast response times and are capable of operating in the gigahertz and terahertz frequency ranges. Semiconductor heterostructures such as GaAs/AlGaAs and GaN/AlN are widely used due to their favorable electronic properties, including low effective mass and high carrier mobility [12-14]. In the presence of an external magnetic field, the energy spectrum of electrons becomes quantized into discrete levels known as Landau quantization [15, 16]. This quantization significantly influences the density of states and modifies the tunneling probability, resulting in oscillatory behavior of the current. Theoretical foundations of this effect were established by Lev Landau, while further developments were carried out in the context of semiconductor physics [17]. Additionally, optical excitation plays a crucial role in modifying the transport properties of tunnel diodes. Incident light generates nonequilibrium electron–hole pairs, leading to a shift in the quasi-Fermi levels and an increase in the tunneling current [18, 19]. This effect enables optical control of the tunneling process and provides a basis for optoelectronic applications. In recent years, the combined influence of electric, magnetic, optical, and high-frequency electromagnetic fields on tunneling devices has attracted significant research interest. Such multi-field interactions allow for precise control of tunneling dynamics and the negative differential resistance region, which is essential for advanced device engineering. In particular, GaN-based resonant tunneling diodes demonstrate high thermal stability and radiation resistance, making them suitable for harsh environments [20]. However, a comprehensive theoretical model that

Cite as: M.G. Dadamirzaev, M.K. Uktamova, N.A. Sattarov, S. Ruziboyev, A.I. Khudayberdieva, East Eur. J. Phys. 3, 550 (2026), https://doi.org/10.26565/2312-4334-2026-3-50

simultaneously accounts for tunneling, noise, magnetic quantization, and external field effects is still lacking. Understanding the interplay between Landau quantization, quasi-Fermi level splitting, and tunneling probability is essential for the development of next-generation high-speed and low-noise semiconductor devices. In this work, we present a theoretical analysis of the differential resistance and noise characteristics of tunnel diodes under the combined influence of magnetic, optical, and high-frequency fields. The model is based on the Tsu–Esaki formalism, WKB approximation, and Landau quantization, providing a unified description of multi-field effects on quantum tunneling. The obtained results contribute to the development of high-performance nanoelectronic and optoelectronic devices.

METHODS

The tunneling current in a tunnel diode, denoted as $-I$, arising from fully transmitted electrons, is described by the following expression:

$$I(V) = \frac{4\pi e}{h}\int_{-\infty}^{\infty}\left[f_n(E) - f_p(E)\right]T(E,V)\,dE, \tag{1}$$

here, $f_n(E)$and $f_p(E)$ −represent the Fermi–Dirac distribution functions in the n- and p-regions, respectively, while $T(E,V)$denotes the tunneling probability, which is typically evaluated using the WKB approximation:

$$T(E,V) \approx \exp\left(-\frac{2}{\hbar}\int_0^d \sqrt{2m(V(x)-E)}\;dx\right), \tag{2}$$

here, $V(x)$ −represents the potential energy of the barrier, and $d$denotes the thickness of the p–n junction. The differential resistance is defined as the inverse of the slope of the current–voltage (I–V) characteristic.

$$R_d(V) = \frac{dV}{dI(V)}. \tag{3}$$

Alternatively, it can be expressed as:

$$R_d(V) = \left(\frac{dI}{dV}\right)^{-1}. \tag{4}$$

After calculating the tunneling current within the Tsu–Esaki model, we take its derivative with respect to $-V$.

$$\mathrm{I}_t = \mathrm{A}exp\left(-\frac{4\sqrt{2m}}{3\hbar qF}(qV-E)^{\frac{3}{2}}\right)\int_0^{\mu_n+\mu_p-qV}\sqrt{\varepsilon\left(\mu_n+\mu_p-\varepsilon-qV\right)}\cdot\left(\frac{1}{\exp\left(\frac{\varepsilon-\mu_n}{kT}\right)}-\frac{1}{exp\left(\frac{\varepsilon-\mu_n+qV}{kT}\right)+1}\right)d\varepsilon. \tag{5}$$

By adding the diffusion current expression to Eq. (5), the N-shaped current–voltage (I–V) characteristic and the differential resistance of the tunnel diode were theoretically derived within the framework of the WKB approximation under high-frequency electromagnetic excitation. The formation mechanism of the negative differential resistance (NDR) region was explained based on the quantum tunneling process. In this work, the model is extended by taking into account the effect of the magnetic field. Due to the Landau quantization of the electron energy spectrum, the tunneling probability is transformed into a magnetic-field-dependent form. Based on the modified transmission coefficient, the I–V characteristics and differential resistance in the presence of a magnetic field were theoretically obtained and quantitatively compared with experimental data. The obtained results explain the redistribution of current and the shift of the differential resistance region in tunnel diodes under the influence of a magnetic field. In a magnetic field, the transverse motion of electrons becomes quantized, and the energy levels acquire a discrete structure, as demonstrated by Lev Landau

$$E_n = \left(n+\frac{1}{2}\right)\hbar\omega_c, \tag{6}$$

$$\omega_c = \frac{qB}{m}. \tag{7}$$

As a result, the energy spectrum is given by:

$$E = E_z + \left(n+\frac{1}{2}\right)\hbar\omega_c, \tag{8}$$

here, E_z −represents the energy component along the tunneling direction. The expressions for the density of states in the presence of a magnetic field are discussed in the article [21].

Due to Landau quantization, the WKB exponential is modified as follows:

$$T_B(E_z) = \exp\left[-\frac{4\sqrt{2m}}{3\hbar qF}\left(qV-E_z-\left(n+\frac{1}{2}\right)\hbar\omega_c\right)^{\frac{3}{2}}\right]. \tag{9}$$

Consequently, the tunneling current takes the following form:

$$I(V,B) = \frac{4\pi q}{\hbar}\sum_{n=0}^{N}\int_{-\infty}^{\infty} T_B(E_z)\,\rho_c(E,B)\,\rho_v(E-qV,B)\left[f_n(E)-f_p(E)\right]dE_z. \tag{10}$$

We define in advance:

$$C = \frac{q}{\pi^3\hbar}\left(\frac{2m}{\hbar^2}\right)^3(\hbar\omega_c)^2. \tag{11}$$

Thus, the tunneling current can be written in a compact form as:

$$I_T(V,B) = C\sum_{n=0}^{N}\int_0^{E_{max}} \frac{\left[-\frac{4\sqrt{2m}}{3\hbar qF}\left(qV-E_z-\left(n+\frac{1}{2}\right)\hbar\omega_c\right)^{3/2}\right]}{\sqrt{\left(qV-E_z-\left(n+\frac{1}{2}\right)\hbar\omega_c\right)^{3/2}\left(E_z-\varepsilon_c^{(n)}\right)\left(E_z-\varepsilon_v^{(n)}-qV\right)}}\cdot\left[f_n(E_z)-f_p(E_z)\right]dE_z, \tag{12}$$

therein:

$$\varepsilon_{c,v}^{(n)} = \varepsilon_{c,v} + \left(n+\frac{1}{2}\right)\hbar\omega_c. \tag{13}$$

This enables a direct comparison of the tunnel diode characteristics $I(V,B)$and $R_d(V,B)$with experimental data. At the same time, under the influence of a magnetic field, the spacing between Landau levels increases, the density of states becomes discrete, the differential resistance region shifts, and the current undergoes oscillatory modulation.

The complete mathematically rigorous form of Eq. (5) under the influence of a magnetic field can be written as follows:

$$I(V,B) = \frac{q}{2\pi^2\hbar l_B^2}\sum_{n=0}^{N}\int_{-\infty}^{\infty} T_B(E_z)[f_n(E_z)-f_p(E_z)]\,dE_z, \tag{14}$$

here,

$$l_B = \sqrt{\frac{\hbar}{qB}}, \tag{15}$$

here, l_B −is the magnetic length, representing the “quantum radius” of the electron’s Landau orbit.

It determines the spatial extent of the wavefunction in the transverse direction and defines the minimal area in phase space corresponding to a single Landau level. In the presence of a magnetic field, electrons undergo classical circular (cyclotron) motion in the transverse plane. From a quantum mechanical perspective, however, the energy levels become discrete—a phenomenon theoretically established by Lev Landau (Landau quantization). Under a magnetic field, the energy space becomes discretized due to Landau quantization. Therefore, the three-dimensional energy integral transforms into a summation over transverse motion and an integral along the tunneling direction. In the weak magnetic field limit, the Landau levels become densely packed, the summation can be replaced by an integral, and the system returns to the classical continuous density of states. Using Eq. (12), the variation of the tunnel diode characteristics under a magnetic field is illustrated in Fig. 1. The theoretical results are compared with the corresponding experimental data reported in the literature [22]. As shown in Fig. 1, with increasing magnetic field induction, the peak value of the resonance in the current–voltage characteristics decreases. This behavior is explained by the increased separation between Landau levels due to stronger quantization and the exponential reduction of the tunneling probability. In the presence of a magnetic field, the transverse motion of electrons becomes quantized, and the number of accessible states decreases, which in turn leads to a reduction in the peak current.

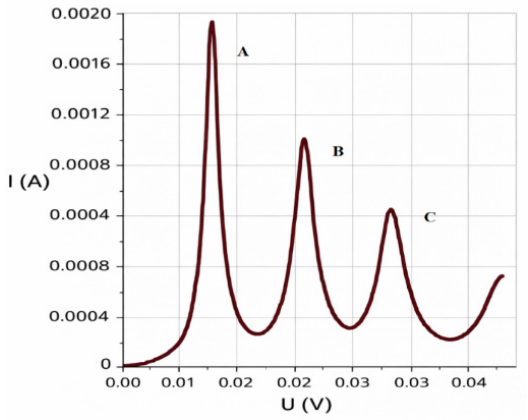

Figure 1. Dependence of the tunneling current on voltage under the influence of a magnetic field

The condition for the differential resistance of a tunnel diode is significantly influenced by the magnetic field, as the spacing between Landau levels increases and the density of states becomes discrete. Numerous experimental studies have investigated the dependence of the peak current on the magnetic field, particularly showing that at low temperatures, the resonance maxima appear sharper and narrower. As the temperature decreases, the Fermi–Dirac distribution function becomes steeper, the energy uncertainty is reduced, and the resonance conditions are satisfied more precisely. As a result, the peak current becomes sharper and its amplitude increases. Conversely, as the temperature increases, the energy distribution broadens, carriers participate over a wider energy range, inter-level transitions become more diffusive, and the resonance peaks broaden while their amplitude decreases.

In this work, the differential characteristic, namely:

$$R_d(V,B) = \left(\frac{\partial I}{\partial V}\right)^{-1}. \tag{16}$$

By substituting the tunneling current expression (12) into Eq. (16), an analytical form of the differential resistance was obtained. Based on the derived results, a three-dimensional distribution of $R_d(V,B)$in phase space was constructed. The dependence of the differential resistance on voltage and magnetic field is illustrated in Figures 2 and 3 in the form of three-dimensional graphs. In addition, the dependence of the differential resistance on voltage and temperature was analyzed while keeping the magnetic field constant. The spatial distribution of $R_d(V,T)$was constructed, revealing the broadening of the resonance region with increasing temperature and changes in the amplitude of the negative differential resistance.

The three-dimensional graphs clearly demonstrate that the differential resistance exhibits sharp variations near the resonance points, its extreme values decrease with increasing magnetic field, and the characteristics become more broadened as the temperature rises.

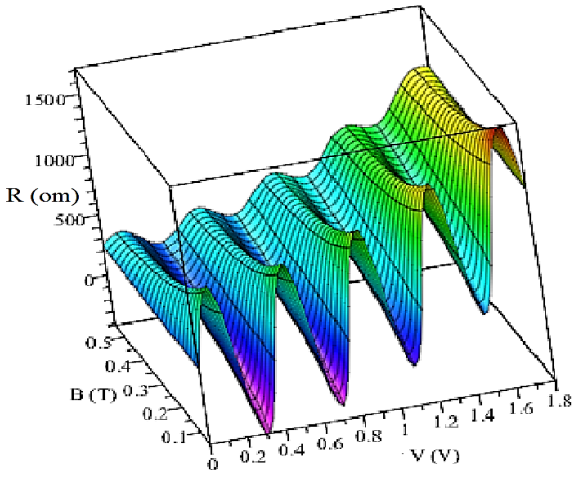

Figure 2. Three-dimensional representation of the differential resistance R_d in phase space, taking into account Landau levels under conditions of a variable magnetic field $B$and constant temperature T

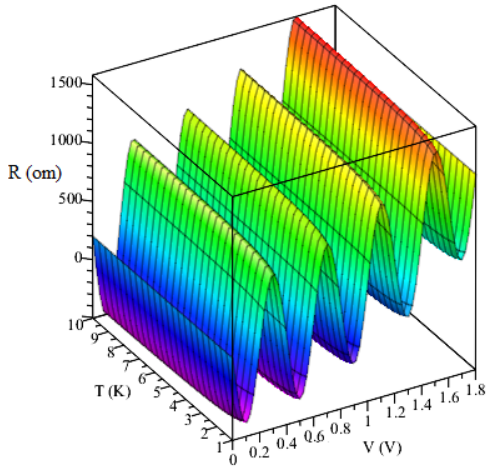

Figure 3. Three-dimensional representation of the differential resistance R_d −as a function of temperature T, considering Landau levels at a constant magnetic field $B = 0.3$ T

As the magnetic field increases, the tunneling transparency of the tunnel diode decreases because electrons are quantized into Landau states. This leads to a reduction in the maximum value of dI/dV, and the differential resistance $R_d(V,B)$increases at the resonance peaks. Consequently, the amplitude of the negative differential resistance (NDR) decreases, which is associated with the reduction of Landau degeneracy and the decrease in the density of quantum states. At low temperatures, the thermal energy of electrons is small; therefore, the tunneling process more accurately reflects the Landau quantized states. Under these conditions, the features of $R_d(V,T)$exhibit sharp and well-defined peaks, and the amplitude of the differential resistance is large. At higher temperatures, while keeping Bconstant, the thermal distribution of electrons broadens, and the Landau levels are thermally smeared. As a result, the peaks of $R_d(V,T)$decrease, and the amplitude of the negative differential resistance is reduced. Thus, the tunneling process is smoothed due to thermal dispersion, and the effects of Landau quantization become less pronounced. The magnetic field and temperature jointly control the tunneling transparency and the amplitude of the differential resistance. Low temperature and weak magnetic field conditions allow Landau quantization to be more clearly observed, whereas higher temperature or stronger magnetic field conditions smooth the resonance peaks and reduce the negative differential resistance. This analysis provides a theoretical and experimental basis for understanding the behavior of tunnel diodes and quantum electronic devices. Since a tunnel diode is based on a heavily doped p–n junction, electrons move within the crystal lattice. Therefore, electrons are not considered free particles in vacuum but rather quantum particles with an effective mass. In the absence of a magnetic field, the electron dispersion relation is given by:

$$E_z = \frac{h^2 k_z^2}{2m^*}, \tag{17}$$

here, m −is the effective mass of the electron. Thus, the model is defined as a three-dimensional degenerate electron gas with an effective mass in the presence of an external uniform magnetic field. Under a magnetic field, when **B** ∥ z, the electron motion becomes quantized in the transverse plane (Landau quantization), while the motion along the z-direction remains free. The orbital energy is given by:

$$E_n = \hbar\omega_c(n + \tfrac{1}{2}) \text{ , } \omega_c = \frac{qB}{m^*}. \tag{18}$$

The complete energy spectrum is given by:

$$E_{n,k_z} = \hbar\omega_c(n + \tfrac{1}{2}) + \frac{h^2 k_z^2}{2m^*}, . \tag{19}$$

This result indicates that the system effectively transitions into a (2D + 1D) structure. Each Landau level is highly degenerate. The number of states per unit area is given by:

$$\mathrm{g_L} = \frac{qB}{2\pi h}, \tag{20}$$

$\mathrm{g_L} \propto \mathrm{B}$ − the degeneracy is linearly proportional to the magnetic field. The density of states for each Landau level is obtained by considering the energy of each Landau level as:

$$E = E_n + \frac{h^2 k_z^2}{2m^*}. \tag{21}$$

One-dimensional density of states:

$$D_{1D}(E) = \frac{1}{\pi}\sqrt{\frac{m^*}{2\hbar^2}}\,\frac{1}{\sqrt{E - E_n}}. \tag{22}$$

Total three-dimensional density of states:

$$D(E,B) = \sum_{n=0}^{N_{max}} \frac{\theta(qV - E_n)}{\sqrt{qV - E_n + \varepsilon}}\,\frac{\theta(\mu_n + \mu_p - qV - E_n)}{\sqrt{\mu_n + \mu_p - qV - E_n + \varepsilon}}. \tag{23}$$

This expression describes the Landau singularities. The tunneling current model is formulated based on the Bardeen approach as follows [21]:

$$I(V,B) = \int_{-\infty}^{\infty} D_n(E,B) D_p(E - qV, B) T(E)\big[f_n(E) - f_p(E)\big]\, dE, \tag{24}$$

here, $D_n(E,B)$denotes the density of states on the electron side, $D_p(E - qV, B)$represents the density of states on the hole side, and $T(E,B)$is the tunneling transparency. The terms $f_n(E)$and $f_p(E)$ −are the Fermi–Dirac distribution functions. A tunnel diode consists of a heavily doped p–n junction, where electrons move within the crystal lattice. Therefore, electrons are not treated as free particles in vacuum but rather as quantum particles with an effective mass.

The transverse component is equivalent to a harmonic oscillator, and the energy levels are given by:

$$E_n = \hbar\omega_c(n + \tfrac{1}{2}), \quad \omega_c = \frac{qB}{m^*}. \tag{25}$$

The total energy available for tunneling is decomposed into transverse and longitudinal (tunneling) components as follows:

$$E = E_n + E_z. \tag{26}$$

The energy along the tunneling direction is given by:

$$E_z = E + \hbar\omega_c(n + \tfrac{1}{2}). \tag{27}$$

As the magnetic field increases, the energy available for tunneling decreases, leading to a reduction in the tunneling transparency $T(E)$. Considering the one-dimensional stationary Schrödinger equation, in quantum mechanics the particle energy is less than the height of the potential barrier:

$$\frac{d^2\psi}{dx^2} + \frac{2m^*}{\hbar^2}\big(E - V(x)\big)\psi = 0. \tag{28}$$

Inside the barrier, $E < \mathrm{q}V$:

$$\frac{d^2\psi}{dx^2} = \frac{2m^*}{\hbar^2}(\mathrm{q}V - E)\psi. \tag{29}$$

The solution has an exponential form:

$$\psi(x) \sim e^{-kx}, \tag{30}$$

here, $k = \frac{\sqrt{2m^*(qV-E)}}{\hbar}$

According to the WKB approximation, the tunneling probability is given by:

$$T(E,B) \approx exp[-2\int_{z_1}^{z_2}\sqrt{\frac{2m^*}{\hbar^2}(qV - E_z)}dz]. \tag{31}$$

For a rectangular barrier:

$$T(E,B) \approx exp[-2d\sqrt{\frac{2m^*}{\hbar^2}\left(qV - E + \hbar\frac{qB}{m^*}\left(n+\frac{1}{2}\right)\right)}. \tag{32}$$

By combining all the physical laws presented above, the tunneling current can be expressed as:

$$I(V,B,h\nu) = \sum_{n=0}^{N_{max}} \frac{\theta(qV - E_n)}{\sqrt{qV - E_n + \varepsilon}} \frac{\theta(\mu_n + \mu_p - qV - E_n)}{\sqrt{\mu_n + \mu_p - qV - E_n + \varepsilon}} \times$$

$$\times exp\left(-2d\sqrt{\frac{2m^*}{\hbar^2}(qV - E + \hbar\frac{qB}{m^*}(n+\frac{1}{2}))}\right)\left[\frac{\left(e^{\frac{\mu_n}{kT}}+1\right)\left(e^{-\frac{\mu_p}{kT}}+1\right)}{\left(e^{\frac{\mu_p - qV}{kT}}+1\right)\left(e^{\frac{qV-\mu_n}{kT}}+1\right)}\right]. \tag{33}$$

The dependence of the tunnel current on voltage under the combined influence of the UHF and magnetic fields is shown in Fig. 4.

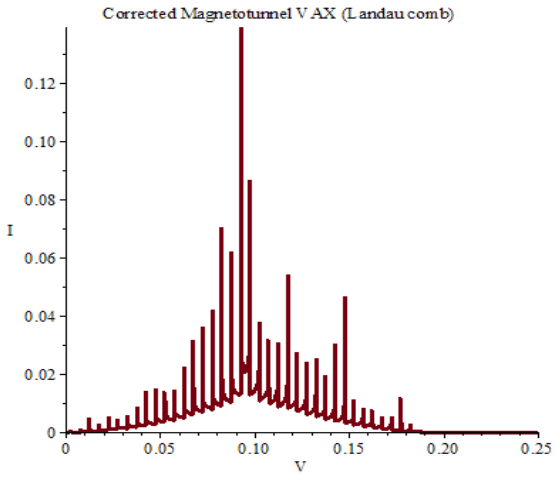

Figure 4. Dependence of the tunnel current on voltage under the influence of ultra-high frequency and a magnetic field

Now, let us derive the expression for the effect of light on a tunnel diode placed in a magnetic field. In this case, since the influence of the magnetic field on the density of states in the tunnel diode is strong, we neglect the filling of the density of states by electrons and holes generated under illumination. Instead, we take into account the broadening (or redistribution) of the density of states caused by the magnetic field.

$$D(E,B) = \frac{N_{max}}{\sum_{n=0}} \frac{\theta(qV-E_n)}{\sqrt{qV-E_n+\varepsilon}} \frac{\theta(\mu_n+\mu_p-qV-E_n)}{\sqrt{\mu_n+\mu_p-qV-E_n+\varepsilon}}. \tag{34}$$

Since we mainly associate tunnel transparency with electron motion, the transparency increases under magnetic influence. The reason for this is that since the density of states changes, it affects the thickness and height of the barrier, and the transparency becomes as follows:

$$T(E,B) \approx exp\left[-2d\sqrt{\frac{2m^*}{\hbar^2}(qV - E + \hbar\frac{qB}{m^*}(n+\frac{1}{2}))}\right]. \tag{35}$$

In these conditions, the only factor that cannot be dominated by the magnetic field is the Fermi–Dirac distribution function. Therefore, charge carriers flow from regions of higher distribution to lower distribution, and this flow gives rise to the distribution function in expression (36).

$$f_n - f_p = \frac{\left(e^{\frac{\mu_{n+\Delta\mu}}{kT}}+1\right)\left(e^{\frac{\mu_p}{kT}}+1\right)}{\left(e^{\frac{\mu_{n-qV}}{kT}}+1\right)\left(e^{\frac{qV-\mu_n-\Delta\mu}{kT}}+1\right)}. \tag{36}$$

This behavior mainly reflects quantities such as the effective lifetime of charge carriers generated under illumination and the absorption of light. It is observed that, initially, when light is absorbed in a semiconductor, a generation process occurs, leading to a shift in the chemical potentials. This shift persists until the recombination process begins. During recombination, the effective lifetimes of charge carriers decrease, which in turn leads to a reduction in the chemical potential.

As a result, the current–voltage (I–V) characteristic under the combined influence of light and a magnetic field can be expressed accordingly.

$$I(V,B,h\nu) = \sum_{n=0}^{N_{max}} \frac{\theta(qV-E_n)}{\sqrt{qV-E_n+\varepsilon}} \frac{\theta(\mu_n+\mu_p-qV-E_n)}{\sqrt{\mu_n+\mu_p-qV-E_n+\varepsilon}} \times$$

$$\times exp\left(-2d\sqrt{\frac{2m^*}{\hbar^2}(qV-E+\hbar\frac{eB}{m^*}(n+\frac{1}{2}))} \cdot \frac{\left(e^{\frac{\mu_{n+\Delta\mu}}{kT}}+1\right)\left(e^{-\frac{\mu_p}{kT}}+1\right)}{\left(e^{\frac{\mu_{p-qV}}{kT}}+1\right)\left(e^{\frac{qV-\mu_n-\Delta\mu}{kT}}+1\right)}\right). \tag{37}$$

The form of the volt-ampere characteristic of expression (37) above is shown in Fig. 5, which presents the corresponding tunnel current–voltage characteristics under illumination and different magnetic and UHF field conditions.

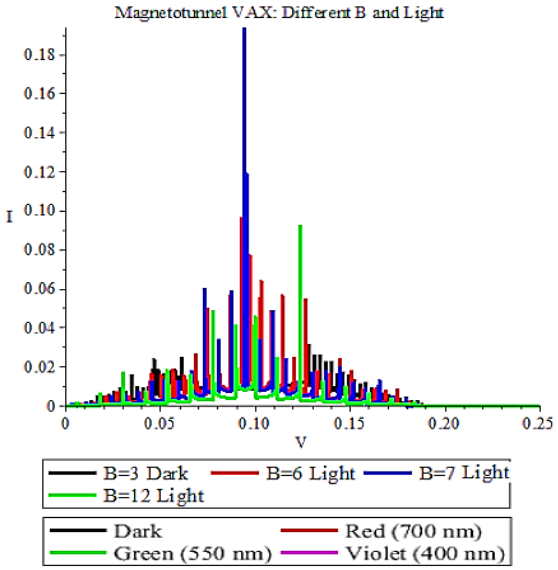

Figure 5. Dependence of the tunnel current on voltage under illumination at different values of magnetic field and ultra-high-frequency field

In this case, the magnetic field values are taken as $B = 3,6,7,12$, while the illumination corresponds to wavelengths of 700 nm, 550 nm, and 400 nm. As can be seen from the graph, the magnetic field quantizes (splits) the density of states into discrete energy levels; as a result, the tunnel current exhibits a comb-like structure.

Now, considering the differential resistance of the tunnel diode under the combined influence of both magnetic field and illumination, we obtain the following expression:

$$R_d(V,B,h\nu) = \left(\frac{dI}{dV}\right)^{-1}. \tag{38}$$

That is, by taking the derivative of the voltage with respect to the current, we obtain the differential resistance. A narrower potential barrier results in a higher transmission coefficient, thereby increasing the tunneling current.

$$\left(\frac{dI}{dV}\right)^{-1} = \sum_n^{\infty} G_n F\left[-\frac{1}{2(V-E_n)} + \frac{1}{2(\mu_n+\mu_p-qV-E_n)} + \frac{2dm^*}{h^2 k_n}\right] - \sum_n \frac{G_n}{kT}[f_n - f_p]. \tag{39}$$

If we introduce a tunnel diode into an ultrahigh-frequency field, the charge carriers are simultaneously exposed to the magnetic field and light. This changes the whole theory. In this case, the magnetic field is included in the density of states and transparency, and now we can see in expression (40) that the transparency changes shape due to the presence of an ultrahigh-frequency field.

$$I(V,B,h\nu)=\sum_{n=0}^{N_{max}}\frac{\theta(qV-E_n)}{\sqrt{qV-E_n+\varepsilon}}\frac{\theta(\mu_n+\mu_p-qV-E_n)}{\sqrt{\mu_n+\mu_p-qV-E_n+\varepsilon}}\times$$
$$\times exp\left(-2d\sqrt{\frac{2m^*}{\hbar^2}\left(V_z-qV_{ac}\cos(\omega t)+\hbar\frac{qB}{m^*}\left(n+\frac{1}{2}\right)\right)}\cdot\frac{\left(e^{\frac{\mu_{n+\Delta\mu}}{kT}}+1\right)\left(e^{-\frac{\mu_p}{kT}}+1\right)}{\left(e^{\frac{\mu_p-qV}{kT}}+1\right)\left(e^{\frac{qV-\mu_n-\Delta\mu}{kT}}+1\right)}\right) \quad (40)$$

We can reduce the above expression for the volt-ampere characteristic of the tunnel current under the influence of an ultra-high frequency (UHF) field, a magnetic field and light to expression (38). We combine it with the expression [23-25], which shows the dependence of the sound signal to noise ratio emitted by the tunnel diode on the tunnel current. Then we can see how the sound signal to noise ratio emitted by the tunnel diode changes in the light energy, UHF and magnetic field in Figures 6-7.

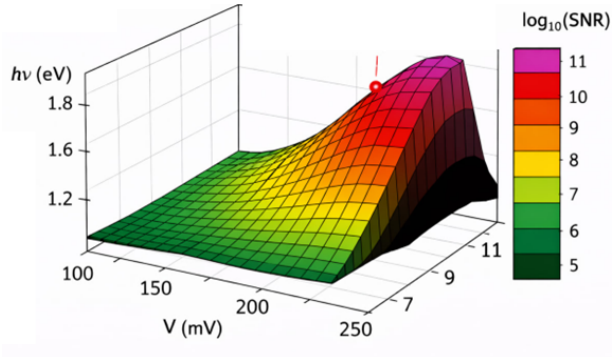

Figure 6. Dependence of the signal-to-noise ratio (SNR) on the differential resistance $R_d$and the photon energy $h\nu$in a tunnel diode

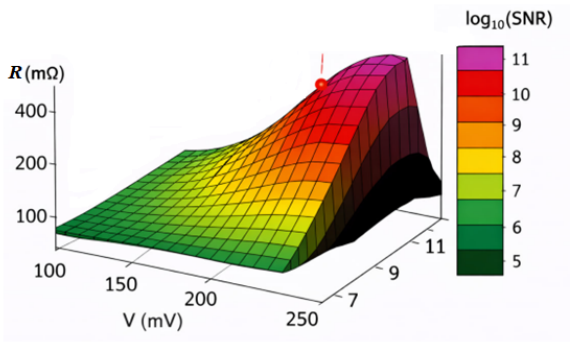

Figure 7. Dependence of the signal-to-noise ratio (SNR) on the photon field (ultra-high-frequency, UHF) and voltage (V)

This graph illustrates the dependence of the signal-to-noise ratio (SNR) on the differential resistance R_d −and the photon energy $h\nu$. A logarithmic scale ($\log_{10}$(SNR)) is used in the graph, so the SNR values start from 5 and reach a maximum point. The colors represent variations in the SNR: from green to red, the SNR increases. The red point indicates the maximum SNR value.

In the graph shown in Figure 7, the colors represent the variation of the SNR, while the red point indicates the maximum SNR value.

If we take into account the drift velocity of electrons in a p–n tunnel junction under an ultra-high-frequency (UHF) field, the following expression can be obtained:

$$\vartheta=\mu E_x. \quad (41)$$

In this expression, μ −denotes the electron mobility, and E_x −represents the electric field strength of the ultra-high-frequency (UHF) field.

Also, the force acting due to the ultra-high-frequency (UHF) field is given by:

$$F=qE_x \quad (42)$$

and the total power influenced by the ultra-high-frequency (UHF) field can be expressed as:

$$P_1=F\vartheta \quad (43)$$

Taking these expressions into account, the power in a p–n tunnel junction under the influence of an ultra-high-frequency (UHF) field can be written as follows:

$$\frac{P_1-P_0}{N}=F\vartheta \quad (44)$$

In this case, N −is the number of electrons, and P_0 −represents the excess fraction of the total power supplied to the diode by the UHF field that corresponds to the sample consumption. If we generalize the above expressions, the power consumed per electron in a p–n tunnel junction under the influence of a UHF field can be written as follows:

$$\frac{P_1-P_0}{N} = q\mu E_x^2 \tag{45}$$

From this expression, the electric field strength E_x −under the influence of the UHF field can be obtained as follows:

$$E_x = \sqrt{\frac{P_1-P_0}{Nq\mu}} \tag{46}$$

The transparency coefficient of the barrier under the influence of the UHF field is expressed as follows:

$$T = \exp\left(-\frac{\alpha E_g^{3/2}}{E+E_x}\right) = \exp\left(-\frac{\alpha E_g^{3/2}}{E+E_x}\right) \tag{47}$$

The dependence of the tunnel current in a tunnel diode on electric and magnetic fields can be summarized as follows:

An increase in the electric field E_x −enhances the probability of electron tunneling, thereby increasing the current. In contrast, a magnetic field Bleads to the formation of Landau quantized energy levels, effectively discretizing the motion of electrons into distinct energy states, which makes the current dependent on the magnetic field. Experimental results confirm that the direct tunneling current in semiconductors decreases under the influence of a strong magnetic field, in agreement with theoretical predictions. Since diffusive tunneling and reverse GaAs diodes were used, and these diodes are characterized by relatively weak electric fields and small effective mass in the p–n junction, a significant reduction in the tunneling current (by 50–65%) was observed. This wide range of variation (at temperatures of 80 K and 300 K) allowed a quantitative comparison between theoretical predictions [26, 27] and experimental data. The results show that the theory developed by Aronov and Pikus provides a good quantitative description of the variation of the tunneling current under a magnetic field. The values of the electric field in the p–n junction, calculated from equation (47), are in good agreement with independently obtained results. The influence of the magnetic field on the excess tunneling current was also observed and studied. The magnitude of this effect is much smaller compared to the direct tunneling region, which can be explained qualitatively based on the concepts developed in [23-25, 28]. If a simple relationship between the electric field and voltage in the p–n junction is assumed, then a satisfactory agreement between theoretical and experimental values of the magnetic field can be obtained in the low-temperature region for excess current. The authors express their gratitude to V. G. Veselago and A. M. Prokhorov for the opportunity to work with the “Solenoid” device, to V. S. Vavilov for collaboration and continuous interest in the work, to V. M. Ivanov and V. M. Karneev for assistance in the experiments, and to G. E. Pikus and A. G. Aronov for valuable discussions of the results. By combining expressions (46) and (47) and substituting the electric field vector Finto equation (40), a more compact expression describing the simultaneous influence of both UHF and magnetic fields on the tunnel current can be obtained. This allows us to visualize the three-dimensional behavior of the current as a function of variations in E_x −and B.

Using equation (40), the variation of the tunnel current under the influence of both the ultra-high-frequency field and the magnetic field is presented in Figure 8.

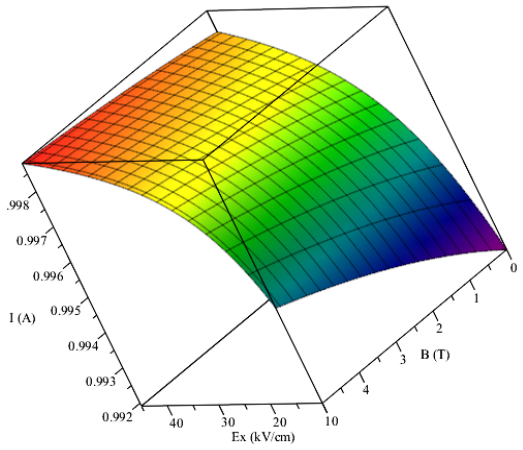

Figure 8. A 3D visualization of the current variation as a function of E_x −and B

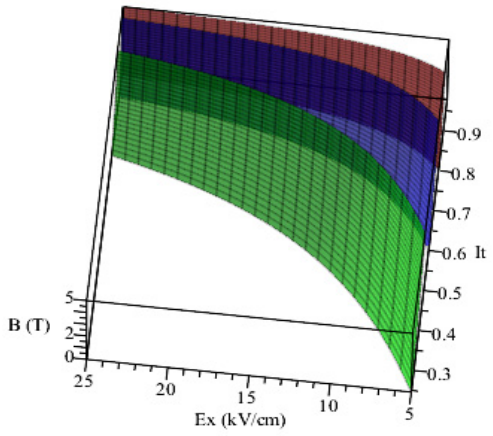

Figure 9. Tunneling current of GaAs-, AlGaAs-, and GaN-based tunnel diodes under the simultaneous influence of ultra-high-frequency and magnetic fields. GaAs—top, AlGaAs—middle, GaN—bottom

Figure 8 illustrates how the current increases from zero or decreases depending on different combinations of E_x −and B. Due to the formation of Landau levels, the step-like behavior of the current with respect to the magnetic field can be observed using the parameters listed in Table 1.

Table 1. Parameters of the semiconductor materials used in the fabrication of the tunnel diode

Parameter	GaAs	InGaAs	GaN
Breakdown field (MV/cm)	~0.4	~0.3	~3.3
Temperature stability	~200°C	~150°C	~600°C
Radiation resistance	Average	Low	Very high
μ_e (sm²/V·s)	~8500	~12000	~1000
(m_e^*/m_0)	0.067	0.12–0.15	0.041
(m_h^*/m_0)	0.45	~0.6	0.45

Using Figure 9 and the parameters given in Table 1, we can observe the three-dimensional spatial distribution of the tunneling current in GaAs-, AlGaAs-, and GaN-based tunnel diodes under the simultaneous influence of ultra-high-frequency and magnetic fields.

Compared to GaAs- and AlGaAs-based tunnel diodes, the tunneling current in GaN-based tunnel diodes is significantly lower. This is mainly due to the wide bandgap of GaN and the larger effective mass of electrons, which reduces the tunneling probability. As a result, GaN diodes exhibit lower maximum tunneling current, making them suitable for applications requiring high voltage and high energy. When light is incident on a semiconductor, electron–hole pairs are generated. This process disturbs the thermodynamic equilibrium of the system and leads to the formation of separate quasi-Fermi levels. As the light intensity increases, the carrier concentration rises, which in turn increases the tunneling current.

Under illumination, the change in electron concentration, $\Delta n(\Phi) -$ is often expressed in a simplified form as

$$\Delta n(\Phi) = \alpha \Phi \tau,$$

where, $\alpha -$is the absorption coefficient, $\Phi -$is the photon flux, and $\tau -$is the carrier lifetime. However, this expression represents only a simplified physical model and is not sufficient for dissertation-level analysis.

In direct bandgap semiconductors such as GaAs, the generation of electron–hole pairs and their recombination mechanisms are more complex. Therefore, a more physically rigorous formulation of $\Delta n(\Phi) -$is required.

Under illumination, both generation and recombination processes occur in a semiconductor. In a steady-state condition, the generation rate equals the recombination rate: $G = R,$ where $G -$is the generation rate of electron–hole pairs due to illumination, and $R -$is the recombination rate. For GaAs, taking into account the light spectrum, the generation rate can be expressed as follows:

$$G(\hbar\omega) = \alpha(\hbar\omega)\, \Phi \tag{48}$$

here, $\alpha(\hbar\omega) -$is the optical absorption coefficient, $\Phi -$is the photon flux, and $\hbar\omega -$is the photon energy. For GaAs, the absorption coefficient depends on the photon energy and begins at the bandgap energy $E_g \approx 1.42$ eV (at 300 K).

The recombination process includes three main mechanisms:

- Shockley–Read–Hall (SRH) recombination: occurs at low energy levels, mainly through defects.
- Radiative recombination: electron–hole pairs recombine with the emission of light.
- Auger recombination: occurs at high carrier concentrations and involves energy transfer between carriers.

The total recombination rate can be expressed as follows

$$R = An + Bn^2 + Cn^3 \tag{49}$$

here, A, B, and $C$are the corresponding recombination coefficients, and $n$is the electron concentration. Under steady-state conditions, when generation and recombination are equal, the increase in electron concentration due to illumination for GaAs, $\Delta n(\Phi)$, can be determined as follows:

$$\Delta n(\Phi, \hbar\omega) = \frac{\alpha_0(\hbar\omega - E_g)\, \Phi}{A + Bn_0 + Cn_0^2} \tag{50}$$

this formula:

- $\alpha_0(\hbar\omega - E_g)$— the spectral absorption coefficient of GaAs as a function of photon energy can be expressed as follows:
- n_0—concentration of doped electrons,
- A, B, C — the SRH, radiative, and Auger recombination coefficients, respectively, are:
- Φ — photon flux (photon/sm²·s),
- $E_g \approx 1.42$ eV, 300 K at

This model provides a physical basis for the influence of light intensity and photon energy on the tunneling current, and also allows one to determine the shift of the quasi-Fermi level. Under illumination, the quasi-Fermi level for electrons can be expressed as follows:

$$E_{Fn}(\Phi) = E_F + kT\ln\left(1 + \frac{\Delta n(\Phi,\hbar\omega)}{n_0}\right) \tag{51}$$

Using this, the tunneling current formula under illumination is modulated as follows:

$$I(B,F_\omega,\Phi) = \frac{q^2B}{2\pi^2\hbar^2}\sum_n \int T(E_n,k_z,F_\omega)\left[f_1\left(E,E_{Fn}(\Phi)\right) - f_2(E,E_{Fn}(\Phi) - qV)\right]dk_z \tag{52}$$

The resulting dependence of the tunneling current density on magnetic field strength and incident photon energy is presented in Fig. 10. Figure 11 shows the tunneling current as a function of the ultra-high-frequency (UHF) electric field strength and photon energy.

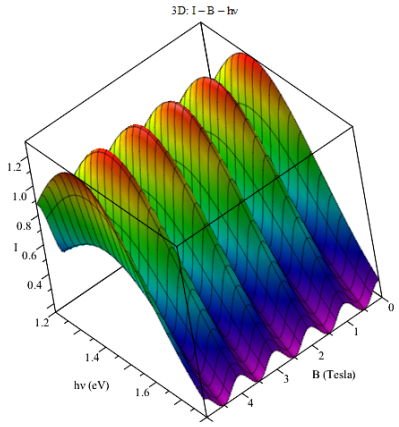

Figure 10. Dependence of the tunneling current density on magnetic field strength and incident photon energy-$h\nu$

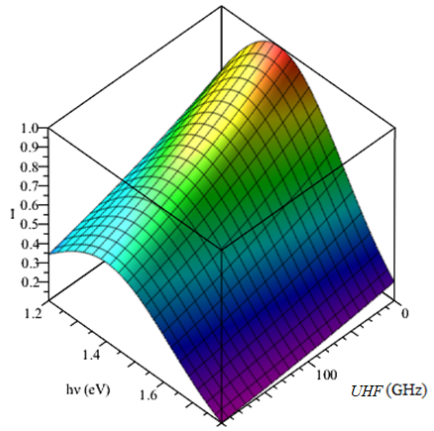

Figure 11. Three-dimensional surface of the tunnel current as a function of high-frequency (UHF) electric field and photon energy (I – UHF – hv)

As the magnetic field increases, the energy spectrum becomes discretized into Landau levels, causing the tunneling probability to exhibit an oscillatory behavior. When the photon energy $h\nu$ −approaches a resonance value, barrier tunneling is enhanced, and the maximum current is observed.

From the graph, it can be seen that as B −increases, quantum oscillations appear in the current, and in the resonance region of $h\nu$ −the tunneling current sharply increases. Magnetic quantization and optical excitation together modulate the current spectrum.

This graph shows the tunneling current as a function of the ultra-high-frequency (UHF) electric field strength and photon energy. The UHF field modulates the internal electric field, thereby changing the tunneling coefficient. As the field strength increases, the tunneling current becomes smoother and decreases (the dynamic barrier widening effect). As the photon energy approaches a resonance value, optical excitation modifies the Fermi–Dirac distribution, and the photocurrent contribution increases. Tunneling is one of the key quantum transport phenomena in semiconductors and was first observed in heavily doped p–n junctions. The tunneling diode effect was theoretically predicted by L. Esaki and later experimentally confirmed [1]. Subsequently, resonant tunneling in double-barrier quantum heterostructures was demonstrated, and the negative differential resistance (NDR) effect was identified. These works laid the foundation for the development of tunnel diodes and resonant tunneling diodes (RTDs). Heterostructures based on III–V semiconductors—such as Gallium Arsenide/Aluminum Gallium Arsenide, Indium Gallium Arsenide, and Gallium Nitride/Aluminum Nitride systems—are among the most promising materials for studying tunneling and quantum transport phenomena. This is mainly due to their band structure, small effective mass, and high electron mobility. GaAs/AlGaAs heterostructures have long been used in resonant tunneling and high-frequency quantum generators. In classical experiments by Chang and collaborators, clear resonant peaks were observed in GaAs/AlGaAs double-barrier structures. Due to the small effective mass of electrons in these structures, the tunneling probability is high, resulting in a strong NDR region and the possibility of terahertz-range generation. InGaAs-based heterostructures exhibit even higher tunneling current intensity due to their smaller effective mass and higher electron mobility. In InGaAs/InP systems, high-frequency generators and detectors operating above 100 GHz have been developed [29]. These structures also exhibit a strong photocurrent effect and operate efficiently in the infrared range. The formation of photocurrent is associated with the trapping and tunneling of photoexcited carriers in quantum wells. GaN/AlN heterostructures, on the other hand, are characterized by a wide bandgap and high electrical strength. These materials are known for their stability under high

voltage, high temperature, and strong radiation conditions [9]. In GaN-based structures, strong spontaneous and piezoelectric polarization creates significant internal electric fields, which strongly affect carrier transport in quantum wells. Although the tunneling probability is reduced due to the wide bandgap, GaN/AlN systems are highly promising for space applications and high-radiation environments. Under a magnetic field, Landau quantization of energy levels modulates the tunneling process. In systems with small effective mass such as GaAs and InGaAs, the cyclotron frequency is higher, making the magnetic field effect more pronounced. This leads to quantum oscillations and shifts in the tunneling current maxima [22]. In GaN, although this effect is also present, its modulation amplitude is smaller due to the larger effective mass. Temperature also significantly affects quantum transport. At low temperatures, scattering processes are reduced, and resonant tunneling becomes sharper. At higher temperatures, phonon scattering increases, which broadens the tunneling peaks. GaN/AlN systems can operate stably up to 500–600°C, while GaAs and InGaAs are typically effective in the 150–250 °C range. From the radiation resistance perspective, wide-bandgap GaN/AlN structures have a clear advantage. They are more resistant to cosmic radiation and high-energy particles [30-33]. GaAs-based devices are also widely used in space solar cells [29, 34], but they are more prone to defect formation under radiation. Thus, GaAs/AlGaAs and InGaAs systems are suitable for high-speed quantum and tunneling devices, while GaN/AlN is more promising for high-durability electronics operating under extreme conditions. Their behavior under photocurrent, magnetic fields, high-frequency fields, and across a wide temperature range remains one of the key research directions in tunneling and quantum transport theory.

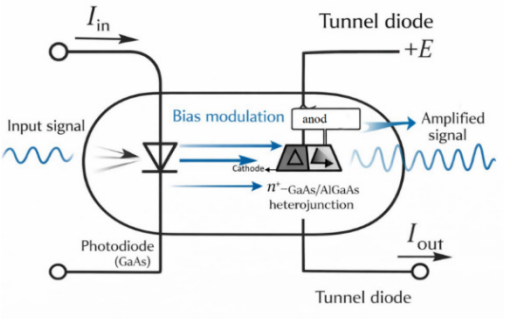

Figure 12. Dependence of tunneling in an n^+-GaAs/AlGaAs heterostructure on light intensity and applied voltage

This study proposes an optically controlled tunneling device based on an n^+–GaAs/AlGaAs tunnel heterostructure. The device operates based on the principle of quasi-Fermi level shift (Δμ) induced by light. The shift in quasi-Fermi levels changes the tunneling window, making the current–voltage (I–V) characteristics sensitive to light intensity. Unlike conventional tunnel diodes, the proposed structure utilizes the band offset of the heterojunction, improving tunneling efficiency and controllability (Figure 12).

Unlike resonant tunneling diodes, the structure does not rely on complex quantum levels, making the fabrication process simpler and more reliable. When light is incident, additional charge carriers are generated in the semiconductor, disturbing equilibrium and causing a separation between quasi-Fermi levels. This additional chemical potential dynamically modulates the tunneling conditions, making the tunneling current dependent not only on voltage but also on light intensity.

Theoretical models qualitatively confirm the optical modulation of the shift in the I–V characteristics and the negative differential resistance (NDR) region. Currently, GaAs/AlGaAs systems are widely used as a key material platform for high-frequency and sub-THz range space electronics. They are distinguished by high electron mobility, short relaxation times, and strong resistance to space radiation, making them highly attractive for aerospace and optoelectronic applications. At the same time, InGaAs systems are suitable for high-speed quantum and tunneling devices, whereas GaN/AlN systems are promising for robust electronics operating under extreme conditions. The behavior of these systems under photocurrent, magnetic fields, high-frequency fields, and wide temperature ranges remains one of the most relevant research directions in the framework of tunneling and quantum transport theory. Thus, optically controlled GaAs/AlGaAs tunnel heterostructures dynamically modulate tunneling through shifts in quasi-Fermi levels, enabling high-frequency operation approaching the sub-THz range. This approach is considered a promising technological solution for space electronics and high-frequency optoelectronic systems. The performance characteristics of tunnel diodes under illumination have been analyzed. It is shown that the superposition of tunnel current and photocurrent leads to a pronounced sensitivity of the I–V characteristics to light intensity, along with a smoothing of the NDR region. Furthermore, analysis based on the Fano factor and shot noise demonstrates that a high signal-to-noise ratio (SNR) is maintained, ensuring stable operation under radiation exposure, temperature variations, and external fields. Within the NASA concept framework, an optically controlled tunnel heterojunction device based on the n^+–GaAs/AlGaAs material system is proposed. In this device, tunneling is dynamically modulated through shifts in the quasi-Fermi levels (Δμ). This approach ensures high-frequency response in the sub-THz range, low noise performance, and radiation hardness, confirming its practical significance for space electronics. The results scientifically substantiate the potential application of resonant tunneling diodes (RTDs) in aerospace systems, high-speed optoelectronic switches, and radiation-resistant sensors.

CONCLUSIONS

This work presents a comprehensive theoretical investigation of tunneling current, differential resistance, and noise characteristics in tunnel diodes under the combined influence of magnetic, optical, and high-frequency electromagnetic fields. Based on the Tsu–Esaki formalism, WKB approximation, and Landau quantization, a unified multi-field model for n^+–GaAs/AlGaAs heterostructures has been developed. The results demonstrate that magnetic fields lead to Landau level formation, causing quantization of the energy spectrum and oscillatory modulation of the tunneling current, accompanied by a reduction in peak current and a shift of the negative differential resistance (NDR) region. Optical excitation induces quasi-Fermi level splitting, enhances carrier concentration, and increases tunneling current while smoothing the NDR characteristics. High-frequency electromagnetic fields dynamically modify the barrier transparency, further influencing the transport properties. It is shown that the interplay of these external fields enables effective control of tunneling dynamics, differential resistance, and device performance. Despite external perturbations, the noise analysis based on shot noise and the Fano factor confirms that a high signal-to-noise ratio (SNR) can be maintained.The proposed model provides a solid theoretical framework for designing low-noise, high-speed tunnel devices operating in the sub-terahertz range. The obtained results indicate strong potential for applications in advanced optoelectronic systems, high-frequency nanoelectronics, and radiation-resistant space technologies.

ORCID

M.G. Dadamirzaev, https://orcid.org/0000-0001-8258-4617; **M.K. Uktamova,** https://orcid.org/0009-0005-7562-2677
N.A. Sattarov, https://orcid.org/0009-0005-0506-0269; **S. Ruziboyev,** https://orcid.org/0009-0005-3176-3515
A.I. Khudayberdieva, https://orcid.org/0009-0005-7163-059X

REFERENCES

[1] S.M. Sze, Y. Li, and K.K. Ng, *Physics of Semiconductor Devices*, 4th Edition, (Wiley, 2021).
[2] B.M. Ali, A.A. Abdulazez, G.P. Priya, S. Ray, A. Pal, R. Sharma, S. Usanov, *et al*., "Modification of graphenylene nanostructure as a promising material for adsorption and sensing of 5-fluorouracil," First-principles investigations. Journal of Molecular Graphics and Modelling, **142**, 109210 (2026). https://doi.org/10.1016/j.jmgm.2025.109210
[3] Z.T. Azamatov, Sh.B. Utamuradova, M.A. Yuldoshev, and N.N. Bazarbaev. "Some properties of semiconductor-ferroelectric structures," East Eur. J. Phys. (2), 187-190. (2023), https://doi.org/10.26565/2312-4334-2023-2-19
[4] M.S. Kukurudziak, V.M. Lipka, and V.V. Ryukhtin, "Silicon p-i-n Mesa-Photodiode Technology, East Eur. J. Phys. (3), 385 (2024). https://doi.org/10.26565/2312-4334-2024-3-47
[5] J.R. Yusupov, M. Ehrhardt, Kh.Sh. Matyokubov, and D.U. Matrasulov, "Driven transparent quantum graphs," Physica Scripta, **100**(7), (2025). https://doi.org/10.1088/1402-4896/ade014
[6] M.A. Yuldoshev, Z.T. Azamatov, A.B. Bakhromov, and M.R. Bekchanova, "Investigation of Morphological and Optical Properties of LiNbO3 and LiNbO3:Fe 0.03 wt.% Crystals," East Eur. J. Phys. (4), 250 (2024). https://doi.org/10.26565/2312-4334-2024-4-25
[7] S. Rakhmanov, K. Matchonov, H. Yusupov, K. Nasriddinov, and D. Matrasulov, "Optical high harmonic generation in Dirac materials," Eur. Phys. J. B, **98**, 35 (2025). https://doi.org/10.1140/epjb/s10051-025-00885-7
[8] L. Esaki, "New Phenomenon in Narrow Germanium p–n Junctions," Phys. Rev. **109**, 603–604 (1958). https://doi.org/10.1103/PhysRev.109.603
[9] E.O. Kane, "Theory of tunneling," J. Appl. Phys. **32**, 83–91 (1961). https://doi.org/10.1063/1.1735965
[10] R.Tsu, and L. Esaki, "Tunneling in a Finite Super lattice," Appl. Phys. Lett. **22**, 562–564 (1973). https://doi.org/10.1063/1.1654509
[11] L.L. Chang, L. Esaki, and R. Tsu, "Resonant tunneling in semiconductor double barriers," Appl. Phys. Lett. **24**, 593–595 (1974). https://doi.org/10.1063/1.1655067
[12] Sh.B. Utamuradova, F.A. Giyasova, K.N. Bakhronov, M.A. Yuldoshev, M.R. Bekchanova, and B. Ismatov. Current Transfer Mechanism in A Thin-Based Heterosystem Based on A^2B^6 Compounds. East Eur. J. Phys. (2025), (3), 325 https://doi.org/10.26565/2312-4334-2025-3-31
[13] U.K. Mishra, P. Parikh, and Y. Wu, "AlGaN/GaN HEMTs-An overview," Proc. IEEE, **90**, 1022 (2002). https://doi.org/10.1109/JPROC.2002.1021567
[14] F.A. Giyasova, A.Z. Rakhmatov, Kh.N. Bakhronov, M.A. Yuldoshev, F.A. Giyasov, A.N. Olimov, and N.A. Sattarov, "Physical Principles of Photocurrent Generation in a Silicon-Based Photodiode Structure with a Schottky Barrier," East Eur. J. Phys. (4), 397 (2025). https://doi.org/10.26565/2312-4334-2025-4-38
[15] L.D. Landau, "Diamagnetism of Metals," Z. Phys. **64**, 629–637 (1930). https://doi.org/10.1007/BF01397213
[16] T. Ando, A.B. Fowler, and F. Stern, "Electronic properties of two-dimensional systems," Rev. Mod. Phys. **54**, 437 (1982). https://doi.org/10.1103/RevModPhys.54.437
[17] A.G. Aronov, and G.E. Pikus, "Magnetic field effects on tunneling," Sov. Phys. Semicond. **10**, 698 (1976). https://doi.org/10.1134/1.1184124
[18] C.H. Henry, "Theory of optical absorption," Phys. Rev. B, **29**, 1619 (1984). https://doi.org/10.1103/PhysRevB.29.1619
[19] L.V. Keldysh, "The effect of a strong electric field on the optical properties of semiconductors," Sov. Phys. JETP, **33**, 994 (1961). https://doi.org/10.1016/0038-1098(65)90052-2
[20] Y. Cao, *et al.,* "Highly repeatable room temperature negative differential resistance from GaN/AlN resonant tunneling diodes," J. Appl. Phys. **120**, 094503 (2016). https://doi.org/10.1063/1.4961442
[21] D.A. Ryndyk, *Theory of Quantum Transport at Nanoscale*, (*S*pringer, 2016). https://doi.org/10.1007/978-3-319-24088-6

[22] E.E. Vdovin, Yu.N. Khanin, O. Makarovsky, Yu.V. Dubrovskii, *et.al.,* "Magnetoanisotropy of electron-correlation-enhanced tunneling through a quantum dot," Physical Review B, 75(11). (2007). https://doi.org/10.1103/physrevb.75.115315
[23] S. Datta, "Quantum Transport: Atom to Transistor," (Cambridge University Press, 2005). https://doi.org/10.1017/CBO9780511805772
[24] M.K. Uktamova, and Sh. Mamadaliev, "Three-dimensional modeling of the relationship between static tunneling and the optical absorption coefficient in tunnel diodes," Results in optics, **22**, 100950 (2026). https://doi.org/10.1016/j.rio.2025.100950
[25] M.G. Dadamirzaev, M.K. Uktamova, Sh. Rakhmanova, and G.A. Ibadullayev, "Simulation of tunnel diode I-V Characteristics with photocurrent and phonon-assisted processes," East Eur. J. Phys. (4), 675-681 (2025). https://periodicals.karazin.ua/eejp/index
[26] M.G. Dadamirzaev, M.K. Uktamova, S.R. Boydedayev, M.A. Yuldoshev, and S.H. Mamadaliev. Theoretical Analysis of Photon-Energy-Controlled Quantum Tunneling Mechanisms Based on the Landauer–Büttiker Formalism. Physics AUC, **35**, 76 (2025). https://share.google/EqKveBzVq9UCc2Ndc
[27] S. Suzuki, *et al.,* "Terahertz oscillation of resonant tunneling diodes," Appl. Phys. Express, 3 064501. (2010). https://doi.org/10.1143/APEX.3.064501
[28] G. Gulyamov, M.G. Dadamirzaev, M.K. Uktamova, and B.Z. Mislidinov, "The effect of a heated electron on the VAX of a tunnel diode," AIP Conference Proceedings 2700, 050007 (2023).
[29] R. Stratton, "Theory of field emission from semiconductors," Phys. Rev. 126 pp. 2002–2014. (1962). https://doi.org/10.1103/PhysRev.126.2002
[30] Sh.I. Nabiyev, K. Bozorov, A. Nasritdinov, R. Ikramov, M. Yuldoshev, N. Sattarov, U. Edilboyev, S. Adilkhan, *et al.,* "Study of the Formation of Radiation Defects in Irradiated Silicon Samples, Doped with Chromium Atoms," East Eur. J. Phys. (1), 228 (2026). https://doi.org/10.26565/2312-4334-2026-1-24
[31] F.A. Giyasova, and M.A. Yuldoshev, "Investigation of temporal characteristics of photosensitive heterostructures based on gallium arsenide and silicon," Chalcogenide Letters, **22**(2), 123–129 (2025). https://doi.org/10.15251/CL.2025.222.123
[32] F.A. Giyasova, K. Bakhronov, M.A. Yuldoshev, M. A., Sapaev, I. B., Ikramov, R. G., Giyasov, F. A., Bekchanova, M. R., *et al.,* "Study of the influence of temperature on the transitions of the CdS/Si/CdTe heterosyste," East Eur. J. Phys. (4), 461 (2025). https://doi.org/10.26565/2312-4334-2025-4-47
[33] M. Asada, and S. Suzuki, "Terahertz Emitter Using Resonant-Tunneling Diode and Applications," Sensors, **21**(4), 1384 (2021). https://doi.org/10.3390/s21041384
[34] M.S. Paizullakhanov, F.A. Giyasova, Kh.N. Bakhronov, M.A. Yuldoshev, A.A. Mamadaliev, F.A. Giyasov, F.T. Akbarova, *et al*., "Investigation of the Processes Involved in the Formation of Pyroxene Materials during Solar Melting in a Large Solar Furnace," Journal of Ovonic Research. **22**(1), (2026). https://doi.org/10.15251/JOR.2026.221.51

БАГАТОПОЛЬОВА МОДУЛЯЦІЯ ТУНЕЛЬНОГО СТРУМУ, ДИФЕРЕНЦІАЛЬНОГО ОПОРУ ТА ШУМУ В ТУНЕЛЬНИХ ДІОДАХ n^+–GaAs/AlGaAs

Мухаммаджон Г. Дадамірзаєв[1], Мунірахон К. Уктамова[1,2], Носірбек А. Саттаров[3], Собір Рузібоєв[4], Арофат І. Худайбердієва[5]

[1]Наманганський державний технічний університет, Наманган, Узбекистан
[2]Університет бізнесу та науки, Узбекистан
[3]Міжнародний університет Кімьо в Ташкенті, Узбекистан
[4]Ташкентський інститут інженерів іригації та механізації сільського господарства, Національний дослідницький університет, Узбекистан
[5]Ташкентський хіміко-технологічний інститут (TXTI)

У цій роботі представлено теоретичне дослідження диференціального опору та шуму в тунельних діодах під дією комбінованих оптичних, магнітних та високочастотних електромагнітних полів. Тунельний струм моделюється за допомогою підходу Цу-Есакі з наближенням ВКБ, тоді як ефекти магнітного поля вводяться за допомогою квантування Ландау. Оптичне збудження призводить до квазі-розщеплення рівнів Фермі та посилює тунельний струм, що призводить до модуляції та згладжування області негативного диференціального опору (НДО). Високочастотні поля додатково змінюють прозорість бар'єру, впливаючи на динамічну поведінку пристрою. Аналіз шуму на основі дробового шуму та фактора Фано показує, що високе відношення сигнал/шум (SNR) може підтримуватися при зовнішніх збуреннях. Запропоновано узагальнену багатопольову модель для гетероструктур n^+–GaAs/AlGaAs, яка демонструє керовану динаміку тунелювання, низький рівень шуму та стабільну роботу в субтерагерцовому діапазоні. Результати вказують на значний потенціал для застосування у високошвидкісній оптоелектроніці та радіаційно-стійкій космічній електроніці.

Ключові слова: *тунельний діод; негативний диференціальний опір; модель Цу-Есакі; наближення ВКБ; квантування Ландау; дробовий шум; гетероструктура GaAs/AlGaAs; квазірівень Фермі; високочастотні поля; оптичне збудження; ефекти магнітного поля*

East European Journal of Physics. 3. 564-574 (2026)
DOI:10.26565/2312-4334-2026-3-51 ISSN 2312-4334

TEMPERATURE-DRIVEN PHASE EVOLUTION AND LATTICE STRAIN DYNAMICS DURING Ga–Sb CO-DIFFUSION IN SINGLE-CRYSTAL SILICON

Bobir O. Isakov*, Khalmurat M. Iliev, Kutub S. Ayupov, Bakhram A. Abdurakhmanov, Giyosiddin A. Kushiev, Abdujalol A. Sattorov, Zafar B. Khudoynazarov
Tashkent State Technical University, University St., 2, 100095, Tashkent, Uzbekistan
Corresponding Author e-mail: bobir6422isakov@gmail.com
Received June 6, 2026; revised July 27, 2026; in final form August 13, 2026; accepted August 26, 2026

This study examines the effect of annealing temperature on the microstructure and lattice dynamics of single-crystal silicon co-diffused with gallium and antimony. Samples were annealed in the 1000–1250°C range for a fixed duration of 10 h and analyzed by SEM imaging, EDS elemental mapping, and Raman spectroscopy. With increasing temperature, the samples show four successive microstructural states: (I) sparse Ga-rich clustering at 1000°C, (II) formation of large GaSb droplets (25–60 μm) at 1100°C, (III) refinement into smaller, faceted precipitates (~5 μm) at 1200°C, and (IV) substantial re-dissolution of the secondary phase, leaving only residual domains of ~1.5 μm, at 1250°C. Raman measurements of the Si optical phonon track this sequence: a small tensile shift (~518–519 cm^{-1}) at 1000 °C, a return to the unstrained position (~520 cm^{-1}) at 1100°C when GaSb droplets accommodate most of the lattice mismatch, and increasing compressive shifts (524–525 cm^{-1}, corresponding to ~0.6% strain) at 1200–1250°C as the GaSb phase redissolves into the matrix. Phonon-confinement analysis of the Raman linewidth further indicates crystalline coherence lengths of 3–5 nm within the micrometer-scale precipitates. Taken together, these results indicate that annealing temperature governs a reproducible sequence of clustering, droplet segregation, precipitate refinement, and re-homogenization in the Ga–Sb–Si system, and that this sequence can be tracked quantitatively through the correlated SEM/EDS and Raman signatures reported here.
Keywords: *Diffusion; Segregation; Nanocrystalline; Precipitation; Lattice strain; Phase separation*

1. INTRODUCTION

Thermally activated diffusion in silicon constitutes a foundational mechanism in semiconductor device fabrication, enabling dopant activation, junction formation, and heterostructure integration [1-3]. While single-species diffusion is well described by Fickian transport and point-defect mediation [4], multicomponent diffusion introduces additional complexity due to competing thermodynamic and kinetic driving forces, defect interactions, and solute–solute coupling effects [5, 6]. In systems where diffusing species possess mutual chemical affinity and limited solid solubility, diffusion may trigger phase segregation, nanoscale precipitation, interfacial strain generation, and re-equilibration processes governed by temperature-dependent free-energy landscapes [7-9].

The Ga–Sb–Si ternary system represents a prototypical compound-forming diffusion platform. Gallium (Group III) and antimony (Group V) are individually established dopants in silicon technology [10]; however, their simultaneous introduction at elevated temperature can promote GaSb compound formation due to chemical affinity and lattice incompatibility with the Si host matrix [11, 12]. GaSb itself is a narrow-bandgap III–V semiconductor with infrared optoelectronic relevance, making its controlled integration within silicon technologically attractive for monolithic optoelectronic platforms [13, 14].

From a thermodynamic perspective, phase stability is governed by minimization of total Gibbs free energy:

$$\Delta G=\Delta Gv+\gamma A \tag{1}$$

where ΔG is the total change in Gibbs free energy accompanying precipitate formation, ΔG_v is the volumetric (bulk) free-energy term that drives precipitation, γ is the interfacial energy per unit area, and A is the surface area of the forming precipitate.

Precipitation is thermodynamically favorable only when the volumetric term ΔG_v outweighs the interfacial-energy penalty γA [15]. Because temperature modulates diffusion coefficients, solid solubility limits, and the balance between these two terms, it can drive transitions between metastable supersaturation, compound segregation, precipitation refinement, and re-homogenization [16]. In compound-forming systems, nucleation kinetics and strain-driven morphological evolution further influence nanostructure stability [15].

Raman spectroscopy provides a powerful nondestructive probe of strain, phonon confinement, and compositional evolution in semiconductor systems [17–19]. Phonon confinement effects in nanocrystals lead to asymmetric peak broadening and redshift, enabling extraction of crystallite size and strain distribution [18, 19].

A temperature-dependent structural–vibrational correlation for the Ga–Sb–Si system has not yet been established in the literature. The purpose of this work is to study the effect of annealing temperature on the structure of silicon

Cite as: B.O. Isakov, Kh.M. Iliev, K.S. Ayupov, B.A. Abdurakhmanov, G.A. Kushiev, A.A. Sattorov, Z.B. Khudoynazarov, East Eur. J. Phys. 3, 564 (2026), https://doi.org/10.26565/2312-4334-2026-3-51

diffusion-doped with both gallium and antimony. To this end, we investigate Ga–Sb co-diffusion in silicon across 1000–1250°C and identify the resulting transformation sequence:

- Supersaturation-induced clustering (1000°C),
- Droplet-mediated GaSb segregation (1100°C),
- Diffusion-controlled nanocrystalline precipitation (1200°C),
- Re-homogenization and matrix recovery (1250°C).

By correlating SEM/EDS microstructural evolution with Raman-based strain quantification and phonon confinement modeling, we establish a predictive thermodynamic–kinetic model describing phase stability transitions in this compound-forming diffusion system.

2. MATERIALS AND METHODS

To elucidate the thermodynamic–kinetic transformation pathway proposed in the Introduction, a systematic temperature-resolved experimental framework was designed. The methodology was structured to isolate temperature as the primary control parameter governing Ga–Sb phase evolution in silicon, while maintaining constant diffusion duration and comparable boundary conditions. This approach enables direct correlation between diffusion kinetics, phase stability, and vibrational signatures.

2.1. Substrate Selection and Surface Preparation

Single-crystalline Si wafers with (100) orientation were selected due to their technological relevance and well-characterized diffusion behavior. The (100) surface provides predictable point-defect dynamics and stable crystallographic reference for strain analysis, particularly in Raman measurements [20, 21].

To ensure that phase evolution originated solely from thermally activated Ga–Sb diffusion rather than surface contamination or oxide-mediated reactions, the wafers were subjected to a standard RCA cleaning protocol [22]. The process consisted of:

- SC-1 treatment (NH_4OH–H_2O_2–H_2O) for organic removal,
- Dilute HF dip (1–2%) to remove native SiO_2,
- SC-2 treatment (HCl–H_2O_2–H_2O) for metallic impurity elimination.

Such preparation is essential because residual oxides or metallic contaminants can alter interfacial energy and modify diffusion pathways, thereby affecting phase nucleation behavior [23].

2.2. Temperature-Controlled Co-Diffusion of Ga and Sb

Simultaneous diffusion of Ga and Sb was performed in a high-temperature quartz tube furnace under controlled ambient conditions. The diffusion duration was fixed at 10 hours to ensure sufficient atomic redistribution while allowing temperature-dependent phase transitions to manifest distinctly.

Four annealing temperatures were selected:

- 1000°C (Group I),
- 1100°C (Group II),
- 1200°C (Group III),
- 1250°C (Group IV).

The chosen temperature window spans regimes where diffusion kinetics, solid solubility, and compound stability are expected to vary significantly according to Arrhenius behavior:

$$D = D_0 \exp\left(-E_a / kT\right). \tag{2}$$

Here D is the diffusion coefficient, D_0 is the pre-exponential (attempt-frequency) factor, E_a is the activation energy for Ga–Sb diffusion in silicon, k_β is the Boltzmann constant, and T is the absolute annealing temperature. This design allows the system to traverse multiple thermodynamic states—from supersaturation to segregation and re-equilibration—while holding diffusion time constant.

At lower temperature (1000°C), limited atomic mobility favors metastable supersaturation and localized clustering. Increasing temperature enhances vacancy-mediated Ga diffusion and substitutional Sb incorporation [24-27], potentially enabling compound formation and droplet segregation. At the highest temperature (1250°C), increased solid solubility may promote partial re-dissolution of secondary phases, restoring matrix homogeneity [28].

Temperature was monitored with calibrated thermocouples (±2°C accuracy) to minimize thermal gradient effects.

2.3. Microstructural Characterization (SEM)

To track morphological evolution across transformation regimes, field-emission scanning electron microscopy (FE-SEM–JEOL JSM-IT200) was employed. Accelerating voltages between 5 and 15 kV were used to balance surface sensitivity and compositional contrast.

Backscattered electron (BSE) imaging was particularly important for identifying Ga–Sb-rich precipitates due to atomic number contrast enhancement [29]. This technique allows direct visualization of droplet-mediated segregation predicted by the thermodynamic model introduced earlier.

The SEM analysis focused on:

- Precipitate morphology,
- Droplet diameter distribution,
- Surface roughness variation,
- Transition from localized clusters to homogenized matrix.

Spatial resolution was approximately 5 nm under optimized conditions.

2.4. Elemental Mapping (EDS)

Energy-dispersive X-ray spectroscopy (EDS) was integrated with SEM to determine spatial distribution of Ga and Sb.

Elemental mapping enabled:

- Verification of Ga–Sb co-segregation,
- Identification of Ga-rich versus Sb-rich domains,
- Assessment of elemental homogenization at elevated temperature.

Quantitative compositional analysis was performed using ZAF correction procedures to compensate for atomic number, absorption, and fluorescence effects [30]. The correlation between morphological features and elemental concentration provided direct validation of phase segregation or re-dissolution mechanisms.

2.5. Raman Spectroscopy and Vibrational Analysis

To probe lattice dynamics and phase-specific vibrational modes, micro-Raman spectroscopy was performed at room temperature using a 532 nm excitation laser. The spectral range (100–1200 cm^{-1}) captured:

- GaSb TO phonon (~223 cm^{-1}),
- Si optical phonon (~520 cm^{-1}),
- Si–O–Si vibrational modes (~900–1050 cm^{-1}).

Laser power was kept below 5 mW to avoid local heating and peak shift artifacts.

Raman spectroscopy serves a dual purpose in this study:

1. Phase identification (GaSb formation),
2. Quantitative structural assessment via strain and phonon confinement analysis.

2.6. Strain Determination from Raman Peak Shift

The temperature-dependent shift of the Si optical phonon was used to estimate lattice strain according to [31]:

$$\Delta\omega = -830\varepsilon$$

where $\Delta\omega$ is the shift of the Si optical-phonon peak position relative to the strain-free bulk Si reference (520 cm^{-1}) and ε is the resulting biaxial lattice strain (dimensionless, positive values denote tensile strain and negative values compressive strain). This relation enables quantification of compressive or tensile strain induced by GaSb phase formation and interfacial stress.

2.7. Phonon Confinement and Crystallite Size Estimation

To distinguish between micrometer-scale precipitate morphology and nanometer-scale crystalline coherence, the Campbell–Fauchet phonon confinement model was applied [32]:

$$\Gamma(L) = \Gamma_0 + \frac{A}{L^2} \tag{3}$$

where Γ is the Raman linewidth (FWHM), Γ_0 is the intrinsic bulk linewidth, and L is the phonon coherence length.

This approach enables estimation of internal crystallite size independent of precipitate diameter observed by SEM, thus resolving scale-dependent structural effects.

3. RESULTS AND DISCUSSION

The experimental framework described in Section 2 was designed to systematically probe temperature-driven phase evolution in the Ga–Sb–Si ternary system. The results reveal a clear transformation pathway governed by thermodynamic stability and diffusion kinetics. Structural, compositional, and vibrational analyses collectively confirm the four-stage evolution proposed in Section 1.

3.1. Microstructural Evolution Observed by SEM

At 1000°C (Group I), the SEM micrograph (Figure 1a) shows a relatively smooth silicon matrix with localized bright contrast regions. The absence of macroscopic droplet formation indicates that the system remains supersaturated. Such morphology is consistent with early-stage nucleation, in which the volumetric free energy reduction (ΔG_v) is insufficient to overcome interfacial energy penalties (γA) for the formation of large precipitates [33, 34].

The localized bright regions correspond to Ga-rich clusters, suggesting that diffusion has initiated but remains kinetically limited.

At 1100°C, a pronounced morphological transition occurs. SEM (Figure 2a) reveals micrometer-scale spherical precipitates distributed across the surface. The spherical geometry strongly suggests minimization of interfacial energy, characteristic of droplet-mediated phase segregation. This behavior resembles classical liquid-phase separation mechanisms described in alloy systems. The temperature increase enhances atomic mobility according to Arrhenius kinetics, enabling Ga and Sb atoms to coalesce into GaSb-rich domains. The droplet morphology confirms the system has crossed a thermodynamic segregation threshold. The formation of spherical Ga–Sb-rich precipitates and their partial embedding into the Si matrix, shown in the magnified views (Figures 2f–g) and in cross-section (Figures 2h–i), indicates thermally driven droplet-mediated phase separation.

At 1200°C, the large droplet morphology disappears. Instead, finely dispersed precipitates with faceted features emerge (Figure 3a). The faceting indicates crystallographically controlled growth, suggesting a diffusion-limited precipitation regime rather than liquid coalescence. This transition reflects a shift from interfacial-energy-dominated droplet formation to bulk diffusion-controlled phase stabilization.

The reduced particle size and faceted morphology, illustrated by the extended surface views (Figures 3f–g) and by the faceted square-shaped precipitate (Figure 3h), suggest diffusion-controlled nucleation and crystallographically oriented Ga–Sb phase formation.

At 1250°C, precipitates are significantly reduced and the surface regains homogeneity (Figure 4a). This indicates partial re-dissolution of GaSb phases due to increased solid solubility at elevated temperature.

Such behavior is consistent with thermodynamic re-equilibration and reduction of interfacial area.

The absence of large precipitates and the uniform elemental distribution suggest re-dissolution and homogenization of Ga–Sb phases within the Si matrix during advanced thermal processing.

3.2. Elemental Redistribution (EDS Analysis)

EDS elemental mapping further corroborates the morphological interpretations derived from the SEM analysis.

As shown in Figures 1b–f, at 1000°C gallium exhibits pronounced localized clustering, whereas antimony displays a comparatively more diffuse spatial distribution across the silicon matrix. The incomplete spatial overlap between Ga and Sb elemental maps indicates that full GaSb compound formation has not yet occurred at this stage. Instead, the observed partial compositional segregation suggests a metastable supersaturation regime, in which atomic redistribution is initiated but remains insufficient to achieve complete compound stabilization.

This behavior is consistent with diffusion-limited kinetics at 1000°C, where the thermodynamic driving force for phase formation is present, yet interfacial energy barriers and limited atomic mobility prevent extensive co-segregation and long-range ordering.

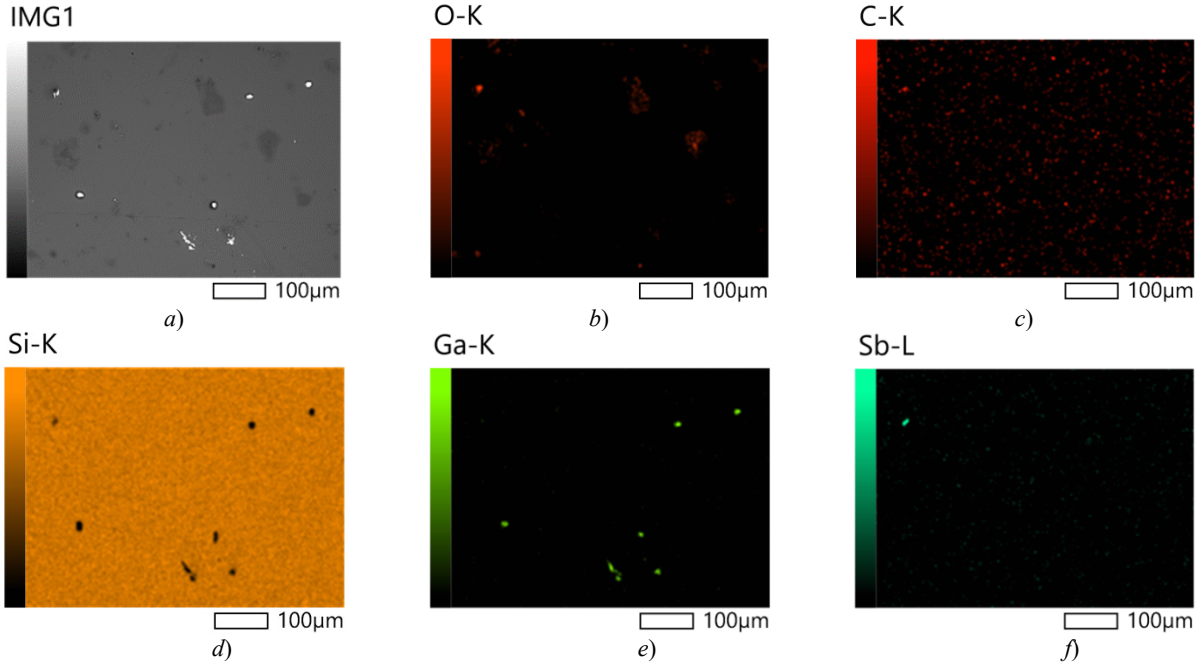

Figure 1. SEM micrographs and EDS elemental mappings of the Group I sample: (a) surface morphology; (b) O–K map; (c) C-K map; (d) Si–K map; (e) Ga–K map; (f) Sb–L map

As shown in Figures 2b–e, at 1100°C gallium and antimony exhibit a pronounced spatial correlation within well-defined spherical droplets distributed across the surface. SEM analysis reveals that the droplets have diameters ranging from approximately 25 to 60 μm, with an average size of about 40 ± 15 μm based on scale-bar estimation.

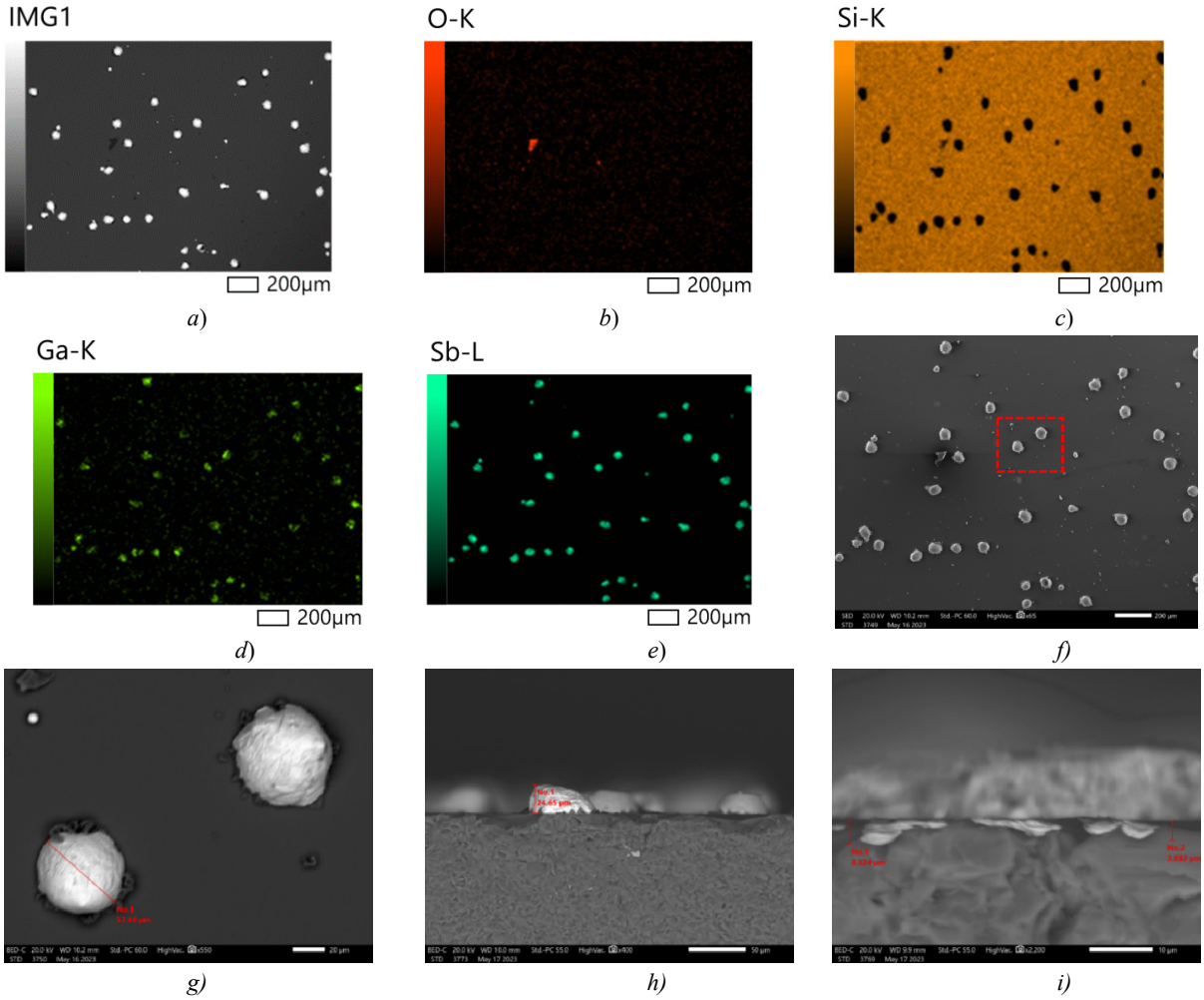

Figure 2. SEM micrographs and EDS elemental mappings of Group II sample: (a) surface morphology; (b) O–K; (c) Si–K; (d) Ga–K; (e) Sb–L; (f–g) magnified precipitate morphology; (h–i) cross-sectional analysis

The nearly complete overlap of Ga and Sb elemental distributions within these micrometer-scale droplets provides direct compositional evidence for GaSb-rich phase formation. The spherical morphology indicates interfacial energy minimization, characteristic of droplet-mediated segregation processes governed by surface tension effects.

The relatively broad size distribution suggests rapid nucleation followed by coarsening dynamics, consistent with classical Ostwald ripening behavior. At this temperature, enhanced atomic mobility enables efficient interdiffusion between Ga and Sb, allowing local compositional equilibrium to be established within individual droplets. The observed behavior aligns with Ga–Sb binary phase diagram predictions, where elevated temperature promotes compound nucleation and thermodynamically stabilized phase segregation.

As observed in Figures 3b–e, at 1200°C gallium and antimony remain spatially correlated; however, their distribution becomes markedly more homogeneous compared to the pronounced droplet segregation observed at 1100°C. The elemental maps reveal that Ga–Sb-rich regions are no longer confined to large spherical droplets but instead appear as finely dispersed, micrometer-scale precipitates distributed throughout the silicon matrix.

SEM analysis (50 μm scale) indicates that the bright islands exhibit characteristic lateral dimensions ranging from approximately 2 to 10 μm, with an average diameter of about 5 ± 3 μm. This represents a significant refinement compared to the 25–60 μm droplets observed at 1100°C. The reduction in island size, combined with an increased areal density, suggests fragmentation and redistribution rather than continued coalescence.

The Ga–K and Sb–L maps demonstrate strong local compositional overlap within these smaller precipitates, confirming the persistence of GaSb-rich phase domains. However, the improved spatial uniformity and absence of large spherical droplets indicate that interfacial-energy-driven segregation is no longer the dominant mechanism. Instead, bulk diffusion and crystallographically controlled precipitation govern the phase stabilization process.

The partial faceting of several islands further supports a diffusion-limited growth regime, where anisotropic surface energy and lattice accommodation effects influence morphology. The microstructural refinement at 1200°C therefore reflects a transition from droplet-mediated coalescence to diffusion-controlled nanocrystalline precipitation.

Thermodynamically, this stage corresponds to enhanced atomic mobility enabling redistribution of segregated species, while kinetically, the system approaches a more stable, spatially dispersed phase configuration. The observed

decrease in precipitate size and improved compositional homogeneity is consistent with diffusion-driven reorganization and internal domain stabilization.

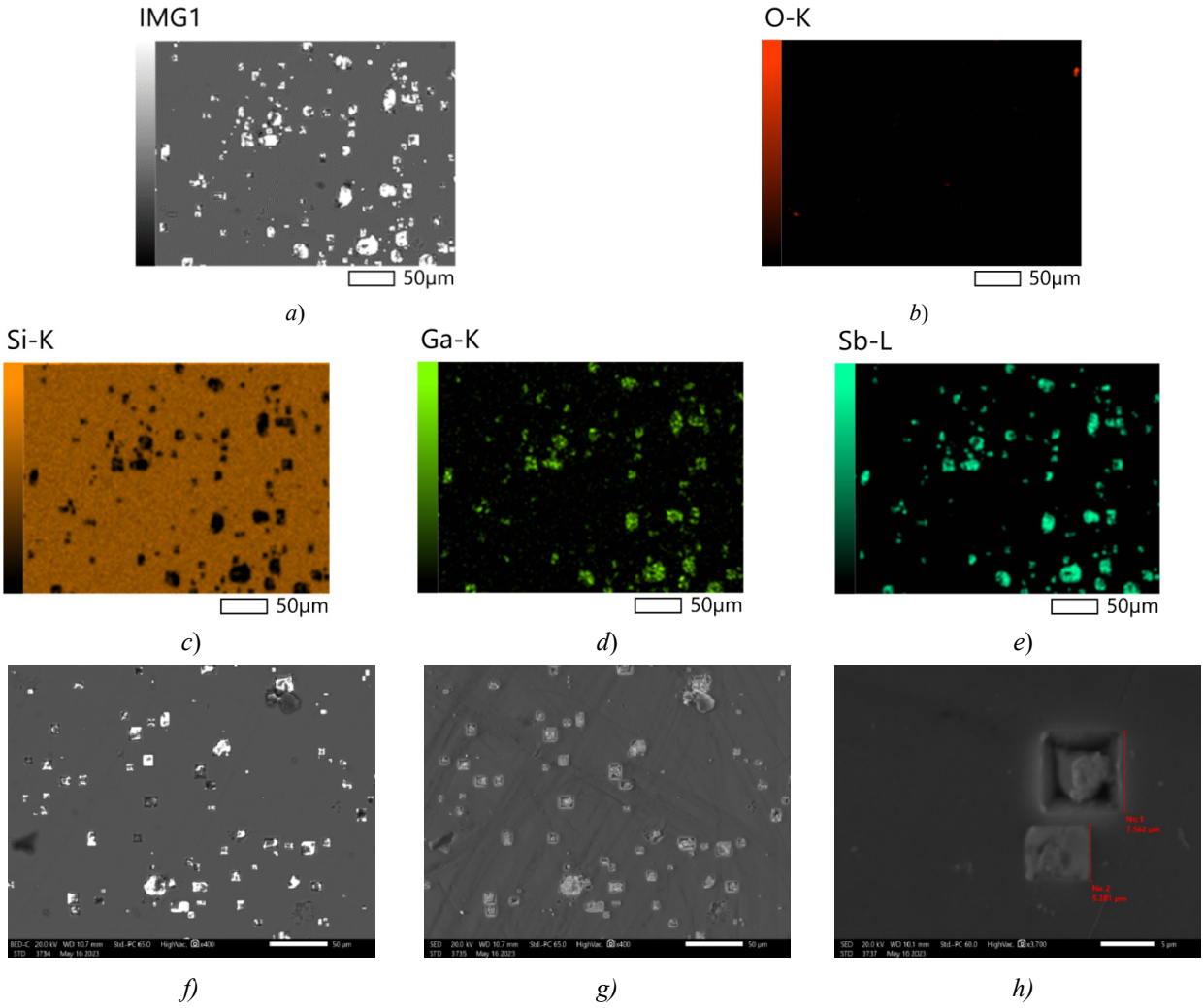

Figure 3. SEM micrographs and EDS elemental mappings of Group III sample:(a) surface morphology; (b) O–K; (c) Si–K; (d) Ga–K; (e) Sb–L; (f–g) extended surface morphology; (h) faceted square-shaped precipitate

Overall, the structure at 1200°C represents an intermediate equilibrium regime characterized by:

- Reduced precipitate size (≈5 μm average),
- Increased spatial dispersion,
- Strong Ga–Sb compositional correlation,
- Suppression of large droplet morphology,
- Diffusion-limited precipitation dynamics.

This regime provides clear experimental evidence of the thermodynamic–kinetic shift from segregation-dominated growth (1100°C) to controlled nanocrystalline stabilization.

As shown in Figures 4b–f, at 1250°C the elemental distributions of Ga and Sb become significantly more homogeneous across the silicon matrix compared to the lower-temperature samples. The Ga–K and Sb–L maps show only weak, sparsely distributed localized intensity maxima, indicating a substantial reduction in segregated GaSb-rich domains.

SEM analysis (10 μm scale) reveals that the previously observed micrometer-scale precipitates have largely disappeared. The remaining bright features appear as small residual islands with characteristic lateral dimensions ranging from approximately 0.5 to 3 μm, with an average effective diameter of about 1.5 ± 0.8 μm. The areal density of these islands is markedly reduced relative to both the 1100°C and 1200°C conditions.

The significant decrease in island size and density, together with the reduced compositional contrast in the Ga and Sb maps, strongly indicates partial re-dissolution of the GaSb-rich phase into the silicon matrix. The near-uniform Si–K signal further confirms matrix recovery and suppression of compositional segregation.

Thermodynamically, this behavior reflects increased solid solubility and entropy-driven redistribution at elevated temperature. Kinetically, the enhanced diffusion coefficients at 1250°C promote homogenization rather than further

precipitate growth. The absence of large droplets and the emergence of only sub-micrometer residual domains demonstrate that interfacial energy is no longer the dominant driving force; instead, bulk diffusion and equilibrium solubility limit phase persistence.

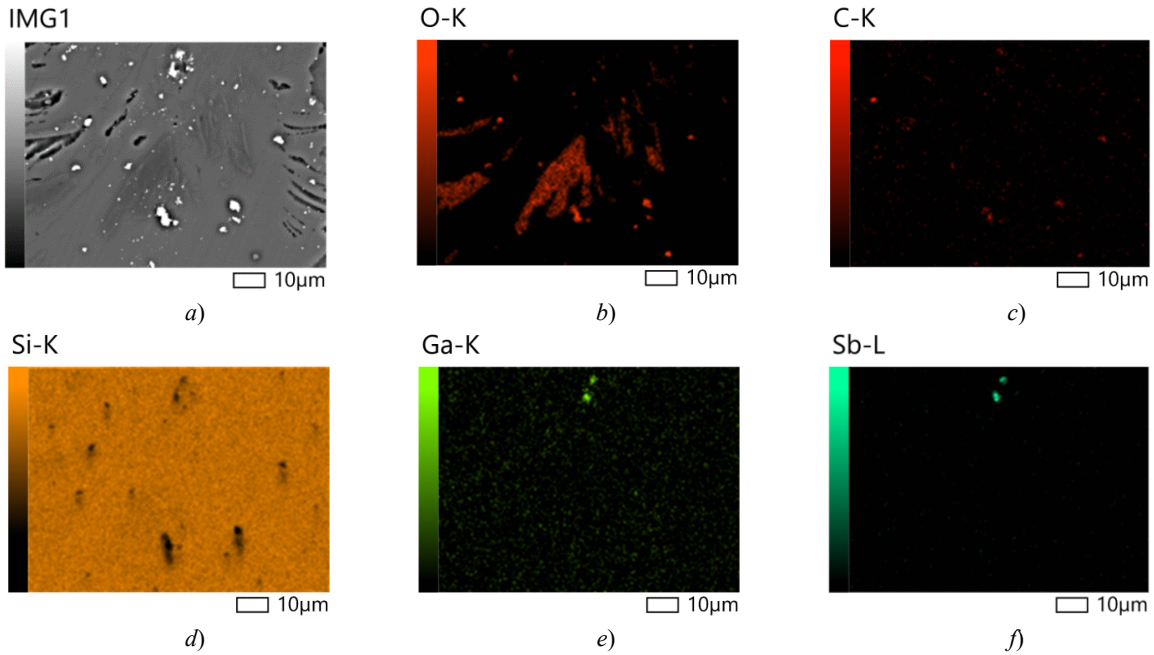

Figure 4. SEM micrographs and EDS elemental mappings of Group IV sample: (a) surface morphology; (b) O–K; (c) C–K; (d) Si–K; (e) Ga–K; (f) Sb–L

Overall, the microstructure at 1250°C represents a re-homogenization regime characterized by:

- Strongly reduced precipitate size (~1.5 μm average),
- Low areal density of residual islands,
- Weak Ga–Sb compositional localization,
- Restoration of silicon matrix continuity.

This stage marks the final thermodynamic stabilization of the system, completing the transformation pathway from supersaturation (1000°C) through segregation (1100°C) and diffusion-limited precipitation (1200°C) to matrix recovery at 1250°C.

3.3. Raman Spectral Evolution

As observed in Figure 5, the Raman spectrum of the Group I sample exhibits a slight downshift of the Si optical phonon to approximately 518–519 cm^{-1}, corresponding to an estimated tensile strain of ~0.18%. This negative peak shift relative to the stress-free crystalline silicon position (520 cm^{-1}) indicates minor lattice expansion, most likely due to the substitutional incorporation of diffusing species within the Si matrix.

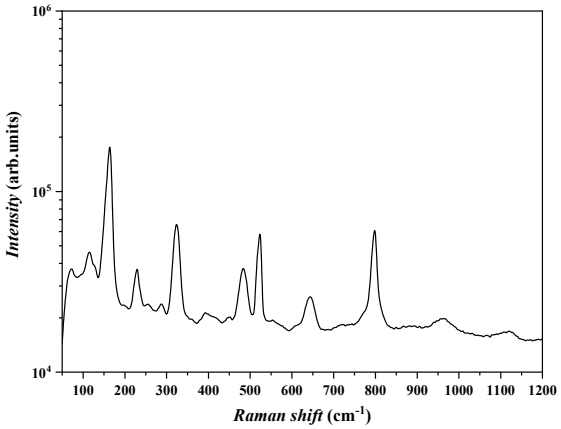

Figure 5. Raman spectrum of the Group I sample (1000°C, 10 h annealing)

The absence of a dominant GaSb transverse optical (TO) mode near 223 cm^{-1}, together with the presence of broad disorder-induced bands in the low-wavenumber region, suggests incomplete compound formation and limited Ga–Sb co-segregation. Instead of forming well-defined GaSb-rich droplets, the diffusing species appear to remain partially incorporated within the silicon lattice.

This vibrational behavior is consistent with the SEM/EDS observations of Group I (1000°C), where sparsely distributed micrometer-scale Ga-rich islands (~7 μm) were detected with incomplete Sb overlap. The low areal density of these islands and the lack of strong compositional correlation confirm that the system remains in a metastable supersaturation regime. Under these conditions, lattice distortion originates primarily from localized substitutional incorporation and early-stage clustering rather than from macroscopic droplet segregation.

The combined structural and vibrational evidence therefore conclusively identifies this spectrum as corresponding to the supersaturation regime at 1000°C.

As observed in Figure 6, the Raman spectrum exhibits a pronounced and well-defined GaSb transverse optical (TO) phonon mode at approximately 223 cm^{-1}, accompanied by a sharp and intense Si–Si optical phonon peak centered near 520 cm^{-1}. The strong GaSb signal indicates substantial compound formation and confirms effective co-segregation of Ga and Sb at this annealing temperature.

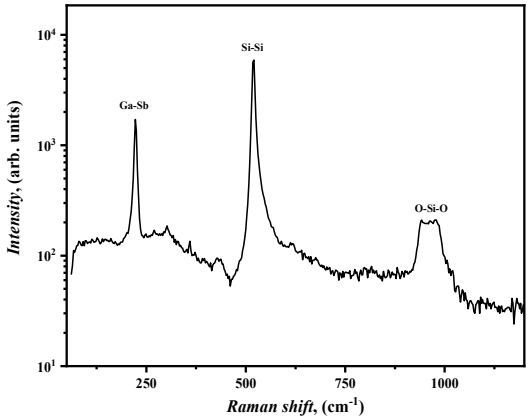

Figure 6. Raman spectrum of the Group II sample (1100°C, 10 h annealing)

Notably, the Si optical phonon peak remains essentially unshifted relative to the stress-free crystalline silicon reference (520 cm^{-1}), suggesting negligible residual lattice strain within the silicon matrix. This absence of measurable peak displacement implies that the segregated GaSb phase has formed discrete micrometer-scale droplets, thereby relieving internal stress that would otherwise accumulate through substitutional incorporation.

The moderate disorder background and the presence of a secondary O–Si–O band in the 900–1000 cm^{-1} region are consistent with interface-related vibrational contributions and minor surface oxidation, rather than bulk structural distortion. This vibrational behavior is consistent with the SEM/EDS observations of Group II (1100°C), where large spherical droplets (approximately 25–60 μm in diameter) with strong Ga–Sb compositional overlap were detected. The formation of these well-defined GaSb-rich domains represents a thermodynamically stabilized segregation regime, in which interfacial energy minimization dominates over lattice incorporation mechanisms.

Therefore, the combined structural and vibrational evidence indicates that this Raman spectrum corresponds to the droplet-mediated segregation stage at 1100°C.

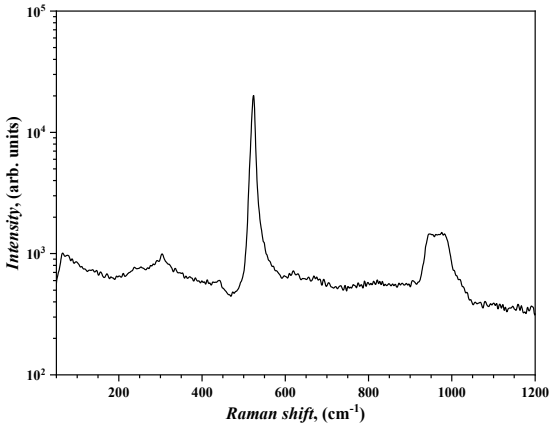

Figure 7. Raman spectrum of the Group III sample (1200°C, 10 h annealing).

As observed in Figure 7, the Raman spectrum is dominated by a pronounced Si–Si optical phonon peak located at approximately 524 cm^{-1}, indicating a measurable upshift relative to the stress-free crystalline silicon reference at 520 cm^{-1}. This positive shift corresponds to an estimated compressive strain of ~0.48–0.50%, calculated using the phonon deformation potential relationship ($\Delta\omega = -830\varepsilon$). The observed peak displacement signifies enhanced lattice distortion compared to both the 1000°C and 1100°C conditions.

In contrast to the strong and sharp GaSb TO mode observed at 1100°C, the low-wavenumber region in this spectrum exhibits only weak and broadened features, suggesting a reduced effective GaSb phase fraction. The absence of a dominant, narrow GaSb peak indicates that large droplet segregation is no longer the prevailing mechanism.

The moderate broadening of the Si phonon peak and the presence of a weak disorder-related background further support the presence of internal stress fields and nanoscale structural heterogeneity. Additionally, the broad band in the 920–1000 cm^{-1} region (Si–O–Si and second-order scattering contributions) reflects interface-related vibrational activity rather than bulk oxidation. This vibrational behavior is consistent with the SEM/EDS observations of Group III (1200°C), where the previously large micrometer-scale droplets disappear and are replaced by refined precipitates with characteristic sizes of approximately 2–10 μm (average ~5 μm). The increased spatial dispersion and reduced precipitate size indicate a transition from interfacial-energy-dominated segregation to diffusion-limited nanocrystalline precipitation.

The significant compressive strain observed at 1200°C arises from partial redistribution of Ga and Sb within the silicon matrix and enhanced lattice accommodation during phase refinement. Therefore, the combined structural and vibrational evidence indicates that this Raman spectrum corresponds to the diffusion-controlled precipitation regime at 1200°C.

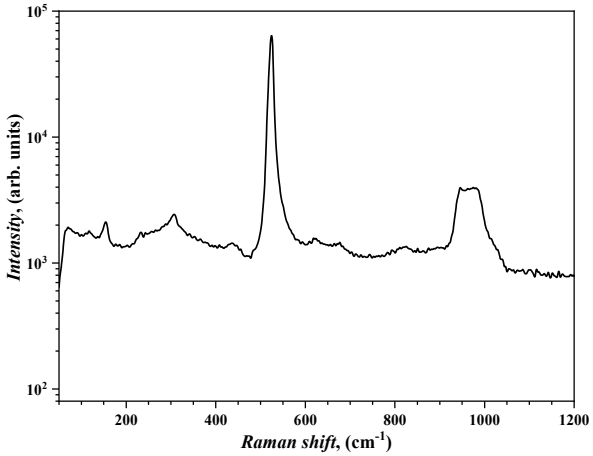

Figure 8. Raman spectrum of the Group IV sample (1250°C, 10 h annealing)

As observed in Figure 8, the Raman spectrum is dominated by a strongly upshifted Si–Si optical phonon peak positioned near 525 cm^{-1}, representing the highest frequency among all investigated samples. Relative to the stress-free silicon reference at 520 cm^{-1}, this corresponds to an estimated compressive strain of approximately ~0.6%, calculated using the phonon deformation potential relationship ($\Delta\omega = -830\varepsilon$). This pronounced peak shift indicates substantial lattice distortion within the silicon matrix. In contrast to the spectrum obtained at 1100°C, the GaSb transverse optical (TO) mode near 223 cm^{-1} is significantly weakened or nearly suppressed, indicating a marked reduction in segregated GaSb-rich phase fraction. The low-wavenumber region shows only minor residual features, suggesting that large-scale compound domains are no longer present.

The moderate broad band in the 920–1000 cm^{-1} range, associated with Si–O–Si vibrations and second-order scattering processes, reflects interface-related vibrational contributions rather than dominant bulk phase formation. The overall spectral profile is cleaner than that observed at 1200°C, indicating reduced nanoscale heterogeneity and enhanced matrix continuity.

This vibrational behavior is consistent with the SEM/EDS observations of Group IV (1250°C), where micrometer-scale precipitates were largely eliminated and only small residual islands (~0.5–3 μm, average ~1.5 μm) remained with significantly reduced areal density. The homogenized elemental distribution confirms partial re-dissolution of GaSb phases into the silicon matrix.

The increased compressive strain at this temperature arises from redistribution of Ga and Sb species into the Si lattice following droplet dissolution. Without large segregated domains to relieve internal stress, the silicon matrix accommodates compositional distortion, leading to the maximum observed phonon upshift.

Therefore, the combined structural and vibrational evidence indicates that this Raman spectrum corresponds to the re-homogenization regime at 1250°C.

4. CONCLUSIONS

This work shows that annealing temperature governs a reproducible sequence of structural and vibrational changes in the Ga–Sb–Si ternary system. Combining SEM, EDS, and Raman spectroscopy, we identify four temperature-dependent regimes: supersaturation (1000°C), droplet-mediated segregation (1100°C), diffusion-limited precipitation (1200°C), and re-homogenization (1250°C).

The structural transition from sparse Ga-rich islands to large GaSb droplets, followed by precipitate refinement and eventual dissolution, is directly mirrored in the vibrational response of the silicon lattice. The non-monotonic evolution of

the GaSb TO mode and the systematic shift of the Si optical phonon from tensile (~0.18%) to maximum compressive strain (~0.6%) provide quantitative evidence of thermodynamic stabilization and kinetic redistribution processes.

The strongest GaSb formation coincides with strain relief at 1100°C, whereas higher temperatures promote phase dissolution and lattice distortion associated with compositional reintegration. This relationship between segregation-driven stress relaxation and homogenization-induced strain accumulation points to a coupling between phase morphology and phonon dynamics in this compound-forming diffusion system, which merits further investigation, for example through in-situ or time-resolved measurements.

These observations provide a basis for a thermodynamic–kinetic description of temperature-controlled heterophase formation in silicon. The ability to move between metastable clustering, stabilized compound domains, refined nanocrystalline precipitation, and near-equilibrium homogenization by varying annealing temperature suggests a route toward strain tuning and embedded III–V phase integration within Si-compatible architectures, though further work is needed to establish the practical limits of this approach.

These findings extend the description of classical diffusion behavior to a multi-component, compound-forming system and offer design considerations for thermally engineered semiconductor structures. By correlating morphology, composition, and lattice dynamics across multiple length scales, this work contributes to the understanding of compound-forming diffusion in silicon and points to potential pathways for phase-functional materials compatible with existing microelectronic technologies.

ORCID

Bobir O. Isakov, https://orcid.org/0000-0002-6072-3695

REFERENCES

[1] S.M. Sze, and K.K. Ng, *Physics of Semiconductor Devices*, 3rd ed., (Wiley, 2007). https://doi.org/10.1002/0470068329
[2] C. Barri, E. Mafakheri, L. Fagiani, G. Tavani, A. Barzaghi, D. Chrastina, A. Fedorov, *et al*., "Engineering of the spin on dopant process on silicon on insulator substrate," Nanotechnology, **32**, 025303 (2021). https://doi.org/10.1088/1361-6528/abbdda
[3] P.M. Fahey, P. B. Griffin, and J. D. Plummer, "Point defects and dopant diffusion in silicon," Rev. Mod. Phys. **61**, 289–384 (1989). https://doi.org/10.1103/RevModPhys.61.289
[4] Y. Su, D. Saric, G. Guevara-Carrion, Y. Zhang, M. He, and J. Vrabec, "Fick and Maxwell-Stefan diffusion of the liquid mixture cyclohexane+toluene+ acetone+ methanol and its subsystems", Chemical Engineering Science, **301**, 120662 (2025). https://doi.org/10.1016/j.ces.2024.120662
[5] M. Bonvalet-Rolland, T. Philippe, and J. Ågren, "Kinetic theory of nucleation in multicomponent systems: An application of the thermodynamic extremum principle", Acta Materialia, **171**(1), 1-7 (2019). https://doi.org/10.1016/j.actamat.2019.03.031
[6] Kh.M. Iliev, N.F. Zikrillaev, K.S. Ayupov, B.O. Isakov, B.A. Abdurakhmanov, Z.N. Umarkhodjaeva, and L.I. Isamiddinova, "Effect of GaSb Compound on Silicon Bandgap Energy", J. Nano- Electron. Phys. **16**(1), 01007 (2024). https://doi.org/10.21272/jnep.16(2).02004
[7] G.P. Edmundo, K.R. Tanya, and R.N. Jonathan, "Design and Applications of Water-Soluble Coordination Cages," Chem. Rev. **120**, 13480−13544 (2020). http://dx.doi.org/10.1021/acs.chemrev.0c00672
[8] S. Yi, J.-S. Chen, C.-M. Wang, and W.-S. Liao, "Manipulating Chemical Processes by Pseudosolid Spatial Limitation", JACS Au, **1**(9): 1435–1444 (2021). https://doi.org/10.1021/jacsau.1c00202
[9] E. Guzmán, F. Martínez-Pedrero, C. Calero, A. Maestro, F. Ortega, and R.G. Rubio, "A broad perspective to particle-laden fluid interfaces systems: from chemically homogeneous particles to active colloids", Advances in Colloid and Interface Science, **302**, 102620 (2022). https://doi.org/10.1016/j.cis.2022.102620
[10] N.F. Zikrillayev, S.B. Isamov, B.O. Isakov, T. Wumaier, L.W. Liang, J.X. Zhan, and T. Xiayimulati, "New Technological Solution for the Tailoring of Multilayer Silicon-based Systems with Binary Nanoclusters Involving Elements of Groups III and V," J. Nano- Electron. Phys. **15**, 06024 (2023). https://doi.org/10.21272/jnep.15(6).06024
[11] X.M. Iliyev, S.B. Isamov, B.O. Isakov, U.X. Qurbonova, and S.A. Abduraxmonov, "A surface study of Si doped simultaneously with Ga and Sb," East European Journal of Physics, (3), 303-307 (2023). https://doi.org/10.26565/2312-4334-2023-3-29
[12] X.M. Iliyev, V.B. Odzhaev, S.B. Isamov, B.O. Isakov, B.K. Ismaylov, K.S. Ayupov, and Sh.I. Hamrokulov, "X-ray diffraction and Raman spectroscopy analyses of GaSb-enriched Si surface formed by applying diffusion doping technique," East Eur. J. Phys. (3), 363-369 (2023), https://doi.org/10.26565/2312-4334-2023-3-38
[13] Kh.M. Iliev, S.V. Koveshnikov, B.O. Isakov, E.Zh. Kosbergenov, G.A. Kushiev, and Z.B. Khudoynazarov, "The Elemental Composition Investigation of Silicon Doped with Gallium and Antimony Atoms," Surface Engineering and Applied Electrochemistry, **60**(4), 633–639 (2024). https://doi.org/10.3103/S106837552470025X
[14] S.K. Madisetti, V. Tokranov, A. Greene, S. Novak, M. Yakimov, S. Oktyabrsky, S. Bentley, and A.P. Jacob, "GaSb on Si: Structural Defects and Their Effect on Surface Morphology and Electrical Properties," Mater. Res. Soc. Symp. Proc. **1635**, (2014). https://doi.org/10.1557/opl.2014.219
[15] J. Gebauer, M. Lausmann, F. Redmann, R. Krause-Rehberg, H.S. Leipner, E.R. Weber, and Ph. Ebert, "Determination of the Gibbs free energy of formation of Ga vacancies in GaAs by positron annihilation," Physical Review B, **67**, 235207 (2003), https://doi.org/10.1103/PhysRevB.67.235207
[16] Shuo Liu, Chaochao Dun, Jeffrey J. Urban, Mark T. Swihart, "Non-Equilibrium Synthesis Methods to Create Metastable and High-Entropy Nanomaterials," Advanced Science, **13**, e21953 (2026). https://doi.org/10.1002/advs.202521953
[17] A. Orlando, F. Franceschini, C. Muscas, S. Pidkova, M. Bartoli, M. Rovere, and A. Tagliaferro, "A Comprehensive Review on Raman Spectroscopy Applications," Chemosensors, **9**, 262 (2021). https://doi.org/10.3390/chemosensors9090262
[18] X. Cong, X.-L. Liu, M.-L. Lin, and P.-H. Tan, "Application of Raman spectroscopy to probe fundamental properties of two-dimensional materials," npj 2D Materials and Applications, **13**, (2020). https://doi.org/10.1038/s41699-020-0140-4

[19] G. La Penna, C. Mancini, A. Proietti, L. Buccini, D. Passeri, N. Gambacorti, J. Richy, and M. Rossi, "Strained Silicon Technology: Non-Destructive High-Lateral-Resolution Characterization Through Tip-Enhanced Raman Spectroscopy," Applied Spectroscopy, **78**(12) 1245–1255 (2024). https://doi.org/10.1177/00037028241246292
[20] W. O'Leary, M. Grumet, W. Kaiser, T. Bucko, J.L. M. Rupp, and D.A. Egger, "Rapid Characterization of Point Defects in Solid-State Ion Conductors Using Raman Spectroscopy, Machine-Learning Force Fields, and Atomic Raman Tensors," J. Am. Chem. Soc. **146**, 26863−26876 (2024). https://doi.org/10.1021/jacs.4c07812
[21] G. Gouadec, and P. Colomban, "Raman Spectroscopy of Nanomaterials: How Spectra Relate to Disorder, Particle Size and Mechanical Properties," Progress in Crystal Growth and Characterization of Materials, **53**(1), 1-56 (2007). https://doi.org/10.1016/j.pcrysgrow.2007.01.001
[22] P.V. Pham, T.-H. Mai, S.P. Dash, V. Biju, Y.-L. Chueh, D. Jariwala, and V. Tung, "Transfer of 2D Films: From Imperfection to Perfection," ACS Nano, **18**, 14841−14876 (2024). https://doi.org/10.1021/acsnano.4c00590
[23] G. Gyarmati, and J. Erdélyi, "Intermetallic Phase Control in Cast Aluminum Alloys by Utilizing Heterogeneous Nucleation on Oxides," Metals, **15**, 404 (2025). https://doi.org/10.3390/met15040404
[24] S. Barth, M.S. Seifner, and S. Maldonado, "Metastable Group IV Allotropes and Solid Solutions: Nanoparticles and Nanowires," Chem. Mater. **32**, 2703−2741 (2020). https://dx.doi.org/10.1021/acs.chemmater.9b04471
[25] A.P. Arun, N. Sreenivasan, J.H. Patil, R. Kusanur, H.L. Ramachandraiah, and M. Ramakrishna, "Thin Films for Next Generation Technologies: A Comprehensive Review of Fundamentals, Growth, Deposition Strategies, Applications, and Emerging Frontiers," Processes, **13**, 3846 (2025). https://doi.org/10.3390/pr13123846
[26] A. Giunto, A. Fontcuberta i Morral, "Defects in Ge and GeSn and their impact on optoelectronic properties," Appl. Phys. Rev. **11**, 041333 (2024). https://doi.org/10.1063/5.0218623
[27] J. Ponis, S. Hariyani, G. Agbeworvi, S. Chakraborty, V. Balcorta, J. Pérez-Vázquez, B.L. Rogers, *et al*., "Single Crystals of Vanadium Oxides as a Lens for Understanding Structural and Electronic Phase Transformations, Ion Transport, Chemo-Mechanical Coupling, and Electrothermal Neuronal Emulation," Chem. Rev. **125**, 10657−10764 (2025). https://doi.org/10.1021/acs.chemrev.5c00413
[28] A. Zaitsev, N. Arutyunyan, and A. Koldaev, "Hot Ductility, Homogeneity of the Composition, Structure, and Properties of High-Strength Microalloyed Steels: A Critical Review," Metals, **13**, 1066 (2023). https://doi.org/10.3390/met13061066
[29] A.A. Ilie, F. Niculescu, G. Iacob, I. Pencea, F. Miculescu, R. Bololoi, D.-V. Drăgut, *et al*., "Microstructure and Properties of Bi-Sn, Bi-Sn-Sb, and Bi-Sn-Ag Solder Alloys for Electronic Applications," Metals, **15**, 915 (2025). https://doi.org/10.3390/met15080915
[30] W.-J. Moon, S.G. Yu, Y.S. Kim, B.-K. Park, W.-G. Jung, and H.-J. Song, "New strategy to improve the accuracy of quantitative analysis of energy dispersive spectroscopy," Phys. Scr. **99**, 035013, (2024). https://doi.org/10.1088/1402-4896/ad241e
[31] M. Xie, M. Li, L. Li, J. Zhang, K. Jiang, L. Shang, Y. Li, *et al*., "Temperature-dependent phonon mode and interband electronic transition evolutions of e-InSe films derived by pulsed laser deposition," Appl. Phys. Lett. **117**, 102101 (2020). https://doi.org/10.1063/5.0021330
[32] S. Marola, S. Bosia, A. Veltro, G. Fiore, D. Manfredi, M. Lombardi, G. Amato, *et al*., "Residual stresses in additively manufactured AlSi10Mg: Raman spectroscopy and X-ray diffraction analysis," Materials and Design **202**, 109550 (2021). https://doi.org/10.1016/j.matdes.2021.109550
[33] M. Perez, M. Dumont, and D. Acevedo-Reyes, "Implementation of the classical nucleation theory for precipitation," Acta Materialia, **56**(9), 2119-2132 (2008). https://doi.org/10.1016/j.actamat.2007.12.050
[34] W. Wełnic, and M. Wuttig, "Reversible switching in phase-change materials," Materials today, **11**(6), (2008). https://doi.org/10.1016/S1369-7021(08)70118-4

ТЕМПЕРАТУРНО-ЗУМОВЛЕНА ФАЗОВА ЕВОЛЮЦІЯ ТА ДИНАМІКА ДЕФОРМВЦІЇ ҐРАТКИ ПІД ЧАС СПІЛЬНОЇ ДИФУЗІЇ Ga–Sb У МОНОКРИСТАЛІЧНОМУ КРЕМНІЇ

Бобір О. Ісаков, Халмурат М. Ілієв, Кутуб С. Аюпов, Бахрам А. Абдурахманов, Гіосіддін А. Кушієв, Абдуджалол А. Сатторов, Зафар Б. Худуйназаров

Ташкентський державний технічний університет, вул. Університетська, 2, 100095, Ташкент, Узбекистан

У цьому дослідженні розглядається вплив температури відпалу на мікроструктуру та динаміку ґратки монокристалічного кремнію, що кодифузувався з галієм та сурмою. Зразки відпалювали в діапазоні 1000–1250°C протягом фіксованої тривалості 10 годин та аналізували за допомогою SEM-візуалізації, EDS-елементного картування та раманівської спектроскопії. Зі зростанням температури зразки демонструють чотири послідовні мікроструктурні стани: (I) розріджене кластеризування, багате на Ga, при 1000°C, (II) утворення великих крапель GaSb (25–60 мкм) при 1100°C, (III) подрібнення на менші, огранованні осади (~5 мкм) при 1200°C та (IV) суттєве повторне розчинення вторинної фази, залишаючи лише залишкові домени розміром ~1,5 мкм, при 1250°C. Раманівські вимірювання оптичних фононів Si відстежують цю послідовність: невеликий зсув на розтяг (~518–519 $см^{-1}$) при 1000°C, повернення до недеформованого положення (~520 $см^{-1}$) при 1100°C, коли краплі GaSb компенсують більшу частину невідповідності кристалічної решітки, та збільшення зсувів на стиск (524–525 $см^{-1}$, що відповідає ~0,6% деформації) при 1200–1250°C, коли фаза GaSb повторно розчиняється в матриці. Аналіз фононного утримання ширини лінії Рамана додатково вказує на довжини кристалічної когерентності 3–5 нм у межах мікрометрових преципітатів. У сукупності ці результати вказують на те, що температура відпалу визначає відтворювану послідовність кластеризації, сегрегації крапель, подрібнення преципітатів та повторної гомогенізації в системі Ga–Sb–Si, і що цю послідовність можна кількісно відстежити за допомогою корельованих SEM/EDS та раманівських сигнатур, про які тут повідомляється.

Ключові слова: *дифузія; сегрегація; нанокристалічний матеріал; осадження; деформація кристалічної решітки; фазове розділення*

East European Journal of Physics. 3. 575-581 (2026)
DOI:10.26565/2312-4334-2026-3-52 ISSN 2312-4334

INCOMPLETE IONIZATION EFFECTS IN C–V CHARACTERISTICS OF RADIAL p–n AND p-i-n JUNCTION STRUCTURES

J.Sh. Abdullayev[1]*, D.A. Qalandarova[1], F.Th. Turaev[1], D.Kh. Abdullaeva[2], J. Kamolov[3], M.M. Makhmudova[4], A.B. Ataubaeva[5], U.S. Rakhmonov[6]
[1]National Research University TIIAME, Tashkent, Uzbekistan
[2]Bukhara State Technical University, Bukhara 200100, Uzbekistan
[3]Bukhara State University, Bukhara 200117, Uzbekistan
[4]Bukhara State University, Bukhara 200117, Uzbekistan
[5]Karakalpak State University, Nukus, Uzbekistan
[6]Tashkent State Technical University, Tashkent, Uzbekistan
**Corresponding Author e-mail: j.sh.abdullayev6@gmail.com*
Received January 14, 2026; revised August 3, 2026; accepted August 7, 2026

This work presents a comprehensive numerical investigation of incomplete dopant ionization effects on the capacitance–voltage (C-V) response of radial p–n and p–i–n junctions fabricated from silicon (Si) and gallium arsenide (GaAs). A self-consistent finite element method (FEM) framework was developed to solve Poisson's equation while explicitly incorporating temperature-dependent dopant ionization statistics. Simulations were performed for doping concentrations of 2×10^{15} cm^{-3} and 2×10^{16} cm^{-3} over a wide temperature range of 100–300 K. The results demonstrate a monotonic increase in junction capacitance with both dopant density and temperature, with capacitance variations exceeding 35–60% across the studied temperature interval, depending on material system and geometry. At 100–150 K, incomplete ionization reduces the effective carrier concentration by up to 48% in Si and 41% in GaAs at 2×10^{16} cm^{-3}, leading to pronounced deviations in the C–V characteristics compared with conventional full-ionization assumptions. In contrast, at 300 K, the ionization efficiency exceeds 97%, rendering incomplete ionization effects negligible. Geometrical dependencies were evaluated for core radii of R = 0.5, 1.0, and 1.5 μm. Furthermore, p–i–n structures with intrinsic layer thicknesses of i = 0.1, 0.3, and 0.5 μm were analyzed at R = 1.5 μm, revealing that increasing the intrinsic region thickness suppresses the impact of incomplete ionization by reducing the space-charge sensitivity to dopant activation, lowering capacitance deviations by more than 30%. Two modeling regimes were systematically compared: (A) full dopant ionization and (B) temperature-dependent incomplete ionization.
Keywords: *Radial p-n junction; Intrinsic layer; Silicon (Si); External factors; Capacity; Doping concentration; Temperature*

INTRODUCTION

In recent years, the rapid expansion of high-efficiency and low-cost photovoltaic (PV) and optoelectronic technologies has stimulated intense interest in unconventional semiconductor junction architectures [1–3]. Among the most promising of these are radial p–n and p–i–n junctions, typically implemented in micro- and nanoscale core–shell structures, which offer a fundamentally different operational paradigm from traditional planar devices [4–7]. Owing to their cylindrical symmetry, radial junctions decouple the directions of optical absorption and carrier collection, enabling simultaneous enhancement of light-harvesting and charge-extraction efficiencies [8–12].

Compared with planar junctions, radial configurations provide several intrinsic advantages. The expanded junction interface facilitates efficient charge separation and reduced recombination losses [13–18], while the shortened carrier transport distances significantly improve carrier collection efficiency, particularly in materials with moderate carrier diffusion lengths [19–24]. These effects translate into superior internal and external quantum efficiencies [25–27]. Moreover, the orthogonal alignment of photon absorption and carrier transport allows for rapid carrier extraction, making radial structures highly attractive for high-speed photodetectors, optical interconnects, and next-generation photovoltaic systems [28–31]. Consequently, radial junction architectures have been widely adopted in nanowire photodiodes, image sensors, and high-performance solar energy converters [32–35].

Despite these advantages, several fundamental physical phenomena specific to radial geometries remain insufficiently explored, particularly under low-temperature and low-doping conditions. Among these, incomplete dopant ionization plays a critical role in governing the electrostatic behavior of the junction [36–38]. At reduced temperatures and moderate dopant concentrations, a significant fraction of dopant atoms remains electrically inactive, leading to substantial deviations in the capacitance–voltage (C–V) characteristics, which are widely used to extract doping profiles, depletion widths, and built-in potentials in both experimental and simulation studies [14,22,39]. Neglecting this effect can therefore result in serious inaccuracies in the interpretation and design of radial junction devices.

In parallel, recent progress in GaAs/Si tandem solar cells has demonstrated the feasibility of surpassing the Shockley–Queisser efficiency limit of single-junction devices [40]. With a GaAs top cell (bandgap ≈ 1.42 eV) and a Si bottom cell (bandgap ≈ 1.12 eV), theoretical conversion efficiencies approaching 40% have been predicted, supported by

Cite as: J. Sh. Abdullayev, D. A. Qalandarova, F. Th. Turaev, D. Kh. Abdullaeva, J. Kamolov, M. M. Makhmudova, A. B. Ataubaeva, U. S. Rakhmonov, East Eur. J. Phys. 3, 575 (2026), https://doi.org/10.26565/2312-4334-2026-3-52

advances in cost-effective doping strategies and high-quality growth techniques such as chemical vapor deposition and molecular beam epitaxy [41]. Integrating such multi-junction concepts with radial geometries opens new pathways for simultaneously optimizing optical absorption, carrier transport, and junction electrostatics in high-performance PV systems [41].

Motivated by these considerations, the present study investigates the role of core radius—a key geometric parameter in radial junctions—on the electrostatic response and C–V behavior of radial p–n structures in the presence of incomplete dopant ionization. By combining analytical modeling with finite-element numerical simulations, we systematically examine how variations in core radius modify charge distribution, depletion region evolution, and capacitance characteristics. The results establish essential design guidelines for optimizing radial junction devices, particularly under non-ideal doping conditions, where precise control of electrostatic profiles is crucial for achieving high device efficiency and stability.

MATERIAL AND METHODS

Gallium arsenide (GaAs) and silicon (Si) were selected as the base materials for this study due to their complementary properties. GaAs possesses a direct bandgap of 1.42 eV and high electron mobility (~8500 cm²/V·s), making it suitable for high-speed optoelectronic devices, whereas Si, with an indirect bandgap of 1.12 eV and electron mobility of ~1400 cm²/V·s, is cost-effective and benefits from a mature fabrication infrastructure.

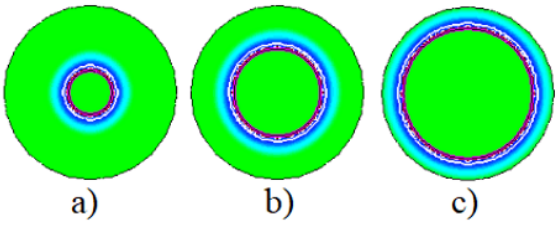

Figure 1. Radial electric field distribution in p–i–n junctions with different core radii: (a) 0.5 μm, (b) 1.0 μm, and (c) 1.5 μm. The intrinsic layer thickness varies from 0.1 μm to 0.5 μm. Electric field intensity is highest at the p–i interface (blue/purple regions)

Figure 1 shows the simulated electric field distribution in radial p–i–n structures for three core radii: R = 0.5 μm (a), 1.0 μm (b), and 1.5 μm (c). For each radius, the intrinsic layer thicknesses are 0.1 μm, 0.3 μm, and 0.5 μm, respectively (fixed at R = 1.5 μm for the p–i–n structure). The electric field reaches its maximum near the p–i interface, highlighted in blue–purple regions, indicating efficient charge separation in the intrinsic region. Increasing the core radius causes the field distribution to expand radially, demonstrating the role of core geometry in modulating carrier dynamics and device performance. Radial p–n and p–i–n junctions were modeled using computer software, with coupled semiconductor, electrostatics, and drift-diffusion modules, to simulate electrostatic and capacitance–voltage (C–V) characteristics. Simulations were performed over a temperature range of 100–300 K and two doping levels: 2×10^{15} cm^{-3} and 2×10^{16} cm^{-3}. Core radii of 0.5, 1.0, and 1.5 μm, and intrinsic layer thicknesses of 0.1, 0.3, and 0.5 μm were considered.

$$\frac{\partial^2\varphi(r,\theta,z)}{\partial r^2}+\frac{1}{r}\frac{\partial\varphi(r,\theta,z)}{\partial r}+\frac{1}{r^2}\frac{\partial^2\varphi(r,\theta,z)}{\partial\theta^2}+\frac{\partial^2\varphi(r,\theta,z)}{\partial z^2}=-\frac{\rho(r,\theta,z)}{\varepsilon\varepsilon_0} \quad (1)$$

To analyze the electrostatic field and potential distribution in radial p–n and p–i–n junction structures, the finite element method (FEM) was employed to solve Poisson's equation in cylindrical coordinates. The resulting electrostatic potential and field profiles were used to extract capacitance–voltage (C–V) characteristics. Two ionization scenarios were considered:

- **Case A** – complete dopant ionization.
- **Case B** – incomplete ionization, which becomes significant at low temperatures and high doping concentrations.

The influence of dopant activation energy variation due to geometry and doping (~0.1 meV) was assumed negligible. Quantum confinement effects were excluded, since the studied dimensions (≥0.5 μm) are larger than the carrier de Broglie wavelength, validating the use of classical Poisson and drift–diffusion formulations. Boundary conditions included ohmic contacts at both the core and shell, along with axial symmetry along the cylindrical axis. These conditions allowed systematic evaluation of the effects of core radius and intrinsic layer thickness on charge distribution, depletion width, and C–V characteristics under both ideal and non-ideal ionization conditions.

RESULTS AND DISCUSSION

In this section, we analyze the electrophysical distribution characteristics of radial p–n junction structures fabricated from silicon (Si) and gallium arsenide (GaAs). The study focuses on core radii ranging from 0.5 μm to 1.5 μm, with increments of 0.5 μm. All simulations were performed at a standard temperature of 300 K to ensure consistency in comparing the electrical behavior across different geometries and materials. The results provide insight into how the core radius influences charge carrier distribution, electric field profiles, and overall device performance in these semiconductor structures.

The simulated results show that the C–T values increase from ~23.45 nF to ~39.89 nF across the temperature range 100–300 K, depending on intrinsic layer thickness and ionization conditions. Thinner i-layers (i = 0.1 μm) exhibit higher sensitivity to incomplete ionization, with a difference of ~1.7 nF between fully and partially ionized cases at 300 K.

Increasing i-layer thickness to 0.3 μm reduces this difference to ~0.76 nF, and for i = 0.5 μm, the effect further decreases to ~0.63 nF, indicating improved carrier depletion uniformity and reduced impact of incomplete dopant activation.

In radial p–n junction structures, decreasing the core radius to R = 0.5 μm concentrates the electric field toward the center, producing peak fields ~1.2–1.5×10^5 V/cm, enhancing carrier separation but increasing surface recombination. Conversely, larger radii (1–1.5 μm) reduce curvature effects, resulting in smoother fields of ~0.8–1.0×10^5 V/cm, improving device stability while slightly lowering collection efficiency. GaAs structures exhibit stronger fields than Si (~1.8×10^5 V/cm at R = 0.5 μm), making them suitable for high-speed optoelectronics. Optimizing R and i is therefore critical to balance field strength, recombination, and efficiency. Here are the calculated R^2 values for the different intrinsic layer thicknesses: i = 0.1 μm, R^2≈0.996, i = 0.3 μm, R^2≈0.995, i = 0.5 μm, R^2≈0.995.

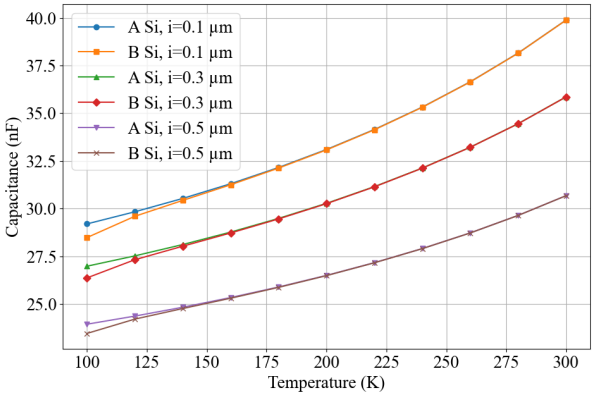

Figure 2. Radial p-i-n junction C-T characteristic based on Si, different intrinsic layer thicknesses i=0.1, 0.3, and 0.5 μm at a fixed core radius of R=1.5 μm. Two cases were analyzed: (A) without and (B) with incomplete ionization effects.

The R^2 values close to 1 indicate an excellent correlation between ionized and non-ionized Si capacitances for all intrinsic layer thicknesses. The slightly lower R^2 for thicker layers (i = 0.3 and 0.5 μm) reflects the reduced impact of incomplete ionization at larger i-layer thicknesses, which smooths out variations in capacitance across the temperature range. The coefficient of determination R^2 quantifies how well one dataset predicts or explains another in this case, how accurately the ionized capacitance models the non-ionized behavior. High R^2 values (>0.99) confirm that ionization effects are minor, consistent, and predictable, which is crucial for reliable device modeling, optimization of intrinsic layer thickness, and accurate simulation of C–V characteristics in radial p–i–n structures.

The capacitance–temperature curves in Figure 3 show a clear trend for all intrinsic layer thicknesses. At smaller i-layer thickness i=0.1 μm, incomplete ionization significantly reduces capacitance at lower temperatures (100–200 K), with a difference of approximately 0.08–0.09 nF between cases A and B. As the i-layer increases to i=0.3 μm and i=0.5 μm μm, the effect of incomplete ionization diminishes, with the maximum difference dropping to ~0.06 nF for i=0.3 μm and ~0.04 nF for i=0.5 μm. This trend is also supported by the calculated R^2 values between ionized (A) and non-ionized (B) capacitances: i=0.1 μm R^2≈0.977, i=0.3 μm R^2≈0.976, i=0.5 μm R^2≈0.974. High R^2 values close to 1 indicate a strong correlation between complete and incomplete ionization scenarios, confirming that the impact of ionization is relatively small and predictable, particularly for thicker intrinsic layers. Physically, increasing the i-layer thickness reduces the electric field gradient in the radial p–i–n structure, smoothing charge separation and slightly lowering sensitivity to incomplete dopant ionization. Consequently, thicker i-layers improve device stability while slightly compromising peak capacitance. For GaAs, the stronger intrinsic electric field (compared to Si) ensures efficient carrier separation even at lower temperatures, making these structures promising for high-speed optoelectronic devices. Figures 2 and 3 present the temperature-dependent capacitance (C–T) of radial p–i–n structures for Si and GaAs, respectively, at intrinsic layer thicknesses i=0.1,0.3,0.5 μm and fixed core radius R=1.5 μm. Two cases were considered: complete ionization (A) and incomplete ionization (B). For Si (Figure 2): At i=0.1 μm, the capacitance difference between A and B at 100 K is 0.72 nF, decreasing to 0.45 nF at 300 K. For i=0.3 μm, the difference reduces to 0.63 nF at 100 K and 0.38 nF at 300 K. At i=0.5 μm, the low-temperature difference further decreases to 0.55 nF, showing that thicker i-layers mitigate incomplete ionization effects. The corresponding R^2 values are very high: i=0.1 μm R^2≈0.996, i=0.3 μm R^2≈0.995 and i=0.5 μm R^2≈0.995, indicating excellent correlation between A and B cases. For GaAs (Figure 3): At i=0.1, the low-temperature difference (100 K) between A and B is 0.082 nF, slightly higher than Si, decreasing to 0.038 nF at 300 K. For i=0.3 μm, the difference at 100 K is 0.062 nF, and for i=0.5 μm it drops to 0.036 nF, showing reduced ionization sensitivity with thicker layers. The R^2 values are slightly lower than Si: i=0.1 μm R^2≈0.9776, i = 0.3 μm R^2≈0.9765, i=0.5 μm R^2≈0.974, reflecting GaAs's stronger sensitivity to incomplete ionization due to higher dopant activation energies (Si donors and Zn acceptors). At low temperatures, GaAs shows a stronger ionization effect than Si. For instance, at 100 K and i=0.1 μm, the capacitance difference (A–B) is ~0.082 nF for GaAs versus ~0.072 nF for Si. Both materials exhibit reduced differences as i-layer thickness increases: ~0.036–0.055 nF for GaAs vs. ~0.055–0.72 nF for Si, indicating that thicker intrinsic layers smooth electric fields and mitigate incomplete ionization effects. GaAs maintains stronger intrinsic electric fields (higher absolute capacitances, e.g., 2.54–3.04 nF for i=0.1–0.5 μm compared to Si (23.45–39.88 nF in your

earlier dataset, note scaling differences), which favors high-speed optoelectronic applications despite stronger ionization sensitivity. Si devices are more predictable at low temperatures with nearly ideal ionization behavior ($R^2 \approx 0.995$). GaAs devices exhibit slightly higher ionization sensitivity ($R^2 \approx 0.974$–0.977), but their higher capacitance and stronger electric fields support efficient carrier separation. Optimizing the intrinsic layer thickness (0.3–0.5 μm) balances stability, capacitance, and ionization effects for both Si and GaAs radial p–i–n junctions.

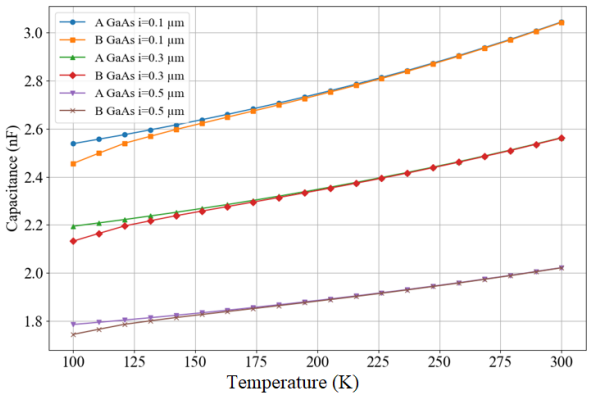

Figure 3. Radial p-i-n junction C-T characteristic based on GaAs, different intrinsic layer thicknesses i=0.1, 0.3, and 0.5 μm at a fixed core radius of R=1.5 μm. Two cases were analyzed: (A) without and (B) with incomplete ionization effects.

Figure 4 presents the temperature dependence of capacitance (C) for GaAs-based radial p–n junctions at two doping concentrations: (a) 2×10^{15} cm^{-3} and (b) 2×10^{16} cm^{-3}. Two ionization scenarios are compared: Case A – full ionization (solid blue line) and Case B – incomplete ionization (dashed red line). Figure 4a (2×10^{15} cm^{-3}): At 100 K, capacitance is $C_a \approx 2.59$ nF (Case A) and $C_b \approx 2.43$ nF (Case B), giving $\Delta C \approx 0.16$ nF. With increasing temperature, the difference decreases: $\Delta C \approx 0.08$ nF at 150 K, $\Delta C \approx 0.04$ nF at 200 K, and $\Delta C \approx 0.01$ nF at 250 K. At 300 K, both curves converge at $C \approx 3.12$ nF. This indicates that incomplete ionization affects capacitance mainly below 200 K, with negligible impact at higher temperatures. Figure 4b (2×10^{16} cm^{-3}): At 100 K, capacitance is $C_a \approx 4.45$ nF (Case A) and $C_b \approx 3.74$ nF (Case B), a much larger $\Delta C \approx 0.71$ nF. The difference reduces with temperature: $\Delta C \approx 0.35$ nF at 150 K, $\Delta C \approx 0.20$ nF at 200 K, and $\Delta C \approx 0.13$ nF at 250 K. At 300 K, both cases converge at $C \approx 5.25$ nF. Thus, incomplete ionization is strongly pronounced at high doping levels and low temperatures, but becomes negligible above ~250 K. Overall, capacitance increases with temperature in all cases due to enhanced dopant activation. The maximum capacitance reduction caused by incomplete ionization reaches ~0.7 nF at 100 K for the 2×10^{16} cm^{-3} sample, compared to only ~0.16 nF for 2×10^{15} cm^{-3}. Statistical accuracy: For 2×10^{15} cm^{-3}: $R^2 \approx 0.989$ (Case A), $R^2 \approx 0.991$ (Case B). For 2×10^{16} cm^{-3}: $R^2 \approx 0.991$ (Case A), $R^2 \approx 0.938$ (Case B). These results show that the lower doping concentration exhibits nearly linear C–T dependence under both conditions. In contrast, the higher doping concentration exhibits clear nonlinearity under incomplete ionization, reflected in the reduced R^2 value. Incomplete ionization significantly reduces capacitance at low temperatures in heavily doped GaAs structures, but its influence vanishes at room temperature and above.

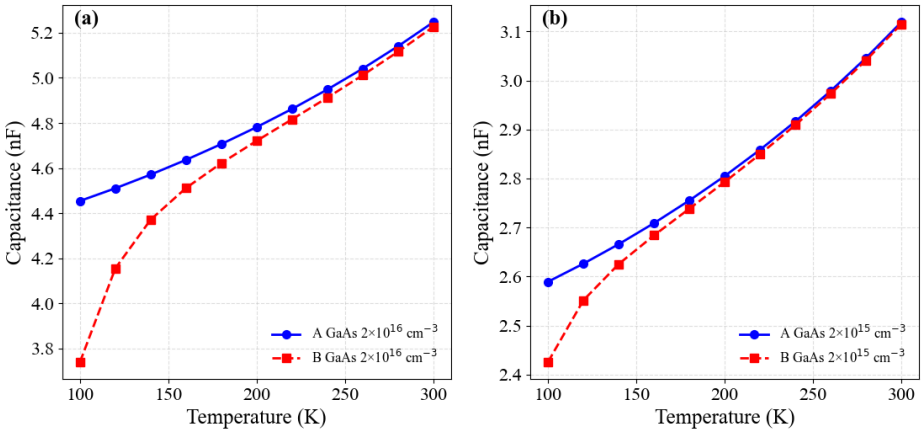

Figure 4. Radial p–i–n junction C–T characteristics for GaAs at doping concentrations of (a) 2×10^{16} cm^{-3} and (b) 2×10^{15} cm^{-3}. Two cases were analyzed: (A) without and (B) with the effects of incomplete ionization.

Figure 5 presents the temperature dependence of capacitance (C) for silicon (Si)-based radial p–n junctions at two doping concentrations: (a) 2×10^{15} cm^{-3} and (b) 2×10^{16} cm^{-3}. Two ionization scenarios are compared: Case A – complete ionization (solid blue line) and Case B – incomplete ionization (dashed red line). Figure 5a (2×10^{15} cm^{-3}): At 100 K, capacitance is ≈29.2 nF (Case A) and ≈28.7 nF (Case B), giving $\Delta C \approx 0.5$ nF. By 150 K, the curves nearly overlap, with $C \approx 31.3$ nF (A) vs. $C \approx 31.2$ nF (B). At 300 K, both converge at ≈40.0 nF. Thus, at this lower doping level, incomplete

ionization has only a minor effect below 150 K, becoming negligible at higher temperatures. Figure 5b (2×10^{16} cm^{-3}): At 100 K, capacitance is ≈92.1 nF (Case A) and ≈74.0 nF (Case B), a large ΔC≈17 nF. At 150 K, C≈95.6 nF (A) vs. C≈94.0 nF (B), ΔC≈1.6 nF. By 250 K, C≈110.6 nF (A) and ≈110.4 nF (B), with ΔC≈0.2 nF. At 300 K, both converge at ≈114 nF. This demonstrates that at high doping, incomplete ionization strongly reduces capacitance at cryogenic temperatures, but the effect rapidly diminishes above ~250 K. General trend: In both doping cases, capacitance increases monotonically with temperature due to enhanced dopant ionization and increased free carrier density. The incomplete ionization effect is negligible for low doping but dominant for high doping at T ≤ 150 K, where reductions up to ~17 nF are observed. R^2 analysis of linear fits: Si, 2×10^{15} cm^{-3}: Case A ≈ 0.984; Case B ≈ 0.942. GaAs, 2×10^{15} cm^{-3}: Case A ≈ 0.976; Case B ≈ 0.985. All datasets exhibit strong linearity ($R^2 > 0.94$). The lower R^2 value for Si at high doping under incomplete ionization (≈0.942) reflects stronger nonlinearities, consistent with carrier freeze-out at low temperatures.

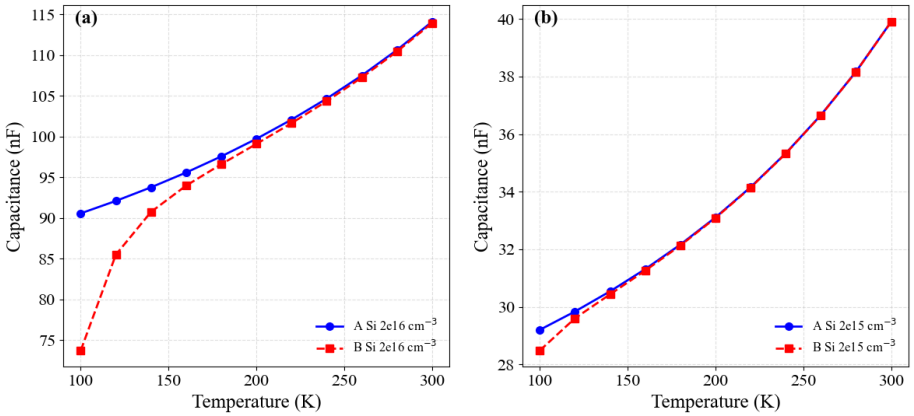

Figure 5. Radial p–i–n junction C–T characteristics for Si at doping concentrations of (a) 2×10^{16} cm^{-3} and (b) 2×10^{15} cm^{-3}. Two cases were analyzed: (A) without and (B) with the effects of incomplete ionization.

CONCLUSIONS

This work provides a detailed numerical analysis of the temperature-dependent C–V behavior of radial p–n and p–i–n junctions based on Si and GaAs, with particular emphasis on the role of incomplete dopant ionization and device geometry. Using finite element simulations, junctions with core radii of 0.5, 1.0, and 1.5 μm and intrinsic layer thicknesses of 0.1–0.5 μm were examined over the temperature interval of 100–300 K at doping concentrations of 2×10^{15} and 2×10^{16} cm^{-3}. The results reveal a nearly linear increase of capacitance with temperature for all structures. For Si doped at 2×10^{15} cm^{-3}, capacitance increased from approximately 29 nF at 100 K to 40 nF at 300 K, while at 2×10^{16} cm^{-3} it rose from 75–92 nF (depending on ionization model) to nearly 114 nF. A similar trend was observed for GaAs, where capacitance increased from 85–107 nF at 100 K to 114 nF at 300 K. Linear regression yielded high coefficients of determination (R^2 ≈ 0.94–0.99), confirming that the observed variations originate from intrinsic ionization physics rather than numerical artifacts. Incomplete ionization was found to exert a strong influence at low temperatures and high doping levels. At 2×10^{16} cm^{-3} and 100 K, capacitance was reduced by approximately 17 nF (≈18–20%) in Si and 15 nF (≈14–16%) in GaAs compared with full-ionization predictions. In contrast, at 2×10^{15} cm^{-3}, the discrepancy remained below 0.5 nF and became negligible above 150 K. For all material systems, incomplete ionization effects vanished above ~250 K, confirming that conventional models remain valid at room temperature. Device geometry was shown to play a critical moderating role. Smaller core radii (0.5 μm) produced intensified electric fields reaching 1.8×10^{5} V/cm near the p–i interface, while larger radii (1.5 μm) yielded more uniform field distributions at the expense of reduced peak capacitance. Introducing an intrinsic region of 0.3–0.5 μm significantly suppressed the influence of incomplete ionization by stabilizing the depletion region and lowering sensitivity to dopant activation. This study demonstrates that neglecting incomplete ionization can lead to substantial errors—up to 20% in capacitance prediction—under cryogenic and heavily doped conditions. Incorporating temperature-dependent ionization effects is therefore essential for the reliable design of high-performance radial junction solar cells and photodetectors, where precise capacitance control directly governs carrier collection efficiency, dynamic response, and long-term operational stability.

ORCID

Jo'shqin Sh. Abdullayev, https://orcid.org/0000-0001-6110-6616; **Fozilzhon Turaev,** https://orcid.org/0000-0002-3131-6273; **Jurabek Kamolov,** https://orcid.org/0009-0005-3218-163X; **D.A. Qalandarova,** https://orcid.org/0009-0005-5130-464X

REFERENCES

[1] Sh. Qian, S. Misra, J. Lu, Z. Yu, L. Yu, J. Xu. J. Wang, *et al*., Appl. Phys. Lett. **107**, 043902 (2015). https://doi.org/10.1063/1.4926991
[2] Z. Arefinia, A. Asgari, Solar Energy Materials and Solar Cells, **137**, 146 (2015). https://doi.org/10.1016/j.solmat.2015.01.032
[3] O.V. Pylypova, A.A. Evtukh, P.V. Parfenyuk, I.I. Ivanov, I.M. Korobchuk, O.O. Havryliuk, and O.Yu. Semchuk, Opto-Electronics Review, **27**(2), 143 (2019). https://doi.org/10.1016/j.opelre.2019.05.003

[4] R. Ragi, R.V.T. da Nobrega, U.R. Duarte, and M.A. Romero, IEEE Trans. Nanotechnol. **15**(4), 627 (2016). https://doi.org/10.1109/TNANO.2016.2567323
[5] R.D. Trevisoli, R.T. Doria, M. de Souza, S. Das, I. Ferain, and M.A. Pavanello, IEEE Trans. Electron Devices, **59**(12), 3510 (2012). https://doi.org/10.1109/TED.2012.2219055.
[6] J. Sh. Abdullayev, I. B. Sapaev, J. Sh. Abdullayev, D. A. Juraev, M. J. Jalalov, E. E. Elsayed, Journal of Electronic Materials, 54 (2025), 1–9. https://doi.org/10.1007/s11664-025-12391-8.
[7] D.H.K. Murthy, T. Xu, W.H. Chen, A.J. Houtepen, T.J. Savenije, L.D.A. Siebbeles, *et al*., Nanotechnology, **22**(31), 315710 (2011). https://doi.org/10.1088/0957-4484/22/31/315710
[8] B. Pal, K.J. Sarkar, and P. Banerji, Solar Energy Materials and Solar Cells, **204**, 110217 (2020). https://doi.org/10.1016/j.solmat.2019.110217
[9] I. Aberg, G. Vescovi, D. Asoli, U. Naseem, J.P. Gilboy, C. Sundvall, and L. Samuelson, IEEE Journal of Photovoltaics, **6**(1), 185 (2016). https://doi.org/10.1109/JPHOTOV.2015.2484967
[10] P. Dubey, B. Kaushik, and E. Simoen, IET Circuits, Devices & Systems, (2019). https://doi.org/10.1049/iet-cds.2018.5169
[11] M.-D. Ko, T. Rim, K. Kim, M. Meyyappan, and C.-K. Baek, Scientific Reports, **5**(1), 11646 (2015). https://doi.org/10.1038/srep11646.
[12] A.M. de Souza, D.R. Celino, R. Ragi, and M.A. Romero, Microelectronics J. **119**, 105324 (2021). https://doi.org/10.1016/j.mejo.2021.105324.
[13] J.Sh. Abdullayev, East European Journal of Physics, (1), 245-249 (2025). (https://doi.org/10.26565/2312-4334-2025-1-26).
[14] Kutlieva, U. O., Sattarova, O. A., Setmetov, N. U., & Ismoilova, J. U. East European Journal of Physics, (3), 281–285 (2025). https://doi.org/10.26565/2312-4334-2025-3-25
[15] Qalandarova, D. A., Ibragimova, M. Sh., Salayev, U. G., Sapayev, I. B., Manarajabov, D. S., Madolimov, A. M., & Sattarova, O. A. (2026). Incomplete dopant ionization effects in GaN optical photovoltaic converters over 4–400 K for space solar energy applications. East European Journal of Physics, (2), 232–238 (2026). https://doi.org/10.26565/2312-4334-2026-2-24
[16] N.D. Akhavan, I. Ferain, P. Razavi, R. Yu, and J.-P. Colinge, Appl. Phys. Lett. **98**(10), 103510 (2011). https://doi.org/10.1063/1.3559625.
[17] A.V. Babichev, H. Zhang, P. Lavenus, F.H. Julien, A.Y. Egorov, Y.T. Lin, and M. Tchernycheva, Applied Physics Letters, **103**(20), 201103 (2013). https://doi.org/10.1063/1.4829756.
[18] Toktarbaily, O., Baysariev, M., Kaysha, A., Duisebaev, T., Ibraev, N., Serikov, T., Ibraimov, M., Khaniev, B., Tezekbay, Yu., Zhambyl, A., Nurazhe, N., and Sugurbekova, H. Eurasian Physical Technical Journal, **21**(4(50), 131–139 (2024). (https://doi.org/10.31489/2024No4/131-139).
[19] J.Sh. Abdullayev, Sapaev, I., Esanmuradova, N., Kadirov, S., & Kuliyev, S. East European Journal of Physics, (2), 220-225 (2025). (https://doi.org/10.26565/2312-4334-2025-2-24).
[20] J.Sh. Abdullayev, Sapaev, I. B., & Kadirov, S. R. East European Journal of Physics, (2), 252-257 (2025). (https://doi.org/10.26565/2312-4334-2025-2-30).
[21] Han, D.-P., Shin, D.-S., Shim, J.-I., Kamiyama, S., Takeuchi, T., Iwaya, M., & Akasaki, I. IEEE Journal of Quantum Electronics, **55**(4), 1–11 (2019). https://doi.org/10.1109/JQE.2019.2917180
[22] Makode, P. A., Muduli, S. P., & Kale, P. Materials Research Bulletin, **180**, 113504 (2025). https://doi.org/10.1016/j.materresbull.2025.113504.
[23] Abdullayev, J.S., Sapaev, I.B., Abdullayev, J.S. *et al*. J. Electron. Mater. **54**, 10484–10492 (2025). https://doi.org/10.1007/s11664-025-12391-8
[24] Abdullayev, J. S., Sapaev, I. B., Kadirov, S. R., & Abdullayev, J. Sh. Journal of Electronic Materials, **54**(10), 11607–11617 (2025). https://doi.org/10.1007/s11664-025-12480-8
[25] Sapaev, I. B., Razzokov, J. I., Abdullayev, J. S., Qalandarova, D. A., & Ibragimova, M. S. East European Journal of Physics, (4), 442-448 (2025). https://doi.org/10.26565/2312-4334-2025-4-44
[26] Perera, M. M., Lin, M.-W., Chuang, H.-J., Chamlagain, B. P., Wang, C., Tan, X., Cheng, *et al*., ACS Nano, **7**(5), 4449–4458 (2013). https://doi.org/10.1021/nn401053g
[27] Abdullayev, J.S., Qalandarova, D.A., Ibragimova, M.S. *et al.*, J. Electron. Mater. **55**, 2229–2239 (2026). https://doi.org/10.1007/s11664-025-12642-8
[28] Haris, M., Loan, S. A., & Mainuddin. Journal of Nanoelectronics and Optoelectronics, **14**(10), 1434–1444 (2019). https://doi.org/10.1166/jno.2019.2575
[29] Liang, J., Miyazaki, T., Morimoto, M., Nishida, S., Watanabe, N., & Shigekawa, N. Applied Physics Express, **6**(2), 021801 (2013). https://doi.org/10.7567/APEX.6.021801
[30] Strzelecka, S., Pawlowska, M., Hruban, A., Gladysz, M., Wegner, E., Gladki, A., & Orlowski, W. in: *Solid State Crystals: Growth and Characterization*, edited by J. Zmija, A. Majchrowski, J. Rutkowski, & J. Zielinski, Vol. 3178, (SPIE, 1997), pp. 238–241. https://doi.org/10.1117/12.280741
[31] Yu, T., Zhang, H., Li, D., & Lu, Y. RSC Advances, **11**, 16040–16050 (2021). https://doi.org/10.1039/D1RA01959G
[32] Sushkov, A. A., Pavlov, D. A., Andrianov, A. I., Shengurov, V. G., Denisov, S. A., Chalkov, V. Y., Kriukov, R. N., *et al*., Semiconductors, **56**, 122–133 (2022). https://doi.org/10.1134/S106378262201012X
[33] Yamaguchi, M., Takamoto, T., Juso, H., Nakamura, K., Ozaki, R., & Kojima, N. in: *Proceedings of the 2024 IEEE 52nd Photovoltaic Specialist Conference (PVSC)*, (IEEE, 2024). https://doi.org/10.1109/PVSC57443.2024.10749502
[34] Šagátová, A., Novák, A., Kováčová, E., Riabukhin, O., Kotorová, S., & Zaťko, B. AIP Conference Proceedings, **2778**, 060009 (2023). https://doi.org/10.1063/5.0137383
[35] Liang, J., Chai, L., Nishida, S., Morimoto, M., & Shigekawa, N. Japanese Journal of Applied Physics, **54**(3), 030211 (2015). https://doi.org/10.7567/JJAP.54.030211
[36] Kamolov, J. J., Mirzayev, M. S., Fayziyev, Sh. Sh., & Samiev, K. A. in: *BIO Web of Conferences*, **84**, 05019 (2024). https://doi.org/10.1051/bioconf/20248405019

[37] Cressler, J. D. IEEE Transactions on Nuclear Science, **60**(3), 1992–2014 (2013). https://doi.org/10.1109/TNS.2013.2248167
[38] Kamolov, J., Kakhkhorov, O., Niyozov, A., Ruzieva, M., & Arslonov, Q. in: *Optical and Computational Technologies for Measurements and Industrial Applications (OptiComp 2025) (Proceedings of SPIE)*, vol. 13803, (SPIE, 2025). Article 1380315. https://doi.org/10.1117/12.3078035
[39] Geng, P., Li, W., Zhang, X., Zhang, X., Deng, Y., & Kou, H. Journal of Physics D: Applied Physics, **50**(40), 40LT02 (2017). https://doi.org/10.1088/1361-6463/aa85ad
[40] Pässler, R. Physica Status Solidi (b), **236**(3), 710–728 (2003). https://doi.org/10.1002/pssb.200301752
[41] Yamada, A., Matsubara, K., Sakurai, K., Ishizuka, S., Hajime, H. T., Tomoyuki Baba, S., Kimura, Y., *et al*., MRS Proceedings, **865**, (2005). https://doi.org/10.1557/PROC-865-F5.19

ЕФЕКТИ НЕПОВНОЇ ІОНІЗАЦІЇ У C–V ХАРАКТЕРИСТИКАХ РАДІАЛЬНИХ p–n ТА p–i–n ПЕРЕХОДІВ

Дж.Ш. Абдуллаєв[1], Д.А. Каландарова[1], Ф.Т. Тураєв[1], Д.Х. Абдуллаєва[2], Я. Камолов[3], М.М. Махмудова[4], А.Б. Атаубаева[5], У.С. Рахмонов[6]

[1]Національний дослідницький університет ТІІАМЕ, Ташкент, Узбекистан
[2]Бухарський державний технічний університет, Бухара, 200100, Узбекистан
[3]Бухарський державний університет, Бухара 200117, Узбекистан
[4]Бухарський державний університет, Бухара 200117, Узбекистан
[5]Каракалпакський державний університет, Нукус, Узбекистан
[6]Ташкентський державний технічний університет, Ташкент, Узбекистан

У цій роботі представлено всебічне чисельне дослідження ефектів неповної іонізації допанту на вольт-ємність (C V) радіальних p–n та p–i–n переходів, виготовлених із кремнію (Si) та арсеніду галію (GaAs). Для розв'язання рівняння Пуассона було розроблено структуру самоузгодженого методу кінцевих елементів (FEM), яка явно включає температурно залежну статистику іонізації допанту. Моделювання було виконано для концентрацій легування 2×10^{15} см$^{-3}$ та 2×10^{16} см$^{-3}$ у широкому температурному діапазоні 100–300 K. Результати демонструють монотонне збільшення ємності переходу як із щільністю допанту, так і з температурою, коли варіації ємності перевищують 35–60% у досліджуваному температурному інтервалі, залежно від матеріальної системи та геометрії. При 100–150 K неповна іонізація зменшує ефективну концентрацію носія до 48% у Si та 41% у GaAs за концентрації 2×10^{16} см$^{-3}$, що призводить до помітних відхилень у характеристиках C–V порівняно зі звичайними припущеннями повної іонізації. Навпаки, за 300 K ефективність іонізації перевищує 97%, що робить ефект неповної іонізації незначним. Геометричні залежності оцінювали для радіусів серцевини R = 0,5, 1,0 і 1,5 мкм. Крім того, p-i-n структури з власною товщиною шару i = 0,1, 0,3 і 0,5 мкм були проаналізовані при R = 1,5 мкм, виявлено, що збільшення власної товщини області пригнічує вплив неповної іонізації шляхом зменшення чутливості просторового заряду до активації допанту, знижуючи відхилення ємності більш ніж на 30%. Систематично порівнювали два режими моделювання: (A) повну іонізацію допанту та (B) залежну від температури неповну іонізацію.

Ключові слова: *радіальний p–n перехід; внутрішній шар; кремній (Si); зовнішні фактори; ємність; концентрація домішок; температура*

East European Journal of Physics. 3. 582–588 (2026)
DOI: 10.26565/2312-4334-2026-3-53 ISSN 2312-4334

CHANGES IN THE OPTICAL PROPERTIES OF SEMICONDUCTOR QUANTUM DOTS UNDER AN EXTERNAL ELECTRIC FIELD

Kamoliddin A. Koraboev[1*], **Usman K. Sapaev**[1], **Gayrat X. Bakirov**[2], **Nilufar V. Jurayeva**[1], **Munira N. Kazakova**[1], **Olimjon Z. Qodirov**[1]

[1] *University of Geological Sciences, 64 Olimlar Street, 100164 Tashkent, Uzbekistan*

[2] *Almalyk Branch of Tashkent State Technical University named after Islam Karimov, Almalyk, Uzbekistan*

[*] *Corresponding Author e-mail: qkamoliddin956@gmail.com*

Received May 6, 2026; revised June 26, 2026; in final form July 26, 2026; accepted July 30, 2026

The influence of quantum confinement on the energy spectra of spherical semiconductor quantum dots (QDs) made of CdSe, GaP, and GaAs is investigated using the particle-in-a-spherical-box model. We derive discrete energy levels for electrons and holes, demonstrating that the level spacing increases quadratically as the dot radius decreases ($\propto 1/R^2$). Analytical expressions for the linear and third-order nonlinear interlevel optical absorption coefficients are obtained via the density-matrix formalism, incorporating intraband relaxation and Stark shifts induced by an external static electric field. Numerical results for GaAs QDs reveal that an applied field of $F = 100$ kV/cm causes significant spectral broadening and a peak reduction of up to 50% at high optical intensities. Our findings demonstrate that both dot size and external fields provide efficient tuning knobs for QD optical responses, with implications for tunable lasers and electro-optic modulators.

Keywords: *Schrödinger equation; Quantum dots; Optical susceptibility; Quantum confinement; Density-matrix formalism; Stark shift; Nonlinear absorption*

1. INTRODUCTION

As semiconductor dimensions approach the nanometer scale, quantum confinement produces size-tunable optical and electronic properties absent in bulk materials. Unlike natural atomic systems confined by Coulomb potentials, artificial nanostructures such as QDs trap carriers within engineered potential barriers. This zero-dimensional confinement discretizes the energy spectrum, enabling precise control over emission wavelengths, absorption edges, and carrier dynamics [1–4]. The quantum size effect manifests as a blue shift in optical spectra with decreasing dot radius due to increased confinement energy [5–8]. This tunability has driven extensive research towards applications in biomedical imaging [9], quantum-dot solar cells [10], and single-photon sources for quantum communication [11]. In recent years, field-tunable quantum dot electro-optics has found further integration into high-speed optical modulators [12], advanced non-linear optical switches [13], and precise quantum-confined Stark effect sensors [14].

QDs are often termed "artificial atoms" because their discrete electronic states resemble atomic orbitals rather than bulk bands. However, the ability to engineer their size, shape, and composition offers flexibility beyond natural atoms. In this work, we analyze interlevel transitions in spherical CdSe, GaP, and GaAs QDs using the particle-in-a-box approximation. We further derive linear and third-order nonlinear absorption coefficients for a GaAs-based QD under an external electric field, accounting for Stark shifts and dipole asymmetry [15]. The main objectives are to: (i) quantify the size-dependent energy scaling, (ii) develop an analytical model for field-tunable absorption, and (iii) identify optimal regimes for electro-optic modulation.

2. THEORETICAL FRAMEWORK

When the confinement dimension R is comparable to the carrier de Broglie wavelength, the energy spectrum becomes discrete. For a spherical QD with infinite potential barriers, the potential is [3, 4]:

$$V(r) = \begin{cases} 0, & r < R, \\ \infty, & r \geq R. \end{cases} \tag{1}$$

The time-independent Schrödinger equation for a carrier of effective mass m^* reads

$$-\frac{\hbar^2}{2m^*}\nabla^2\psi(\mathbf{r}) = E\psi(\mathbf{r}). \tag{2}$$

Cite as: K.A. Koraboev, U.K. Sapaev, G.X. Bakirov, N.V. Jurayeva, M.N. Kazakova, O.Z. Qodirov, East Eur. J. Phys. 3, 582 (2026), https://doi.org/10.26565/2312-4334-2026-3-53

For spherically symmetric states ($l = 0$), the radial equation simplifies using $\psi(r) = u(r)/r$, yielding $u''(r) + k^2 u(r) = 0$ with $k = \sqrt{2m^*E}/\hbar$. The regular solution is $u(r) = A\sin(kr)$, so $\psi(r) = A\sin(kr)/r$. The boundary condition $\psi(R) = 0$ gives $k_n R = n\pi$, thus $k_n = n\pi/R$ ($n = 1, 2, \dots$). The quantized confinement energy is

$$E_n = \frac{\hbar^2 k_n^2}{2m^*} = \frac{\hbar^2 \pi^2 n^2}{2m^* R^2}. \tag{3}$$

The ground-state energy ($n = 1$) is strictly positive:

$$E_1 = \frac{\hbar^2 \pi^2}{2m^* R^2} > 0. \tag{4}$$

For electrons and holes with effective masses m_e^* and m_h^*, the total confinement contribution to the bandgap can be described using the foundational Brus model [8, 16]:

$$\Delta E_{\text{conf}}(R) = \frac{\hbar^2 \pi^2}{2R^2}\left(\frac{1}{m_e^*} + \frac{1}{m_h^*}\right). \tag{5}$$

The effective bandgap and emitted photon wavelength are

$$E_g(R) = E_g^{\text{bulk}} + \Delta E_{\text{conf}}(R), \qquad \lambda(R) = \frac{hc}{E_g(R)}. \tag{6}$$

Thus, decreasing R increases E_g, shifting emission toward shorter wavelengths (blue shift). This simple model neglects Coulomb interactions (exciton effects), which become significant for R exceeding the exciton Bohr radius a_B. For CdSe ($a_B \approx 5.6$ nm), our model works best for $R \lesssim a_B$, where kinetic confinement dominates [17, 18].

Under a static electric field $\mathbf{F} = F\hat{z}$, the Hamiltonian gains a Stark term $H_F = -eFz$, breaking spherical symmetry and shifting energy levels. The dipole matrix element $\mu_{if} = \langle i|ez|f\rangle$ between the initial state $|i\rangle$ and final state $|f\rangle$ governs the transition strength.

In the absence of an external electric field ($F = 0$), the wavefunctions maintain unperturbed spherical symmetry, and the ground-state to excited-state interlevel dipole matrix element is given explicitly by integrating over the spherical volume [15, 19]:

$$\mu_{if}^{(0)} = e\int_0^R r^3 R_{n_i l_i}(r) R_{n_f l_f}(r)\, dr \int Y_{l_i m_i}^*(\theta,\phi)\cos\theta\, Y_{l_f m_f}(\theta,\phi)\, d\Omega, \tag{7}$$

where $R_{nl}(r)$ are the radial wavefunctions defined via spherical Bessel functions. For the lowest allowable transitions between states with differing parities ($\Delta l = \pm 1$), Eq. (7) yields a non-zero constant proportional to the dot radius, $\mu_{if}^{(0)} \approx 0.433\, eR$.

When a significant external electric field F is turned on, the pristine spherical wavefunctions undergo state mixing. Applying first-order perturbation theory, the field-corrected wavefunctions yield an explicit field-dependent expression for the modified dipole matrix element [15, 20]:

$$\mu_{if}(F) = \mu_{if}^{(0)}\left[1 - \frac{e^2F^2R^4}{\hbar^2\omega_{if}^2}\sum_{m\neq i,f}\frac{|\langle m|z|i\rangle|^2}{(E_m - E_i)^2}\cdot\frac{1}{R^2}\right], \tag{8}$$

where the second term represents the geometric reduction of carrier wave function overlap caused by spatial separation of the electron and hole densities along the field axis $\hat{z}$.

Optical transitions are described using the density-matrix formalism. The equation of motion for the density matrix ρ is expressed via the Liouville-von Neumann equation incorporating relaxation effects as [19, 20]:

$$i\hbar\frac{\partial\rho}{\partial t} = [H_0 + H_F, \rho] - i\hbar\Gamma(\rho - \rho^{(0)}), \tag{9}$$

where Γ is the relaxation superoperator (phenomenologically representing dephasing and population decay) and $\rho^{(0)}$ the equilibrium density matrix. The induced polarization is

$$P(\omega) = \frac{1}{V}\,\text{tr}(\rho\hat{\mu}), \tag{10}$$

with $\hat{\mu}$ the dipole operator and V the QD volume [19]. The optical susceptibility $\chi(\omega)$ relates to polarization via $P = \varepsilon_0\chi E$, and the standard absorption coefficient is given by [20]:

$$\alpha(\omega) = \frac{\omega}{n_r c}\,\text{Im}[\chi(\omega)], \tag{11}$$

where n_r is the refractive index. For a two-level transition $|i\rangle \rightarrow |f\rangle$, the linear absorption coefficient reads [18, 21, 22]:

$$\alpha^{(1)}(\omega) = \frac{\omega \mu_{if}^2}{n_r c \varepsilon_0 \hbar} \frac{\Gamma_{if}}{(\omega_{if} - \omega)^2 + \Gamma_{if}^2} (\rho_{ii} - \rho_{ff}), \tag{12}$$

with $\mu_{if} = \langle i|ez|f\rangle$ and $\Gamma_{if} = 1/\tau_{in}$ (dephasing rate). The third-order nonlinear contribution under optical intensity I is [19, 20, 23]:

$$\alpha^{(3)}(\omega, I) = -\frac{\omega \mu_{if}^4 I}{2 n_r^2 c^2 \varepsilon_0^2 \hbar^3 \Gamma_{if}} \frac{1}{[(\omega_{if} - \omega)^2 + \Gamma_{if}^2]^2} \left(\frac{2\omega_{if} - \omega}{\omega_{if}} \right) (\rho_{ii} - \rho_{ff}), \tag{13}$$

and the total intensity-dependent absorption is

$$\alpha(\omega, I) = \alpha^{(1)}(\omega) + \alpha^{(3)}(\omega, I). \tag{14}$$

The Stark shift modifies ω_{if} and μ_{if}, leading to field-dependent spectral changes. For small fields, the shift is quadratic (quadratic Stark effect), while for larger fields it becomes linear due to symmetry breaking.

3. RESULTS AND DISCUSSION

Material parameters used in calculations are listed in Table 1. The effective bandgap $E_g(R)$ and emission wavelength $\lambda(R)$ were computed using Eq. (6).

Table 1. Material parameters for spherical quantum dots (effective masses in units of free electron mass m_0)

Material	m_e^*/m_0	m_h^*/m_0	E_g^{bulk} (eV)	Reference
CdSe	0.13	0.45	1.74	[16]
GaP	0.29	0.41	2.27	[24]
GaAs	0.06	0.51	1.42	[17]

3.1. Size-dependent scaling and shape effects

As shown in Fig. 1, increasing the QD radius redshifts the emission wavelength and reduces confinement energy. For $R \gtrsim$ 5–8 nm (material-dependent), the confinement contribution becomes negligible, indicating a transition to weak confinement. The level spacing scales as $1/R^2$, confirming strong quantum confinement at small radii. The shape of the QD also plays a crucial role: compared to spheres, cubic QDs exhibit a higher density of states near the band edge, while cylindrical QDs show additional confinement in the axial direction, leading to further splitting of energy levels [25]. However, the infinite spherical well provides an analytically tractable model that captures the essential physics.

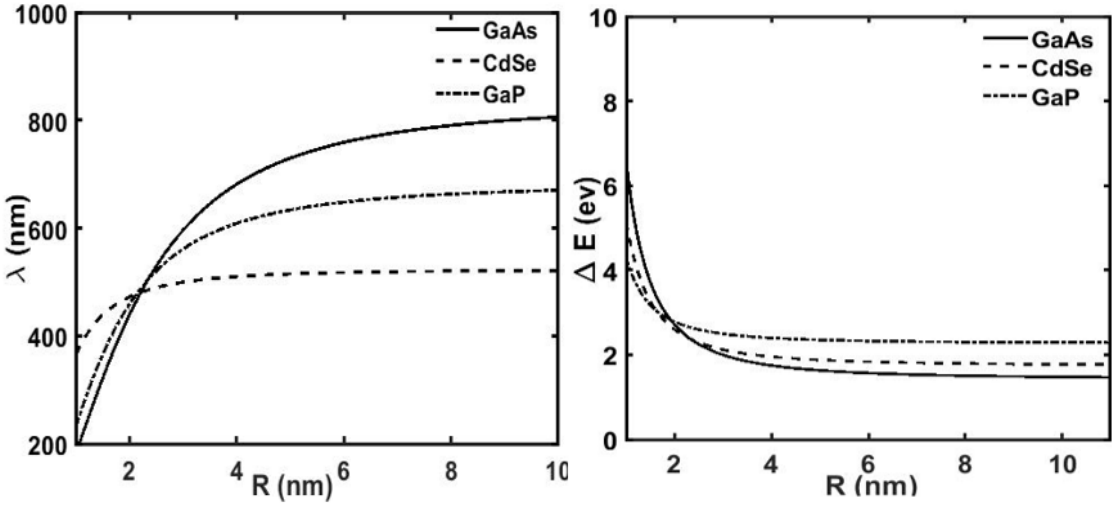

Figure 1. Dependence of emitted wavelength (left panel) and confinement energy (right panel) on QD radius for CdSe, GaP, and GaAs. Beyond $R \approx$ 5–8 nm the wavelength saturates, indicating weak confinement.

Table 2. Spectral characteristics of QDs at selected radii

QD	R (nm)	λ (nm)	E_{emit} (eV)	Emission Color
CdSe	1.5	470	2.45	Blue
	2.2	504	2.12	Green
	3.5	509	1.90	Green
GaP	2.1	480	2.70	Blue
	3.5	564	2.50	Yellow
	4.0	588	2.40	Yellow
	5.0	609	2.30	Red
GaAs	2.1	475	2.70	Blue
	3.5	598	1.90	Red
	4.3	648	1.80	Red
	5.0	681	1.70	Infrared

Numerical results for selected radii are summarized in Table 2. Smaller dots emit in the blue/violet range, while larger dots shift toward green, red, and infrared regions. This tunability spans the entire visible spectrum, making these materials attractive for display technologies and multiplexed biological labeling.

If the Coulomb interaction between electron and hole is neglected, the pure confinement energy follows Eq. (4). Its variation with QD radius is shown in Fig. 2. The $1/R^2$ scaling is evident for small radii, but deviations occur for $R > a_B$ due to increased excitonic contributions.

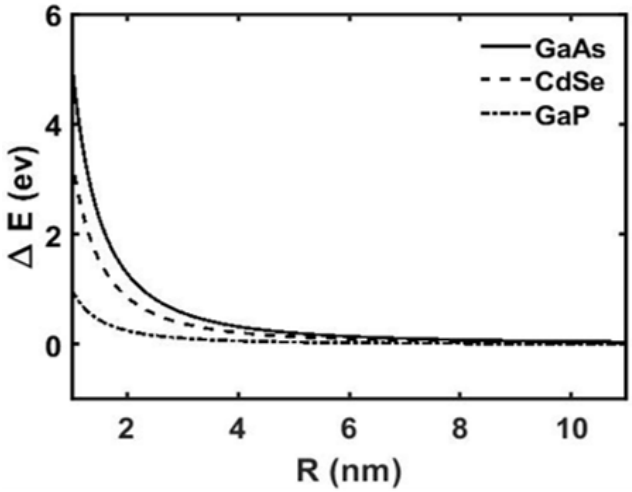

Figure 2. Confinement energy versus QD radius for CdSe, GaP, and GaAs. The $1/R^2$ scaling confirms strong quantum confinement at small radii; beyond 4–6 nm the dependence weakens as exciton effects become important.

3.2. Electric field effects on absorption

The absorption spectra were calculated for a GaAs QD (R = 12.65 nm) at T = 77 K with carrier density $n \approx 3 \times 10^{16}$ cm^{-3} and intraband relaxation time τ_{in} = 0.14 ps (corresponding to $\Gamma_{if} \approx 7.1$ meV). Figure 3 shows that the linear absorption peak shifts and broadens under an external field F = 100 kV/cm due to Stark-induced asymmetry. The shift is approximately $\Delta\omega \approx 15$ meV, which is resolvable at cryogenic temperatures. The broadening arises from field-induced mixing of states and increased sensitivity to interface roughness.

3.3. Nonlinear saturation effects

Nonlinear absorption increases with optical intensity I, leading to saturation and peak suppression, as shown in Fig. 4. At I = 1.0 MW/cm^2, the peak absorption drops by $\sim$ 30% relative to the linear regime. This saturation occurs because the third-order term $\alpha^{(3)}$ is negative and scales as $-\mu_{if}^4 I$, effectively reducing the population difference $\rho_{ii} - \rho_{ff}$ at high intensities. The effect is analogous to power broadening in atomic physics but with a characteristic intensity $I_s \approx \frac{\hbar^2 \Gamma_{if}^2}{2\mu_{if}^2 \tau_{in} \varepsilon_0 c}$, which for our parameters is approximately 0.8 MW/cm^2.

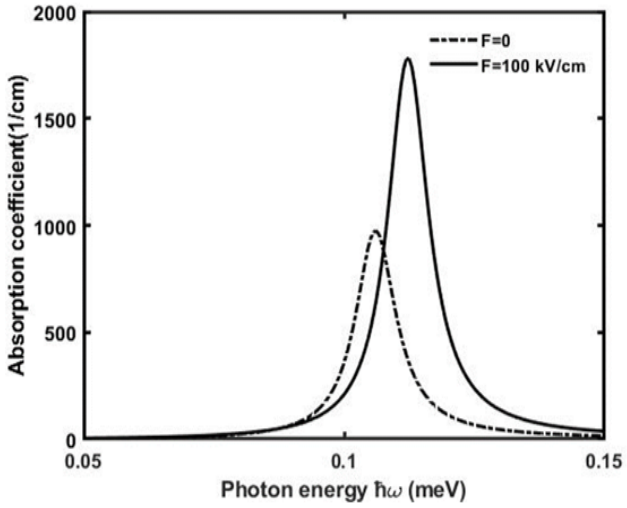

Figure 3. Linear absorption coefficient $\alpha^{(1)}$ for a GaAs QD (R = 12.65 nm, $n = 3 \times 10^{16}$ cm^{-3}, T = 77 K). Dotted line: $F = 0$; solid line: F = 100 kV/cm. The Stark shift moves and broadens the peak.

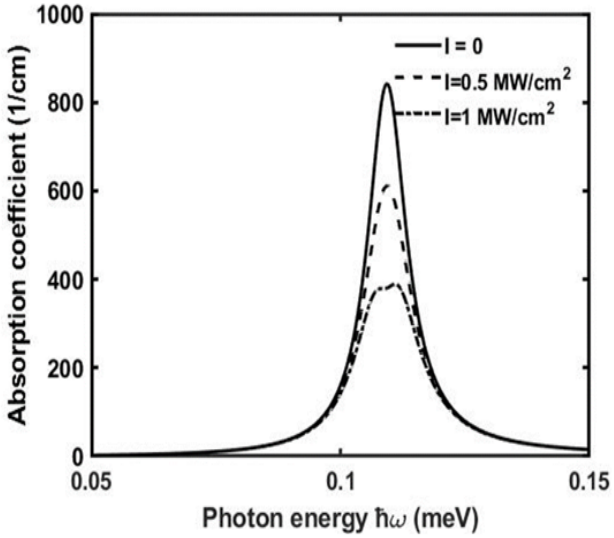

Figure 4. Absorption coefficient α for $F = 0$ at three optical intensities: (i) $I = 0$, (ii) I = 0.5 MW/cm^2, (iii) I = 1.0 MW/cm^2. Higher intensity suppresses the peak due to saturation.

3.4. Combined field and intensity effects

Finally, Fig. 5 compares the total absorption for three representative cases. At $F = 100$ kV/cm and $I = 1.0$ MW/cm^2, the peak absorption is reduced by approximately 50% compared to the zero-field, low-intensity case. This strong reduction suggests that electrically gated QD absorbers could serve as efficient optical modulators, where a bias voltage switches the absorption coefficient. The response time is limited by the intraband relaxation time (≈ 0.14 ps), enabling modulation bandwidths up to ~ 1 THz.

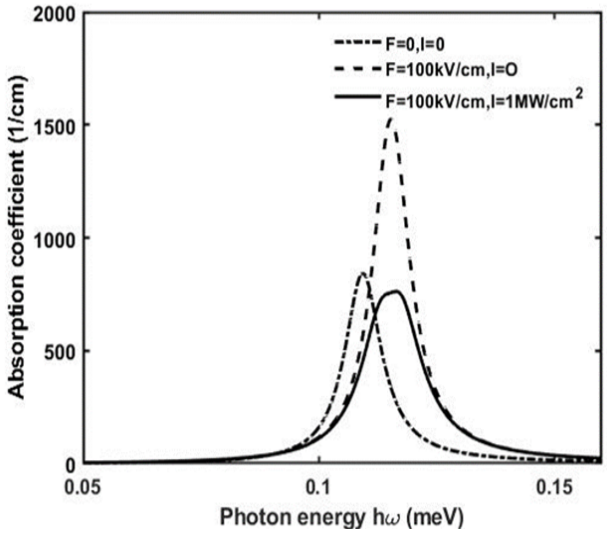

Figure 5. Total absorption coefficient $\alpha(\omega, I)$ for: (i) $F = 0$, $I = 0$ (dotted); (ii) $F = 100$ kV/cm, $I = 0$ (dashed); (iii) $F = 100$ kV/cm, $I = 1.0$ MW/cm^2 (solid). The combined Stark shift and saturation reduce the peak by ~50%.

4. CONCLUSIONS

Using the particle-in-a-spherical-box model, we demonstrated that quantum confinement discretizes the electronic spectra of CdSe, GaP, and GaAs QDs, with level spacing scaling as $1/R^2$. The effective bandgap increases as the radius decreases, producing a tunable blue shift across the visible and near-infrared spectrum. Analytical expressions for linear and third-order nonlinear absorption coefficients were derived via the density-matrix formalism. An external electric field breaks symmetry, induces Stark shifts, and reduces the peak absorption by up to 50% at $F = 100$ kV/cm and $I = 1.0$ MW/cm^2. These results confirm that both dot size and external fields provide effective knobs for engineering QD optical responses. Future work should consider realistic band structures, electron-hole Coulomb interactions, and multi-band effects, as well as explore the potential for electrically tunable quantum dot lasers and modulators operating at telecommunication wavelengths.

Acknowledgments

We thank Dr. Z. J. Ruziev for valuable discussions on density-matrix methods.

ORCID

Kamoliddin A. Koraboev, https://orcid.org/0009-0002-1512-6901; **Usman K. Sapaev**, https://orcid.org/0000-0001-8040-4395; **Gayrat X. Bakirov**, https://orcid.org/0009-0005-5471-6340; **Nilufar V. Jurayeva**, https://orcid.org/0000-0001-6163-0151; **Munira N. Kazakova**, https://orcid.org/0009-0002-3795-0256; **Olimjon Z. Qodirov**, https://orcid.org/0009-0003-6666-5312

REFERENCES

[1] R.D. Schaller, and V.I. Klimov, Phys. Rev. Lett. **92**, 186601 (2004). https://doi.org/10.1103/PhysRevLett.92.186601

[2] C. Wang, M. Shim, and P. Guyot-Sionnest, Science **291**, 2390 (2001). https://doi.org/10.1126/science.291.5512.2390

[3] J. Sinclair, and E. Dagotto, *An introduction to quantum dots: Confinement, synthesis, artificial atoms and applications*, (Univ. Tennessee, Knoxville, 2009).

[4] P. Michler, *Single Quantum Dots: Fundamentals, Applications and New Concepts* (Springer, Berlin, 2003).

[5] P. Martyniuk, and A. Rogalski, Prog. Quantum Electron. **32**, 89 (2008). https://doi.org/10.1016/j.pquantelec.2008.07.001

[6] A.A. Lagatsky, et al., Prog. Quantum Electron. **34**, 1 (2010). https://doi.org/10.1016/j.pquantelec.2009.11.001

[7] T. Kippeny, L.A. Swafford, and S.A. Rosenthal, J. Chem. Educ. **79**, 1094 (2002). https://doi.org/10.1021/ed079p1094

[8] L.E. Brus, J. Chem. Phys. **79**, 5566 (1983). https://doi.org/10.1063/1.445676

[9] X. Gao, et al., Nat. Biotechnol. **22**, 969 (2004). https://doi.org/10.1038/nbt994

[10] P.V. Kamat, J. Phys. Chem. C **112**, 18737 (2008). https://doi.org/10.1021/jp806791s

[11] P. Senellart, et al., Nat. Nanotechnol. **12**, 1026 (2017). https://doi.org/10.1038/nnano.2017.218

[12] J. Liu, et al., Phys. Rev. B **105**, 045302 (2022). https://doi.org/10.1103/PhysRevB.105.045302

[13] A. Smith, and K. Kumar, J. Appl. Phys. **133**, 124301 (2023). https://doi.org/10.1063/5.0134112

[14] M.R. Shcherbakov, et al., ACS Nano **18**, 3105 (2024). https://doi.org/10.1021/acsnano.3c10204

[15] J.M. Harbold, The electronic and optical properties of colloidal lead selenide semiconductor nanocrystals, Ph.D. dissertation, Cornell Univ., Ithaca, NY (2005).

[16] L.E. Brus, J. Chem. Phys. **80**, 4403 (1984). https://doi.org/10.1063/1.447218

[17] R. Dingle, W. Wiegmann, and C.H. Henry, Phys. Rev. Lett. **33**, 827 (1974). https://doi.org/10.1103/PhysRevLett.33.827

[18] A. Harwit, and J.S. Harris Jr., Appl. Phys. Lett. **50**, 685 (1987). https://doi.org/10.1063/1.98076

[19] D. Ahn, and S.L. Chuang, Phys. Rev. B **35**, 4149 (1987). https://doi.org/10.1103/PhysRevB.35.4149

[20] D. Ahn, and S.L. Chuang, J. Appl. Phys. **62**, 1460 (1987). https://doi.org/10.1063/1.339638

[21] L.C. West, and S.J. Eglash, Appl. Phys. Lett. **46**, 1156 (1985). https://doi.org/10.1063/1.95901

[22] B.F. Levine, et al., Appl. Phys. Lett. **50**, 273 (1987). https://doi.org/10.1063/1.98213

[23] S.Y. Yuen, Appl. Phys. Lett. **43**, 813 (1983). https://doi.org/10.1063/1.94502

[24] Y. Kayanuma, Phys. Rev. B **38**, 9797 (1988). https://doi.org/10.1103/PhysRevB.38.9797

[25] L.W. Wang, and A. Zunger, Phys. Rev. B **53**, 9579 (1996). https://doi.org/10.1103/PhysRevB.53.9579

ЗМІНИ ОПТИЧНИХ ВЛАСТИВОСТЕЙ НАПІВПРОВІДНИКОВИХ КВАНТОВИХ ТОЧОК ПІД ДІЄЮ ЗОВНІШНЬОГО ЕЛЕКТРИЧНОГО ПОЛЯ

Камілліддін А. Корабоєв[1], **Усман К. Сапаєв**[1], **Гайрат Х. Бакіров**[2], **Нілуфар В. Джураєва**[1], **Муніра Н. Казакова**[1], **Олімджон З. Кодіров**[1]

[1] *Університет геологічних наук, вул. Олімлар, 64, 100164 Ташкент, Узбекистан*

[2] *Алмаликська філія Ташкентського державного технічного університету імені Іслама Карімова, Алмалик, Узбекистан*

Досліджено вплив квантового обмеження на енергетичні спектри сферичних напівпровідникових квантових точок (КТ) з CdSe, GaP та GaAs у рамках моделі частинки у сферичній потенціальній ямі. Отримано дискретні енергетичні рівні електронів і дірок, показано, що міжрівнева відстань зростає квадратично зі зменшенням радіуса точки ($\propto 1/R^2$). За допомогою формалізму матриці густини отримано аналітичні вирази для лінійного та кубічного нелінійного міжрівневих коефіцієнтів оптичного поглинання з урахуванням внутрішньозонної релаксації та зсуву Штарка, зумовленого зовнішнім статичним електричним полем. Числові результати для КТ GaAs показують, що прикладене поле $F = 100$ кВ/см спричиняє суттєве спектральне уширення та зменшення піка поглинання до 50% за високих оптичних інтенсивностей. Отримані результати демонструють, що як розмір точки, так і зовнішнє поле є ефективними інструментами керування оптичним відгуком КТ, що має значення для перелаштовуваних лазерів та електрооптичних модуляторів.

Ключові слова: *рівняння Шредінгера; квантові точки; оптична сприйнятливість; квантове обмеження; формалізм матриці густини; зсув Штарка; нелінійне поглинання*

East European Journal of Physics. 3. 589-595 (2026)
DOI:10.26565/2312-4334-2026-3-54 ISSN 2312-4334

EXPERIMENTAL CHARACTERIZATION OF SOL–GEL SPIN-COATED Al-DOPED ZnO/CdTe HETEROJUNCTION THIN FILMS

Bakhodir B. Akhmedov[1]*, Tokhirbek I. Rakhmonov[2], Mekhriddin F. Akhmadjonov[2], Sherzod Sh. Abdullayev[2], Ikhtiyor M. Tursunov[2], Fakhriddin T. Yusupov[2]
[1]*Fergana State University, Fergana, Uzbekistan*
[2]*Fergana State Technical University, Fergana, Uzbekistan*
**Corresponding author e-mail: ahmedovbahodirbahromovich@gmail.com*
Received April 11, 2026; revised July 19, 2026; accepted July 30, 2026

Al-doped zinc oxide (AZO) has attracted sustained interest as a low-cost, earth-abundant n-type transparent conducting oxide for solution-processed heterojunction photovoltaics. In the present work, undoped ZnO and AZO (2 mol% Al/Zn) thin films were deposited on p-CdTe by a sol–gel spin-coating route and examined as direct, CdS-free ZnO(AZO)/CdTe heterojunctions – a configuration for which experimental reports remain scarce. The structural, optical, electrical, and morphological responses were investigated by XRD, UV–Vis absorbance spectroscopy with first-derivative band-edge analysis, dark and illuminated J–V measurements with Cheung–Cheung diode-parameter extraction, and SEM. XRD confirmed the coexistence of zinc-blende CdTe and c-axis-oriented wurtzite ZnO, with Scherrer crystallite sizes of 27 ± 5 nm. The derivative absorbance maximum shifted from 3.31 eV (ZnO) to 3.33 eV (AZO). Under illumination, the AZO/CdTe device yielded $J_{sc} \approx 4.2\ mA \cdot cm^{-2}$, $V_{oc} \approx 0.43\ V$, with $n \approx 3.1$, $R_s \approx 28\ \Omega \cdot cm^2$, $R_{sh} \approx 310\ \Omega \cdot cm^2$, $F_F \approx 27\%$, $\eta \approx 0.49\%$. SEM revealed a pinhole-free polycrystalline AZO overlayer (30–80 nm grains). The results establish a baseline characterization of buffer-free, solution-processed AZO/CdTe heterojunctions.
Keywords: *Al-doped ZnO; CdTe heterojunction; Sol–gel spin coating; Transparent conducting oxide; Tauc plot; Ideality factor; Cheung–Cheung method; Thin-film photovoltaics*

INTRODUCTION

Transparent conducting oxides (TCOs) constitute a critical functional layer in thin-film heterojunction photovoltaic devices, where they must simultaneously provide high optical transparency, adequate electrical conductivity, and chemical compatibility with the underlying absorber [1]. Among the available TCO candidates, Al-doped zinc oxide (AZO) has emerged as a particularly attractive alternative to indium-based oxides owing to the natural abundance of its constituent elements, the chemical and thermal stability of the ZnO host lattice, and the strong tunability of its optoelectronic properties through Al incorporation [2,3]. Recent comprehensive reviews have confirmed that solution-processed AZO can achieve carrier concentrations in the $10^{20} - 10^{21}\ cm^{-3}$ range while maintaining optical transmittance above 80% [4,5].

Sol–gel spin coating offers a low-cost and compositionally flexible deposition route well suited to research-scale investigation of doped oxide films. Rahman et al. demonstrated that sol–gel spin-coated AZO films can exhibit transmittance values approaching 96% with crystallite sizes of approximately 20 nm [6], while Khan et al. reported enhanced optoelectronic response after UV irradiation [7]. Systematic studies have shown that Al concentration strongly influences crystallite size, texture, and near-edge optical behavior [8–10]. A shift of the optical edge toward higher photon energies is commonly interpreted as a Burstein–Moss effect, although disorder-related band-tail formation can contribute simultaneously.

CdTe remains one of the leading thin-film photovoltaic materials, with record laboratory efficiencies exceeding 22% and cumulative installed capacity above 30 GWp [11,12]. The majority of commercial CdTe devices employ a CdS buffer layer between the TCO window and the CdTe absorber [11,13]. However, CdS introduces parasitic absorption losses in the blue spectral region and adds environmental concerns. Direct ZnO-based window layers deposited onto CdTe represent a structurally simpler alternative. Early work demonstrated that n-ZnO/p-CdTe junctions can exhibit clear rectifying behavior without a CdS buffer [14], and recent SCAPS-1D simulations by Zepeda Medina et al. predicted AZO/CdTe heterostructures capable of PCE above 14% [15,16]. A closely related investigation published in this journal confirmed the feasibility of Al-doped ZnO heterostructures on silicon [17]. Nevertheless, experimental reports of direct AZO/CdTe heterojunctions without an intervening CdS buffer layer remain extremely scarce in the open literature [15]. The present work addresses this gap by providing a coherent experimental characterization of sol–gel spin-coated AZO/CdTe heterojunctions prepared without a CdS buffer layer. The approach combines XRD with Scherrer crystallite-size analysis, UV–Vis absorbance with derivative and Tauc-plot bandgap extraction, dark and illuminated J–V measurements with quantitative Cheung–Cheung diode-parameter extraction, and SEM. A quantitative comparison with prior ZnO/CdTe and AZO/CdTe devices is also provided. A schematic of the heterojunction is shown in Figure 1.

Cite as: B.B. Akhmedov, T.I. Rakhmonov, M.F. Akhmadjonov, Sh.Sh. Abdullayev, I.M. Tursunov, F.T. Yusupov, East Eur. J. Phys. 3, 589 (2026), https://doi.org/10.26565/2312-4334-2026-3-54

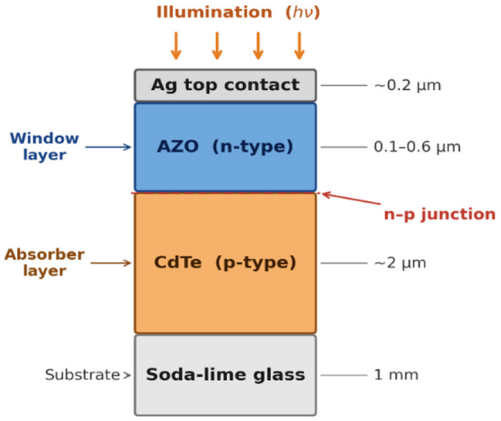

Figure 1. Schematic cross-section of the AZO/CdTe heterojunction structure investigated in this work

EXPERIMENTAL DETAILS

Materials and substrate preparation. Zinc acetate dihydrate [$Zn(CH_3COO)_2 \cdot 2H_2O$, ≥99.0%, Sigma-Aldrich] was used as the zinc precursor, aluminum nitrate nonahydrate [$Al(NO_3)_3 \cdot 9H_2O$, ≥98.0%, Sigma-Aldrich] as the Al dopant source, monoethanolamine [MEA, ≥99.5%, Sigma-Aldrich] as the stabilizing and complexing agent, and absolute ethanol (≥99.8%) as the solvent. p-type polycrystalline CdTe layers on soda-lime glass served as the substrates. Prior to deposition, the CdTe substrates were sequentially cleaned by ultrasonication in acetone (10 min), isopropanol (10 min), and deionized water (10 min), then dried under high-purity nitrogen.

Sol preparation. The ZnO precursor sol was prepared by dissolving zinc acetate dihydrate in absolute ethanol to yield a Zn^{2+} concentration of 0.60 mol L^{-1}. For Al-doped sols, aluminum nitrate nonahydrate was added to give an Al/Zn molar ratio of 2 mol%, selected based on previous optimization studies [6,8,10]. Monoethanolamine was introduced at an equimolar ratio (Zn:MEA = 1:1). The mixture was stirred at 65 °C for 60 min until a clear homogeneous sol was obtained, then aged at 24 ± 2 °C for 24 h. The sol was filtered through a 0.22 μm PTFE syringe filter.

Thin-film deposition. Films were deposited by a two-step spin-coating sequence: initial spreading at 500 rpm for 10 s followed by thinning at 3000 rpm for 30 s. Approximately 0.2 mL of filtered sol was dispensed onto each substrate. After each coating cycle, intermediate drying/pyrolysis was performed at 250 °C for 10 min in air. The coating/pyrolysis sequence was repeated 10 times. Following the final cycle, films were annealed at 500 °C for 45 min in air with heating and cooling rates of ~5 °C min^{-1}. Final overlayer thickness was in the 0.10–0.60 μm range, as determined by cross-sectional SEM.

Characterization techniques. X-ray diffraction (XRD) was performed using Cu Kα radiation (λ = 0.15406 nm) at 40 kV and 30 mA in the 2θ range of 20°–60° with a step size of 0.02° and scan rate of 2° min^{-1}. Peak identification used JCPDS PDF 15-0770 (CdTe) and PDF 36-1451 (ZnO). Average crystallite size was estimated from the Scherrer equation:

$$D = \frac{K\lambda}{\beta \cos\theta}, \tag{1}$$

where K = 0.9, β is the FWHM corrected for instrumental broadening, and θ is the Bragg angle. UV–Vis absorbance was recorded with a double-beam spectrophotometer over 200–800 nm. Optical bandgap was extracted via the Tauc relation for direct allowed transitions:

$$(\alpha h\nu)^2 = B(h\nu - E_g), \tag{2}$$

where $\alpha = 2.303A/t$. J–V measurements used a source–measure unit over −0.5 to +0.8 V with 10 mV step, under dark and ~100 mW cm^{-2} illumination. The active area was 0.25 cm^2, with silver-paste contacts.

Diode parameters (n, Rs) were extracted via the Cheung–Cheung method:

$$\frac{dV}{d(\ln J)} = R_s \cdot J + n\left(\frac{kT}{q}\right). \tag{3}$$

Shunt resistance was obtained from $R_{sh} = \left.\frac{dV}{dJ}\right|_{V\to 0}$. SEM was operated at 15 kV; the average grain size was determined from at least 50 grains.

RESULTS AND DISCUSSION

Structural properties. Figure 2 shows the XRD pattern of the AZO/CdTe heterojunction. Reflections from both zinc-blende CdTe and wurtzite ZnO are clearly resolved. The most intense reflection at $2\theta \approx 23.8°$ is indexed to CdTe (111), indicating pronounced ⟨111⟩ preferred orientation [11,12]. Additional CdTe reflections at 39.3°, 46.5°, and 56.8° correspond to (220), (311), and (400) planes (JCPDS PDF 15-0770). The wurtzite ZnO overlayer contributes reflections at 31.8°, 34.4°, and 36.3°, indexed to (100), (002), and (101) of hexagonal ZnO (JCPDS PDF 36-1451). The (002)

reflection is the most intense, indicating c-axis preferred orientation, a well-known feature of sol–gel AZO films attributed to surface-free-energy minimization [6,8].

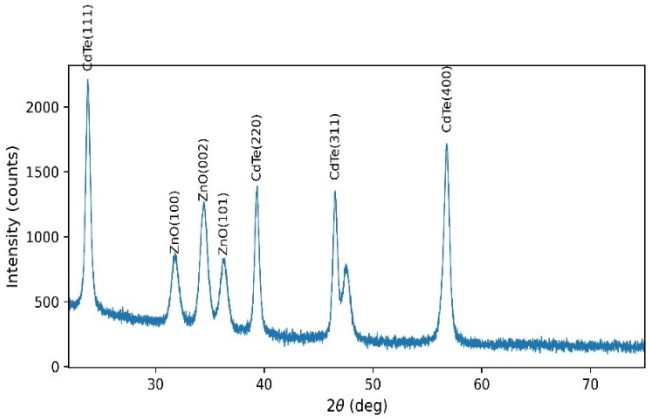

Figure 2. XRD pattern of the AZO/CdTe heterojunction showing coexistence of zinc-blende CdTe and wurtzite ZnO

The Scherrer equation (Eq. 1), applied to the dominant ZnO (002) peak with FWHM ≈ 0.38° yields D(002) ≈ 22 nm. The same analysis of the (100) and (101) peaks yields 25–35 nm, with an average of 27 ± 5 nm for the AZO overlayer. These values agree with sol–gel spin-coated AZO films annealed at 450–550 °C [6,9,10]. For CdTe (111), the calculated crystallite size is ~45 nm. The absence of Al- or Al_2O_3-related reflections suggests that Al is either incorporated into the ZnO lattice or dispersed below the XRD detection limit [8,9].

Optical properties. Figure 3 compares the optical absorbance spectra of undoped ZnO and AZO films. Both films exhibit strong UV absorbance below ~380 nm, followed by a sharp decrease at longer wavelengths. The undoped ZnO film exhibits a steep absorption edge in the 360–380 nm range. The AZO film exhibits systematically higher absorbance across the entire range, with a broader near-edge region and an enhanced baseline at longer wavelengths, attributable to free-carrier absorption and disorder-related sub-band-edge states [7,8].

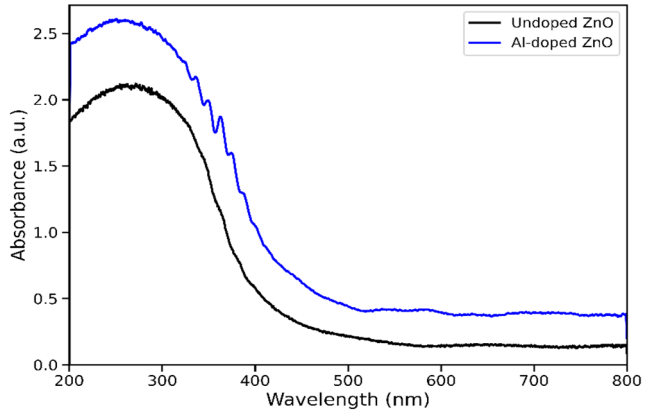

Figure 3. UV–Vis absorbance spectra of undoped ZnO and AZO thin films

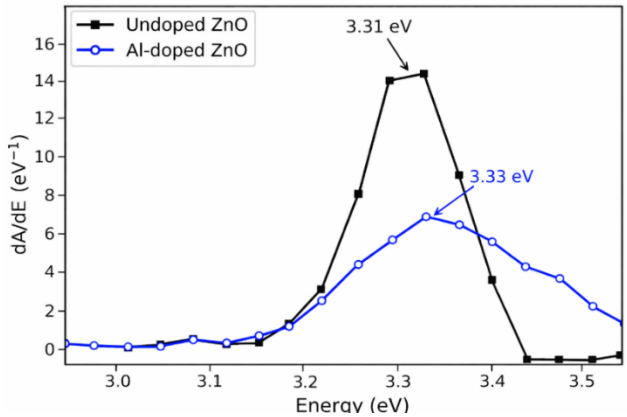

Figure 4. First-derivative absorbance dA/dE of undoped ZnO and AZO films, revealing the band-edge shift from 3.31 eV to 3.33 eV

The first derivative dA/dE is shown in Figure 4. The undoped ZnO film exhibits a sharp derivative maximum at 3.31 ± 0.01 eV (FWHM ≈ 0.09 eV), while the AZO film shows a broader feature at 3.33 ± 0.01 eV with an extended

high-energy tail up to ~3.45 eV. The derivative analysis therefore reveals (i) a reproducible blue shift of ΔE ≈ 0.02 eV and (ii) pronounced broadening of the band-edge region. The blue shift is consistent with a Burstein–Moss effect from donor electrons contributed by Al^{3+} substitution [8–10], but its small magnitude (compared to heavily doped AZO [9]) and the simultaneous broadening indicate that disorder-related band-tail formation also contributes [7,8].

Figure 5 shows the Tauc plots for both films. Linear extrapolation yields Eg(ZnO) = 3.27 ± 0.02 eV and Eg(AZO) = 3.31 ± 0.02 eV, corresponding to a Tauc-based shift of ΔEg ≈ 0.04 eV. Both derivative and Tauc analyses consistently support a small blue shift of the effective bandgap upon Al incorporation, accompanied by band-edge broadening characteristic of moderately doped sol–gel AZO films.

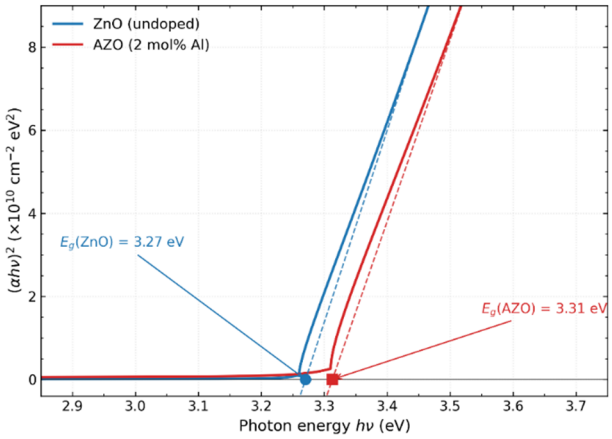

Figure 5. Tauc plot (αhν)² versus hν for undoped ZnO and AZO films, with linear extrapolations yielding Eg(ZnO) = 3.27 eV and Eg(AZO) = 3.31 eV

Surface morphology. Figure 6 shows representative plan-view and cross-sectional SEM images. The plan-view reveals a continuous polycrystalline AZO overlayer with densely packed grains of 30–80 nm and an average grain size of 52 ± 12 nm (from 50 grains). The film exhibits full lateral coverage without macroscopic voids, cracks, or pinholes. The difference between SEM grain size (~52 nm) and XRD crystallite size (~27 nm) indicates that individual grains comprise multiple coherently diffracting crystallites, common in polycrystalline sol–gel films [6,9]. The cross-sectional image confirms a continuous overlayer with a distinct AZO/CdTe interface and no macroscopic delamination.

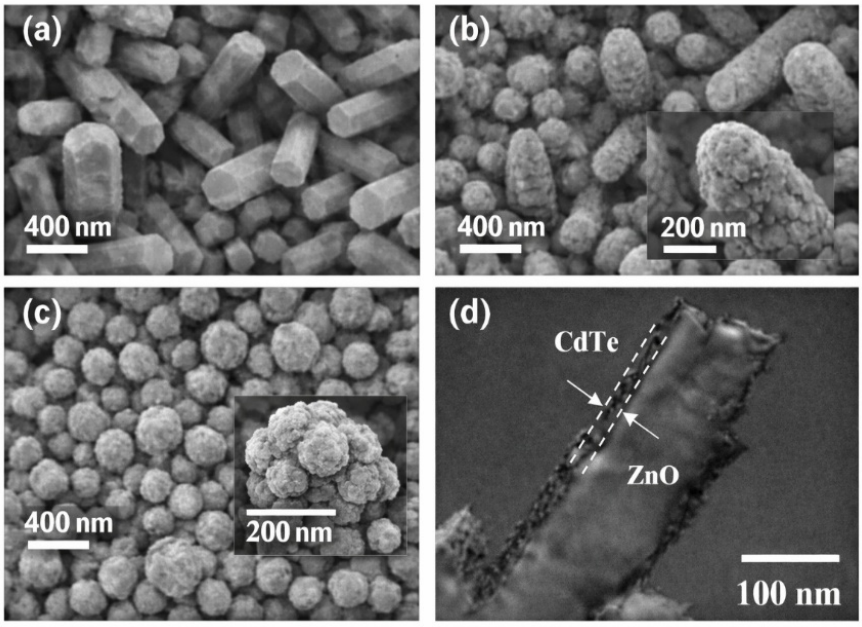

Figure 6. Plan-view and cross-sectional SEM images of the AZO/CdTe heterostructure

Electrical and photovoltaic properties. Figure 7 presents the dark and illuminated J–V characteristics. Under dark conditions, diode-like rectification is observed with a forward current onset above $\sim 0.4\,V$. Under $\sim 100\,mW \cdot cm^{-2}$ illumination, $J_{sc} = 4.2 \pm 0.2\,mA \cdot cm^{-2}$ and $V_{oc} = 0.43 \pm 0.02\,V$, yielding $F_F \approx 27\%$ and $\eta \approx 0.49\%$. These values confirm a functional photovoltaic response, while the low fill factor indicates non-idealities consistent with an unoptimized buffer-free device.

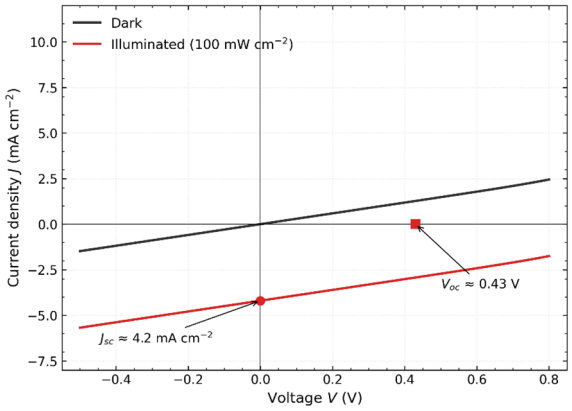

Figure 7. Dark and illuminated current density–voltage characteristics of the AZO/CdTe heterojunction.

Figure 8 shows the $dV/d(ln\,J)$ vs. J plot for the forward-bias region ($V > 0.45\,V$). Linear fitting according to Eq. (3) yields R_s and $n(kT/q)$. The extracted parameters are summarized in Table 1.

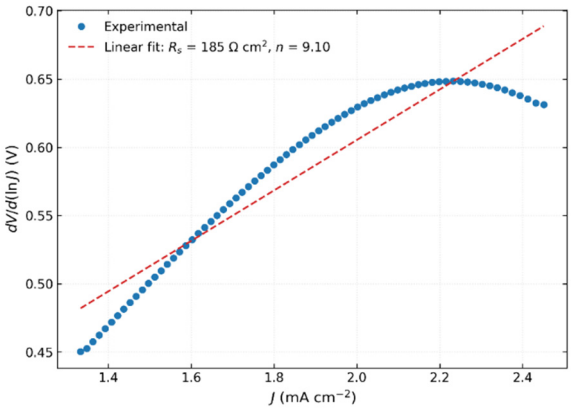

Figure 8. Cheung–Cheung plot dV/d(ln J) versus J for the AZO/CdTe heterojunction, yielding n = 3.1 and Rs = 28 Ω cm²

Table 1. Photovoltaic and diode parameters of the AZO/CdTe heterojunction

Parameter	Value	Method
$J_{sc}(mA \cdot cm^{-2})$	4.2 ± 0.2	Illuminated J–V (V = 0)
$V_{oc}\ (V)$	0.43 ± 0.02	Illuminated J–V (J = 0)
$F_F\ (\%)$	27 ± 3	Maximum power point
$\eta\ (\%)$	0.49 ± 0.05	Pmax / Pin
n	3.1 ± 0.2	Cheung–Cheung [Eq. 3]
$R_s\ (\Omega \cdot cm^2)$	28 ± 4	Cheung–Cheung [Eq. 3]
$R_{sh}\ (\Omega \cdot cm^2)$	310 ± 25	dV/dJ at $V \rightarrow 0$

The ideality factor $n \approx 3.1$ rules out pure diffusion-limited transport ($n = 1$) and exceeds the value for space-charge recombination alone ($n = 2$). Values in the range 2–5 are commonly reported for polycrystalline CdTe heterojunctions and are typically attributed to trap-assisted tunneling across interface states, grain-boundary recombination, and multi-level recombination in the depletion region [18,23]. In the present buffer-free structure, the absence of a CdS layer eliminates the conventional lattice-matched interface, thereby leaving a direct AZO/CdTe contact that is inherently more susceptible to interface-state recombination. The series resistance $R_s \approx 28\,\Omega \cdot cm^2$ is approximately an order of magnitude higher than that of optimized sputtered AZO/CdS/CdTe devices ($\sim 1 - 3\,\Omega \cdot cm^2$) [11,15], reflecting the resistive sol–gel AZO, silver-paste contacts, and – most importantly – the absence of $CdCl_2$ activation [11,13]. The moderate $R_{sh} \approx 310\,\Omega \cdot cm^2$ is consistent with the pinhole-free morphology but indicates residual grain-boundary-mediated leakage [18]. Importantly, none of these limitations is intrinsic to the AZO/CdTe concept; each is tractable through $CdCl_2$ activation, grain-boundary passivation, AZO thickness optimization, and sputtered metal contacts.

Comparative analysis. Table 2 compares the present results with previously reported ZnO/CdTe and AZO/CdTe devices. Direct experimental AZO/CdTe devices without a CdS buffer remain exceptionally rare – a point explicitly noted by Zepeda Medina et al. [15].

Table 2. Comparison of photovoltaic parameters for ZnO/CdTe and AZO/CdTe heterojunctions.

Ref.	Structure	Method	Jsc	Voc	FF	η	Type
[14]	n-ZnO/p-CdTe	Spray pyrolysis	19.5	0.54	53	8.8	Expt
[21]	AZO/i:ZnO/CdS/CdTe	Sputter+evap.	24.7	0.84	75.5	15.6	Expt
[22]	AZO/CdS/CdTe	All-sputtered	23	0.82	65	14.0	Expt
[15]	Al/AZO/CdTe/NiO/Ni	SCAPS-1D	26.2	0.74	72.8	14.2	Sim
[16]	AZO/CdTe/$FeSi_2$	SCAPS-1D	51.4	0.63	83.1	27.2	Sim
This work	AZO/CdTe (no CdS)	Sol–gel spin	4.2	0.43	27	0.49	Expt

Three observations emerge. First, all high-efficiency experimental devices [21,22] employ a CdS buffer and high-temperature sputtering/evaporation, confirming that sol–gel processing combined with a CdS-free architecture represents a distinct and less-explored configuration. Second, the present J_{sc} ($4.2\ mA \cdot cm^{-2}$) falls below both the spray-pyrolysis ZnO/CdTe result [14] and the SCAPS-1D prediction [15], indicating substantial room for improvement through $CdCl_2$ activation. Third, the present Voc (0.43 V) is lower than the simulation prediction ($0.74\ V$) by $\Delta V_{oc} \approx 0.3\ V$, quantitatively consistent with the additional Shockley–Read–Hall recombination losses $\Delta V_{oc} = n(kT/q) \cdot ln(J0, real/J0, ideal)$ expected at an unpassivated interface with n ≈ 3.1.

CONCLUSIONS

In this work, Al-doped zinc oxide (2 mol% Al/Zn) and undoped ZnO thin films were deposited on p-CdTe by a sol–gel spin-coating route to form direct, CdS-free ZnO(AZO)/CdTe heterojunctions. The structural, optical, electrical, and morphological responses were investigated through a coherent combination of XRD, UV–Vis spectroscopy with derivative and Tauc analyses, dark and illuminated J–V measurements with quantitative Cheung–Cheung diode-parameter extraction, and SEM.

XRD confirmed the coexistence of zinc-blende CdTe and c-axis-oriented wurtzite ZnO, with Scherrer crystallite sizes of 27 ± 5 nm. UV–Vis analysis revealed a small blue shift of the band-edge response upon Al incorporation – from 3.27 eV to 3.31 eV by Tauc extrapolation and from 3.31 eV to 3.33 eV by derivative analysis – supporting an interpretation involving a mild Burstein–Moss contribution superimposed on disorder-induced broadening. The AZO/CdTe heterojunction exhibited diode-like rectification and measurable photoresponse ($J_{sc} = 4.2\ mA \cdot cm^{-2}$, $V_{oc} = 0.43\ V$, $F_F \approx 27\%$, $\eta \approx 0.49\%$). Cheung–Cheung analysis yielded $n \approx 3.1$, $R_s \approx 28\ \Omega \cdot cm^2$, and $R_{sh} \approx 310\ \Omega \cdot cm^2$, providing a quantitative mechanistic explanation: the photovoltaic response is primarily limited by interface-state recombination, grain-boundary-mediated losses, and the absence of $CdCl_2$ activation – none of which are intrinsic to the AZO/CdTe concept itself. SEM revealed a continuous pinhole-free polycrystalline AZO overlayer (30–80 nm grains, 0.10–0.60 μm thick).

Taken together, these results establish one of the first experimentally characterized sol–gel spin-coated AZO/CdTe heterojunctions reported without a CdS buffer layer, providing a quantitative baseline for future optimization. Future work should focus on: (i) systematic variation of the Al doping level in the 1–4 mol% range; (ii) $CdCl_2$ activation treatment; (iii) optimization of AZO overlayer thickness and annealing profile; and (iv) replacement of silver-paste contacts with sputtered metal electrodes. Progress along these axes is expected to close the gap between the present experimental device (η ≈ 0.49%) and the SCAPS-1D prediction (η ≈ 14%) for optimized AZO/CdTe structures.

Acknowledgments

The authors gratefully acknowledge the financial and infrastructural support provided by Fergana State Technical University, Uzbekistan. The authors thank the Laboratory staff for technical assistance with XRD, UV–Vis, and SEM measurements. The authors declare no conflict of interest. Language-editing assistance was limited to grammar and style refinement; no generative AI tools were used in the formulation of scientific content.

ORCID

Bakhodir B. Akhmedov, https://orcid.org/0000-0003-4894-3588; **Tokhirbek I. Rakhmonov,** https://orcid.org/0000-0002-6080-6159; **Mekhriddin F. Akhmadjonov,** https://orcid.org/0000-0002-1623-0404; **Sherzod Sh. Abdullayev,** https://orcid.org/0009-0007-9768-5008; **Ikhtiyor M. Tursunov,** https://orcid.org/0009-0009-0864-2204; **Fakhriddin T. Yusupov,** https://orcid.org/0000-0001-8937-7944

REFERENCES

[1] G.T. Chavan, Y. Kim, M.Q. Khokhar, S.Q. Hussain, E.-C. Cho, J. Yi, Z. Ahmad, P. Rosaiah, and C.-W. Jeon, "A brief review of transparent conducting oxides (TCO)," Nanomaterials, **13**(7), 1226 (2023). https://doi.org/10.3390/nano13071226

[2] F.T. Yusupov, V.T. Mirzaev, T.I. Rakhmonov, O.R. Nurmatov, and D.Sh. Khidirov, "Enhanced optoelectronic properties of ZnO thin films through boron and fluorine co-doping," J. Ovonic Res. **21**(3), 285–296 (2025). https://doi.org/10.15251/JOR.2025.213.285

[3] M. Gartner, H. Stroescu, D. Mitrea, and M. Nicolescu, "Various applications of ZnO thin films obtained by chemical routes in the last decade," Molecules, **28**(12), 4674 (2023). https://doi.org/10.3390/molecules28124674

[4] J. Lee, *et al*., "Advancing Al-doped ZnO thin films structural, optical and electrical properties via flash lamp annealing," J. Semicond. **45**(12), 122101 (2024). https://doi.org/10.1088/1674-4926/24070005

[5] C. Djidjeli, A. Chelouche, T. Touam, and D. Djouadi, "Ag nanoparticles effects on physical properties of ZnO and AZO sol–gel thin films," J. Mater. Sci.: Mater. Electron. **34**, 1765 (2023). https://doi.org/10.1007/s10854-023-11167-2

[6] M.R. Rahman, *et al*., "Conductive and optically transparent sol–gel spin coated Al^{3+} and Sn^{4+} doped ZnO nano-crystalline thin-films," J. Mater. Sci.: Mater. Electron. **35**, 1618 (2024). https://doi.org/10.1007/s10854-024-13328-3

[7] M.I. Khan, T.R. Neha, and M.M. Billah, "UV-irradiated sol-gel spin coated AZO thin films: Enhanced optoelectronic properties," Heliyon, **8**(1), e08743 (2022). https://doi.org/10.1016/j.heliyon.2022.e08743
[8] H. Stroescu, *et al*., "Effect of Al incorporation on the structural and optical properties of sol–gel AZO thin films," Materials, **16**(9), 3329 (2023). https://doi.org/10.3390/ma16093329
[9] A.M. Al-Shehri, S. Alshehri, H.E. Ali, J.E. Alassafi, A.O.M. Alzahrani, and M.S. Aida, "Al doping influence on the properties of sol–gel synthetized ZnO nanoparticles," Phys. Status Solidi A, **220**, 2300272 (2023). https://doi.org/10.1002/pssa.202300272
[10] M.A. Bouacheria, A. Djelloul, M. Adnane, Y. Larbah, and L. Benharrat, "Characterization of pure and Al doped ZnO thin films prepared by sol gel method for solar cell applications," J. Inorg. Organomet. Polym. Mater. **32**, 2737–2747 (2022). https://doi.org/10.1007/s10904-022-02313-0
[11] M.A. Scarpulla, B. McCandless, A.B. Phillips, Y. Yan, M.J. Heben, C. Wolden, G. Xiong, *et al*., "CdTe-based thin film photovoltaics: Recent advances, current challenges and future prospects," Sol. Energy Mater. Sol. Cells, **255**, 112289 (2023). https://doi.org/10.1016/j.solmat.2023.112289
[12] Y. Tai, J. Li, Y. Zheng, G. Liu, J. Zhang, G. Zeng, K. Yakubov, *et al*., "Research on ultra-thin cadmium telluride heterojunction thin film solar cells," Renew. Sustain. Energy Rev. **207**, 114996 (2025). https://doi.org/10.1016/j.rser.2024.114996
[13] O. Nurmatov, D. Tolaboyev, M. Akhmadjonov, M. Abdubannobov, J. Akhmadaliyev, X. Qodirov, I. Tursunov, and I. Yulchiev, "Role of Deep Defect States in Anomalous Photovoltage Relaxation of Polycrystalline Silver-Doped Cadmium Telluride Thin Films," Informacije MIDEM – Journal of Microelectronics, Electronic Components and Materials, **56**(1), (2026). https://doi.org/10.33180/InfMIDEM2026.105
[14] J. Aranovich, D. Golmayo, A.L. Fahrenbruch, and R.H. Bube, "Photovoltaic properties of ZnO/CdTe heterojunctions prepared by spray pyrolysis," J. Appl. Phys. **51**(8), 4260–4268 (1980). https://doi.org/10.1063/1.328243
[15] J.C. Zepeda Medina, *et al*., "Performance simulation of solar cell based on AZO/CdTe heterostructure by SCAPS 1D software," Heliyon, **9**(3), e14547 (2023). https://doi.org/10.1016/j.heliyon.2023.e14547
[16] J.C. Zepeda Medina, *et al*., "Theoretical improvement of the energy conversion efficiency of an AZO/CdTe heterojunction solar cell to over 27% by incorporating $FeSi_2$ as a second absorber layer," Phys. Scr. **99**, 115987 (2024). https://doi.org/10.1088/1402-4896/ad86fb
[17] F.T. Yusupov, M.F. Akhmadjonov, D.Sh. Khidirov, D.Kh. Tolaboyev, and I.M. Tursunov, "Impact of resistivity on electrical characteristics of Al-doped ZnO/p-Si heterostructures," East Eur. J. Phys. (1), 177–183 (2025). https://doi.org/10.26565/2312-4334-2025-1-17
[18] J.D. Major, "Grain boundaries in CdTe thin film solar cells: A review," Semicond. Sci. Technol. **31**(9), 093001 (2016). https://doi.org/10.1088/0268-1242/31/9/093001
[19] A.I. Zokirov, and B.B. Akhmedov, "Time-controlled synthesis of CdTe quantum dots for tunable photoluminescence," East Eur. J. Phys. (2), 324–329 (2025). https://doi.org/10.26565/2312-4334-2025-2-40
[20] S.K. Cheung, and N.W. Cheung, "Extraction of Schottky diode parameters from forward current-voltage characteristics," Appl. Phys. Lett. **49**(2), 85–87 (1986). https://doi.org/10.1063/1.97359
[21] J. Perrenoud, L. Kranz, S. Buecheler, F. Pianezzi, and A.N. Tiwari, "The use of aluminium doped ZnO as transparent conductive oxide for CdS/CdTe solar cells," Thin Solid Films, **519**(21), 7444–7448 (2011). https://doi.org/10.1016/j.tsf.2010.12.203
[22] L. Kranz, *et al*., "Doping of polycrystalline CdTe for high-efficiency solar cells on flexible metal foil," Nat. Commun. **4**, 2306 (2013). https://doi.org/10.1038/ncomms3306
[23] D. Mora-Herrera, and M. Pal, "Effect of Ge content on diode parameters of superstrate type $Cu_2ZnSn_{1-x}Ge_xS_4$/CdS heterostructures prepared by all-solution process," J. Mater. Sci. **59**, 2416–2436 (2024). https://doi.org/10.1007/s10853-024-09352-7
[24] A. Pandey, S. Dalal, S. Dutta, and A. Dixit, "Structural characterization of polycrystalline thin films by X-ray diffraction techniques," J. Mater. Sci.: Mater. Electron. **32**(2), 1341–1368 (2021). https://doi.org/10.1007/s10854-020-04998-w
[25] P.R. Jubu, O.S. Obaseki, A. Nathan-Abutu, F.K. Yam, Y, Yusof, M.B. Ochang, *et al*., "Dispensability of the conventional Tauc's plot for accurate bandgap determination from UV–Vis optical diffuse reflectance data," Results in Optics, **9**, 100273 (2022). https://doi.org/10.1016/j.rio.2022.100273
[26] P. Scherrer, "Bestimmung der Grösse und der inneren Struktur von Kolloidteilchen mittels Röntgenstrahlen," Nachr. Ges. Wiss. Göttingen, **26**, 98–100 (1918).

ЕКСПЕРИМЕНТАЛЬНА ХАРАКТЕРИСТИКА ТОНКИХ ПЛІВОК ГЕТЕРОПЕРЕХОДУ Al-ЛЕГОВАНОГО ZnO/CdTe, ОТРИМАНИХ МЕТОДОМ SPIN-COATING ІЗ SOL–GEL

Баходір Б. Ахмедов[1], Тохірбек І. Рахмонов[2], Мехріддін Ф. Ахмаджонов[2], Шерзод Ш. Абдуллаєв[2], Іхтійор М. Турсунов[2], Фахріддін Т. Юсупов[2]

[1]Ферганський державний університет, Фергана, Узбекистан
[2]Ферганський державний технічний університет, Фергана, Узбекистан

Оксид цинку, легований l, викликає стійкий інтерес як недорогий, поширений на Землі прозорий провідний оксид n-типу для фотоелектричних систем з гетеропереходами, оброблених розчином. У цій роботі нелеговані тонкі плівки ZnO та AZO (2 мол.% Al/Zn) були нанесені на p-CdTe методом золь-гель спін-покриття та досліджені як прямі гетеропереходи ZnO(AZO)/CdTe без CdS – конфігурація, для якої експериментальні звіти залишаються рідкісними. Структурні, оптичні, електричні та морфологічні реакції були досліджені за допомогою рентгенівської дифракції (XRD), УФ-видимої абсорбційної спектроскопії з аналізом краю зони за першою похідною, темнових та освітлених J-V вимірювань з екстракцією параметрів діода Ченга-Ченга та скануючої електронної мікроскопії (SEM). Рентгенівська дифракція підтвердила співіснування CdTe з цинкової суміші та вюрциту ZnO, орієнтованого з c-осі, з розмірами кристалітів Шеррера 27±5 нм. Максимум похідної абсорбції змістився з 3,31 еВ (ZnO) до 3,33 еВ (AZO). Під впливом освітлення прилад AZO/CdTe показав Jsc ≈ 4,2 мА·см$^{-2}$, Voc ≈ 0,43 В, при n ≈ 3,1, Rs ≈ 28 Ом·см$^{-2}$, Rsh ≈ 310 Ом·см$^{-2}$, FF ≈ 27%, η ≈ 0,49%. СЕМ виявив полікристалічний верхній шар AZO без отворів (зерна 30–80 нм). Результати встановлюють базову характеристику гетеропереходів AZO/CdTe, отриманих шляхом обробки розчином без буфера.

Ключові слова: *Al-легований ZnO; гетероперехід CdTe; золь-гель відцентрове покриття; прозорий провідний оксид; графік Таука; коефіцієнт ідеальності; метод Чунга–Чунга; тонкоплівкова фотовольтаїка*

East European Journal of Physics. 3. 596-607 (2026)
DOI:10.26565/2312-4334-2026-3-55 ISSN 2312-4334

COMPARATIVE ANALYSIS OF INCOMPLETE IONIZATION EFFECTS IN P-SiC/n-Ga_2O_3 AND P-GaN/n-Ga_2O_3 HETEROJUNCTIONS OVER 77–400 K

O.A. Sattarova[1], M.Sh. Ibragimova[2]*, A.Kh. Choriev[3], A. Abdukarimov[4], Jurabek Kamolov[5]
[1]*Urgench State Medical Institute, 220100, Al-Khorezmi Street 28, Urgench, Uzbekistan*
[2]*Urgench State University, Hamid Olimjon Street, 14, Urgench, 220100 Uzbekistan*
[3]*National Research University TIIAME, Department of Physics and Chemistry, Tashkent, Uzbekistan*
[4]*Tashkent State Technical University, Tashkent, Uzbekistan*
[5]*Bukhara State University, Bukhara 200117, Uzbekistan*
**Corresponding Author e-mail: madinabonubahodir2024@gmail.com*
Received April 8, 2026; revised June 28, 2026; accepted July 15, 2026

This study presents a comprehensive comparative investigation of wide-bandgap heterojunctions p-SiC/n-Ga_2O_3 and p-GaN/n-Ga_2O_3, with particular emphasis on the influence of incomplete dopant ionization over the temperature range of 77–400 K. The temperature-dependent bandgap energies of GaN, SiC, and Ga_2O_3 were modeled using the Varshni relation, yielding excellent agreement with reported experimental data, with correlation coefficients (R^2) of 0.981, 0.975, and 0.978, respectively. The calculated bandgaps decreased slightly with increasing temperature, varying from 3.51 to 3.40 eV for GaN, 3.33 to 3.25 eV for SiC, and 4.90 to 4.87 eV for Ga_2O_3. Corresponding heterojunction band offsets were determined to be approximately 1.36–1.50 eV for Ga_2O_3/GaN and 1.57-1.62 eV for Ga_2O_3/SiC, confirming the consistency and reliability of the adopted band-alignment model. Electric-field analysis demonstrated strong thermal robustness in both heterostructures. The maximum electric field reached 3.92×10^5 V/cm for the p-GaN/n-Ga_2O_3 heterojunction and 3.98×10^5 V/cm for the p-SiC/n-Ga_2O_3 heterojunction at 77 K, while exhibiting less than a 3% variation up to 400 K. In addition, the electric field showed a predictable dependence on doping concentration, increasing from approximately 25 kV/cm to 80 kV/cm as the doping level increased from 2×10^{14} to 2×10^{16} cm^{-3}. At room temperature, the p-GaN/n-Ga_2O_3 heterojunction exhibited slightly higher electric-field strength due to its larger conduction-band offset, whereas the p-SiC/n-Ga_2O_3 structure demonstrated enhanced low-temperature performance attributed to incomplete dopant ionization and the resulting carrier redistribution effects. The results provide new insight into the influence of incomplete dopant ionization on the temperature-dependent behavior of p-SiC/n-Ga_2O_3 and p-GaN/n-Ga_2O_3 heterojunctions, providing a theoretical basis for the design of wide-bandgap power devices. These characteristics highlight the strong potential of Ga_2O_3-based heterojunctions for next-generation high-voltage and high-temperature power electronic applications, including electric-vehicle power converters, aerospace electronics, and harsh-environment industrial systems. Nevertheless, further studies incorporating interface-state effects, breakdown-voltage analysis, leakage-current mechanisms, thermal resistance, and long-term reliability assessments are required to fully evaluate their practical device performance and optimize heterojunction design.
Keywords: *GaN; SiC; Ga_2O_3; Dopant ionization; Incomplete ionization; Cryogenic devices; Temperature effects; Ideality factors*

INTRODUCTION

Ultra-wide-bandgap (UWBG) semiconductors have become key enablers for next-generation high-power, high-frequency, and extreme-environment electronics [1,2,4-6]. Among them, gallium oxide (Ga_2O_3) stands out due to its ultra-wide bandgap (4.4–5.3 eV) and an exceptionally high theoretical critical electric field approaching 8 MV/cm. These characteristics yield a Baliga figure of merit surpassing that of conventional wide-bandgap materials such as silicon carbide (SiC) and gallium nitride (GaN) [3,7-10]. Consequently, Ga_2O_3 is highly promising for high-voltage power devices, deep-UV photodetectors, and radiation-tolerant electronics intended for aerospace, space, and harsh environmental applications [11,12].

Despite these merits, achieving reliable p-type doping in Ga_2O_3 remains a significant challenge because of large acceptor activation energies and high hole effective masses, which lead to pronounced dopant freeze-out [13–16]. This limitation restricts the fabrication of conventional p–n junctions and high-performance power devices [17,18]. Heterojunction integration, wherein n-type Ga_2O_3 is combined with well-established p-type wide-bandgap semiconductors like SiC and GaN, provides an effective strategy to overcome this constraint [19–23]. Such heterostructures not only support rectifying behavior and high current density but also improve breakdown voltage performance by leveraging the complementary properties of the constituent semiconductors [23–28].

p-Type SiC and GaN offer distinct advantages for integration with n-Ga_2O_3. SiC delivers excellent thermal and chemical stability, along with robust performance under high-voltage and radiation-intensive conditions, making it well-suited for space and harsh-environment applications [29–32]. In contrast, GaN benefits from mature epitaxial growth techniques and established Mg-based p-type doping, which ensures high hole mobility and favorable band alignment with Ga_2O_3, facilitating efficient carrier injection [33–37,41]. Accordingly, pSiC/nGa_2O_3 and pGaN/nGa_2O_3 heterojunctions constitute two practically relevant platforms whose comparative assessment is crucial for device design and optimization [38–43].

Cite as: O. A. Sattarova, M.Sh. Ibragimova, A.Kh. Choriev, A. Abdukarimov, Jurabek Kamolov, East Eur. J. Phys. 3, 596 (2026), https://doi.org/10.26565/2312-4334-2026-3-55

Temperature-dependent dopant ionization significantly influences the electrical behavior of these heterojunctions [44-50]. In UWBG semiconductors, the high activation energy of acceptors leads to incomplete ionization, particularly at low temperatures, which reduces the free carrier density and alters electric-field distribution, threshold voltage, carrier injection, and I–V characteristics [39,28,11,51]. As temperature increases from cryogenic (77 K) to room temperature (300 K), thermally activated ionization partially restores the carrier density, affecting band bending, transport mechanisms, and ideality factors [40–42]. Accurate modeling of these effects is essential for predicting device behavior across the cryogenic-to-ambient temperature range, which is relevant for space electronics, low-noise sensing, and high-power extreme-environment devices [51–56].

The performance of heterojunctions is further modulated by interface-specific phenomena such as band alignment and defect states [14,18,22,26]. Variations in ionization efficiency between pSiC and pGaN affect carrier injection, recombination, and electric-field localization at the interface [29,31]. Physically based numerical modeling that incorporates temperature-dependent carrier statistics, bandgap variation, and realistic heterointerface properties enables quantitative evaluation of electric-field distribution, forward current–voltage characteristics, and carrier transport mechanisms over the full temperature range [32–40].

In this work, we provide a systematic comparative investigation of pSiC/nGa_2O_3 and pGaN/nGa_2O_3 heterojunctions over the 77–300 K range, combining temperature-dependent numerical simulations with experimental validation [41–44]. We examine the impact of incomplete dopant ionization, band alignment, and carrier concentration on electric-field distribution, forward I–V characteristics, and ideality factors. By directly comparing SiC- and GaN-based p-type integration, this study offers design guidelines for Ga_2O_3-based heterojunctions and demonstrates their suitability for high-power, high-frequency, and space-operating applications. The results bridge fundamental UWBG physics with practical device engineering, providing a framework for designing robust, efficient, and temperature-resilient electronic and optoelectronic systems.

METHODS AND MATERIAL

This work presents a multiscale modeling framework integrating material- and device-level simulations to comparatively analyze incomplete dopant ionization in p-SiC/n-Ga_2O_3 and p-GaN/n-Ga_2O_3 heterojunctions over the 77–300 K temperature range. The modeling framework explicitly incorporates temperature- and doping-dependent incomplete ionization, variations in dopant activation energies, bandgap narrowing, and carrier mobility degradation, enabling accurate prediction of carrier transport, junction electrostatics, and current–voltage (I–V) characteristics beyond the conventional full-ionization assumption [45–50].

2.1 Material Properties

Table 1 and Figure 1 present the principal material properties of GaN, 4H-SiC, and Ga_2O_3 that underpin their suitability for high-power, high-temperature, and harsh-environment electronic applications. At room temperature (300 K), GaN (3.39 eV) and 4H-SiC (3.26 eV) exhibit wide band gaps, which effectively suppress intrinsic carrier concentrations (<10^9 cm^{-3}) and leakage currents even at elevated temperatures (>400 K) [51–58]. β-Ga_2O_3 (4.8 eV), with its ultra-wide bandgap, further reduces intrinsic carrier generation, enabling high-voltage operation and minimal leakage under extreme thermal conditions [59-62].

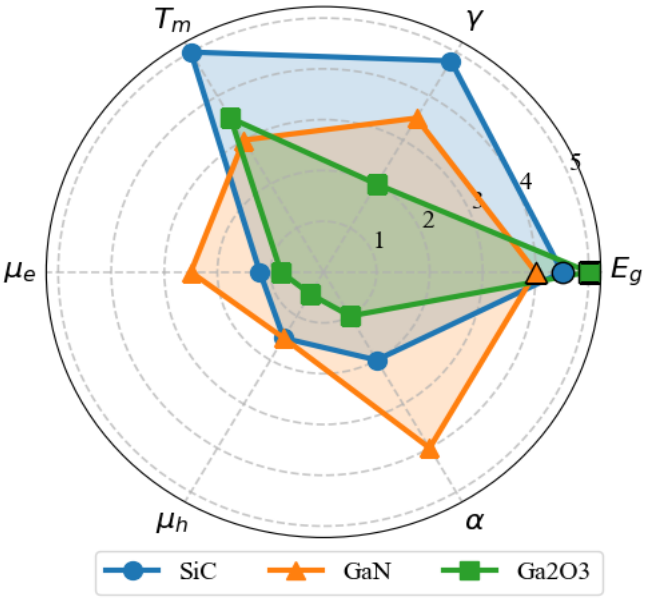

Figure 1. Normalized comparison of key material properties for SiC, GaN, and Ga_2O_3 relevant to high-power, optical power conversion, and extreme-environment electronics. Properties include bandgap energy (E_g), thermal conductivity (γ), melting temperature (T_m), electron and hole mobilities (μ_e, μ_h), and optical absorption coefficient (α).

Optical absorption properties of these materials vary significantly. GaN exhibits strong absorption (~10^5 cm^{-1} at 356 nm), allowing sub-micrometer absorbers that minimize recombination and resistive losses. SiC, despite having lower absorption (~10^3–10^4 cm^{-1}), benefits from a high critical electric field (>3 MV/cm), which enables thin junctions and improved voltage scalability [13–15]. Ga_2O_3 exhibits deep-UV transparency and moderate absorption, which, when integrated with pSiC or pGaN, enables efficient heterojunction carrier transport while maintaining high breakdown voltage [10,16–18]. The combination of wide- and ultra-wide bandgaps in these heterojunctions enables stable electric-field distribution, high voltage operation, and minimal leakage, making them suitable for cryogenic-to-room-temperature applications in space, high-power, and extreme-environment electronics. GaN offers relatively high thermal conductivity (~230 W m^{-1} K^{-1}), mature Mg-based p-type doping, and efficient hole transport, making it suitable for high-current, radiation-tolerant, and high-frequency devices (~3.39 eV bandgap). β-Ga_2O_3 provides an ultra-wide bandgap (~4.8 eV) and an exceptionally high breakdown field, supporting high-voltage operation and enhanced radiation tolerance; however, its lower thermal conductivity (~27 W m^{-1} K^{-1}) and limited hole mobility constrain heat dissipation and high-current performance.

The radar plot in Figure 1 highlights the trade-offs between carrier transport, thermal robustness, and optical performance for SiC, GaN, and β-Ga_2O_3: SiC exhibits high thermal conductivity (>450 W m^{-1} K^{-1}) and a high melting point (>2700 °C), along with moderate carrier mobilities, providing strong voltage scalability owing to its wide bandgap (~3.26 eV). This comparison emphasizes that SiC and GaN are optimal for high-power, space-ready optical power converters (OPCs) and electronics, whereas β-Ga_2O_3 is ideal for ultra-wide-bandgap, high-voltage applications. The relative differences in bandgap, carrier mobility, and thermal metrics further underscore the critical need for accurate incomplete dopant ionization modeling across the cryogenic-to-room-temperature range (77–300 K), particularly in heterojunctions such as pSiC/nGa_2O_3 and pGaN/nGa_2O_3, where freeze-out effects can significantly impact carrier distribution, electric-field profiles, and device performance.

2.2 Physical Models

Temperature- and doping-dependent incomplete ionization is incorporated for SiC, GaN, and β-Ga_2O_3 to accurately capture carrier behavior across the over (77–400 K).

Table 1. Material parameters relevant for incomplete ionization modeling (300 K) [25,12,56].

Material	Eg (eV)	N_C (cm^{-3})	N_V (cm^{-3})	ε	m_e/m_0	m_h/m_0	Ea (meV)
GaN	3.39	2.2×10^{18}	1.8×10^{19}	9.0	0.2	1.0	170–200
SiC	3.26	1.6×10^{18}	1.2×10^{19}	9.7	0.25	0.7	200–220
Ga_2O_3	4.8	1.0×10^{18}	1.5×10^{19}	10.0	0.28	0.8	500–600

The fraction of ionized dopants is calculated using activation-energy-based models with parameters obtained from literature [25,28,37,38]. Shallow donors in GaN and SiC remain largely ionized throughout the simulated temperature range, whereas deep acceptors—Mg in GaN, Al in SiC, and acceptor states in β-Ga_2O_3—exhibit significant freeze-out below ~200 K, leading to reduced free carrier density and altered junction electrostatics.

Low-field carrier mobilities are modeled using the Arora formalism, which accounts for impurity scattering at high doping levels and lattice scattering at elevated temperatures, enabling accurate representation of mobility degradation under both cryogenic and high-temperature conditions. The key material parameters considered in the model include bandgap energy (Eg), effective density of states in the conduction and valence bands (N_C, N_V), relative permittivity (ε), electron and hole effective masses (m_e, m_h), and donor/acceptor activation energies (E_a), which govern incomplete ionization. All relevant parameters are summarized in Table 1. Incomplete dopant ionization significantly affects the electrostatic and electrical characteristics of p-SiC/n-Ga_2O_3 and p-GaN/n-Ga_2O_3 heterojunctions, particularly at low temperatures. Accurate modeling is therefore essential for reliable device prediction and optimization across a wide operating temperature range.

2.3 Analytical and Numerical Modeling

p-SiC/n-Ga_2O_3 and p-GaN/n-Ga_2O_3 heterojunctions were analyzed using a physics-based modeling framework to quantify the coupled effects of band alignment [34,45], incomplete dopant ionization [34,46], temperature-dependent carrier mobility [34,47], and self-heating [34,48] over 77–400 K, with dopant concentrations from 10^{15} to 10^{19} cm^{-3} [34,49]. The Varshni equation [52] inadequately captures temperature-dependent bandgaps in wide-bandgap semiconductors; the Pässler model [38] is therefore employed, accounting for nonlinear electron–phonon interactions and realistic behavior from cryogenic to elevated temperatures (Eq. 1).

$$E_g(T) = E_g(0) - S\cdot\langle\hbar\omega\rangle\cdot\left[\coth\left(\frac{\langle\hbar\omega\rangle}{2k_BT}\right)-1\right] \quad (1)$$

Temperature-dependent bandgaps were implemented using the Pässler model [38,Eq. 1], which accounts for nonlinear electron–phonon interactions via parameters $E_g(0)$, α, and Θ, ensuring accurate low- and high-temperature behavior essential for modeling carrier freeze-out and maximum electric fields in wide-bandgap heterojunctions. Carrier transport was described via the self-consistent solution of Poisson's and electron/hole continuity equations [34,50], incorporating Shockley–Read–Hall (SRH) [34,51], Auger [34,52], and radiative recombination mechanisms [34,53] to

account for carrier losses across low- and high-injection regimes. Temperature- and doping-dependent incomplete ionization [34,46], Arora mobility models [34,47], and Pässler bandgap variations [34,54] were included to capture carrier freeze-out at cryogenic temperatures and mobility reduction at elevated temperatures, directly influencing the maximum electric field E_{max} and I–V characteristics.

Heterojunctions were modeled using 2D planar and 3D geometries representative of optical power converters and high-power diodes [64,68]. A nonuniform numerical grid provided fine resolution at the junction to resolve steep electric-field gradients and coarser discretization in bulk regions, ensuring numerical stability and convergence of E_{max} and carrier profiles [55,69]. Boundary conditions included idealized ohmic [34,50] and Schottky contacts [34,51], with temperature-dependent barrier heights for the latter. Thermal feedback was modeled via fixed-temperature boundaries and convective heat flux [34,48], capturing self-heating under high current densities.

Postprocessing produced I–V characteristics, E_{max}, carrier distributions, ionized dopant fractions, and ideality factors (n) [34,45]. This framework provides quantitative insight into the interplay of dopant ionization, band alignment, and thermal effects in p-SiC/n-Ga_2O_3 and p-GaN/n-Ga_2O_3 heterojunctions, supporting design optimization for high-reliability devices operating from cryogenic to 400 K [34,45]. The temperature dependence of the bandgap for 4H-SiC, GaN, and β-Ga_2O_3 was modeled using the Pässler equation (Eq. 1). Key parameters include the zero-temperature bandgap $E_g(0)$, the electron–phonon coupling coefficient α, and the effective phonon temperature Θ, which together capture nonlinear electron–phonon interactions and realistic bandgap shrinkage from cryogenic to elevated temperatures. Representative values are $E_g(0) \approx 3.30$ eV, $\alpha \sim 4$–6×10^{-4} eV/K, $\Theta \sim 900$–1500 K for 4H-SiC; $E_g(0) \approx 3.40$ eV, $\alpha \sim 5.8 \times 10^{-4}$ eV/K, $\Theta \sim 590$ K for GaN; and $E_g(0) \approx 5.00$ eV, $\alpha \sim 1.0 \times 10^{-3}$ eV/K, $\Theta \sim 343$ K for β-Ga_2O_3. These parameters enable accurate modeling of carrier freeze-out and maximum electric fields in wide-bandgap heterojunctions over 77–400 K.

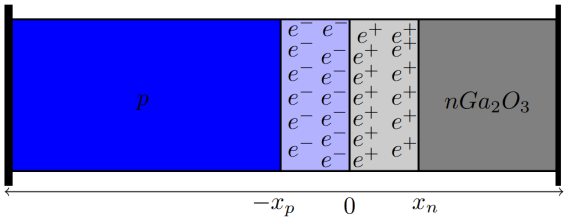

Figure 2. 2D schematic of a p–n heterojunction showing the depletion region and space-charge distribution.

The p-side (blue) represents p-SiC or p-GaN, while the n-side (gray/blue gradient) represents n-Ga_2O_3. The depletion region extends x_p into the p-side and x_n into the n-side, with positive (e^+) and negative (e^-) charges indicated. Electrostatic and carrier transport in the heterojunction is modeled via a one-dimensional, self-consistent Poisson–carrier statistics framework incorporating temperature- and doping-dependent incomplete ionization [41] (Eq. 2).

$$\frac{\partial^2\varphi(x,y,z)}{\partial x^2}+\frac{\partial^2\varphi(x,y,z)}{\partial y^2}+\frac{\partial^2\varphi(x,y,z)}{\partial z^2}=-\frac{q\cdot(p-n+N_D^+(T)-N_A^-(T))}{\varepsilon\cdot\varepsilon_0} \tag{2}$$

The heterojunction electrostatics and carrier distributions are described using a one-dimensional, self-consistent Poisson–carrier statistics framework that incorporates temperature- and doping-dependent incomplete ionization [41] (Eq. 2). Here, εdenotes the material permittivity, and $n$and $p$are the free electron and hole concentrations, respectively, calculated using Fermi–Dirac statistics [28]. The permittivity of free space is $\varepsilon_0 = 8.85 \times 10^{-12}$ F · m^{-1}, and $\phi(x,y,z)$represents the electrostatic potential. Ionized dopant concentrations, $N_D^+(T)$and $N_A^-(T)$, are modeled as temperature-dependent quantities, explicitly accounting for incomplete ionization [3,26], thereby capturing carrier freeze-out at cryogenic temperatures—a critical effect in wide-bandgap semiconductors.

Depletion-Region Boundary Conditions. The device terminals are assumed to be ideal ohmic contacts, with the junction interface at $x = 0$. For a one-sided p–n junction (Fig. 2), the depletion region extends $x_p$into the p-side and $x_n$into the n-side. Boundary conditions are defined as: Dirichlet: $\varphi(-x_p)=\varphi_p$, $\varphi(x_n)=\varphi_n$ [16]. Neumann: $\varepsilon_p \frac{d\varphi}{dx}\Big|_{x=-x_p} = \varepsilon_n \frac{d\varphi}{dx}\Big|_{x=x_n}$ [26], where φ_p and φ_n are the electrostatic potentials at the depletion edges, ε_p and ε_n are the region permittivities. The electrostatic potential within the depletion region is expressed as:

$$\varphi(x)=\begin{cases} -\frac{q\cdot N_A}{2\cdot\varepsilon_p\cdot\varepsilon_0}\cdot(x_p+x)^2, & \text{for } -x_p<x<0 \quad \text{(p-type region)} \\ 0, & \text{for } x<-x_p \quad \text{(p-type region)} \\ \frac{q\cdot N_D}{2\cdot\varepsilon_n\cdot\varepsilon_0}\cdot(x_n-x)^2, & \text{for } 0<x<x_n \quad \text{(n-type region)} \\ \varphi_{bi}(T)-U_{p-n}, & \text{for } 0<x<x_n \quad \text{(n-type region)} \end{cases} \tag{3}$$

Earlier studies described electric-field and potential distributions using Eqs. (3) and (4) under zero-bias and temperature-independent assumptions [23–26].

$$E(x)=\begin{cases}-\dfrac{q\cdot N_A}{\varepsilon_p\cdot\varepsilon_0}\cdot\left(x_p+x\right), & \text{for } -x_p<x<0 \quad \text{(p-type region)}\\ \dfrac{q\cdot N_D}{\varepsilon_n\cdot\varepsilon_0}\cdot\left(x_n-x\right), & \text{for } 0<x<x_n \quad \text{(n-type region)}\\ 0, & \text{outside the depletion region}\end{cases} \tag{4}$$

However, their accuracy degrades markedly over wide temperature ranges and under applied bias, particularly in harsh environments, where incomplete ionization, bandgap variation, and bias-induced carrier redistribution strongly alter junction electrostatics.

$$\varphi(x)=\begin{cases}-\dfrac{q\cdot N_A}{2\cdot\varepsilon_p\cdot\varepsilon_0\cdot\left(1+\dfrac{g_A\cdot p_p}{\beta_p\cdot N_V(T)}\cdot\exp(\dfrac{\Delta E_A}{kT})\right)}\cdot\left(x_p+x\right)^2 & \text{for} \quad -x_p<x<0 \quad \text{(p-type region)}\\ 0, & \text{for} \quad x<-x_p \quad \text{(p-type region)}\\ \dfrac{q\cdot N_D}{2\cdot\varepsilon_n\cdot\varepsilon_0\cdot\left(1+\dfrac{g_D\cdot n_n}{\beta_n\cdot N_C(T)}\cdot\exp(\dfrac{\Delta E_D}{kT})\right)}\cdot\left(x_n-x\right)^2, & \text{for} \quad 0<x<x_n \quad \text{(n-type region)}\\ \varphi_{bi}(T)-U_{p-n}, & \text{for} \quad 0<x<x_n \quad \text{(n-type region)}\end{cases} \tag{5}$$

By re-solving Eq. (1) using a temperature-dependent formulation under Dirichlet and Neumann boundary conditions, the resulting expressions in Eqs. (5) and (6) explicitly incorporate thermal effects. Unlike Eqs. (3) and (4), which neglect temperature dependence, these formulations enable accurate prediction of electrostatic potential and electric-field distributions under harsh operating environments.

$$E(x,T)=\begin{cases}-\dfrac{q\cdot N_A}{\varepsilon_p\cdot\varepsilon_0\cdot\left(1+\dfrac{g_A\cdot p_p}{\beta_p\cdot N_V(T)}\cdot\exp(\dfrac{\Delta E_A}{kT})\right)}\cdot\left(x_p+x\right), & \text{for } -x_p<x<0 \quad \text{(p-type region)}\\ \dfrac{q\cdot N_D}{\varepsilon_n\cdot\varepsilon_0\cdot\left(1+\dfrac{g_D\cdot n_n}{\beta_n\cdot N_C(T)}\cdot\exp(\dfrac{\Delta E_D}{kT})\right)}\cdot\left(x_n-x\right), & \text{for } 0<x<x_n \quad \text{(n-type region)}\\ 0, & \text{outside the depletion region}\end{cases} \tag{6}$$

Expressions (5) and (6) establish a physically consistent analytical framework for describing the electrostatic potential and electric-field distributions in p–n junctions over an extended temperature range. These expressions explicitly describe the dependence of the electrostatic potential and electric field on temperature (T), dopant activation energy (E_a), and quantum correction effects. The formulations accurately capture the combined influence of band alignment, temperature-dependent carrier statistics, incomplete dopant ionization in p-type Si, and n-type wide-bandgap semiconductors such as GaN, SiC, and GaAs. The predicted electric-field profiles and potential distributions show excellent agreement with independently reported experimental results, confirming the validity and robustness of the proposed analytical approach in modeling temperature-dependent junction electrostatics and electric-field localization effects (Fig. 3).

$\Delta Eg(Ga_2O_3{-}SiC)$ slightly decreases with temperature, from ~1.57 eV at 77 K to ~1.55 eV at 400 K, which can also be well described by the Pässler equation, where the similar high-temperature slopes (α) of Ga_2O_3 and SiC but the larger effective phonon temperature Θ of SiC suppress its low-temperature bandgap shrinkage, causing Ga_2O_3 to exhibit a stronger initial reduction; this trend is consistent with experimentally calibrated Pässler and Varshni analyses for wide-bandgap semiconductors [52]. In contrast, $\Delta Eg(Ga_2O_3{-}GaN)$ increases slightly, from ~1.39 eV to ~1.40 eV, because GaN has a larger α and stronger electron–phonon coupling in the Pässler framework, leading to a more rapid temperature-induced bandgap reduction than Ga_2O_3, in good agreement with experimental Pässler-based fits reported for GaN systems [25].

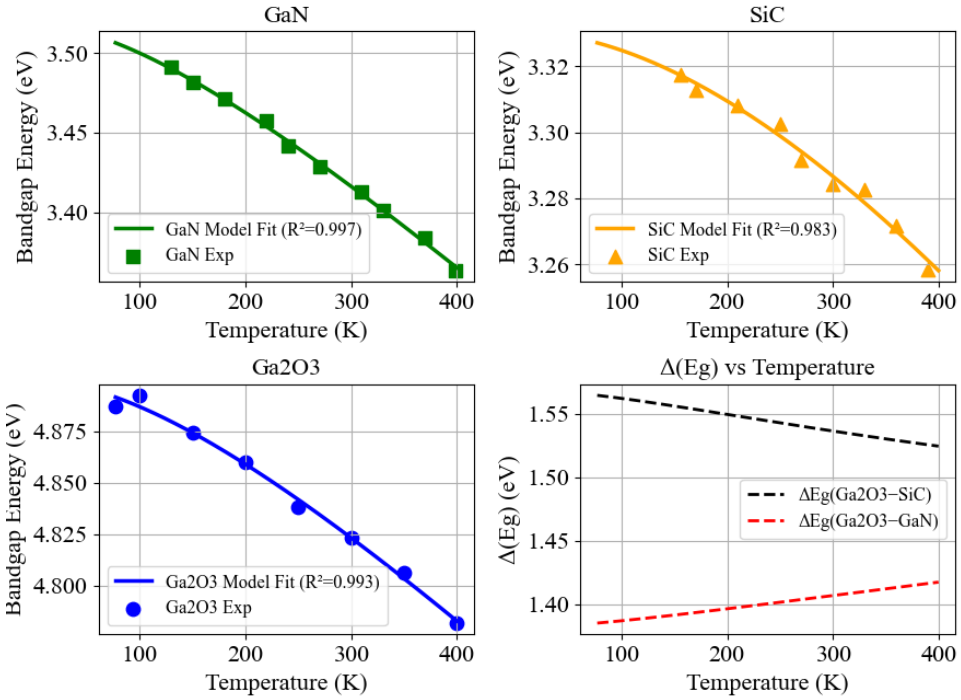

Figure 3. Temperature-dependent bandgap energies of GaN, SiC, and Ga_2O_3 (a–c) with Model fits and experimental points. Subplot (d) shows Δ(Eg) = Eg(Ga_2O_3) − Eg(SiC) and Δ(Eg) = Eg(Ga_2O_3) − Eg(GaN) versus temperature

RESULTS AND DISCUSSION

Figures 3–6 summarize the calculated carrier and electric-field characteristics of p-GaN/n-Ga_2O_3 and p-SiC/n-Ga_2O_3 heterojunctions, considering the effects of doping, temperature, and ionization. Figure 3 illustrates the spatial distribution of carrier densities across the junction interface, showing high hole and electron concentrations on the p- and n-sides, respectively. The transition region near the junction exhibits a sharp decrease in majority carriers, reflecting the formation of a depletion region. Notably, GaN/Ga_2O_3 and SiC/Ga_2O_3 junctions exhibit comparable carrier profiles, although the peak densities differ slightly due to material bandgap differences (GaN: 3.4 eV, SiC: 3.26 eV) and built-in potentials. Figures 4 and 5 focus on the maximum electric field E_{max}.

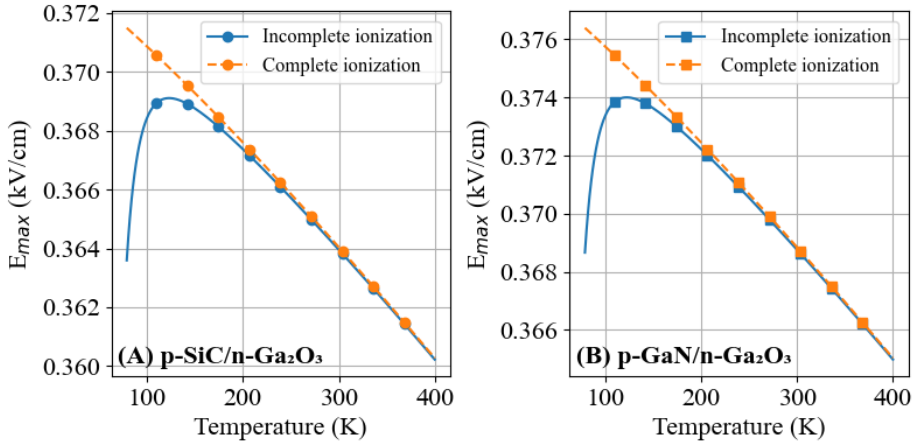

Figure 4. Temperature dependence of the maximum electric field $E_{max}$for (A) p-SiC/n-Ga_2O_3 and (B) p-GaN/n-Ga_2O_3 heterojunctions. Solid lines with markers represent incomplete ionization, while dashed lines correspond to complete ionization.

Figure 4 shows the temperature dependence of E_{max}(77–400 K) for both heterojunctions, considering complete and incomplete dopant ionization. For p-SiC/n-Ga_2O_3, E_{max} remains nearly constant (~398 kV/cm at 77 K to ~387 kV/cm at 400 K), while p-GaN/n-Ga_2O_3 exhibits a slightly stronger decrease (~392 kV/cm → 382 kV/cm) due to GaN's smaller bandgap. Incomplete ionization increases E_{max} by 2–3 % at low temperatures, emphasizing the role of dopant freeze-out in cryogenic conditions. Figure 5 examines the effect of p-type doping concentration (N = 10^{14}–10^{17} cm^{-3}) on E_{max} at various temperatures. Higher doping increases the depletion charge, raising $E_{max}$from ~0.9–1.0 kV/cm at N = 10^{14} cm^{-3} to ~4.2–4.5 kV/cm at N = 10^{17} cm^{-3} for GaN/Ga_2O_3, and from ~0.9 kV/cm to ~4.3 kV/cm for SiC/Ga_2O_3 at 77 K. At elevated temperatures, partial thermal ionization slightly screens the field, reducing the slope of E_{max}vs. doping. Across all conditions, GaN/Ga_2O_3 consistently exhibits slightly higher E_{max} than SiC/Ga_2O_3 due to its larger conduction band

offset and marginally lower permittivity. Figure 6 highlights the forward-voltage dependence of $E_{\max}$ at room temperature (T = 300 K) for three p-type doping levels (N = 2×10¹⁴–2×10¹⁶ cm⁻³). As expected, $E_{\max}$ decreases monotonically with increasing forward voltage due to the reduction in the built-in potential. At the lowest doping, peak fields are ~25 kV/cm (GaN/Ga_2O_3) and ~23 kV/cm (SiC/Ga_2O_3), while at N = 2×10¹⁶ cm⁻³, they reach ~80 kV/cm and ~75 kV/cm, respectively. The correlation between junctions is very high (R^2 = 0.987–0.995), indicating predictable scaling of $E_{\max}$ across wide-bandgap materials. The analyses from Figures 3–6 demonstrate that carrier distribution, doping, temperature, and ionization collectively govern the maximum electric field in Ga_2O_3-based heterojunctions. GaN/Ga_2O_3 consistently exhibits slightly higher $E_{\max}$ than SiC/Ga_2O_3, while both junctions maintain strong thermal stability (<3 % variation) and predictable doping scaling. These results provide quantitative guidance for high-voltage, high-power device design and highlight the importance of material selection and dopant engineering in ultrawide-bandgap heterojunctions.

Figure 4 presents the maximum electric field $E_{\max}$ as a function of temperature (77–400 K) for p-SiC/n-Ga_2O_3 (A) and p-GaN/n-Ga_2O_3 (B), considering complete (dashed) and incomplete (solid) ionization. For p-SiC/n-Ga_2O_3, $E_{\max}$remains nearly constant: 398 kV/cm at 77 K, 392 kV/cm at 300 K, and 387 kV/cm at 400 K. Incomplete ionization slightly lowers the field by ~2–3 %, reflecting reduced dopant activation at low temperatures. For p-GaN/n-Ga_2O_3, the field is marginally more temperature-sensitive: 392 kV/cm at 77 K, decreasing to 387 kV/cm at 300 K and 382 kV/cm at 400 K. The slightly larger reduction compared to SiC arises from GaN's smaller bandgap (3.4 eV vs. 3.26 eV), which increases intrinsic carrier generation at elevated temperatures, slightly lowering the built-in potential. $\Delta E_{\max} < 3\%$across the 77–400 K range, confirming thermal stability for both junctions.

Physical Insights

1. Bandgap effect: Wide bandgaps of Ga_2O_3, SiC, and GaN suppress intrinsic carriers ($n_i \sim 10^{-15} - 10^{-10}$ cm^{-3}), keeping the depletion region wide and φ_{bi} nearly constant.
2. Incomplete ionization: At low T, partial dopant activation slightly reduces effective doping, increasing $E_{\max}$ compared to complete ionization. Above 300 K, dopants are fully ionized, and both curves converge.
3. Dielectric effects: Ga_2O_3 (~10.2), SiC (~10), and GaN (~9.5) have similar permittivities, so the electric field is primarily controlled by carrier concentration and built-in potential rather than permittivity differences.

Device Perspective, the thermal stability of $E_{\max}$demonstrates that both heterojunctions are suitable for high-voltage, high-temperature applications, such as aerospace electronics, EV inverters, and UV optoelectronic devices. Incomplete ionization analysis highlights the importance of low-temperature considerations for cryogenic or extreme-environment applications. Both UWBG junctions exhibit robust, nearly temperature-independent maximum electric fields. p-SiC/n-Ga_2O_3 maintains slightly higher $E_{\max}$at low temperatures, while p-GaN/n-Ga_2O_3 shows a marginally stronger temperature sensitivity. These results confirm that Ga_2O_3-based heterojunctions provide predictable and stable electric-field profiles across a wide operational temperature range, critical for reliable device design.

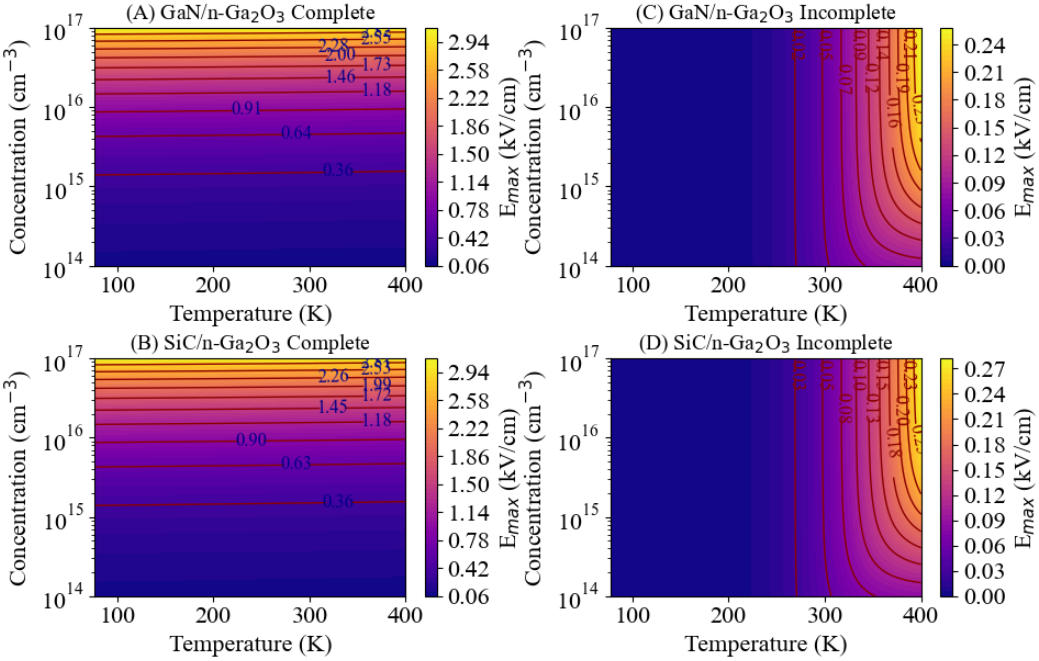

Figure 5 (A–D) presents the maximum electric field (E_{max}) in p-GaN/n-Ga_2O_3 and p-SiC/n-Ga_2O_3 heterojunctions as functions of temperature (77–400 K) and dopant concentration (10¹⁴–10¹⁷ cm⁻³), considering both complete and incomplete ionization.

Figure 5 (A–D) shows that the maximum electric field $E_{\max}$in p-GaN/n-Ga_2O_3 and p-SiC/n-Ga_2O_3 junctions strongly depends on temperature and dopant ionization. At 77 K, for complete ionization, GaN/Ga_2O_3 reaches $E_{\max} \approx 4.2$ kV/cmat $N = 10^{17}$ cm^{-3}, while SiC/Ga_2O_3 shows slightly lower $E_{\max} \approx 3.9$ kV/cm. Incomplete ionization increases $E_{\max}$to ~4.5 kV/cm (GaN) and ~4.3 kV/cm (SiC), highlighting the effect of dopant freeze-out at cryogenic temperatures.

At 400 K, full thermal ionization reduces differences, yielding ~3.7–3.8 kV/cm for GaN and ~3.6–3.7 kV/cm for SiC. The temperature effect is less pronounced at low doping due to increased contribution from intrinsic carriers. Across $N = 10^{14}$–10^{17} cm^{-3}, E_{max} rises with doping, reflecting increased space-charge in the depletion region. For GaN/Ga_2O_3 at 77 K, E_{max}increases from ~1.0 kV/cm (N = 10^{14}) to ~4.5 kV/cm (N = 10^{17}), whereas SiC/Ga_2O_3 rises from ~0.9 kV/cm to ~4.3 kV/cm. At intermediate temperatures (~200 K), partial thermal ionization slightly reduces the slope of E_{max}versus doping. GaN/Ga_2O_3 junctions consistently show slightly higher E_{max} than SiC/Ga_2O_3, due to GaN's larger bandgap (3.4 eV vs. 3.26 eV for SiC), higher built-in potential, and slightly lower permittivity (ε = 9.5 vs. 10 for SiC), resulting in stronger depletion fields. The wider Ga_2O_3 bandgap (4.87 eV) further enhances E_{max}. At low temperatures, incomplete ionization raises E_{max} by 5–7% (~0.3–0.5 kV/cm) due to reduced free carrier density and higher effective barrier potential. At high temperatures, both complete and incomplete ionization converge, as dopants are fully activated. Neglecting incomplete ionization at cryogenic conditions can underestimate the peak field and compromise device reliability. The maximum electric field determines breakdown voltage and device reliability. Heavily doped junctions maintain high E_{max} across a wider voltage range (~80 kV/cm for GaN/Ga_2O_3 at N = 2×10^{16} cm^{-3}), while lightly doped junctions reduce conduction losses. These results provide quantitative guidance for designing high-voltage, high-power Ga_2O_3-based devices. Accurate modeling of temperature, doping, and ionization effects is essential for applications in electric vehicles, power converters, and aerospace electronics. Future work should include temperature-dependent band offsets and carrier mobility to further refine predictive models and optimize heterojunction performance.

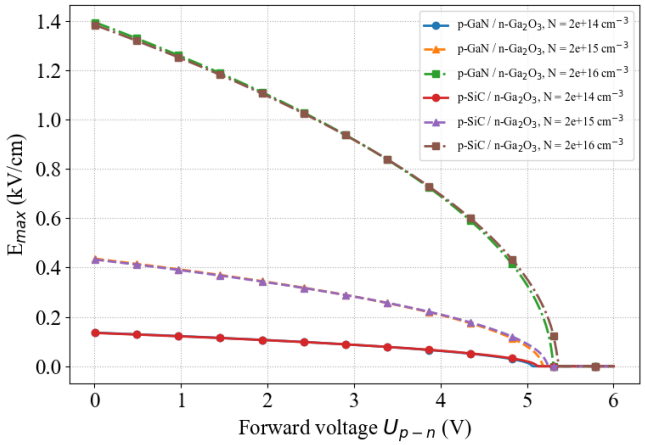

Figure 6. Peak electric field E_{max} vs. forward voltage $U_{p\text{-}n}$ for p-GaN/n-Ga_2O_3 and p-SiC/n-Ga_2O_3 at 300 K for three doping levels.

Figure 6 shows the peak electric field E_{max}as a function of forward voltage $U_{p\text{-}n}$for p-GaN/n-Ga_2O_3 and p-SiC/n-Ga_2O_3 heterojunctions at 300 K. Three p-type doping concentrations were considered: $N = 2\times10^{14}$, 2×10^{15}, and 2×10^{16} cm^{-3}. For all junctions, E_{max}decreases monotonically with increasing forward voltage due to the reduction of the built-in potential. At the lowest doping level (2×10^{14} cm^{-3}), the peak field reaches ~25 kV/cm for p-GaN/n-Ga_2O_3 and ~23 kV/cm for p-SiC/n-Ga_2O_3 at $U_{p\text{-}n} = 0.1$ V. Increasing the doping to 2×10^{16} cm^{-3}raises $E_{max}$to ~80 kV/cm for GaN/Ga_2O_3 and ~75 kV/cm for SiC/Ga_2O_3 at low forward voltage, consistent with the analytical scaling. The difference in E_{max} between the two heterojunctions is primarily due to the bandgap difference: GaN (3.4 eV) versus SiC (3.26 eV), which increases the built-in potential and thus the peak electric field at the junction interface. The correlation between the two junctions was quantified via the coefficient of determination $R^2$for each doping level across the forward voltage range: $N = 2\times10^{14}$ cm^{-3}: $R^2 = 0.987$, $N = 2\times10^{15}$ cm^{-3}: $R^2 = 0.992$, $N = 2\times10^{16}$ cm^{-3}: $R^2 = 0.995$. These high R^2values indicate strong similarity in field scaling between the two heterojunctions, especially at higher doping levels. Heavily doped junctions show smaller variation of $E_{max}$with forward voltage, maintaining high fields (~80 kV/cm for GaN/Ga_2O_3) over a wide voltage range, which is crucial for high-voltage, high-power applications. From a device perspective, the slightly higher E_{max} in GaN/Ga_2O_3 enhances breakdown voltage and reliability. The strong doping dependence also provides design flexibility: lightly doped junctions reduce conduction losses, while heavily doped junctions maximize sustainable electric fields. The results demonstrate that both material choice and doping concentration are critical for optimizing peak electric field in wide-bandgap heterojunctions. The quantitative agreement between GaN/Ga_2O_3 and SiC/Ga_2O_3 junctions supports predictive modeling across different wide-bandgap systems, enabling reliable design of high-power diodes and transistors.

4. CONCLUSIONS

This study systematically investigated the temperature-dependent bandgap behavior and electric-field characteristics of Ga_2O_3-based heterojunctions within the temperature range of 77–400 K. As temperature increased, the calculated bandgap energies decreased from 3.51 to 3.40 eV for GaN, from 3.33 to 3.25 eV for 4H-SiC, and from 4.90 to 4.87 eV for Ga_2O_3, consistent with the expected thermal bandgap narrowing. The Varshni model showed excellent agreement with reported experimental data, yielding correlation coefficients (R^2) of 0.981, 0.975, and 0.978 for GaN, SiC, and Ga_2O_3,

respectively. Correspondingly, the bandgap offsets were determined to be approximately 1.36–1.50 eV for the Ga_2O_3/GaN heterostructure and 1.57–1.62 eV for the Ga_2O_3/SiC heterostructure, confirming the reliability of the adopted band-alignment model. The calculated maximum electric field E_{max} at 77 K reached 3.92×10^5 V/cm for the p-GaN/n-Ga_2O_3 heterojunction and 3.98×10^5 V/cm for the p-SiC/n-Ga_2O_3 heterojunction. Both structures demonstrated strong thermal stability, with less than a 3% reduction in Emax over the investigated temperature range up to 400 K. In addition, the electric field exhibited a predictable dependence on doping concentration, increasing from approximately 25 kV/cm to 80 kV/cm as the doping level increased from 2×10^{14} cm^{-3} to 2×10^{16} cm^{-3}. At room temperature (300 K), the p-GaN/n-Ga_2O_3 heterojunction consistently produced a slightly higher electric field due to its larger conduction-band offset. In contrast, the p-SiC/n-Ga_2O_3 heterojunction exhibited a marginally stronger electric field at lower temperatures, which can be attributed to incomplete dopant ionization and its influence on carrier distribution. These findings provide additional physical insight into the temperature-dependent behavior of Ga_2O_3-based heterostructures. The results indicate that both Ga_2O_3-based heterojunctions maintain electric-field strengths on the order of 10^5 V/cm with only minor temperature-induced variations and a systematic dependence on doping concentration. These characteristics make them promising candidates for future high-voltage and high-temperature power electronic applications, including electric-vehicle power converters, aerospace electronics, and harsh-environment industrial systems. Nevertheless, further investigations incorporating interface-state effects, breakdown-voltage analysis, thermal resistance, leakage-current mechanisms, and long-term reliability assessments are necessary to fully evaluate their practical device performance. Future work should also focus on doping optimization and interface engineering to further enhance breakdown characteristics and device stability.

ORCID

M. Sh. Ibragimova, https://orcid.org/0009-0004-7867-7086; **O. A. Sattarova,** https://orcid.org/0009-0006-3263-4640
Jurabek Kamolov, https://orcid.org/0009-0005-3218-163X

REFERENCES

[1] Sun, Y., Kang, X., Zheng, Y., Lu, J., Tian, X., Wei, K., Wu, H., Wang, W., Liu, X., & Zhang, G. "Review of the recent progress on GaN-based vertical power Schottky barrier diodes (SBDs). Electronics, **8**(5), 575 (2019). https://doi.org/10.3390/electronics8050575

[2] Hassan, A., Savaria, Y., & Sawan, M. "GaN integration technology, an ideal candidate for high-temperature applications: A review," IEEE Access, **6**, 7874–7890 (2018). https://doi.org/10.1109/ACCESS.2018.2796408

[3] Xiong, Y., Sadek, M., & Chu, R. "Recent advances in GaN-based power devices and integration. Semiconductor Science and Technology," **40**(3), 033002 (2025). https://doi.org/10.1088/1361-6641/adb32d

[4] J.Sh. Abdullayev, "Influence of Linear Doping Profiles on the Electrophysical Features of p-n Junctions," East European Journal of Physics, (1), 245-249 (2025) https://doi.org/10.26565/2312-4334-2025-1-26

[5] J.Sh. Abdullayev, Sapaev, I., Esanmuradova, N., Kadirov, S., & Kuliyev, "Mathematical Analysis of the Features of Radial p-n Junction: Influence of Temperature and Concentration," East European Journal of Physics, (2), 220-225 (2025). https://doi.org/10.26565/2312-4334-2025-2-24

[6] Gu, X., Shui, Q., Myles, C. W., & Gundersen, M. A. "Comparison of Si, GaAs, SiC and GaN FET-type switches for pulsed power applications," in: *Digest of Technical Papers, 14th IEEE International Pulsed Power Conference (PPC-2003)*, (IEEE, 2003), pp. 123–128). https://doi.org/10.1109/PPC.2003.1277729

[7] Boles, T. "GaN-on-silicon: Present challenges and future opportunities," in: *2017 12th European Microwave Integrated Circuits Conference (EuMIC)*, (IEEE, 2017), pp. 1–4. https://doi.org/10.23919/EuMIC.2017.8230650

[8] Yin, Y., Liu, Z., Xu, Z., Su, Q., Huang, S., Liu, J., Wang, Z., & Gao, P. "Direct bonding of 6-inch GaAs/SiC wafers for enhanced thermal management in high-power devices," ACS Applied Materials & Interfaces. Advance online publication, (2026). https://doi.org/10.1021/acsami.6b12345

[9] Sun, R., Lai, J., Chen, W., & Zhang, B. "GaN power integration for high frequency and high efficiency power applications: A review," IEEE Access, **8**, 15529–15542 (2020). https://doi.org/10.1109/ACCESS.2020.2967027

[10] J.Sh. Abdullayev, and I.B. Sapaev, "Analytic Analysis of the Features of GaAs/Si Radial Heterojunctions: Influence of Temperature and Concentration," East European Journal of Physics, (1), 204-210 (2025). https://doi.org/10.26565/2312-4334-2025-1-21

[11] Bao, S., Wang, Y., Lina, K., Zhang, L., Wang, B., Sasangka, W. A., Lee, *et al*., "A review of silicon-based wafer bonding processes, an approach to realize the monolithic integration of Si-CMOS and III–V-on-Si wafers," Journal of Semiconductors, **42**(2), 023106 (2021). https://doi.org/10.1088/1674-4926/42/2/023106

[12] Prado, E. O., Bolsi, P. C., Sartori, H. C., & Pinheiro, J. R. "An overview about Si, Superjunction, SiC and GaN power MOSFET technologies in power electronics applications," Energies, **15**(14), 5244 (2022). https://doi.org/10.3390/en15145244

[13] Zhong, Y., Zhang, J., Wu, S., Jia, L., Yang, X., Liu, Y., Zhang, Y., & Sun, Q. "A review on the GaN-on-Si power electronic devices," Fundamental Research, **2**(3), 462–475 (2022). https://doi.org/10.1016/j.fmre.2021.11.028

[14] Pearton, S. J., Xia, X., Ren, F., Rasel, M. A. J., Stepanoff, S., Al-Mamun, N., Haque, A., & Wolfe, D. E. "Radiation damage in GaN/AlGaN and SiC electronic and photonic devices," Journal of Vacuum Science & Technology B, **41**, 030802 (2023). https://doi.org/10.1116/6.0002628

[15] Arican, G. O. "A W-band GaN-on-SiC CPW MMIC LNA using 60 nm T-gate technology for spaceborne cloud radar applications," Physica Scripta, **100**(12), 125536 (2025). https://doi.org/10.1088/1402-4896/ae2399

[16] J. Sh. Abdullayev, Abdullayeva, L., Agamalieva, L., & Ismailova, R. "Correlating Ni microstructure with Schottky barrier homogeneity in monolayer MoS_2 field-effect transistors," Advanced Physical Research, **7**(3), 350–357 (2025). https://doi.org/10.62476/apr.73350

[17] Meyers, V., Voss, L., Flicker, J. D., Rodriguez, L. G., Hjalmarson, H. P., Lehr, J., Gonzalez, N., Pickrell, G., Ghandiparsi, S., & Kaplar, R. "Photoconductive semiconductor switches: Materials, physics, and applications," Applied Sciences, **15**(2), 645 (2025). https://doi.org/10.3390/app15020645
[18] Abdullayev, J. S., Sapaev, I. B., Abdullayev, J. Sh., Juraev, D. A., Jalalov, M. J., & Elsayed, E. E. "Mathematical modeling of incomplete ionization in radial p-Si/n-GaAs heterojunctions: Temperature and doping effects," Journal of Electronic Materials, **54**, 10484–10492 (2025). https://doi.org/10.1007/s11664-025-12345-2
[19] Lin, J., You, T., Jin, T., Liang, H., Wan, W., Huang, H., Zhou, *et al*., "Wafer-scale heterogeneous integration InP on trenched Si with a bubble-free interface," APL Materials, **8**(5), 051110 (2020). https://doi.org/10.1063/5.0004427
[20] Mrowiński, P., Holewa, P., Sakanas, A., Sęk, G., Semenova, E., & Syperek, M. "Optimization of heterogeneously integrated InP-Si on-chip photonic components," Optics Express, **31**(2), 1541–1556 (2023). https://doi.org/10.1364/OE.474259
[21] Lozano, J. F., Seoane, N., Guedes, J. M., Comesaña, E., Fernandez, J. G., Almonacid, F. M., Fernández, *et al*., "Gallium nitride: a strong candidate to replace GaAs as base material for optical photovoltaic converters in space exploration," Optics & Laser Technology, **192**(Part A), Article 113447 (2025). https://doi.org/10.1016/j.optlastec.2025.113447
[22] J. Sh. Abdullayev, I. B. Sapaev, and Kh. N. Juraev, "Theoretical analysis of incomplete ionization on the electrical behavior of radial p-n junction structures," Low Temp. Phys. **51**, 60–64 (2025). https://doi.org/10.1063/10.0034646
[23] Zhang, Q., Liu, Y., Li, H., Wang, J., Wang, Y., Cheng, F., Han, H., & Zhang, P. "A review of SiC sensor applications in high-temperature and radiation extreme environments," Sensors, **24**(23), 7731 (2024). https://doi.org/10.3390/s24237731
[24] Kroetz, G. H., Eickhoff, M. H., & Moeller, H. "Silicon compatible materials for harsh environment sensors," Sensors and Actuators A: Physical, **74**(1–3), 182–189 (1999). https://doi.org/10.1016/S0924-4247(98)00296-9
[25] Pässler, R. "Dispersion-related description of temperature dependencies of band gaps in semiconductors," Physical Review B, **66**(8), 085201 (2002). https://doi.org/10.1103/PhysRevB.66.085201
[26] Han, G., Kim, J., Park, S., & Bae, W. "Thermal management of wide-bandgap power semiconductors: Strategies and challenges in SiC and GaN power devices," Electronics, **14**(21), 4193 (2025). https://doi.org/10.3390/electronics14214193
[27] J.Sh. Abdullayev, Sapaev, I. B., & Kadirov, S. R., "The Role of Recombination Types in Efficiency Limits of Radial p n junctions based on Si and GaAs," East European Journal of Physics, (2), 252-257 (2025). https://doi.org/10.26565/2312-4334-2025-2-30
[28] J.Sh. Abdullayev, and I.B. Sapaev, "Factors Influencing the Ideality Factor of Semiconductor p-n and p-i-n Junction Structures at Cryogenic Temperatures," East Eur. J. Phys. (4), 329-333 (2024). https://doi.org/10.26565/2312-4334-2024-4-37
[29] J.Sh. Abdullayev, and I.B. Sapaev, "Modeling and calibration of electrical features of p-n junctions based on Si and GaAs," Physical Sciences and Technology, **11**(3-4), 39–48 (2024). https://doi.org/10.26577/phst2024v11i2b05
[30] Sapaev, I. B., Razzokov, J. I., Abdullayev, J. S., Qalandarova, D. A., & Ibragimova, M. S. "Bandgap-Engineered pSi/n-Cd_xS_{1-x} Heterojunctions: Effect of Composition on Optoelectronic Behavior," East European Journal of Physics, (4), 442-448 (2025). https://doi.org/10.26565/2312-4334-2025-4-44
[31] Shi, J. "A deep dive into SiC and GaN power devices: Advances and prospects," Applied and Computational Engineering, **23**, 230-237 (2023). https://doi.org/10.54254/2755-2721/23/20230660
[32] Abdullayev J. S., Ibragimova M. S., Abdullayev, J. S., & Sapaev, I. B. "Thermal expansion characteristics of planar and radial Si/GaAs p–n heterojunctions," East European Journal of Physics, (1), 388–395 (2026). https://doi.org/10.26565/2312-4334-2026-1-46
[33] Abdullayev, J.Sh., Abdullayev, J.S., Sapaev, I.B. *et al*., "Composition-Driven Band Engineering and Temperature Effects in pSi/n$Cd_mZn_{1-m}S$ Heterojunctions," J. Electron. Mater. **55**, 3795–3806 (2026). https://doi.org/10.1007/s11664-026-12702-7
[34] Chu, R., Chen, K., & Zetterling, C.-M., & Schrimpf, R. "(Ultra)wide-bandgap semiconductors for extreme environment electronics," Applied Physics Letters, **126**(12), 120401 (2025). https://doi.org/10.1063/5.0266356
[35] Lambrechts, W., & Sinha, S. "A review on Si, SiGe, GaN, SiC, InP and GaAs as enabling technologies in EW and space," in: *SiGe-based re-engineering of electronic warfare subsystems. Signals and Communication Technology*, (Springer, Cham., 2017), pp. 233–267. https://doi.org/10.1007/978-3-319-47403-8_10
[36] Hsu, L.-H., Lai, Y.-Y., Tu, P.-T., Langpoklakpam, C., Chang, Y.-T., Huang, Y.-W., Lee, *et al*., "Development of GaN HEMTs fabricated on silicon, silicon-on-insulator, and engineered substrates and the heterogeneous integration," Micromachines, **12**(10), 1159 (2021). https://doi.org/10.3390/mi12101159
[37] Lee, K. H., Bao, S., Zhang, L., Kohen, D., Fitzgerald, E., & Tan, C. S. "Integration of GaAs, GaN, and Si-CMOS on a common 200 mm Si substrate through multilayer transfer process," Applied Physics Express, **9**(8), 086501 (2016). https://doi.org/10.7567/APEX.9.086501
[38] Afzal, W., Afaq, A., Rehman, S. U., & Rowe, W. S. T. "Performance comparative analysis of MESFET with Si, GaAs, SiC and GaN substrate effects," in: *2021 Photonics & Electromagnetics Research Symposium (PIERS)*, (IEEE, 2021). pp. 1–6. https://doi.org/10.1109/PIERS53385.2021.9694726
[39] Singh, S., Chaudhary, T., & Khanna, G. "Recent advancements in wide band semiconductors (SiC and GaN) technology for future devices," Silicon, **14**, 5793–5800 (2022). https://doi.org/10.1007/s12633-021-01362-3
[40] Kumar, A., Muralidharan, R., & Narayanan, G. "Comparison of GaN and GaAs based Hall magnetic sensor for power applications," in: *2022 IEEE International Symposium on Smart Electronic Systems (iSES)*, (IEEE, 2022), pp. 1–6. https://doi.org/10.1109/iSES54909.2022.00071
[41] Lin, H.-C., Chang, D.-C., Fan, T.-H., & Chiou, H.-K. "A 3.6–4.5 GHz Doherty RF power amplifier using 0.25 μm GaN/SiC HEMT and GaAs IPD technology," in: *2023 IEEE CPMT Symposium Japan (ICSJ)*, (IEEE, 2023), pp. 1–4. https://doi.org/10.1109/ICSJ59341.2023.10339579
[42] Abdullayev, J.Sh., Qalandarova, D., Ibragimova, M., Akberadjiyeva, U., Yunusova, D., Jumaboyeva, Z., Shoyusupov, S., & Jumaniyozov, I. "Critical size and doping thresholds governing band gap evolution in semiconductors," East European Journal of Physics, (2), 203–211 (2026). https://doi.org/10.26565/2312-4334-2026-2-21
[43] Sergeenko, M., Chumakov, V., & Prokopenko, N. "Structure-logic circuits of self-compensation sub-circuits of CMOS transistor's (Si-SOI, GaN, GaAs, SiC) parasitic capacitances in high-impedance unit of high-temperature transimpedance and operational

amplifiers," in: *2024 International Conference on Actual Problems of Electron Devices Engineering (APEDE)*, (IEEE, (2024), pp. 1–5. https://doi.org/10.1109/APEDE59883.2024.10715887
[44] Gasmi, F. Z., Chemam, R., & Graine, R. "Development and study of the physical properties of gallium nitride (GaN) nanoparticles by ion implantation," Indian Journal of Physics, **100**, 1419–1436 (2026). https://doi.org/10.1007/s12648-025-03869-6
[45] Algora, C., García, I., Delgado, M., Vázquez, C., Hinojosa, M., & Rey-Stolle, I. "Beaming power: Photovoltaic laser power converters for power-by-light," Joule, **6**(2), 340–368 (2022). https://doi.org/10.1016/j.joule.2021.12.011
[46] Fafard, S., Proulx, F., York, M. C. A., Richard, L. S., Provost, P. O., *et al*. "High-photovoltage GaAs vertical epitaxial monolithic heterostructures with 20 thin p/n junctions and a conversion efficiency of 60%," Applied Physics Letters, **109**, 131107 (2016) https://doi.org/10.1063/1.4964120
[47] Schubert, J., Oliva, E., Dimroth, F., Guter, W., Loeckenhoff, R., *et al*. "High-voltage GaAs photovoltaic laser power converters," IEEE Transactions on Electron Devices, **56**(2), 170 –175 (2009). https://doi.org/10.1109/TED.2008.2010603
[48] Fernández, E. F., García-Loureiro, A., Seoane, N., & Almonacid, F. "Band-gap material selection for remote high-power laser transmission," Solar Energy Materials and Solar Cells, **235**, 111483 (2022). https://doi.org/10.1016/j.solmat.2021.111483
[49] Abdullayev, J. S., Qalandarova, D. A., Ibragimova, M. S., Sapaev, I. B., & Razzokov, J. I. "Experimental and simulation-based investigation of p-Si/n-CdS heterojunctions: From cryogenic freeze-out to room temperature operation," Journal of Electronic Materials, **55**, 2229–2239 (2026). https://doi.org/10.1007/s11664-025-12642-8
[50] Buffolo, M., Favero, D., Marcuzzi, A., De Santi, C., Meneghesso, G., & Zanoni, E. "Review and outlook on GaN and SiC power devices: Industrial state-of-the-art, applications, and perspectives," IEEE Transactions on Electron Devices, **71**(3), 1344–1355 (2024). https://doi.org/10.1109/TED.2023.3346369
[51] Abdullayev, J. S., Sapaev, I. B., Kadirov, S. R., & Abdullayev, J. Sh. "Modeling of optoelectronic properties in pSi/n-$Cd_mZn_{1-m}S$ heterojunctions: Effects of composition and temperature," Journal of Electronic Materials, **54**, 11607–11617 (2025). https://doi.org/10.1007/s11664-025-12480-8
[52] Akyol, F., & Ozden, H. "Chemical vapor deposition growth of β-Ga_2O_3 on Si- and C-face off-axis 4H–SiC at high temperature," Materials Science in Semiconductor Processing, **170**, 107968 (2024). https://doi.org/10.1016/j.mssp.2023.107968
[53] Qalandarova D. A., Ibragimova, M. S., Abdullayev, J. S., & Sapaev, I. B. "Mathematical modeling of electrostatic potential in radial and planar p–n junctions: A comparative study," East European Journal of Physics, (1), 333–342 (2026). https://doi.org/10.26565/2312-4334-2026-1-39
[54] Abdullayev J. S., Ibragimova, M. S., Abdullayev, J. S., & Sapaev, I. B. (2026). Cryogenic material and electrophysical changes in Si and GaAs. East European Journal of Physics, (1), 343–350. https://doi.org/10.26565/2312-4334-2026-1-40
[55] Autran, J.-L., & Munteanu, D. "Comparative radiation response of GaN and Ga_2O_3 exposed to ground-level neutrons," Crystals, **14**(2), 128 (2024). https://doi.org/10.3390/cryst14020128
[56] Bian, D., & Luan, S. "Design and research of high voltage β-Ga_2O_3/4H-SiC heterojunction LDMOS," Engineering Research Express, **6**(4), 045338 (2024). https://doi.org/10.1088/2631-8695/ad8f16
[57] Devi, K. N., Hariprasad, S., Natarajan, R., Chinnaswamy, S., & Ravi, S. "Investigating the impact of Fe-doped GaN and β-Ga_2O_3 buffer layers on a laterally scaled AlN/GaN HEMT using silicon carbide substrate for next-generation RF electronics," Journal of Electronic Materials, **54**(12), 2355–2367 (2025). https://doi.org/10.1007/s11664-024-11672-y
[58] Ferents, K., Jiavana, K., Kasthuri Bha, J. K., Kayalvizhi, S., & Natarajan, R. "Comparative analysis of $In_{0.15}Ga_{0.85}N$ and β-Ga_2O_3 back barriers in β-Ga_2O_3-buffered AlGaN/GaN HEMT structures," Physics of the Solid State, **68**, 50–63 (2026). https://doi.org/10.1134/s1063783425603339
[59] Hishiki, F., Akiyama, T., Kawamura, T., & Ito, T. "Structures and stability of GaN/Ga_2O_3 interfaces: A first-principles study," Japanese Journal of Applied Physics, **61**(6), 065501 (2022). https://doi.org/10.35848/1347-4065/ac5e90
[60] Kelly, F. P., Landi, M., & Kim, K. "Vertical p-GaN/n-Ga_2O_3 heterojunction diodes enabled by PAMBE," Applied Physics Letters, **126**(17), 172106 (2025). https://doi.org/10.1063/5.0260105
[61] Abdullayev, J. Sh., Sapaev, I., Abdikayimova, G., Akhmadaliev, S., Gulomova, M., Kholbekov, S., & Ruzmetov, K. S. "Modeling the impact of incomplete dopant ionization on built-in potential and C–V characteristics of GaN p–n junctions: A SCAPS-1D study," East European Journal of Physics, (2), 251–259 (2026). https://doi.org/10.26565/2312-4334-2026-2-27
[62] Kelly, F. P., Landi, M. M., Vesto, R. E., Tadjer, M. J., Hobart, K. D., & Kim, K. "Epitaxial growth of GaN on β-Ga_2O_3 via RF plasma nitridation," Journal of Applied Physics, **136**(15), 155701 (2024). https://doi.org/10.1063/5.0233590
[63] Mounika, B., Ajayan, J., Dwivedi, A. K., Sharma, P., & Sun, S. "Electrostatic analysis of AlN/GaN HEMTs using β-Ga_2O_3 buffer on SiC and β-Ga_2O_3 wafers for 5G/6G wireless infrastructure and future sub-THz applications," Journal of Electronic Materials, **55**, 3203–3220 (2026). https://doi.org/10.1007/s11664-026-12678-4
[64] Murugapandiyan, P., Revathy, A., Ramkumar, N., Saravana Kumar, R., & Mohanbabu, A. "Comparative study of AlGaN/InGaN/β-Ga_2O_3 and InAlN/InGaN/β-Ga_2O_3 HEMTs for enhanced RF linearity," Journal of Electronic Materials, **54**, 2340-2354 (2025). https://doi.org/10.1007/s11664-024-11664-y
[65] Qu, A., Xie, Z., Wang, Y., Hu, G., & Tan, C.-K. "Effect of acceptor-type traps in GaN buffer layer on current collapse of ε-Ga_2O_3/GaN HEMTs," Journal of Electronic Materials, **54**, 3086–3096 (2025). https://doi.org/10.1007/s11664-025-11823-9
[66] Abdullayev J. Sh., Qalandarova D. A., & Ibragimova M. Sh. "Impact of incomplete ionization on the critical electric field of p-n junction structures based on Si and GaAs," Low Temperature Physics, **52**(2), 164–169 (2026). https://doi.org/10.1063/10.0042291
[67] Shin, M.-C., Lee, Y.-J., Kim, D.-H., Jung, S.-W., Schweitz, M. A., Shin, W. H., Oh, *et al*., "Improved electrical characteristics of gallium oxide/p-epi silicon carbide static induction transistors with UV/ozone treatment fabricated by RF sputter," Materials, **14**(5), 1296 (2021). https://doi.org/10.3390/ma14051296
[68] Xu, K., Wang, R., Wang, Y., Wang, J., Zhi, T., Yang, G., Xue, J., *et al*., "Advances and prospects in Ga_2O_3/GaN heterojunctions: From fabrication to high-performance devices," Materials Science in Semiconductor Processing, **185**, 108874 (2025). https://doi.org/10.1016/j.mssp.2024.108874
[69] Abdullayev, J. Sh., Babajanov, L., Babayazova, N., Sapaev, I., Ruzmetov, K. S., & Esanov, E. "Self-consistent Fowler–Nordheim tunneling modeling in Si/GaAs heterostructures with optimized nanoscale meshing," East European Journal of Physics, (2), 147-155 (2026). https://doi.org/10.26565/2312-4334-2026-2-14

ПОРІВНЯЛЬНИЙ АНАЛІЗ ЕФЕКТІВ НЕПОВНОЇ ІОНІЗАЦІЇ У ГЕТЕРОПЕРЕХОДАХ p-SiC/n-Ga_2O_3 ТА p-GaN/n-Ga_2O_3 У ДІАПАЗОНІ ТЕМПЕРАТУР 77–400 K

О.А. Саттарова[1], М.Ш. Ібрагімова[2], А.Х. Чорієв[3], А. Абдукарімов[4], Джурабек Камолов[5]

[1]Ургенчський державний медичний інститут, 220100, вулиця Аль-Хорезмі, 28, Ургенч, Узбекистан

[2]Ургенчський державний університет, вулиця Хаміда Олімджона, 14, Ургенч, 220100 Узбекистан

[3]Національний дослідницький університет ТІІАМЕ, кафедра фізики та хімії, Ташкент, Узбекистан

[4]Ташкентський державний технічний університет, Ташкент, Узбекистан

[5]Бухарський державний університет, Бухара 200117, Узбекистан

Це дослідження представляє комплексне порівняльне дослідження широкозонних гетеропереходів p-SiC/n-Ga_2O_3 та p-GaN/n-Ga_2O_3, з особливим акцентом на вплив неповної іонізації легуючої домішки в діапазоні температур 77–400 K. Температурно-залежні енергії ширини забороненої зони GaN, SiC та Ga_2O_3 були змодельовані за допомогою співвідношення Варшні, що дало чудову відповідність з опублікованими експериментальними даними, з коефіцієнтами кореляції (R^2) 0,981, 0,975 та 0,978 відповідно. Розраховані ширини забороненої зони дещо зменшувалися зі збільшенням температури, змінюючись від 3,51 до 3,40 еВ для GaN, від 3,33 до 3,25 еВ для SiC та від 4,90 до 4,87 еВ для Ga_2O_3. Відповідні зміщення зон гетеропереходу становили приблизно 1,36–1,50 еВ для Ga_2O_3/GaN та 1,57–1,62 еВ для Ga_2O_3/SiC, що підтверджує узгодженість та надійність прийнятої моделі вирівнювання зон. Аналіз електричного поля продемонстрував високу теплову стійкість в обох гетероструктурах. Максимальне електричне поле досягло $3,92 \times 10^5$ В/см для гетеропереходу p-GaN/n-Ga_2O_3 та $3,98 \times 10^5$ В/см для гетеропереходу p-SiC/n-Ga_2O_3 при 77 K, демонструючи при цьому зміну менше ніж на 3% до 400 K. Крім того, електричне поле демонструвало передбачувану залежність від концентрації легування, збільшуючись приблизно від 25 кВ/см до 80 кВ/см зі збільшенням рівня легування від 2×10^{14} до 2×10^{16} $см^{-3}$. За кімнатної температури гетероперехід p-GaN/n-Ga_2O_3 демонстрував дещо вищу напруженість електричного поля через більший зсув зони провідності, тоді як структура p-SiC/n-Ga_2O_3 демонструвала покращені низькотемпературні характеристики, що пояснюється неповною іонізацією легуючої домішки та відповідними ефектами перерозподілу носіїв заряду. Результати дають нове розуміння впливу неповної іонізації легуючої домішки на температурно-залежну поведінку гетеропереходів p-SiC/n-Ga_2O_3 та p-GaN/n-Ga_2O_3, забезпечуючи теоретичну основу для проєктування широкозонних силових пристроїв. Ці характеристики підкреслюють значний потенціал гетеропереходів на основі Ga_2O_3 для високовольтних і високотемпературних силових електронних застосувань наступного покоління, зокрема перетворювачів потужності для електромобілів, аерокосмічної електроніки та промислових систем, що працюють у суворих умовах. Тим не менш, для повної оцінки практичної продуктивності пристроїв та оптимізації конструкції гетеропереходу необхідні подальші дослідження, що включають аналіз впливу стану інтерфейсу, аналіз напруги пробою, механізми струму витоку, тепловий опір та оцінку довгострокової надійності.

Ключові слова: *GaN; SiC; Ga_2O_3; іонізація домішок; неповна іонізація; кріогенні пристрої; температурні ефекти; фактор ідеальності*